SAPIENZA
UNIVERSITÀ DI ROMA

Sapienza University of Rome
Department of Earth Sciences
Ph.D. in Earth Sciences

Thesis submitted for the degree of Doctor of Philosophy

Tectonics, Lithology, and Climate Interaction in the Landscape Evolution of Talesh Mountain Range (NW Iranian Plateau)

Ph.D. candidate
Mohammad Moumeni

Supervisors
Prof. Marta Della Seta
Prof. Paolo Ballato
Prof. Reza Nozaem

Contents

Abstract

To comprehend the evolution of a landscape in response to the plate interior crustal deformation and strains over long timescales, it is necessary to investigate the interactions between tectonics, climate, and lithology. Investigating the interaction between these factors and isolating the role of each one yields an applied procedure for the landscape evolution. In this respect, Talesh Mountains which is a prominent tectonic range in the NW of Iranian Plateau and formed by the compressional stresses transferred from the Arabia-Eurasia continental collision, provide a unique case study to explore the interplay between tectonics and surface processes in this tectonically active setting. The range shows a transient landscape resulting from a combination of several tectonic events (Eocene-Pliocene), spatial variation of climatic conditions and rock strength contrasts. The N-NW-trending Talesh Fault is the main active structure, which promotes the recent growth of relief and topographic barrier. The orographic barrier controls the spatial variability of climate by promoting an intense precipitation rate on the Caspian Sea wet flank and low rainfall in the interior of the plateau. To date, the main governing agents that control the architecture of present-day landscape of the region, and its evolutionary path have not been fully studied. This study focuses on the geomorphic response of the river network and drainage divides, to the combined contribution of tectonic uplift, orographic precipitation, and lithological variation in the Talesh Mountains. In detail, I combined geomorphological field survey with quantitative analysis of regional topography, geomorphology and stability of the main drainage divide and with stream profile analysis (i.e., longitudinal profiles, knickpoints characterization, χ-plot and stream projections) and 10Be-derived denudation rates in order to decipher the surface deformation, uplift mechanism and drainage divide evolution in this tectonic setting. Additionally, I performed inverse modelling of the river longitudinal profiles to reconstruct the base level fall history of the region, which gives us insights into the timing of uplift rates of NW margin of the Iranian plateau in the context of topographic development and surface processes with the regional geodynamics of the region. In the Talesh Mountains, the main drainage divide is characterized by spatial variation of rock-types and topographic characteristics (i.e., local relief, slope, channel steepness). Since the exposure of lithologies with different strength can promote drainage reorganization and lead to landscape transience, I isolated the effects of bedrock erodibility on the landscape evolution processes by measuring the mechanical rock strength. I acquired the uniaxial compressive strength of the lithological units in the three sectors of the mountain ranges. To better isolate the lithological signal from tectonic and climate changes on topographic relief in the Talesh Mountains, the values of mean annual rainfall have been taken into the calculation of k_{sn} and χ (k_{snQ} and χ_Q).

The credible scheme for the landscape evolution of the study area is associated to the contrasting erosion rates across the divide. The erosion rates from cosmogenic meteoric ^{10}Be ranging from ~ 100 to 400 m/Myr, with lower values in the interior, and higher values in the plateau exterior correlate with topographic metrics. The spatial pattern of erosion rates shows that drainage networks in the eastern flank of the range, along the plateau margin, are eroding about twice as fast as those in the plateau interior. These contrasting erosion rates caused the divide migration towards the plateau interior. The efficiency of erosion can be determined by the climate and the strength of exposed rocks. However, I can infer that divide migration is occurring in the study area in response to the asymmetric uplift, erosion patterns and is chiefly controlled by topography. While the precipitation variation has potentially been assisting and magnifying the landscape transience. Our results show that climate does not exert a strong control on topography and erosional efficiency in the study area. Accordingly, the results show the presence of an uplift gradient that is holding the divide in place in the northern and southern parts, and the χ metric is sensitive to this uplift rate gradient and represents the expected response of the divide when the uplift is eliminated. Exhumation of strong bedrock units in the northern and southern sectors, and weak ones in the central sector have inhibited and intensified erosion, respectively, and this heterogeneous exhumation of rocks initiated topographic rejuvenation mostly in the central Talesh Mountains to a local scale.

The reconstructed uplift history using inverse modelling indicated a progressive increase in the rock-uplift rate at ~12 Ma which reached its peak at ~ 4 Ma up to ~0.5 mm/yr. Thermochronometry data and river inversion analysis from our ^{10}Be erosion rates dataset, suggest that strain partitioning may have been active at least since ∼10 Ma. We can infer that during the last ~10 Ma a large wavelength process was synchronous with localized shortening and thickening in the Talesh Mts. The configuration of high precipitation, steepness values, millennial meteoric cosmogenic ^{10}Be erosion rates, and longer-term exhumation rates in the eastern flank of the range probably started to develop during the last 10 Ma and led to the progressive coincidence of focused precipitation and tectonic activity. Such feedback may have been amplified during the ∼ 6 to 3-Myr-old base-level drop of the Caspian Sea. Consequently, we suggest possible long-term feedback among tectonics, topography, and surface processes/runoff variability in the Talesh Mts. The erosion rates are set by tectonic activity and the efficiency of these processes which are driven by climate, together with lithology control the orogenic architecture.

Chapter 1

Introduction: Aim of the thesis, regional setting of the study area

1.1.Motivations and descriptions of the thesis

Talesh Mountains show a complex zone in terms of tectonic and surface processes and represent features of a transient landscape resulting from a combination of recent tectonic activity, spatial climate variation and rock strength contrasts. Nevertheless, the effects of these tectonic uplift and deformation phases alongside lithological characteristics and orographic rainfall on the landscape and their footprints on the geomorphological architecture of the study area are not fully understood. Thus, to analyze the landscape evolution at the orogen scale in response to active tectonics, the role of these governing signals should be separated and outlined.

There are several open questions regarding the timing and spatial patterns of surface uplift and these driving factors in the landscape evolution of the Talesh Mts. which is a regional key area to unravel these signals including:

i. Are there any orogen across-strike differences in erosion? How do they vary along the mountain flanks (interior and exterior plateau)?
ii. What are the latest phases of the main uplift rate and their relationship with landscape transience?
iii. What are the long-term effects of protracted tectonic activity and orographic precipitation on landscape evolution?
iv. What are the local and regional scale effects of differences in rock strength and erodibility on the evolution of the landscape?

To answer these questions and fill the gaps, this research is focused on the geomorphic response of the river network and drainage divides, to the combined contribution of tectonic uplift, orographic precipitation, and lithological characteristics of the Talesh Mountains. Moreover, by constraining the uplift history and late Cenozoic evolution process I try to understand the complex feedback between tectonic and climate involved in the surface process. Investigating the interaction between these factors and isolating the role of each one yields an applied procedure to disclose the main governing agent/s that control the architecture of present-day landscape, and its evolutionary path.

Since, drainage divide migration is a fundamental part in the tectonic-climate-erosion interaction system, in detail, I employed geomorphometric approach and utilized the tools for quantifying drainage divide reorganization, spatial variation in the rock uplift rates and knickpoints distribution which will help us to understand uplift mechanism, surface deformation and the evolution of drainage networks in this tectonic setting. To isolate the rock type effect on the landscape, I measured the compressive rock strength through the utilization of a Schmidt hammer and point load test.

Finally, to explore the history of topography development of the region, I analyzed the landscape of the NW Iranian Plateau over different temporal scales. I integrated long-term (apatite fission track data: 10^6–10^8 yrs), mid-term (cosmogenic meteoric ^{10}Be: 10^3–10^5 yrs), and short-term (Optically stimulated luminescence (OSL) from river and lacustrine sediments: 10^3–10^4 yrs) to investigate trajectory of landscape evolution.

I integrated denudation rates from meteoric ^{10}Be and topographic analysis. Furthermore, I investigate the relationships of climate and lithology with catchment-averaged erosion rates and evaluate geomorphic evidence of the divide instability with new dataset of erosion rates. I present 11 erosion rates derived from meteoric ^{10}Be of river-borne sediments on east and western flanks of Talesh Mountains in NW margin of Iranian plateau. Our aims are to identify erosion rate patterns in the interior and exterior of the plateau to determine spatial variability among these erosion rates, their relationship with topographic features of the range, and to identify the governing factors shaping the landscape. Thus, to investigate the role of erosion patterns on the river network and landscape evolution of the range, I analyzed the stream network on catchment scale and drainage divide.

Consequently, I explored the rock-uplift rate history in the region by running some inversion models for the sampled catchments in the plateau interior and exterior and proposed a model for the landscape evolution of the Talesh Mts. in the NW margin of Iranian Plateau.

1.2.Global scale studies on mountain landscape evolution

1.2.1. Isolating tectonic, lithology, and climatic controls

The interaction between climate, tectonics, and lithology often occurs in mountainous environments, making it challenging to separate and measure their individual influences on shaping the topography and erosion processes. In dynamic mountain-building regions, surface processes encompass erosion and sediment deposition mechanisms, influenced by the intricate interactions between tectonic and climatic forces (e.g., Adams et al., 2020; Lague 2014; Whipple et al., 2013).

Tectonic activities result in the uplifting of rock, creating topographical relief and mountain ranges, and studying landscapes offers valuable information about the development of orogenic belts. Rivers are the primary agents responsible for creating most of the topographical relief, and their shapes are the result of a combination of factors, including tectonic activity, climate, lithology, and more (Kirby and Whipple 2001; Ouimet et al. 2009). While, numerous studies concentrate on the geological structure, climate, lithology and etc. on the river profiles, tectonic uplift rate exerts significant influence over river channel (e.g., Sklar and Dietrich 2001; Forte et al. 2016; Wang et al. 2019; Seybold et al. 2021).

1.2.1.1.Tectonic control

In long timescales (10^4- 10^6 yr) tectonics has a fundamental control on base level and drainage divide movement in regional scales (e.g., Ye et al., 2022). River network and drainage divides respond to the uplift gradients by incision, headward erosion, and divide migration in the headwaters, respectively (e.g., Willett et al., 2014; Whipple et al., 2017). In a study in North China, Ye et al. (2022) propose that the drainage divide is migrating from the high-uplift side towards the geometric center of the range, which is driven by the asymmetric uplift. Some studies attribute drainage divide migration to vertical tectonic movement (e.g., He et al., 2019; Su et al., 2020), and others show migration of drainage divide in response to strike-slip faulting (Zeng and Tan, 2023).

The effects of strike-slip faulting regime on the river adjustment by earthquake ruptures and surface processes investigated in several field and laboratory studies (e.g., Goren et al., 2014; Duvall and Tucker, 2015; Li et al., 2021). In another study, in the two main mountain ranges of the Northern Andes, Ott et al. (2023) propose that faster erosion rates in the Eastern Cordillera than to the western flank show asymmetric tectonic uplift. Moreover, they suggest that coupled with landscape evolution, erosion rates illuminate rock uplift patterns through space and time which can be used to comprehend timing of surface uplift and erosion rates patterns in the Central and Eastern Cordillera.

1.2.1.2.Lithological control

In addition to tectonics, and climatic variations, drainage divides migrate in response to difference in rock strength, stratigraphic and structural configuration of the lithological units (Willett et al., 2014 Zondervan et al., 2020).

The rock strength exerts control on the landscape evolution of mountainous regions by (1) governing the ability of material to be removed, displaced, and transported by surface processes (e.g., Gilbert, 1877; Hack, 1975; Schmidt & Montgomery, 1995; Townsend, 2021), and (2) local relief expression by controlling the hillslopes (e.g., Whipple & Tucker, 1999). On the other hand, it is suggested that rock fracture density rather than rock strength controls the river erosion process (e.g., Molnar et al. 2007).

The erodibility coefficient in the stream power incision model which is approximated by lithological type gets incorporated into the landscape evolution models (e.g., Stock & Montgomery, 1999). Since different lithologies have different degrees of erosional resistance, lithology is a crucial element impacting *K*. On the other hand, lithology cannot simply be related to the *K* coefficient without taking climate into account as suggested by Snyder et al. (2000) given that the erosion coefficients under the same lithologic circumstances differ by two orders of magnitude. In a study in North Tianshan where intense weathering breaks down rock material, Hou et al. (2023) show that combinations of sediment supply, fracture density and lithological features could affect the landscape.

Hu et al. (2023) showed that the erosion coefficient for sedimentary rocks is higher than that for metamorphic rocks in Taiwan Island and the Bolivian Andes, and there is no difference in erodibility between metamorphic and intrusive rocks in San Gabriel Mts. and the Qilian Shan. Moreover, they say that in tectonically active ranges for competence rocks such as granites and metamorphic rocks there is no correlation with the *K*, contrary to soft sedimentary rock units. In a study by Zondervan et al. (2020), the drainage divide migration in the High Atlas in NW Africa attributed to the different lithologically and structurally groups of bedrock. They estimated the adjustment timescale in response to changes in erodibility of exposed bedrock. They proposed that the rock erodibility variation alone can influence drainage divide mobility in a collisional mountain belt.

1.2.1.3.Climate effect

Based on Leonard and Whipple (2021) if erosional processes in the landscapes which experience orographically enhanced precipitation are sensitive to spatial and/or temporal variations in precipitation, then changing orographic precipitation patterns should influence mountain landscape evolution. Moreover, SPIM suggests that an increase in precipitation will increase the erosion coefficient.

Some studies suggest that precipitation exerts a strong control on the erosion coefficient (e.g., Ferrier et al., 2013; Adams et al., 2020). On the other hand, the relationship between these factors has not been resolved due to the effects of several perplexed components (e.g., Snyder et al., 2000; Portenga & Bierman, 2011; Hu et al., 2023 and references therein). Hu et al. (2023) found a power function relationship between erodibility coefficient and precipitation with a relatively high correlation. They conclude that climatic factors may be a major controlling factor on the erodibility variations which affects the steepness of the orogens. According to Lamb and Davis (2003), the tectonic uplift of the central Andes and extended aridity are positively correlated, considering the western slope of the orogen's prolonged aridity. Strecker et al. (2007) compared the erosional evolution of the eastern and western flanks of the Andes. They suggest that these changes are connected with the formation of orographic barriers that blocked moisture-bearing winds.

1.3.Talesh Mountains orogenic system

The Arabia- Eurasia continental collision system is one of the few active continental collision zones on Earth due to ongoing convergence along the NNE direction (Fig. 1.1), where the maximum post-collisional deformation occurred in the Late Miocene to Pliocene with accumulation of shortening in Caucasus, Alborz, and Zagros Mts. and the accelerated exhumation was chiefly controlled by surface uplift and erosion (e.g., Allen et al., 2004; Ballato et al., 2011; Agard et al., 2011; Allen, 2021).

The Iranian Plateau is a large actively deforming region which developed in response to the collision between the Arabian and the Eurasian plates (e.g., Allen et al., 2004; Ballato et al., 2011; Agard et al., 2011) (Fig. 1.1). The stress was transferred from the collision zone to the northern margin of the Iranian Plateau (e.g., Berberian, 1983; Jackson et al, 2002; Allen et al, 2003; Guest et al, 2006; Ballato et al, 2008 and 2017). Spatial and temporal evolution of deformation at the northern edge of the Arabia- Eurasia collision zone seems to result from complex interaction between the rigid South Caspian Basin in the north and the Central Iranian Block to the south (e.g., Allen et al., 2003; Ballato et al., 2013). This important NW–SE-oriented structural feature represents an elongated, thickened, and low-topographic relief morphotectonic province (e.g., Ballato et al., 2013, 2017; Vernant et al., 2004), and encompasses actively deforming orogenic belts (Vernant et al., 2004; Ballato et al., 2017). Surface processes may have significantly contributed to redistributing mass, thereby influencing the shallow crustal stress field and fault activity (Ballato et al., 2015).

Talesh Mountains are prominent tectonic features at the NW border of the Iranian Plateau which are influenced by the compressional stresses transferred from the Arabia-Eurasia continental collision. The orogen has a curved geometry that bends around the southwestern margin of the South Caspian Block from EW to NW and WNW (e.g., Madanipour et al., 2013:2017; Allen et al., 2003; Jackson et al., 2002; Berberian, 1983). The regional uplift associated to the activity of the N-NW-trending Talesh Fault which forms a topographic barrier, has an important role in the evolution of the region. In terms of lithological characteristics, the thick Cenozoic strata in the Talesh Mountains chiefly comprise volcanic and volcaniclastic rock units, which were rapidly deposited in an extensional sedimentary basin (Fig. 1.2) (Madanipour et al., 2017 and reference therein).

In the central and northern Talesh Mountains, Cenozoic sedimentary and volcanic sequences are exposed. Older rock units are locally exposed in the core of anticlines (Fig. 1.2) (Vincent et al., 2005; Madanipour et al., 2013). Lower Cenozoic volcanic and volcaniclastic rock units are unconformably covered by coarse- to medium-grained clastic rocks of upper Cenozoic (Fig. 1.2).

This angular unconformity documents that the early-middle Eocene extension was followed by compression in the late Eocene-early Oligocene (Madanipour et al., 2017). This event is interpreted as the beginning of the late Cenozoic orogenic evolution (Madanipour et al., 2013) (Fig. 1.2).

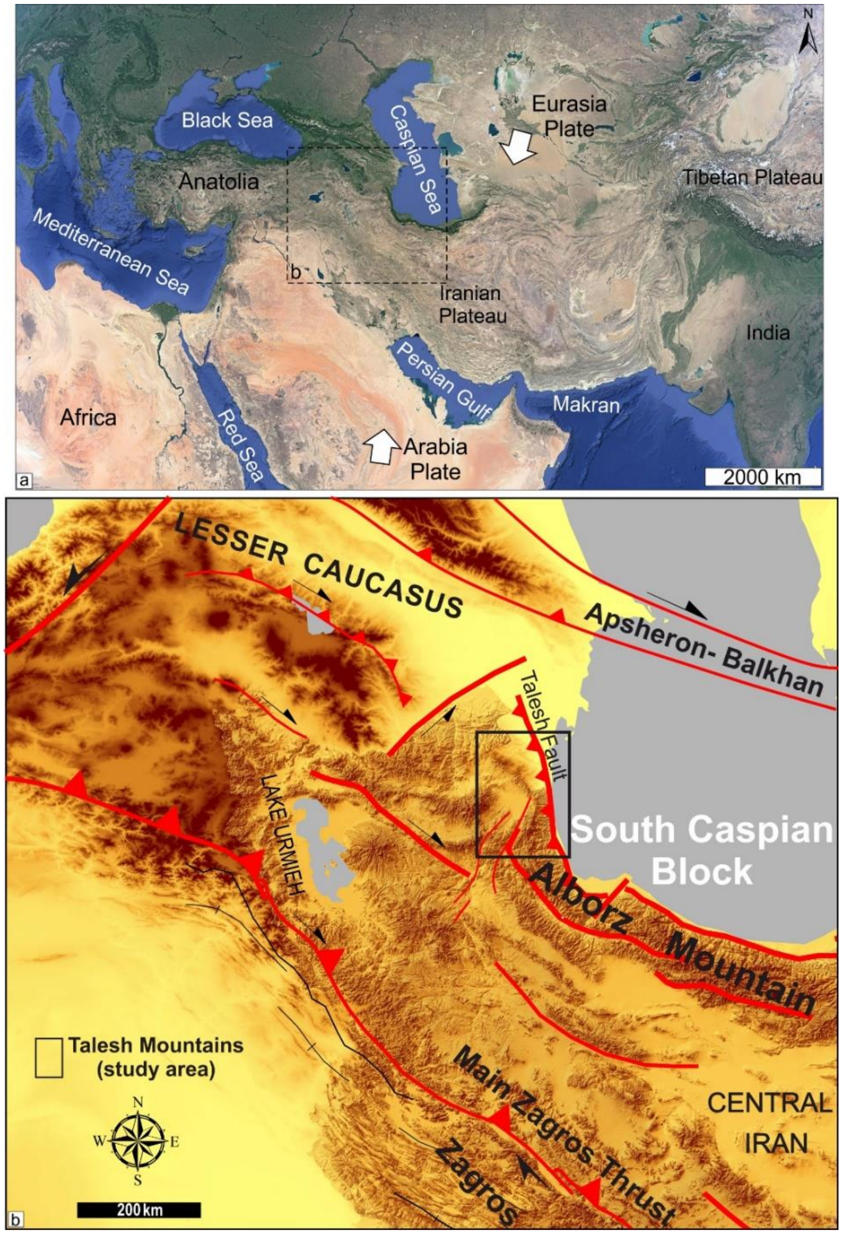

Figure 1.1. Location of the study area. (a) Arabia–Eurasia convergence zone with the main tectonic features. Location of the study area in NW Iranian plateau is shown with black dashed rectangle. (b) SRTM image and simplified tectonic map of NW Iran showing the major fault systems accommodating the Arabia-Eurasia convergence

The basement of the South Caspian Basin (SCB) is overlain by ~20 km of Cenozoic strata (Berberian, 1983). During the late Cenozoic this oceanic lithosphere was subducted northward along the Apsheron-Balkahn sill at a low angle below the Eurasian Plate (Jackson et al., 2002; Allen et al., 2002). Seismic and gravity data suggest southward underthrusting of the SCB beneath the continental crust of the Talesh Mountains (Jackson et al., 2002; Allen et al., 2003; Aziz Zanjan et al., 2013).

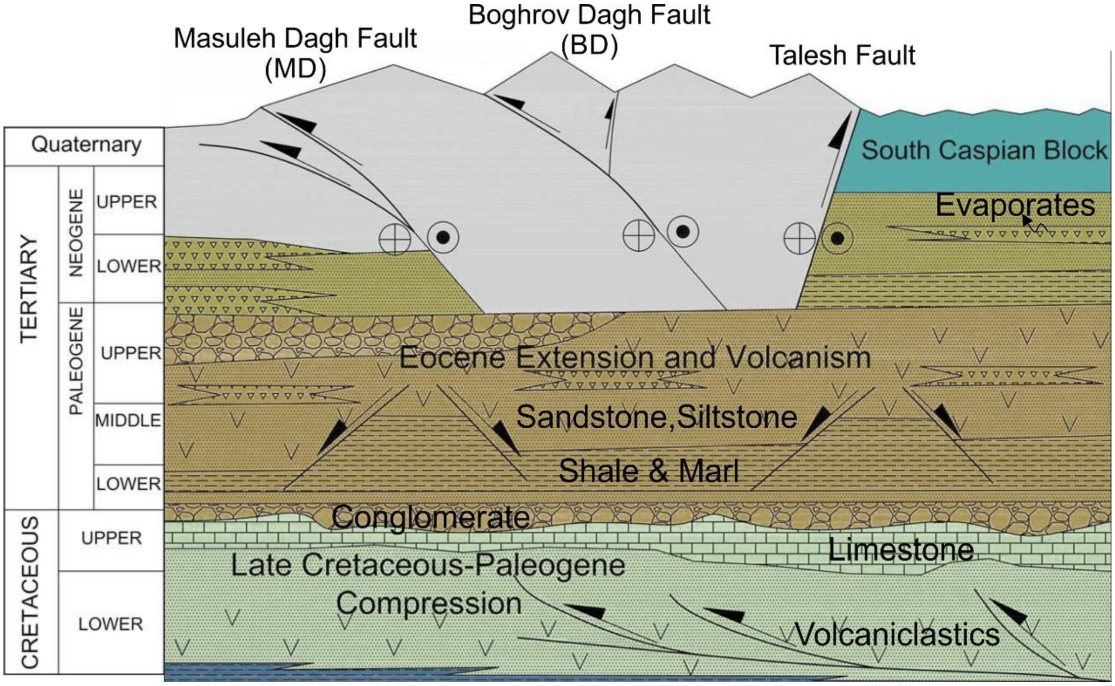

Figure 1.2. Tectonostratigraphic chart of the Talesh Mountains shows major rock units and deformation events from Cretaceous to Quaternary. Adapted from Madanipour et al. (2017), Guest et al. (2006), and Allen et al. (2003).

1.3.1. Seismicity

The seismicity patterns in the Talesh Mts. show a partitioning of oblique strain into strike-slip and dip-slip faulting (Allen et al., 2003; Madanipour et al., 2013 and 2017). The Masouleh Dagh (MD), Boghrov Dagh (BD), and Angut faults are the main structural features in the Talesh Mts. The MD and BD faults are the main structures that juxtapose pre-Cenozoic rocks over Neogene stratigraphic sequences (Madanipour et al., 2017).

Seismicity data and field survey show right-lateral strike-slip movement for these faults in the central Talesh Mts. (Madanipour et al., 2013 and references therein). The present-day active deformation in the western flank of the range in the plateau interior localized along a low angle thrust (Madanipour et al., 2017 and references therein).

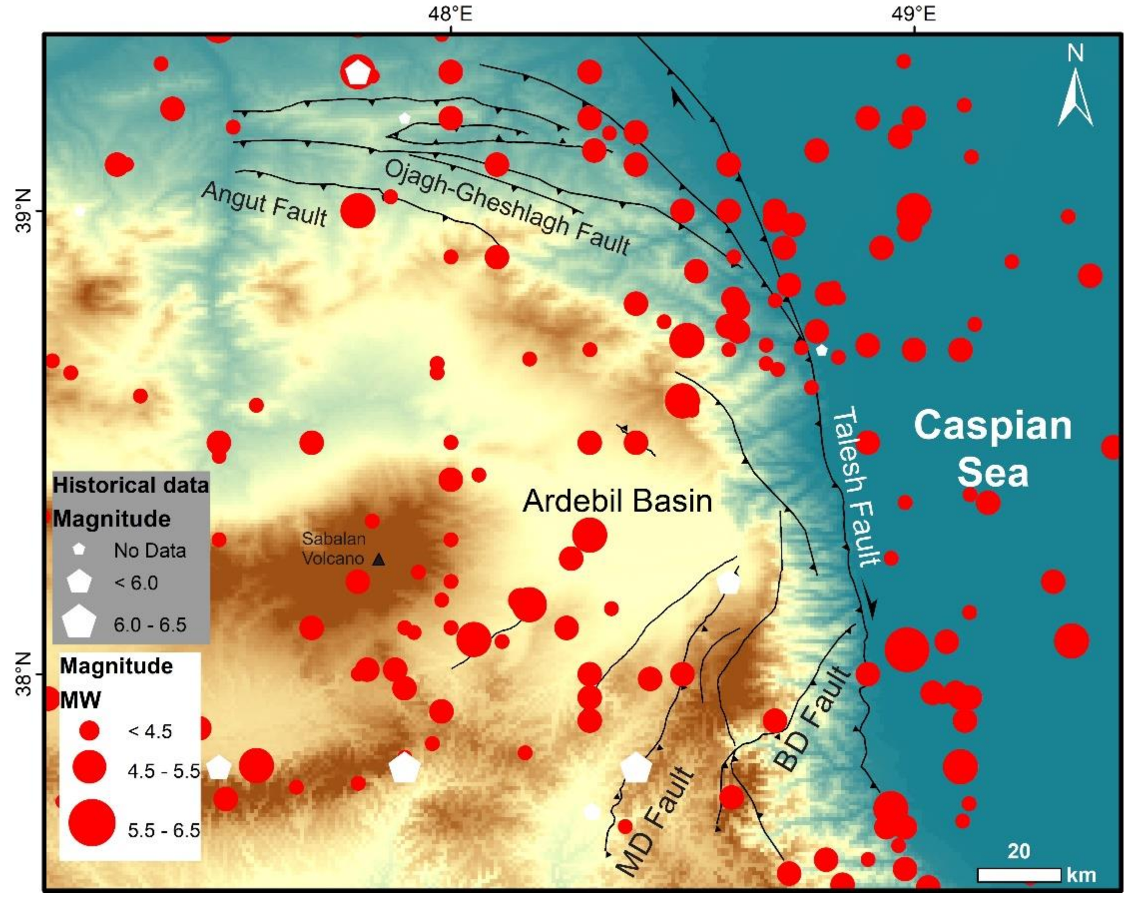

Figure 1.3. Distribution of historical and instrumental earthquakes in NW Iranian Plateau.

The earthquake mechanisms in Talesh Mts. show thrusting on shallow-dipping faults which are different from those in the Alborz Mts. which related to deeper active faults (e.g., Jackson et al., 2002). There is concentrated seismicity along the MD and BD faults (which also have some historical earthquake records) in the southern sector, and Angut and Ojagh-Gheshlagh faults in the northern sector with thrust kinematics (Fig. 1.3). Whereas, in the central sector there is almost no earthquake record. This seismicity pattern is consistent with the asymmetric uplift and deformation along the Talesh Mts.

1.3.2. Structural and lithological configuration

The Talesh Mts. have a curved geometry which is a result of the interaction with the rigid South Caspian Basin during the continental collision of Arabia-Eurasia (Jackson et al., 2002; Allen et al., 2003; Madanipour et al., 2013).

This initially straight terrane (during Eocene), bent after the Eocene into its present day orocline shape (e.g., Rezaeian et al., 2020). In terms of structure, Talesh Mts. can be divided into northern, southern sectors (NW trend) and central sector with a N-S strike (Madanipour et al., 2018). The unconformity (early Oligocene) in the range shows the initiation of regional compression (late Eocene - early Oligocene) after the extension phase and volcanism in late Paleocene-Eocene (Madanipour et al., 2017). Additionally, the lower-middle Miocene unconformity provides evidence for uplift and deformation. Madanipour et al. (2017) suggest that all the faults in the Talesh Mts. in the three sectors of the range had thrust kinematics during the early Oligocene to middle Miocene, and when regional convergent direction changed to N-oriented (middle Miocene) fault kinematic had a strike-slip component in the central sector. Based on restored cross sections in the Talesh Mts. the northern sector of the range experienced a total of ~20 km shortening in the late Cenozoic (Madanipour et al., 2017). The central sector where MD and BD faults strike change to north-south has experienced a total ~6–11 km of late Cenozoic shortening.

In the southern sector of the range, the oldest lithological units comprise carbonate and clastic rocks (lower Paleozoic) which are exposed in the hanging wall of the MD and BD Faults (e.g., Alavi, 1996; Zanchi et al., 2009; Madanipour et al., 2013). Volcanic rocks, clastic, and carbonate units (lower to middle Paleozoic) likely deposited in an extensional basin (Madanipour et al., 2017 and reference therein). The Mesozoic strata of the range composed of carbonate and clastic rock (Triassic to early Jurassic). Late Cretaceous-early Paleocene conglomerate and sandstone in the Talesh Mts. is the result of a compressional event during this time along the Neotethyan subduction zone (e.g., Madanipour et al., 2017). It has been proposed that volcanic and volcaniclastic Cenozoic units in the Talesh Mts. formed in a back-arc extension or transtension basin connected to Neotethyan subduction zone in the northern sector (Vincent et al., 2005; Madanipour et al., 2017).

1.3.3. Exhumation of the range

The detrital apatite fission track and bedrock apatite and zircon U-Th/He data along with stratigraphic growth strata, dominant folding and thrust faulting (Madanipour et al., 2013 and 2017) indicate several major compressional deformation and exhumation phases. Madanipour et al. (2017) proposed three major phases of exhumation in the Talesh Mts. in the late Oligocene (~27–23 Ma), middle Miocene (~18–12 Ma), and early Pliocene (~5 Ma), which in the middle Miocene (~12 Ma) an accelerated exhumation was observed. These phases were considered major tectonic exhumation events during the Late Cenozoic (Madanipour et al., 2017; Chu et al., 2021) and are associated with the early and final collision of Arabia-Eurasia and subsequent structural reorganization (Madanipour et al., 2013). Based on Madanipour et al. (2017), the stress field related to the early Oligocene phase (NE oriented) caused oblique thrust deformation in the entire range. While since ~12 Ma, N-oriented stress field caused thrust kinematics in the northern and southern sectors, and dextral strike-slip kinematic in the central sector. Madanipour et al. (2013) suggest that higher exhumation rate in the north, and southern sectors with respect to the central sector, might be attributed to greater shortening in these parts of the range. Also, the kinematic of the faults which control exhumation, may have been affected by the different orientation of these sectors respect to the regional compressional direction (Madanipour et al. 2013). Moreover, the early Pliocene phase, which was fast, caused the rapid incision of the rivers in the central sector which is attributed to the base-level fall of the Caspian Sea due to its isolation from the Paratethys (Madanipour 2023). This base level fall also extended inside the orogen and captured the rivers which internally drained the Iranian Plateau (Madanipour 2023).

1.3.4. Talesh Mountains orographic system

In the late Cenozoic, since the late Eocene the climate in central and northern Iran was hot and arid (e.g., Davoudzadeh et al., 1997). On the other hand, moisture from the Caspian Sea, forced into concentrated precipitation along the uplifting Alborz ranges (Ballato, 2009 and references therein). Paleoclimate data suggest that during the early-middle Miocene the Alborz range became an efficient orographic barrier (Ballato 2009; Ballato et al., 2010). Thus, since the Miocene, these mountains including Talesh, form an orographic and topographic barrier which separates the interior of the plateau from the Caspian Sea coastal plains (Fig. 1.1b). The positive feedback between orographically induced precipitation and rock-uplift rates must have only recently been established in the region (e.g., Ballato et al., 2010). In terms of modern climate, roughly 1000 mm/yr of precipitation falls along the northern flanks of the Talesh Mountains. On the contrary, the interior of the plateau in the Ardebil Basin the rainfall is less than 300 mm/yr.

1.4. Cosmogenic radionuclides ^{10}Be: an overview

The radioactive cosmogenic isotope Beryllium-10 (^{10}Be) (the word cosmogenic notes the cosmogenic origin) is a very rare, radioactive nuclide that is not present in natural materials and only produced by spallation reactions high energy cosmic ray particles with target nuclei (e.g., Lal, 1991) both in the atmosphere (meteoric) with the atmospheric N and O atoms and within mineral lattices (*in-situ*) in material at the Earth's surface (e.g., Heikkilä, 2007; Willenbring and von Blanckenburg, 2010; Fig. 1.4).

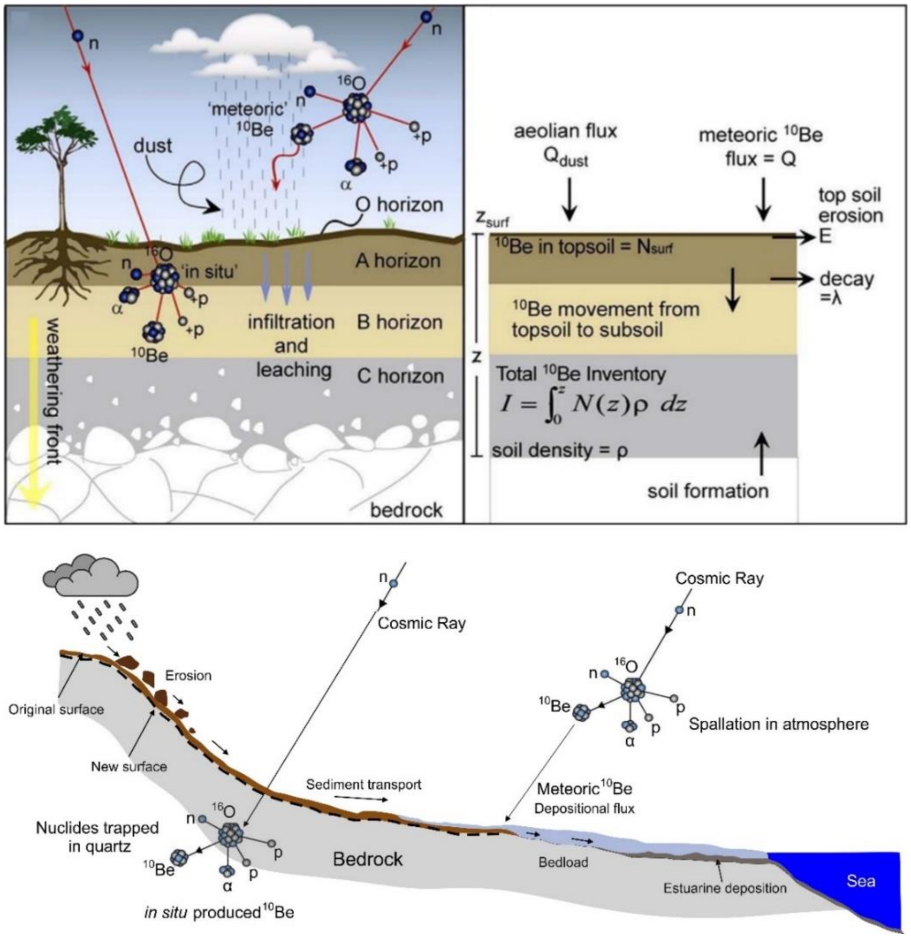

Figure 1.4. Schematic diagrams of production of meteoric ^{10}Be and *in situ* ^{10}Be by spallation with target nuclides in the atmosphere and in mineral lattices, respectively (shown in both soil and river profiles). Definitions of variables which are used to calculate the inventory of meteoric ^{10}Be is shown in the soil profile (adapted from Willenbring and von Blanckenburg, 2010; Padila et al., 2018).

Both in situ-produced and meteoric ^{10}Be accumulate in surficial deposits over time such that the concentration of the nuclide is related to both the age and stability of the surface material (Willenbring and von Blanckenburg, 2010). The production of ^{10}Be is modulated by solar activity and the strength of the geomagnetic field, and it decays radioactively according to the half-lives. ^{10}Be has a very long half-life of 1.5 million years, which means that its decay can mostly be neglected in relation to the short-time periods investigated in this study (e.g., Heikkilä, 2007).

1.4.1. *in situ*-produced ^{10}Be

A small amount of secondary cosmic rays like neutrons, protons, or muons reaches the Earth's surface where *in situ* ^{10}Be nuclides are produced by nuclear interactions in mineral lattices (Lal and Peters, 1967; Faure and Mensing, 2004). *In situ*-produced ^{10}Be has been used in many studies to measure erosion rates on surfaces exposed to cosmic radiation to acquire surface exposure date over the time span of 10^2-10^7 yr, in catchment-scale (e.g., Nishiizumi et al., 1989; Granger et al., 1996; Bierman and Steig, 1996, von Blanckenburg, 2005; Gosse and Phillips, 2001; Cockburn and Summerfield 2004). Nevertheless, *in situ* ^{10}Be techniques have some analytical and technical complications that restrict their applications. For example, it requires a large quantity of pure, coarse-grained quartz, which are not reliably available in sedimentary records, also the analytical requirements are extremely time consuming and expensive (e.g., Willenbring and von Blanckenburg, 2010).

1.4.2. Meteoric ^{10}Be tracer

Meteoric ^{10}Be has been used as a tracer for a wide set of Earth processes occurring over time scales of up to 10^7 years (Graly et al., 2011; and reference therein). Meteoric ^{10}Be in river sediment has been used as a quasi-quantitative proxy for watershed erosion rate (e.g., Brown et al., 1988; You et al., 1988). In this method, it is assumed that the integrated delivery rate of ^{10}Be from the atmosphere equals the flux of ^{10}Be out of the basin through sediment transport such that basin-scale mass loss rates can be calculated. The flux out of the basin was calculated by multiplying the sediment yield of the catchment with the concentration of meteoric ^{10}Be on these sediment samples. The yearly flux of meteoric ^{10}Be is independent of the rate of rainfall (Willenbring and von Blanckenburg, 2010), and the surface concentration is independent of the depth distribution of ^{10}Be in soils. Thus, with this constant flux, predictions of ^{10}Be flux over time are not limited to our knowledge of past precipitation rates, which is promising to use ^{10}Be techniques in modern and past sedimentary deposits where precipitation rates vary. Additionally, annual measurements of meteoric ^{10}Be flux have been used to estimate the long-term meteoric ^{10}Be deposition rate in lieu of measurements over geomorphic time frames (Graly et al., 2011). The application of meteoric ^{10}Be absorbed to sediment, follow the same approach used in *in situ* ^{10}Be where the production of cosmogenic nuclides in a basin eventually equals the export of nuclides from a basin through erosion of sediment (e.g., Granger et al., 1996). All these indicate that meteoric ^{10}Be tracer can serve as a powerful tool as the *in situ* ^{10}Be to derive erosion rates from detrital river sediments (Willenbring and von Blanckenburg, 2010).

1.4.3. Quantifying the atmospheric flux of ^{10}Be

Variation in the production atmospheric ^{10}Be is due to changes in the intensity and orientation of the geomagnetic field which blocks all but the high-energy charged particles consisting of primary galactic cosmic radiation. The geometry of the Earth's magnetic field produces a predictable latitudinal variation with more radiation reaching the poles (Lal and Peters, 1967; Masarik and Beer, 2009; Fig. 1.5a). Several models were introduced to predict fluxes of ^{10}Be. These simulations of the production processes predict the amount of cosmogenic radionuclides produced as a function of solar activity, geomagnetic field intensity, altitude and geomagnetic latitude (e.g., Masarik and Beer, 1999; 2009). Thus, we can use curves of production rate at different given atmospheric thicknesses for given latitudes (e.g., Masarik and Beer, 1999; Fig. 1.5a) to acquire ^{10}Be flux in any region. Another model to estimate the ^{10}Be flux is a mean flux results (Heikkilä, 2007; Field et al., 2006) which was adapted for the long-term solar modulation and average geomagnetic field strength (Willenbring and von Blanckenburg, 2010; Fig. 1.5b).

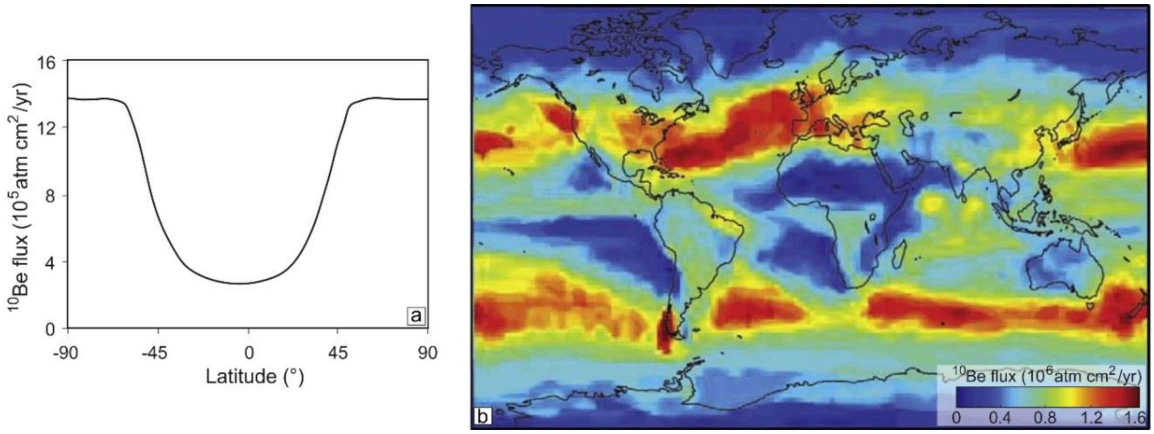

Figure 1.5. Models to estimate the ^{10}Be flux. (a) Depth integrated production rate of ^{10}Be for sea level by latitude for long-term solar modulation and present geomagnetic field intensity (adapted from Masarik and Beer, 1999). (b) Combined production delivery models. Average ^{10}Be flux for the long-term solar modulation factor and long-term geomagnetic field (adapted from Heikkilä, 2007; Field et al., 2006; Willenbring and von Blanckenburg, 2010).

1.5. References

Adams, B.A., Whipple, K.X., Forte, A.M., Heimsath, A.M. & Hodges, K.V. (2020) Climate controls on erosion in tectonically active landscapes. Science Advances, 6(42), eaaz3166. Available from: https://doi.org/ 10.1126/sciadv.aaz3166.

Agard, P., Omrani, J., Jolivet, L., Whitechurch, H., Vrielynck, B., Spakman, W., Wortel, R., 2011. Zagros orogeny: a subduction-dominated process. Geol. Mag. 148, 692–725.

Alavi, M. (1996), Tectono-stratigraphic synthesis and structural style of the Alborz mountain system in northern Iran, J. Geodyn., 21(1),
1–33.

Allen, M.B., Jones, S., Ismail-Zadeh, A., Simmons, M. and Anderson, L., 2002. Onset of subduction as the cause of rapid Pliocene-Quaternary subsidence in the South Caspian basin. Geology, 30(9), pp.775-778.

Allen, M.B., Vincent, S.J., Alsop, G.I., Ismail-zadeh, A. and Flecker, R., 2003. Late Cenozoic deformation in the South Caspian region: effects of a rigid basement block within a collision zone. Tectonophysics, 366(3-4), pp.223-239.

Allen, M., J. Jackson, and R. Walker (2004), Late Cenozoic re-organization of the Arabia-Eurasia collision and the comparison of short-term and long-term deformation rates, Tectonics, 23, TC2008, doi:10.1029/2003TC001530.

Allen, M. B. (2021). Arabia-Eurasia collision. Encyclopedia of Geology, 436–450. https://doi.org/10.1016/b978-0-12-409548-9.12522-9.

Aziz Zanjani, A., Ghods, A., Sobouti, F., Bergman, E., Mortezanejad, G., Priestley, K., Madanipour, S. and Rezaeian, M., 2013. Seismicity in the western coast of the South Caspian Basin and the Talesh Mountains. Geophysical Journal International, 195(2), pp.799-814.

Ballato, P., N. R. Nowaczyk, A. Landgraf, M. R. Strecker, A. Friedrich, and S. H. Tabatabaei (2008), Tectonic control on sedimentary facies pattern and sediment accumulation rates in the Miocene foreland basin of the southern Alborz mountains, northern Iran, Tectonics, 27, TC6001, doi:10.1029/2008TC002278.

Ballato, P., 2009. Tectonic and climatic forcing in orogenic processes: the foreland basin point of view, Alborz mountains, N Iran (Doctoral dissertation, Universität Potsdam).

Ballato, P., Mulch, A., Landgraf, A., Strecker, M.R., Dalconi, M.C., Friedrich, A. and Tabatabaei, S.H., 2010. Middle to late Miocene Middle Eastern climate from stable oxygen and carbon isotope data, southern Alborz mountains, N Iran. Earth and planetary science letters, 300(1-2), pp.125-138.

Ballato, P., C. E. Uba, A. Landgraf, M. R. Strecker, M. Sudo, D. F. Stockli, A. Friedrich, and S. H. Tabatabaei (2011), Arabia-Eurasia continental collision: Insights from late Tertiary foreland-basin evolution in the Alborz Mountains, northern Iran, Geol. Soc. Am. Bull., 123, 106–131.

Ballato, P., D. F. Stockli, M. R. Ghassemi, A. Landgraf, M. R. Strecker, J. Hassanzadeh, A. Friedrich, and S. H. Tabatabaei (2013), Accommodation of transpressional strain in the Arabia-Eurasia collision zone: New constraints from (U-Th)/He thermochronology in the Alborz mountains, N Iran, Tectonics, 32, 1–18, doi:10.1029/2012TC003159.

Ballato, P., Landgraf, A., Schildgen, T. F., Stockli, D. F., Fox, M., Ghassemi, M. R., Kirby, E., & Strecker, M. R. (2015). The growth of a mountain belt forced by base-level fall: Tectonics and surface processes during the evolution of the Alborz Mountains, N Iran. Earth and Planetary Science Letters, 425, 204-218. https://doi.org/10.1016/j.epsl.2015.05.051

Ballato, P., Cifelli, F., Heidarzadeh, G., Ghassemi, M.R., Wickert, A.D., Hassanzadeh, J., Dupont-Nivet, G., Balling, P., Sudo, M., Zeilinger, G. and Schmitt, A.K., 2017. Tectono-sedimentary evolution of the northern Iranian Plateau: insights from middle–late Miocene foreland-basin deposits. Basin Research, 29(4), pp.417-446.

Berberian, M., 1983. The southern Caspian: a compressional depression floored by a trapped, modified oceanic crust. Canadian Journal of Earth Sciences, 20(2), pp.163-183.

Bierman, P. and Steig, E.J., 1996. Estimating rates of denudation using cosmogenic isotope abundances in sediment. Earth surface processes and landforms, 21(2), pp.125-139.

Brown, L., Pavich, M.J., Hickman, R.E., Klein, J. and Middleton, R., 1988. Erosion of the eastern United States observed with 10Be. Earth Surface Processes and Landforms, 13(5), pp.441-457.

Chu, Y., Allen, M.B., Wan, B., Chen, L., Lin, W., Talebian, M. et al. (2021) Tectonic exhumation across the Talesh-Alborz Belt, Iran, and its implication to the Arabia-Eurasia convergence. Earth Science Reviews, 221, 103776. Available from: https://doi.org/10.1016/j.earscirev. 2021.103776

Cockburn, H.A. and Summerfield, M.A., 2004. Geomorphological applications of cosmogenic isotope analysis. Progress in physical Geography, 28(1), pp.1-42.

Davoudzadeh, M., Lammerer, B. and Weber-Diefenbach, K., 1997. Paleogeography, stratigraphy, and tectonics of the tertiary of Iran. NEUES JAHRBUCH FUR GEOLOGIE UND PALAONTOLOGIE ABHANDLUNGEN, 205, pp.33-67.

Duvall, A.R. and Tucker, G.E., 2015. Dynamic ridges and valleys in a strike-slip environment. Journal of Geophysical Research: Earth Surface, 120(10), pp.2016-2026.

Faure, G., Mensing, M.M., 2004. Isotopes: Principles and Applications, 3. John Wiley & Sons, Inc., New Jersey, 896 pp.

Ferrier, K.L., Huppert, K.L. & Perron, J.T. (2013) Climatic control of bedrock river incision. Nature, 496(7444), 206–209. Available from: https://doi.org/10.1038/nature11982.

Field, C.V., Schmidt, G.A., Koch, D. and Salyk, C., 2006. Modeling production and climate-related impacts on 10Be concentration in ice cores. Journal of Geophysical Research: Atmospheres, 111(D15).

Forte AM, Whipple KX, Bookhagen B, Rossi MW (2016) Decoupling of modern shortening rates, climate, and topography in the Caucasus. Earth Planet Sci Lett 449:282–294. https://doi.org/10.1016/j.epsl.2016.06.013.

Gilbert, G.K., 1877. Report on the Geology of the Henry Mountains. US Government Printing Office.

Goren, L., Willett, S.D., Herman, F. and Braun, J., 2014. Coupled numerical–analytical approach to landscape evolution modeling. Earth Surface Processes and Landforms, 39(4), pp.522-545.

Gosse, J.C. and Phillips, F.M., 2001. Terrestrial in situ cosmogenic nuclides: theory and application. Quaternary Science Reviews, 20(14), pp.1475-1560.

Graly, J.A., Reusser, L.J. and Bierman, P.R., 2011. Short and long-term delivery rates of meteoric 10Be to terrestrial soils. Earth and Planetary Science Letters, 302(3-4), pp.329-336.

Guest, B., Axen, G.J., Lam, P.S. and Hassanzadeh, J., 2006. Late Cenozoic shortening in the west-central Alborz Mountains, northern Iran, by combined conjugate strike-slip and thin-skinned deformation. Geosphere, 2(1), pp.35-52.

Hack, J.T., 1975. Dynamic equilibrium and landscape evolution. Theories of landform development, 1, pp.87-102.

He, C., Rao, G., Yang, R., Hu, J., Yao, Q. and Yang, C.J., 2019. Divide migration in response to asymmetric uplift: Insights from the Wula Shan horst, North China. Geomorphology, 339, pp.44-57.

Heikkilä, U., 2007. Modeling of the atmospheric transport of the cosmogenic radionuclides 10Be and 7Be using the ECHAM5-HAM General Circulation Model.

Hou, R., Liu, M., Chen, N., Deng, M., Tian, S., Li, Y., Ni, H. and Han, Z., 2023. Uplift history of the Northern Tianshan constrained from the inversion of river profiles. International Journal of Earth Sciences, 112(1), pp.177-191.

Hu, X., Zhang, Y., Guo, J. and Pan, B., 2023. How does climate affect the topography in tectonically active orogens. Earth Surface Processes and Landforms, 48(6), pp.1267-1280.

Granger, D.E., Kirchner, J.W. and Finkel, R., 1996. Spatially averaged long-term erosion rates measured from in situ-produced cosmogenic nuclides in alluvial sediment. The Journal of Geology, 104(3), pp.249-257.

Jackson, J., Priestley, K., Allen, M. and Berberian, M., 2002. Active tectonics of the south Caspian basin. Geophysical Journal International, 148(2), pp.214-245.

Kirby E, Whipple K (2001) Quantifying differential rock-uplift rates via stream profile analysis. Geology 29(5):415–418. https://doi.org/10.1130/0091-7613(2001)029%3c0415:QDRURV%3e2.0.CO;2

Kirby, E. and Whipple, K.X., 2012. Expression of active tectonics in erosional landscapes. Journal of structural geology, 44, pp.54-75.

Lague, D. The stream power river incision model: Evidence, theory and beyond. Earth Surf. Process Landforms 39, 38–61 (2014).

Lal, D. and Peters, B., 1967. Cosmic ray produced radioactivity on the Earth. In Kosmische Strahlung II/Cosmic Rays II (pp. 551-612). Berlin, Heidelberg: Springer Berlin Heidelberg.

Lal, D., 1991. Cosmic ray labeling of erosion surfaces: in situ nuclide production rates and erosion models. Earth and Planetary Science Letters, 104(2-4), pp.424-439.

Lamb, S. and Davis, P., 2003. Cenozoic climate change as a possible cause for the rise of the Andes. Nature, 425(6960), pp.792-797.

Leonard, J.S. and Whipple, K.X., 2021. Influence of spatial rainfall gradients on river longitudinal profiles and the topographic expression of spatially and temporally variable climates in mountain landscapes. Journal of Geophysical Research: Earth Surface, 126(12), p.e2021JF006183.

Li, Y., Liu, M., Zhang, H. and Shi, Y., 2021. Stream channel offsets along strike-slip faults: Interaction between fault slip and surface processes. Geomorphology, 394, p.107965.

Madanipour, S., T. A. Ehlers, A. Yassaghi, M. Rezaeian, E. Enkelmann, and A. Bahroudi (2013), Synchronous deformation on the orogenic plateau margins, insights from the Arabia-Eurasia collision, Tectonophysics, 608, 440–451.

Madanipour, S., Ehlers, T.A., Yassaghi, A. and Enkelmann, E., 2017. Accelerated middle Miocene exhumation of the Talesh Mountains constrained by U-Th/He thermochronometry: Evidence for the Arabia-Eurasia collision in the NW Iranian Plateau. Tectonics, 36(8), pp.1538-1561.

Madanipour, S., Yassaghi, A., Ehlers, T.A. and Enkelmann, E., 2018. Tectonostratigraphy, structural geometry and kinematics of the NW Iranian Plateau margin: insights from the Talesh Mountains, Iran. American Journal of Science, 318(2), pp.208-245.

Madanipour, S., 2023. Late Miocene–early Pliocene tectonic to erosional exhumation in the northwest of the Arabia–Eurasia collision zone. Earth Surface Processes and Landforms.

Masarik, J. and Beer, J., 1999. Simulation of particle fluxes and cosmogenic nuclide production in the Earth's atmosphere. Journal of Geophysical Research: Atmospheres, 104(D10), pp.12099-12111.

Masarik, J. and Beer, J., 2009. An updated simulation of particle fluxes and cosmogenic nuclide production in the Earth's atmosphere. Journal of Geophysical Research: Atmospheres, 114(D11).

Nishiizumi, K., Winterer, E.L., Kohl, C.P., Klein, J., Middleton, R., Lal, D. and Arnold, J.R., 1989. Cosmic ray production rates of 10Be and 26Al in quartz from glacially polished rocks. Journal of Geophysical Research: Solid Earth, 94(B12), pp.17907-17915.

Ott, R.F., Pérez-Consuegra, N., Scherler, D., Mora, A., Huppert, K.L., Braun, J., Hoke, G.D. and Ruiz, J.R.S., 2023. Erosion rate maps highlight spatio-temporal patterns of uplift and quantify sediment export of the Northern Andes. Earth and Planetary Science Letters, 621, p.118354.

Ouimet WB, Whipple KX, Granger DE (2009) Beyond threshold hillslopes: channel adjustment to base-level fall in tectonically active mountain ranges. Geology 37(7):579–582. https://doi.org/10.1130/G30013A.1

Portenga, E.W. & Bierman, P.R. (2011) Understanding Earth's eroding surface with 10Be. GSA Today, 21(8), 4–10. Available from: https://doi. org/10.1130/G111A.1

Rezaeian, M., Kuijper, C.B., van der Boon, A., Pastor-Galán, D., Cotton, L.J., Langereis, C.G. and Krijgsman, W., 2020. Post-Eocene coupled oroclines in the Talesh (NW Iran): Paleomagnetic constraints. Tectonophysics, 786, p.228459.

Seybold H, Berghuijs WR, Prancevic JP, Kirchner JW (2021) Global dominance of tectonics over climate in shaping river longitudinal profiles. Nat Geosci. https://doi.org/10.1038/s41561-021-00720-5.

Schmidt, K.M. and Montgomery, D.R., 1995. Limits to relief. Science, 270(5236), pp.617-620.

Sklar LS, Dietrich WE (2001) Sediment and rock strength controls on river incision into bedrock. Geology 29(12):1087–1090. https://doi.org/10.1130/0091 7613(2001)029%3c1087:SARSCO%3e2.0.CO;2

Snyder, N.P., Whipple, K.X., Tucker, G.E. & Merritts, D.J. (2000) Landscape response to tectonic forcing: Digital elevation model analysis of stream profiles in the Mendocino triple junction region, northern California. Geological Society of America Bulletin, 112(8), 1250–1263. Available from: https://doi.org/10.1130/0016-7606 (2000)1122.0.co;2.

Stock, J.D. and Montgomery, D.R., 1999. Geologic constraints on bedrock river incision using the stream power law. Journal of Geophysical Research: Solid Earth, 104(B3), pp.4983-4993.

Strecker, M.R., Alonso, R.N., Bookhagen, B., Carrapa, B., Hilley, G.E., Sobel, E.R. and Trauth, M.H., 2007. Tectonics and climate of the southern central Andes. Annu. Rev. Earth Planet. Sci., 35, pp.747-787.

Su, Q., Wang, X., Lu, H. and Xie, H., 2020. Dynamic divide migration as a response to asymmetric uplift: An example from the Zhongtiao Shan, North China. Remote Sensing, 12(24), p.4188.

Townsend, K., 2021. Co-evolution of Rock Strength, Erosion, and Steep Topography (Doctoral dissertation).

Vernant, P., et al. (2004), Present-day crustal deformation and plate kinematics in the Middle East constrained by GPS measurements in Iran and northern Oman, Geophys. J. Int., 157, 381–398.

Vincent, S.J., Allen, M.B., Ismail-Zadeh, A.D., Flecker, R., Foland, K.A. and Simmons, M.D., 2005. Insights from the Talysh of Azerbaijan into the Paleogene evolution of the South Caspian region. Geological Society of America Bulletin, 117(11-12), pp.1513-1533.

Von Blanckenburg, F., 2005. The control mechanisms of erosion and weathering at basin scale from cosmogenic nuclides in river sediment. Earth and Planetary Science Letters, 237(3-4), pp.462-479.

Wang J, Hu Z, Pan B, Li M, Dong Z, Li X, Li X, Bridgland D (2019) Spatial distribution pattern of channel steepness index as evidence for differential rock uplift along the eastern Altun Shan on the northern Tibetan Plateau. Global Planet Change 181:102979. https://doi.org/10.1016/j.gloplacha.2019.102979

Whipple, K.X. and Tucker, G.E., 1999. Dynamics of the stream-power river incision model: Implications for height limits of mountain ranges, landscape response timescales, and research needs. Journal of Geophysical Research: Solid Earth, 104(B8), pp.17661-17674.

Whipple, R. A. DiBiase, B. T. Crosby, Bedrock Rivers (Elsevier, 2013), vol. 9.

Whipple, K.X., Forte, A.M., DiBiase, R.A., Gasparini, N.M. and Ouimet, W.B., 2017. Timescales of landscape response to divide migration and drainage capture: Implications for the role of divide mobility in landscape evolution. Journal of Geophysical Research: Earth Surface, 122(1), pp.248-273.

Willenbring, J.K. and von Blanckenburg, F., 2010. Meteoric cosmogenic Beryllium-10 adsorbed to river sediment and soil: Applications for Earth-surface dynamics. Earth-Science Reviews, 98(1-2), pp.105-122.

Willett, S.D., McCoy, S.W., Perron, J.T., Goren, L. and Chen, C.Y., 2014. Dynamic reorganization of river basins. Science, 343(6175), p.1248765.

Ye, Y., Tan, X. and Zhou, C., 2022. Initial topography matters in drainage divide migration analysis: Insights from numerical simulations and natural examples. Geomorphology, 409, p.108266.

You, C.-F., Lee, T., Brown, L., Shen, J.J., Chen, J.-C., 1988. 10Be study of rapid erosion in Taiwan. Geochimica et Cosmochimica Acta 52, 2687–2691.

Zanchi, A., S. Zanchetta, F. Berra, M. Mattei, E. Garzanti, S. Molyneux, A. Nawab, and J. Sabouri (2009), The Eo-Cimmerian (Late? Triassic) orogeny in North Iran, in South Caspian to Central Iran Basins, Geol. Soc. London, Spec. Publ., vol. 312, edited by M.-F. Brunet, M. Wilmsen, and J. W. Granath, pp. 31–55, doi:10.1144/SP312.3.

Zeng, X. and Tan, X., 2023. Drainage divide migration in response to strike-slip faulting: An example from northern Longmen Shan, eastern Tibet. Tectonophysics, 848, p.229720.

Zhou, C., Tan, X., Liu, Y. and Shi, F., 2022. A cross-divide contrast index (C) for assessing controls on the main drainage divide stability of a mountain belt. Geomorphology, 398, p.108071.

Zondervan, J.R., Stokes, M., Boulton, S.J., Telfer, M.W. and Mather, A.E., 2020. Rock strength and structural controls on fluvial erodibility: Implications for drainage divide mobility in a collisional mountain belt. Earth and Planetary Science Letters, 538, p.116221.

Chapter 2

Geomorphometric analysis: divide stability, river network analysis

1. Interplay between tectonics and surface processes in the evolution of mountain ranges: Insights from landscape dynamics, uplift, and active deformation of Talesh Mountains (NW Iranian Plateau margin)

Mohammad Moumeni[1*], Michele Delchiaro[1], Marta Della Seta[1], Reza Nozaem[2], Paolo Ballato[3], Joel S. Leonard[4], Romano Clementucci[3,5], Javad Rouhi[1]

[1] Department of Earth Sciences, Sapienza University of Rome, Rome, Italy
[2] School of Geology, College of Science, University of Tehran, Tehran, Iran
[3] Department of Sciences, Roma Tre University, Rome, Italy
[4] Department of Geosciences, Colorado State University, Fort Collins, Colorado, USA
[5] Department of Earth Sciences, ETH Zürich, Zürich, Switzerland

2.1. Abstract

Drainage divides are dynamic features of a landscape that migrate over time during the development of river networks. In this study, we focused on the geomorphic response of a landscape to the interplay among tectonics, climate, and lithology in the Talesh Mts. in the northwest of the Iranian Plateau. The footprints of these competing forces have been analyzed by divide stability analysis and applying χ, χ_Q, and Gilbert metrics. Additionally, we examined the effects of bedrock erodibility on landscape evolution processes by measuring the mechanical rock strength of the lithological units in different sectors of the mountain range. The distribution of the χ values suggests a disequilibrium of the drainage networks across the whole main divide and its tendency to migrate toward the interior of the plateau. In contrast, Gilbert metrics, which focuses on a narrow topographic zone across the divide, suggest that the uppermost divide in the northern and southern Talesh Mts. is stable. Moreover, asymmetry in Gilbert metrics across the central part of the range suggests that the divide might be migrating toward the plateau interior. The possible scenario for the whole divide's behavior is associated with the contrasting erosion rates across the divide.

---

[*] Corresponding author: Mohammad Moumeni; Email: mohammad.moumeni@uniroma1.it
Address: Piazzale Aldo Moro, 5, 00185 Roma RM, Italy

In the northern and southern sectors of the Talesh Mts. range, the erosional wave related to the most recent uplift pulses has not reached the divide yet. Mechanism of topographic rejuvenation is controlled by heterogeneous uplift of strong bedrock units in the northern and southern sectors, and weak bedrock units outcropping in the central sector, that initiated topographic rejuvenation largely in the central Talesh Mts. Parallelly, the precipitation has a limited effect in assisting and magnifying the divide mobility, reorganization, and landscape transience. In general, we can infer that divide is in a transient state due to the spatially varying rock uplift and bedrock erodibility.

Keywords:

Divide stability; Landscape evolution; Bedrock erodibility; Uplift and erosion patterns; Talesh Mountains; Iranian Plateau

2.2.Introduction

The evolution of topography is accompanied by changes in river networks (e.g., Whipple, 2004; Willett et al., 2014), which translate tectonics, climate change, and base level rise/fall signals throughout the landscape (e.g., Kirby and Whipple, 2012; Whipple, 2004; Hack, 1957), and set the magnitude of changes in topographic relief (Whipple et al., 2013; Whipple and Tucker, 1999; Howard et al., 1994). Drainage divides are dynamic features of a landscape that migrate over time due to the development of river networks (Fig. 2.1); Willett et al., 2014). Understanding the geomorphic response of a landscape, both along the river network and its drainage divide, is necessary to investigate the interplay among tectonics, climate, and lithology as they record crustal deformation and strain accumulation over long timescales (e.g., Whipple, 2009; Willett, 1999; Expósito et al., 2022; Delchiaro et al., 2023). The Talesh Mts. are a prominent tectonic feature of the NW sector of the Iranian Plateau, which is formed by the compressional stresses transferred across the Arabia-Eurasia continental collision. In the study area, the Masuleh-Dagh and Boghrov-Dagh and the N-NW-trending Talesh faults are the main active structure, which promote the recent growth of relief and topographic barrier to the moisture sourced from Caspian Sea. The orographic barrier controls the spatial variability of climate by enhancing precipitation on the Caspian Sea side and aridity in the interior of the plateau.

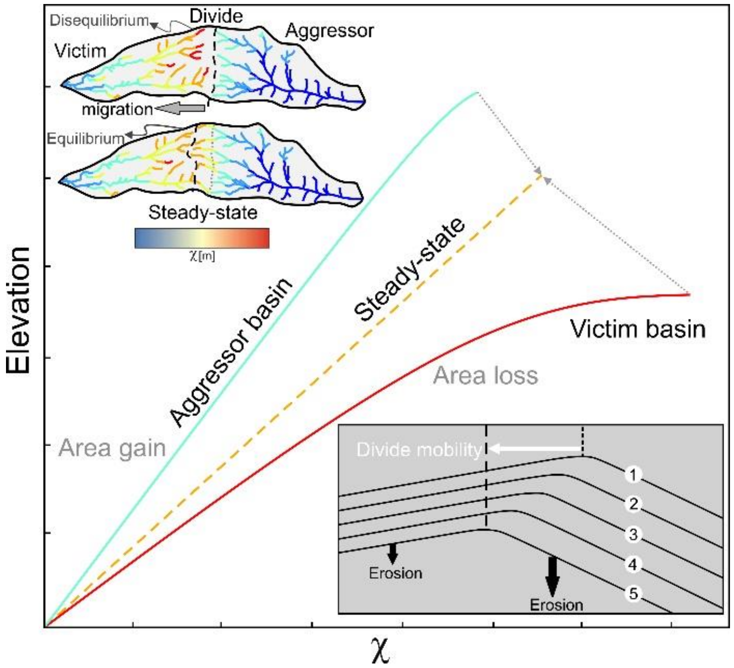

Figure 2.1. Divide mobility, equilibrium and disequilibrium state of river basins and profiles (modified and readapted after Willett et al., 2014; Forte and Whipple, 2018). The inset (lower right) is a Schematic diagram of Gilbert's (1877)'Law of Unequal Declivities'. Based on this law, due to unequal erosion rates across the divide, divides will move towards the side with lower erosion rate. This contrast in erosion rate is probably driven by differences in topographic gradient on both sides of the divide (e.g., Forte and Whipple, 2018).

In addition to tectonics and climate, rock strength contrasts can also lead to landscape transience when alternating lithologies with different resistance are exposed, even in the absence of changes in tectonic activity and climatic conditions (Forte et al., 2016; Zondervan et al., 2020a; Clementucci et al., 2022). In the Talesh Mts. the main drainage divide is characterized by spatial variation of rock-types and topographic characteristics (i.e., local relief, slope, channel steepness).

The effects of these tectonic uplift and deformation phases, as well as of the lithological characteristics and orographic rainfall on the landscape and their impression on the geomorphological architecture of the study area are not fully understood.

The present study focuses on the geomorphic response of the river network and drainage divides to the combined contributions of tectonic uplift, orographic precipitation, and lithological variations of the Talesh Mts. Investigating the interaction between these factors and isolating the role of each yields an applied procedure to reveal the main governing agent/s controlling the architecture of present-day landscape, and its evolutionary path.

We combined a quantitative analysis of regional topography and geomorphology of the main drainage divide with stream profile analysis (i.e., longitudinal profiles, knickpoints characterization, χ-plot and stream projections) in order to decipher the surface deformation, uplift mechanisms and drainage divide evolution.

Since the tectonic signals can be obscured by the effect of climate and lithology, for a precise understanding of the connection between topographic features and their driving factors, it is crucial to examine the influence of rock strength and identify the scenarios in which it can exert a substantial impact on the evolution of topography (e.g., Zondervan et al., 2020b; Clementucci et al., 2022; Mitchell and Forte, 2023). In fact, the exposure of lithologies with different strength can promote drainage reorganization (Gallen, 2018). In light of this, we attempted to isolate the effects of bedrock erodibility on the landscape evolution processes by measuring uniaxial compressive strength (UCS) of the lithological units in three sectors of the mountain range. To better isolate the lithological signal from tectonic and climate effects on topographic relief in the Talesh Mts., we also measured the stream channel metrics (i.e., k_{sn} and χ) by combining them with mean annual rainfall (k_{snQ} and χ_Q; Adams et al., 2020; Leonard et al., 2023).

This methodological approach aims at isolating the effects of orographic rainfall and variability of rock strength from the tectonic signal in the mobility of divide and landscape evolution of mountain ranges.

2.3.Regional framework

2.3.1. Geological setting

The Iranian Plateau is part of the Alpine–Himalayan system of mountain belts (Stoecklin, 1968; Ghorbani, 2013) that extends from the Atlantic Ocean to the Western Pacific. The Plateau is a large actively deforming region that developed in response to the late Eocene to early Miocene collision between the Arabian and Eurasian plates (e.g., Allen et al., 2004; Ballato et al., 2011; Agard et al., 2011; Mouthereau et al., 2012; McQuarrie & van Hinsbergen, 2013 and references therein) (Fig. 2.2). Stress was subsequently transferred from the collision zone to the northern margin of the Iranian Plateau (e.g., Berberian, 1983; Jackson et al, 2002; Allen et al, 2003a, 2003b; Guest et al, 2006; Yassaghi and Madanipour, 2008; Ballato et al, 2008 and 2017; Madanipour et al., 2018). The spatial and temporal evolution of deformation at the northern sectors of the Arabia- Eurasia collision zone seems to result from the interplay between the rigid South Caspian Basin (SCB) in the north and the Central Iranian Block (CIB) to the south (Fig. 2.2; e.g., Allen et al., 2003; Ballato et al., 2013). The Iranian Plateau represents an elongated, thickened, and low relief morphotectonic province and includes actively deforming orogenic belts (Vernant et al., 2004; Ballato et al., 2013, 2017). Surface processes may have significantly contributed to redistributing mass, thereby influencing the shallow crustal stress field and fault activity (Ballato et al., 2015). GPS vectors indicate that the general direction of crustal motion in NW of Iran, respect to a fixed Eurasian frame, is toward the north at rates of 22–23 mm/yr (Fig. 2.2) (Vernant et al., 2004; Reilinger et al., 2006).

The Talesh Mts. at the NW border of the Iranian Plateau are part of the Arabia-Eurasia collision zone (Fig. 2.3) and connect the Alborz Mountains with the Lesser Caucasus. The orogen has a curved geometry that bends around the southwestern margin of the SCB from EW to NW and WNW (e.g., Madanipour et al., 2013:2017; Allen et al., 2003; Jackson et al., 2002; Berberian, 1983). The onset of mountain building and exhumation in the Talesh Mts. occurred in Eocene-Oligocene (Madanipour et al., 2018) and is interpreted as the initial stage of the Arabia-Eurasia continental collision (e.g., Allen et al., 2004; Ballato et al., 2011, 2013; Madanipour et al., 2017, 2018). Since the Miocene, these mountains form an orographic and topographic barrier that separates the Ardebil Basin (interior of the plateau) from the coastal plains of the Caspian Sea (Fig. 2.3). GPS data show clockwise rotation of the SCB with respect to the Talesh Mts. (Djamour et al., 2010, 2011). Additionally, complex deformation at the northwestern Iranian Plateau is reflected in seismicity at the western edge of the SCB and the Talesh Mts. (e.g., Jackson et al., 2002; Madanipour et al., 2018). A minor component of underthrusting of the SCB lithosphere beneath the continental crust of the Talesh Mts. is suggested by seismic and gravity data (e.g., Berberian, 1983; Jackson et al., 2002; Allen et al., 2003).

The Talesh Mts. are composed of Paleozoic to Quaternary rock units. Paleozoic units include volcanic, clastic, and carbonate rocks (Fig. 2.3a). Mesozoic rock units consist primarily of Triassic to Lower Jurassic carbonates and clastics. Cenozoic strata (~8 km of thickness) are chiefly composed of volcanic and volcaniclastic rock units (Fig. 2.3a) that are mostly associated with Eocene magmatism in rapidly subsiding marine basins

(Berberian and King, 1981; Vincent et al., 2005; Madanipour et al., 2013 and 2018). In the northern and central sectors of the Talesh Mts., Cenozoic sedimentary, volcanic, and volcaniclastic sequences are widely exposed, while older rock units crop out solely in the core of some anticlines (e.g., Madanipour et al., 2013, 2018; and references therein; Fig. 2.3a).

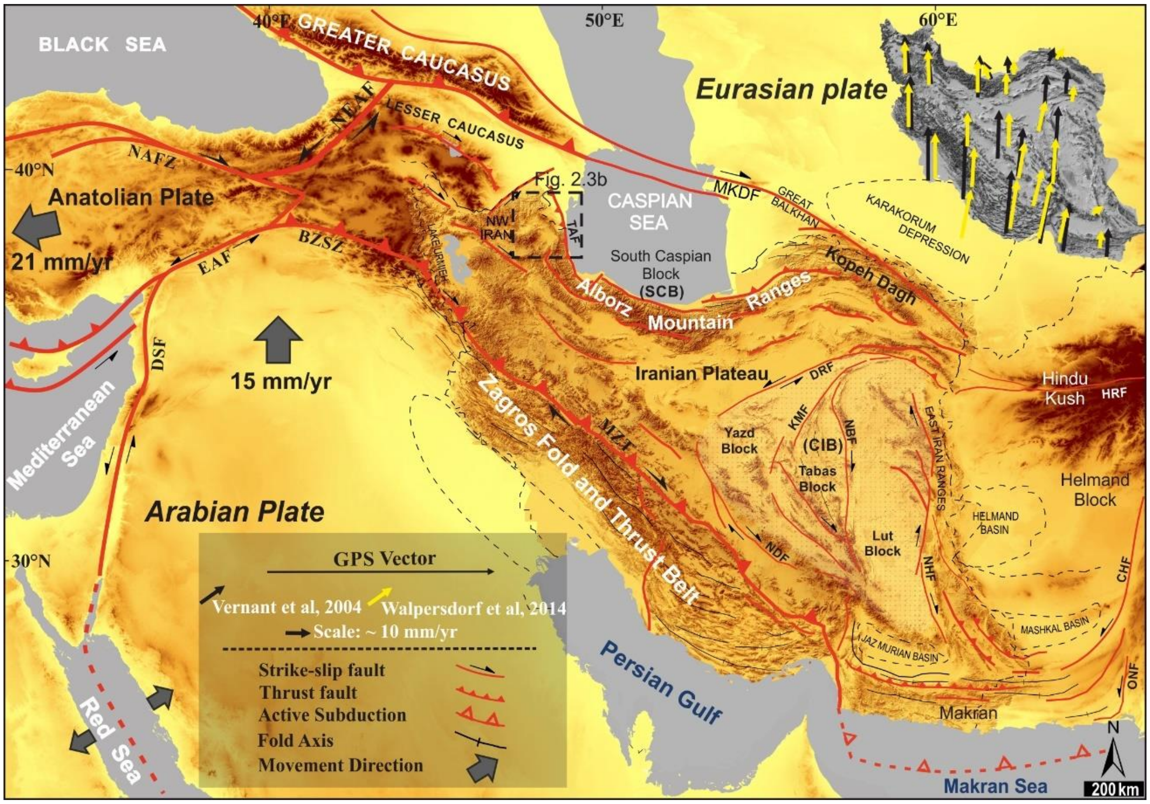

Figure 2.2. Simplified tectonic map of the Arabia- Eurasia collision zone. Shaded-relief of Shuttle Radar Topography Mission (SRTM) (Farr et al., 2007) digital elevation model, showing the main tectonic domains, blocks and the major fault systems accommodating the Arabia-Eurasia convergence. Abbreviations are: MKDF: Main Kopet Dagh Fault, MZT: Main Zagros Thrust, DRF: Doruneh Fault, TAF: Talesh Fault, HRF: Herat Fault, NHF: Nehbandan Fault, CHF: Chaman Fault system, ONF: Ornach-Nal Fault, KMF: Kalmard Fault, NDF: Nain-Dehshir Fault, NBF: Nayband Fault, BZSZ: Bitlis Zagros Suture Zone, EAF: East Anatolian Fault, NAFZ: North Anatolian Fault Zone, NEAF: North-Eastern Anatolian Fault, DSF: Dead Sea Fault. The inset (upper right), shaded relief map shows GPS vectors in Iran relative to stable Eurasia; the data is obtained after Vernant et al., 2004 (black arrows), and Walpersdorf et al., 2014 (yellow arrows); Location of the study area in the NW of Iran is indicated by black dashed square.

2.3.2. Morphological and climatic setting

The geometry of the range highlights the extent of the elevated axial surface with local variations in topographic relief, mountain peaks and incised valleys. The high-standing landscape in the northern and southern sectors are mainly composed of Eocene andesite and volcaniclastic rocks. In the eastern part of the main drainage divide in the wet flank of the range, the topography is dominated by several large anticlines and thrust faults. This topographic contrast between the two sides of the divide is also reflected in the spatial variations of the topographic gradient, distribution of relief, elevation, and precipitation. The occurrence of orographic barriers intercepting moisture sourced in the Caspian Sea determines the disparate distribution of precipitation over the Talesh Mts. (e.g., Zaitchik et al., 2007; Ballato et al., 2010 and references therein). In the late Cenozoic, Iran experienced significant long-term and short-term climatic variations, which most likely influenced erosional and depositional processes (Ballato and Strecker, 2014). Central and northern Iran was characterized by a hot, arid climate since the late Eocene (Jackson et al., 1990; Davoudzadeh et al., 1997). On the other hand, moisture from the Caspian Sea could have been forced into concentrated precipitation along the uplifting Alborz ranges (Ballato, 2009 and references therein). During the early-middle Miocene the Alborz range became an efficient orographic barrier as suggested by paleoclimatic data (Ballato et al., 2010). The positive feedback between orographically induced precipitation and rock-uplift rates must have been established only recently along the northern slope of the Alborz (e.g., Ballato et al., 2015). At present, roughly 1000 mm/yr of precipitation falls along the coast of the Caspian Sea on the northern flank of the Talesh Mts. in the western Alborz ranges (Fig. 2.3b). In contrast, the Ardebil Basin and the plateau interior regions receive less than 300 mm/yr of rainfall that is mostly sourced from the westerly winds.

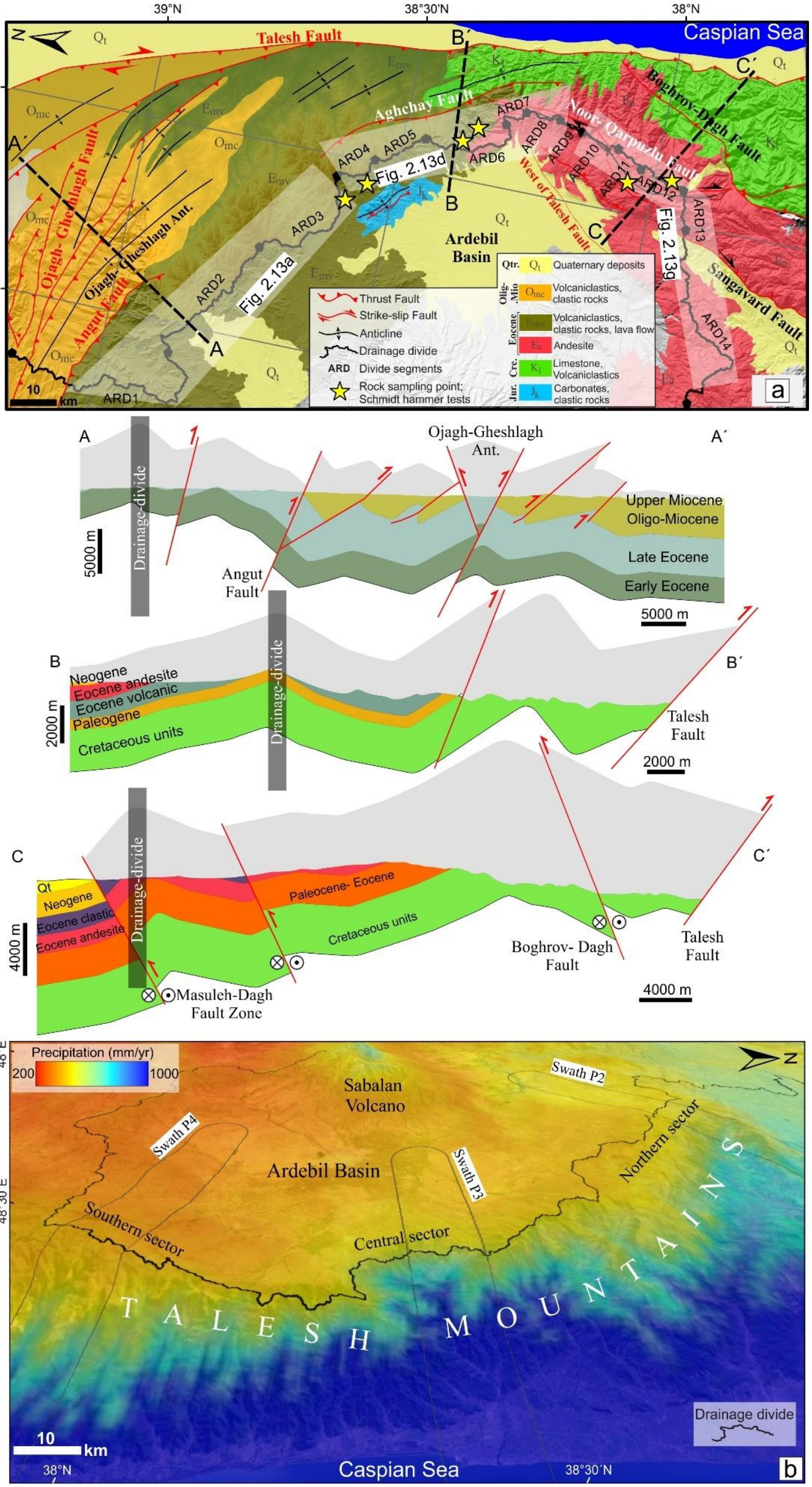

39°N
38°30'N
38°N
48°30'E
48°E
N
Caspian Sea
Talesh Fault
Aghchay Fault
Noor- Qarpuzlu Fault
Boghrov-Dagh Fault
Sangavard Fault
West of Talesh Fault
Ojagh- Gheshlagh Fault
Ojagh-Gheshlagh Ant.
Angut Fault
Ardebil Basin
A
A´
B
B´
C
C´
ARD1
ARD2
ARD3
ARD4
ARD5
ARD6
ARD7
ARD8
ARD9
ARD10
ARD11
ARD12
ARD13
ARD14
Fig. 2.13a
Fig. 2.13d
Fig. 2.13g
Qt
Omc
Emv
Ea
Kl
Jk
10 km
Thrust Fault
Strike-slip Fault
Anticline
Drainage divide
ARD Divide segments
Rock sampling point; Schmidt hammer tests
Qtr. Qt Quaternary deposits
Olig-Mio Omc Volcaniclastics, clastic rocks
Eocene Emv Volcaniclastics, clastic rocks, lava flow
Ea Andesite
Cre. Kl Limestone, Volcaniclastics
Jur. Jk Carbonates, clastic rocks
a
A
A´
Ojagh-Gheshlagh Ant.
Drainage-divide
5000 m
Angut Fault
Upper Miocene
Oligo-Miocene
Late Eocene
Early Eocene
5000 m
B
B´
Neogene
Eocene andesite
Eocene volcanic
Paleogene
Cretaceous units
2000 m
Drainage-divide
Talesh Fault
2000 m
C
C´
Qt
Neogene
Eocene clastic
Eocene andesite
4000 m
Drainage-divide
Paleocene- Eocene
Cretaceous units
Masuleh-Dagh Fault Zone
Boghrov- Dagh Fault
Talesh Fault
4000 m
Precipitation (mm/yr)
200
1000
48°E
48°30'E
N
Sabalan Volcano
Swath P2
Swath P3
Swath P4
Ardebil Basin
Northern sector
Central sector
Southern sector
TALESH MOUNTAINS
Drainage divide
10 km
Caspian Sea
38°N
38°30´N
b

Figure 2.3. (a) Geological map and cross sections of the study area with main structures and lithological units, modified and readapted after Madanipour et al. (2017, 2018); Vincent et al. (2005), Geological Survey of Iran (1975, 1999). The grey-shaded areas above the topography are the exhumed part of the section constructed based on the geometry and kinematics of the main structures. Location of the Ardebil Basin's main drainage divide in Talesh Mountains represented on the structural cross-sections (grey vertical stripes) and geological map. The main divide has been divided into fourteen segments (ARD1-ARD14) to calculate the Gilbert metrics and χ (see methods). The white polygons indicate the north, central, and southern parts of the divide in Talesh Mountains. (b) Digital elevation model with superposed average 30-years annual precipitation pattern from 1970-2000 of the NW of Iran. The data with 30 seconds (~1 km^2) spatial resolution is acquired from WorldClim version 2.1 (Fick and Hijmans, 2017) climate database. P2 to P4 show the locations of the20-km-wide swath profiles of rainfall which are shown in Figure 2.15b-d.

2.4.Methods

To compute geomorphic indices, we used a 30-m digital elevation model (DEM) obtained by the Shuttle Radar Topography Mission (SRTM) (Farr et al., 2007), and a precipitation grid from WorldClim climate database (Fick and Hijmans, 2017). Stream networks and drainage divides were extracted and analyzed in MATLAB using software packages TopoToolbox (Schwanghart and Scherler, 2014), DivideTools (Forte and Whipple, 2018), and the Topographic Analysis Kit (Forte and Whipple, 2019). We calculated the flow accumulation threshold for the fluvial domain (1 km^2) according to procedure by Vergari et al. (2019) to define the channel head, and then extracted the stream network with this threshold area (Fig. S2.1). We computed the concavity index (θ) which is correlated with the uplift rate, and shows concavity degree of the channel, and is defined by m (area index) and n (gradient index) (Fig. S2.2). We analyzed the drainage network characteristics and divide stability by extracting knickpoints and channel metrics k_{sn} and χ, along with their rainfall-weighted versions k_{snQ} and χ_Q (e.g., Perron and Royden 2013; Adams et al., 2020; Whipple et al, 2022; Leonard et al., 2023). We also explored drainage divide stability by using Gilbert's metrics (Forte and Whipple, 2018).

Additionally, several swath profiles across and orthogonal to the main drainage divide were computed to explore the topographic characteristics, including local relief and hypsometric integral (Hi Index; e.g., Pike and Wilson, 1971). To improve the description and the comparison of hypsometry along a swath profile, we rescaled Hi values and used the enhanced transverse hypsometric integral (Thi*) (Pérez-Peña et al., 2017), in which Hi values are weighted by the relative local relief. Finally, we measured the compressive rock strength through the utilization of a Schmidt hammer in the field and point load laboratory test on rock samples to supplement the topographic analyses. The devised workflow is represented in Fig. 2.4.

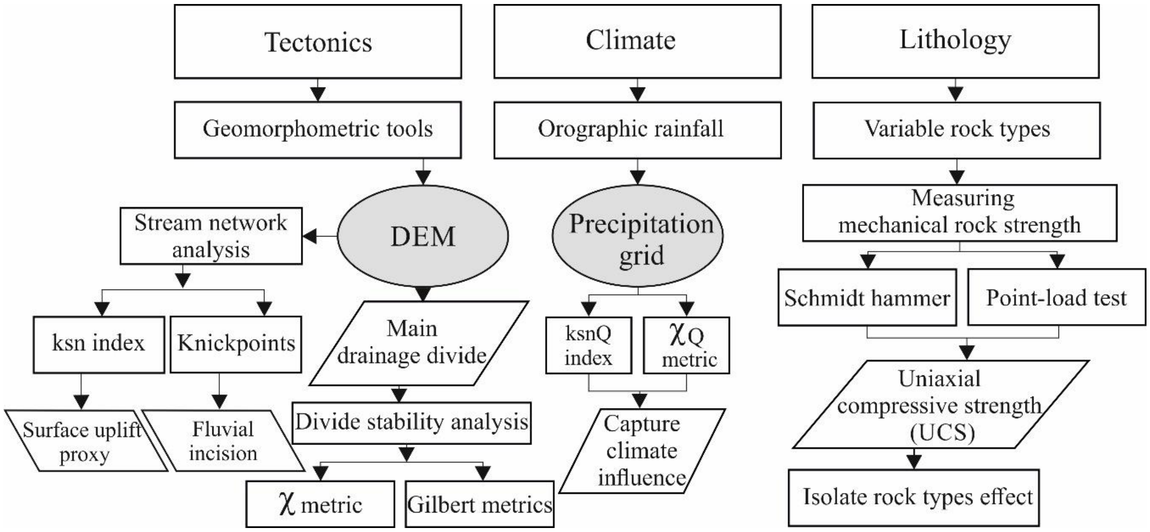

Figure 2.4. Flowchart, and general workflow for isolating the contributions of tectonics, climate and lithology on present day topography.

2.4.1. Stream Power Incision Model (SPIM)

The longitudinal river profiles record information on tectonics, climate, and bedrock lithology (Kirby and Whipple, 2012). The landscape evolution models are driven by incision processes that assume bedrock erosion (E) as a function of upslope area (A) and channel slope (S):

$$E = KA^m S^n, \qquad (1)$$

where K is the fluvial erodibility which depends on rock erodibility, climate and hydrological parameters/ channel geometry, and m and n are empirical constants whose ratio m/n is equivalent to θ_{ref}. Under topographic steady state, when erosion (E) is balanced by uplift (U), Eq. (1) can be rearranged as follows:

$$S = k_s A^{-\theta}. \qquad (2)$$

Eq. (2) is a power-law relation between S and A where θ is the slope and k_s is the steepness index. Differences in values of k_s along the river reflect changes in bedrock uplift rate, or a change in the rock erodibility (Kirby et al., 2003; Wobus et al., 2006; Kirby and Whipple, 2012).

To adjust the amount of concavity and compare different longitudinal profiles, the steepness index is normalized according to the reference concavity index which has been computed by Bayesian Optimization (see Appendix chapter 2). This value is the reference (θ_{ref} = 0.52) concavity index for the study area and has been used for all drainage networks and channels (Fig. S2.2).

Determining the degree to which climate significantly impacts topography continues to be a significant challenge (Montgomery et al., 2001; Burbank et al., 2003). The normalized channel steepness index appears to be the most promising parameter for identifying such an influence (Whipple et al., 2013; Lague, 2014; Adams et al., 2020). Since the k_{sn} is reliant on upstream drainage area as a discharge proxy and assumes that climate is uniform, k_{snQ} can be used as an alternative (e.g., Adams et al., 2020; Leonard and Whipple, 2021; Leonard et al., 2023).

Similar to k_{sn}, k_{snQ} is an empirically supported metric and is not dependent on the stream power model. This metric uses the product of drainage area *(A)* and average upstream rainfall *(P)* estimated from mean annual rainfall (MAP) (WorldClim climate database; Fick and Hijmans, 2017) as an improved discharge proxy (Adams et al., 2020) which allows k_{snQ} to account for spatial rainfall gradient (Leonard and Whipple, 2021; Leonard et al., 2023; and references therein):

$$k_{snQ} = SQ^{\theta_{ref}} \qquad (3)$$

where Q is the water discharge. It has been shown that k_{sn} and k_{snQ} correlate with erosion rates (e.g., Leonard and Whipple, 2021), and the slope of profiles in χ-z and χQ-z is k_{sn} and k_{snQ}, respectively. The interpolated maps for k_{sn} and k_{snQ} are derived from the same stream network, and their color ramps are normalized to represent equivalent data ranges.

The stream power model has been shown to be an effective tool for deciphering tectonic signals in landscapes (e.g., Hack, 1957; Flint, 1974; Kirby and Whipple, 2001). Therefore, in order to analyze the river profiles, we used the integral approach of the detachment-limited stream power model (e.g., Howard, 1994; Perron and Royden, 2013) introduced by

Lague (2014). Therefore, a landscape evolution model for the fluvial domain can be derived by incorporating the SPIM with rock uplift due to tectonics (U):

$$\frac{\partial \mathrm{z(x,t)}}{\partial \mathrm{t}} = U\ (x,t) - K\ (x,t) A\ (x,t)^m \left|\frac{\partial z}{\partial x}\right|^n, \qquad (4)$$

Disruption of balance between rock uplift and river incision is generated by changing in elevation (z) with time (t). On the contrary, when both uplift and incision are balanced, the region is in steady state or dynamic equilibrium, and there is no change in elevation ($dz/dt = 0$). Therefore, equation (4) can be written as:

$$\left|\frac{\partial z}{\partial x}\right| = \left({}^{U}\!/_{K}\right)^{1/n} A(x)^{-\theta}, \qquad (5)$$

where $(U/K)^{1/n}$ is the channel steepness index (k_s).

A transformation of the horizontal spatial coordinates has been proposed (Perron and Royden, 2013) which linearizes the power law relation by the integration of dz/dx with respect to upstream distance (x):

$$\int \frac{dz}{dx} dx = z(x_b) + \left(\frac{U}{KA_0^m}\right)^{1/n} \int_{x_b}^{x} \left(\frac{A_0}{A(x)}\right)^{m/n} dx, \qquad (6)$$

where x_b is the distance at base level, and A_0 is a reference scaling area (1 km^2). Thus, the steady state solution of equations (4- 6) for the simple case of U and K constant in space and time is:

$$z(x) = z(x_b) + \left({}^{U}\!/_{KA_0^m}\right)^{1/n} \chi, \qquad (7)$$

where z_b is the elevation at the river network's base level at $x = x_b$ (e.g., Perron and Royden, 2013; Willett et al., 2014). This method allows to transform the horizontal distance of the river profile to χ reference frame, which is defined by the following equation:

$$\chi = \int_{x_b}^{x} \left(\frac{A_0}{A(x)}\right)^{\theta_{ref}} dx. \qquad (8)$$

The integration is performed upstream from base level to location x. The incorporation of the A_0 gives χ dimensions of length, but the kinematic wave nature of Eq. (4) suggests that χ could equally well represent a time (Willett et al., 2014).

In case of taking the precipitation rate into χ analysis consideration, we can use discharge (Q) instead of drainage area. χ assumes steepness scales with drainage area (k_{sn}), while χ_Q assumes scaling with the product of drainage area and mean rainfall (k_{snQ}). Thus, the χ-transform equations can be expressed as χ_Q (Yang et al., 2015; Leonard and Whipple, 2021; Leonard et al., 2023):

$$z(x) = z(x_b) + k_{snQ}.\chi_Q, \tag{9}$$

$$\chi_\mathrm{Q} = \int_{xb}^{x} \left(\frac{Q_0}{Q(x)}\right)^{\theta_{ref}} dx. \tag{10}$$

The color ramps of the interpolated maps for χ and χ_Q are normalized to represent identical data ranges. We further combine χ parameter with Gilbert metrics to analyze the drainage divide in detail.

2.4.2. Knickpoints and fluvial incision

Knickpoints were extracted using *knickpointfinder* function in TopoToolbox (Schwanghart and Scherler, 2014; Schwanghart and Scherler, 2017) from the smoothed river profiles. For each river profile we calculated the tolerance value separately, which shows uncertainties that are inherent in longitudinal river profiles. This tolerance value is higher than the maximum expected error between the measured and the true river profile. We used this uncertainty estimate derived from each river profile as direct input to *knickpointfinder* (Schwanghart and Scherler, 2017). Lithologic and non-lithological knickpoints were identified by comparing their spatial distribution with available geological maps, satellite images, and χ-elevation plots. Under uniform climate/rock type, knickpoints representing transient adjustment to an increase in rock uplift rate should cluster around the same χ (Perron and Royden, 2013).

We used transient stream profiles to quantify the fluvial incision in the study area. By reconstructing the river profiles from the relict landscape (i.e., upstream of the highest non-lithological knickpoints; e.g., Clark et al., 2006; Schildgen et al., 2012; Miller et al., 2013; Calvet et al., 2015; Fox, 2019), the total magnitude of fluvial incision has been computed for each sector, in the north, central and southern parts of the mountain range.

2.4.3. Divide stability assessment

Drainage divides are dynamic features of a landscape that can migrate leading to a reorganization of the river networks and catchments (Fig. 2.1; e.g., Willett et al., 2014; Perron et al., 2012). The potential role of drainage reorganization as a driver of landscape transience is being increasingly acknowledged (Willett et al., 2014). Therefore, to acquire information about the ongoing drainage system evolution in the study area, the drainage divide stability criteria (χ and Gilbert metrics) were evaluated to examine the stability of the Talesh Mts. divide by considering the overall topography of the region.

2.4.3.1.Analysis of χ and χ_Q

By characterizing the river network topology and geometry, χ determines how tectonic forcing generates variable topography throughout a river basin, provided climate and rock strength are uniform (e.g., Perron and Royden, 2013; Willett et al., 2014). The stability of a divide can be affected by tectonic asymmetric uplift (chiefly controlled by fault activity), and tectonic horizontal advection (e.g., Goren et al., 2014; Forte et al., 2015; Sinclair et al., 2017; Su et al., 2020). We used this framework to assess divide stability in the study area using the *DivideTools* software package (Forte and Whipple, 2018) in TopoToolbox. The examined divide separates the Ardebil Basin watersheds from those in the western Alborz Mountains which flow into the Caspian Sea, which is the final outlet of all the watersheds in the study area. In order to calculate the metrics, all the rivers should end at a common base level. To avoid the fluvial plain adjacent to the Caspian Sea, and thus better target bedrock channels for calculation of metrics, a base level of 40 meters a.s.l. was chosen.

In addition to tectonic uplift, both lithology and climate may considerably influence the stability of the divide (e.g., Perron et al., 2012; Willett et al., 2001 and 2014; Buscher et al., 2017; Forte and Whipple, 2018; Expósito et al., 2022). To account for the influence of spatially variable rainfall in the study area, we also calculated χ_Q metric, which uses the product of drainage area and mean-annual precipitation rather than drainage area alone (Leonard et al., 2023). While χ_Q accounts for variable rainfall, varied rock properties still affect χ_Q values and can potentially bias divide stability interpretations – an effect we attempt to constrain using independent methods detailed in the following sections.

2.4.3.2. Gilbert metrics

In divide stability analysis, if we solely use χ-maps, the current stability of a drainage divide may be interpreted incorrectly because χ integrates signals over the entire drainage basin area (from baselevel to headwaters) but does not account for potential variations in rainfall and rock properties within that area or within the basins across the divide. Gilbert metrics (mean gradient, mean local relief, mean channel bed elevation) (Whipple et al., 2017; Forte and Whipple, 2018), originally postulated based on Gilbert's (1877) law of unequal slopes (Fig. 2.1), provide an alternative approach to assess divide stability, and focus on the topography near the drainage divide where conditions are more likely to be uniform (Whipple et al., 2017; Forte and Whipple, 2018). Like χ and χ_Q, divide stability is interpreted from equal values in Gilbert metrics across the drainage divide, while unequal values may suggest ongoing or future divide motion. The use of the χ metric in concert with the Gilbert metrics can give us more information for interpreting the potential condition of a divide, as disagreements among these different metrics may indicate ongoing adjustment to non-uniform uplift rate and/or spatially/temporally variable erosional efficiency (Forte and Whipple, 2018).

2.4.4. Rock strength mechanical measurements

The aim of this analysis is to estimate the degree of erodibility variation across different rock types. To achieve this, we applied a multi scale testing approach by using two indirect methods including Schmidt hammer rebound values and point-load test measurements and converting them to UCS. Additionally, we used geological strength index (GSI) of jointed rock mass (Hoek and Brown 1997; Hoek et al., 2013) which is a qualitative index and enables us to estimate the strength of a rock mass based on visual inspection of rock outcrops in the fieldwork (Fig. S2.6; see Appendix chapter 2). Thus, we can have a comparison of rock strength in the scale of rock matrix, rock mass and the entire outcrop. We conducted mechanical measurements of rock strength in the field using the Schmidt hammer rebound (e.g., Murphy et al., 2018; Zondervan et al., 2020a; Zondervan et al., 2020b; Chilton and Spotila, 2022), and took rock samples from the drainage divide to analyze in the laboratory by point load test (ASTM, 2008). We did the laboratory measurements and studies in the Laboratory of Engineering Geology, at the Department of Earth Sciences, Sapienza University of Rome.

2.4.4.1. Schmidt hammer rebound index

We used the Schmidt hammer Type-N which is utilized for supplying information on the types of rocks, weakness, and their compressive strengths. Schmidt hammer rebound measurements were collected across the entire divide in the northern, central, and southern sectors of the mountain. A total of over 600 Schmidt hammer values were taken, with approximately 200 rebound readings recorded in each sector. In each sector, two representative samples were collected for specific gravity determination and natural gamma measurements with hydrostatic balance.

The reliability of results obtained using the Schmidt hammer index is often compromised by various factors such as the type of hammer, its orientation, the normalization of rebound values, specimen dimensions, weathering, etc. To address these issues, we used Schmidt hammer chart (Goudie, 2006). The estimation of uniaxial compressive strength (UCS) of the rock types in each sector of the mountain range has been determined by utilizing the average weight per unit volume obtained from laboratory tests (Tables. S2.1, S2.2, and S2.3), the orientation of the hammer, the values of rock strength measured by Schmidt hammer, and plotting them on the Schmidt hammer chart.

2.4.4.2.Point load strength index (PLI)

To test the accuracy of UCS results obtained from Schmidt hammer measurements, and to rule out the effects of rock discontinuities we applied the point load test to samples, which is not sensitive to discontinuities. This approach has been found useful for estimating the uniaxial compressive strength (Broch and Franklin, 1972; ASTM, 2008; Chilton, 2021). In accordance with the guidelines established by ASTM and ISRM (ASTM, 2008; Franklin, 1985), the point load tests on the samples were performed in the laboratory. The location of the samples included two sites in the northern divide sector, two sites in central, and three sites in the southern. Roughly 15-20 tests were performed on each sample resulting in a total of approximately 100 tests. Point Load Strength Index was determined by applying a size correction based on the pre-test sample dimensions by following ISRM guidelines (Franklin, 1985). The data obtained from the tests were then converted to UCS using empirical equations (Tables. S2.4, S2.5, and S2.6).

2.5. Results

2.5.1. Drainage divide stability evaluation

The general orientation of the drainage divide, as well as the strike and axial planes of faults and folds, conforms to the strike of the mountain range (Fig. 2.3). Since a single divide may be heterogeneous, it was useful to segment it and assess the stability of these segments separately (Forte and Whipple, 2018). We segmented the Ardebil Basin main divide into 14 segments (ARD1 to ARD14) (Fig. 2.3a) to calculate the χ metric (Fig. S2.3a) Gilbert metrics (Fig. S2.3b-d) and assess divide stability (Figs. 2.5, 2.6, and 2.7).

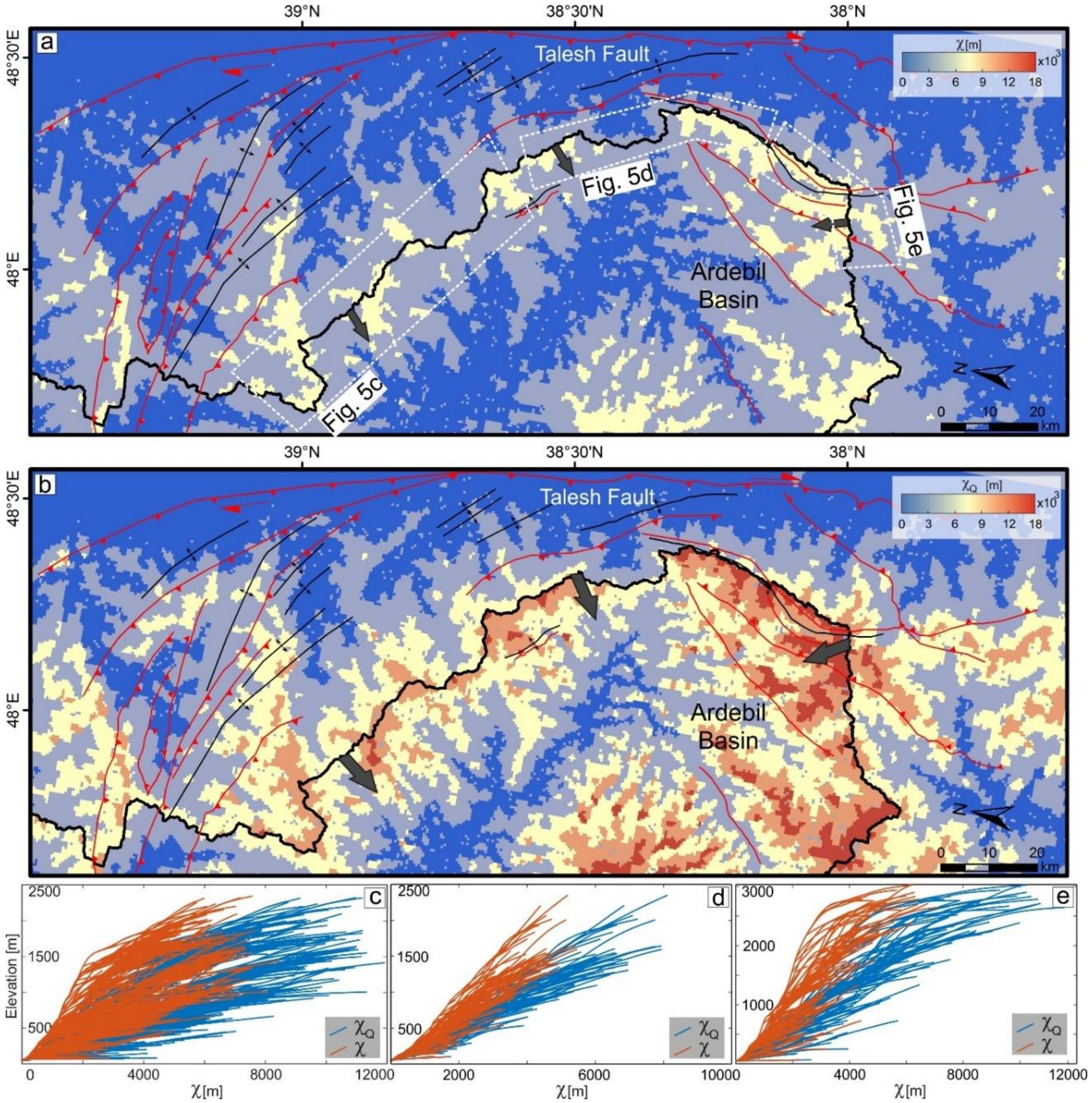

Figure 2.5. Interpolated map of (a) χ and (b) χ_Q. Black arrows show the direction of the divide movement. (c), (d), and (e) Comparisons between χ-z (orange) and χ_Q-z (blue) profiles for catchments in the north, central, and southern parts of the range, respectively.

We segregated the main divide based on visual examination of all the metrics. The main drainage divide in the study area shows large contrasts of χ values (i.e., χ anomalies), which suggests that the divide may be unstable (Figs. 2.5a; S2.3a). χ always indicates movement of the divide towards the interior of the plateau. In contrast, Gilbert metrics suggest the northern and southern parts of the divide to be largely stable (Figs. 2.6, and 2.7). The southern part of the divide is oriented NE-SW and located along the main structures where the local relief (Fig. S2.3d) and k_{sn} values are very high.

Based on the Gilbert metrics on both sides of the divide, the NW-SE oriented segments (ARD1 to ARD3) in the north of Talesh Mts. seem to be in equilibrium, like ARD11 to ARD14 segments in the south. On the other hand, the divide segments in the central Talesh Mts. (ARD4 to ARD8) are suggested to be migrating towards southwest, by both Gilbert metrics and χ due to progressive capture of the main rivers (Fig. 2.8).

Visualizing these metrics' across-divide differences as histograms of the values gives us an assessment of the variability and highlights the discrepancies between the metrics (Forte and Whipple, 2018). The histograms of the χ metric and Gilbert metrics are computed at the channel heads on both sides of each individual sector of the divide (Fig. 2.6). The histograms of the main divide segments indicate that, the ARD1 to ARD3, and ARD11 to ARD14 segments are stable, whereas the ARD4 to ARD10 segments suggest a divide motion towards the interior of the plateau, i.e., to the southwest (ARD4- ARD8) and the west (ARD9, and ARD10) (Figs. 2.6, and 2.7).

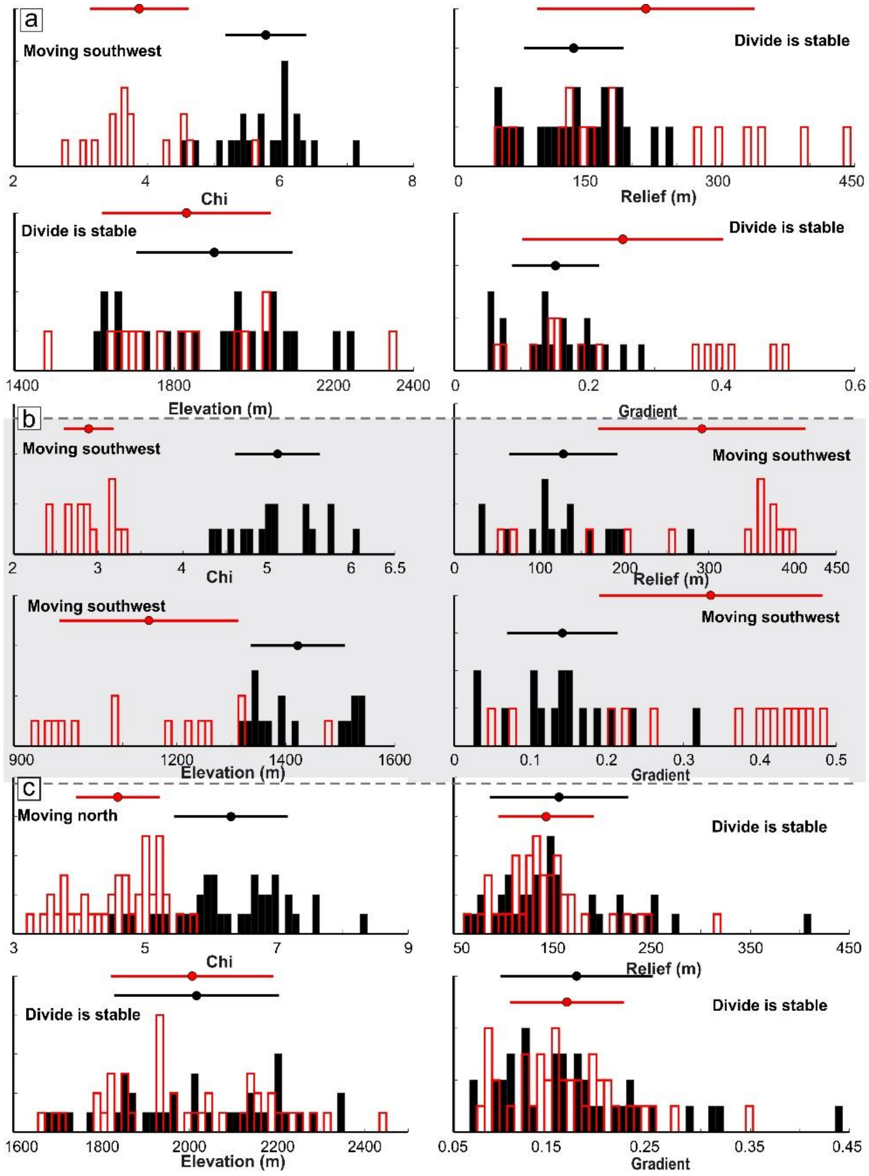

Figure 2.6. Divide stability analysis of the study area. (a), (b), (c) Representative histograms of divide metrics for the ARD3, ARD6, and ARD14 segments, from the north, central, and southern sectors of the Ardebil Basin main drainage divide, respectively. Histograms with black rectangles exhibit watersheds in the interior of the plateau, while white histograms with red outlines show watersheds on the exterior of the plateau (towards Caspian Sea flank).

The results illustrate that the χ and Gilbert metrics are consistent with what is predicted from the histograms across all the divide segments. Overall, as it is shown in Figs. 2.5a and 2.7 the segments of the Ardebil Basin main divide in central Talesh Mts. appear to be unstable and are moving towards SW, whereas the segments in the north and south of the mountains are in equilibrium. The elevation metric (Δ elevation) shows that except for five segments (ARD4 to ARD8), which suggests that the divide moves towards the southwest (interior of the plateau), all the other segments are stable (Fig. 2.7a). The slope (Δ gradient), and local relief (Δ relief) (Fig. 2.7c, and 2.7d respectively), to a large extent are alike. The ARD4 to ARD9 segments, and ARD10 predict the divide motion towards southwest and west respectively, suggesting that all these segments are migrating towards the interior of the plateau. The means of all metrics (Fig. 2.7e) in eight segments (ARD3 to ARD10) in the central Talesh Mts. agree, except for the segments which are in the north (ARD1-ARD2), and south (ARD11-ARD14) of the Talesh Mts. For the divide segments ARD1 to ARD3, and ARD11 to ARD14, the elevation, gradient, and relief metrics (also χ metric for ARD1) show that they are stable using the standard deviation, while χ constantly indicates that divides are not stable (except for ARD1) and should move toward the interior of the plateau (mainly towards SW) (Fig. 2.7). Gilbert metrics and χ to a large extent are consistent in the ARD1 to ARD10 divide segments.

To assess the contributing factors to the stability of divide, the variability in the mean annual precipitation (and hence in the erosional efficiency) across the divide has been considered. Consequently, by taking the annual rainfall into consideration, and recalculating χ and Gilbert metrics, the potential role of climate has been captured. The histograms of the χ and Gilbert metrics with the precipitation effect are presented in Fig. S2.4.

The geometric properties of the divide suggest the existence of wind gaps, hillslope undercutting by rivers, and spatial anomalies in erosion rates, which based on Scherler and Schwanghart (2020) are diagnostic for past or ongoing mobility of drainage divides and could be interpreted as signatures reflecting mobile divides that tap into existing drainage networks. Accordingly, sharp-crested and shortened hillslopes, as well as beheaded streams were recognized in Google Earth images (Fig. 2.8), supporting the divide mobility process in the direction of lower hillslope relief (Figs. S2.3d, and S2.5).

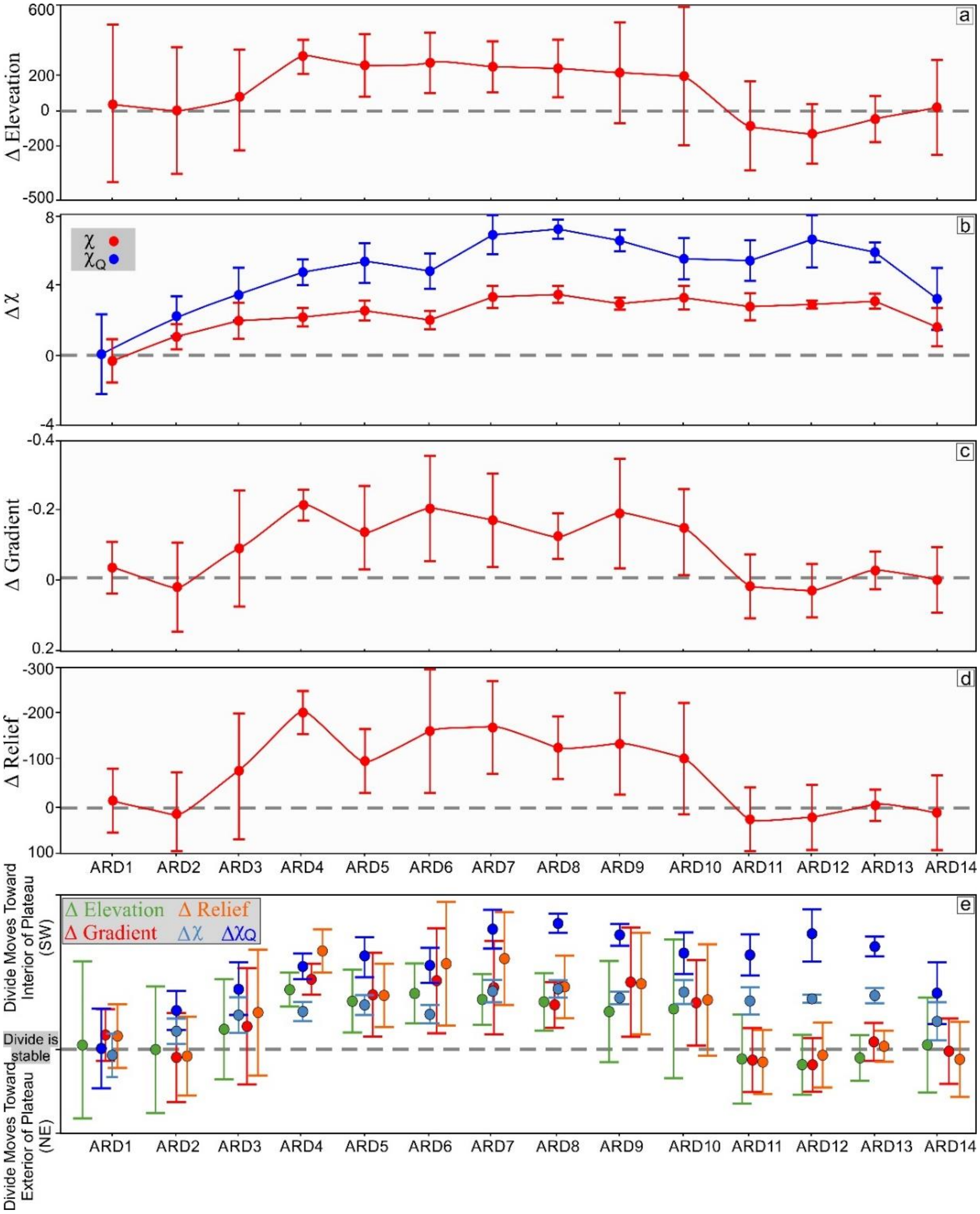

Figure 2.7. Results of Gilbert metrics, χ and χ_Q for the different drainage divide segments. (a), (b), (c), and (d) indicate the stability status and the potential divide mobility direction based on Δ elevation, $\Delta\chi$ (red)- $\Delta\chi_Q$ (blue), Δ gradient, and Δ relief, respectively for the 14 segments of the main divide. The grey dashed line shows the divide stability line. If the error bar determined by bootstrapping for a single divide segment touches the stability line, that segment is stable in that metric. Note that the y-axes of Δ relief and Δ gradient are reversed. Accordingly, the values above and below the divide stability lines suggest divide instability and movement toward the interior (mostly SW), and the exterior of the plateau, respectively. (e) Standardized delta plot for the 14 segments along the main drainage divide. Error bars represent standard deviation.

Additionally, based on Forte and Whipple (2018), in a drainage divide the presence of a χ-anomaly along with the absence of Gilbert anomaly (e.g., ARD11 to ARD14, and to a less extent ARD2 and ARD3 segments; Fig. 2.7e), illuminates a spatial gradient in uplift rate and/or erosional efficiency. The study of the k_{sn} index, longitudinal, and χ-transformed river profiles provide insights for understanding the nature of these spatial gradients.

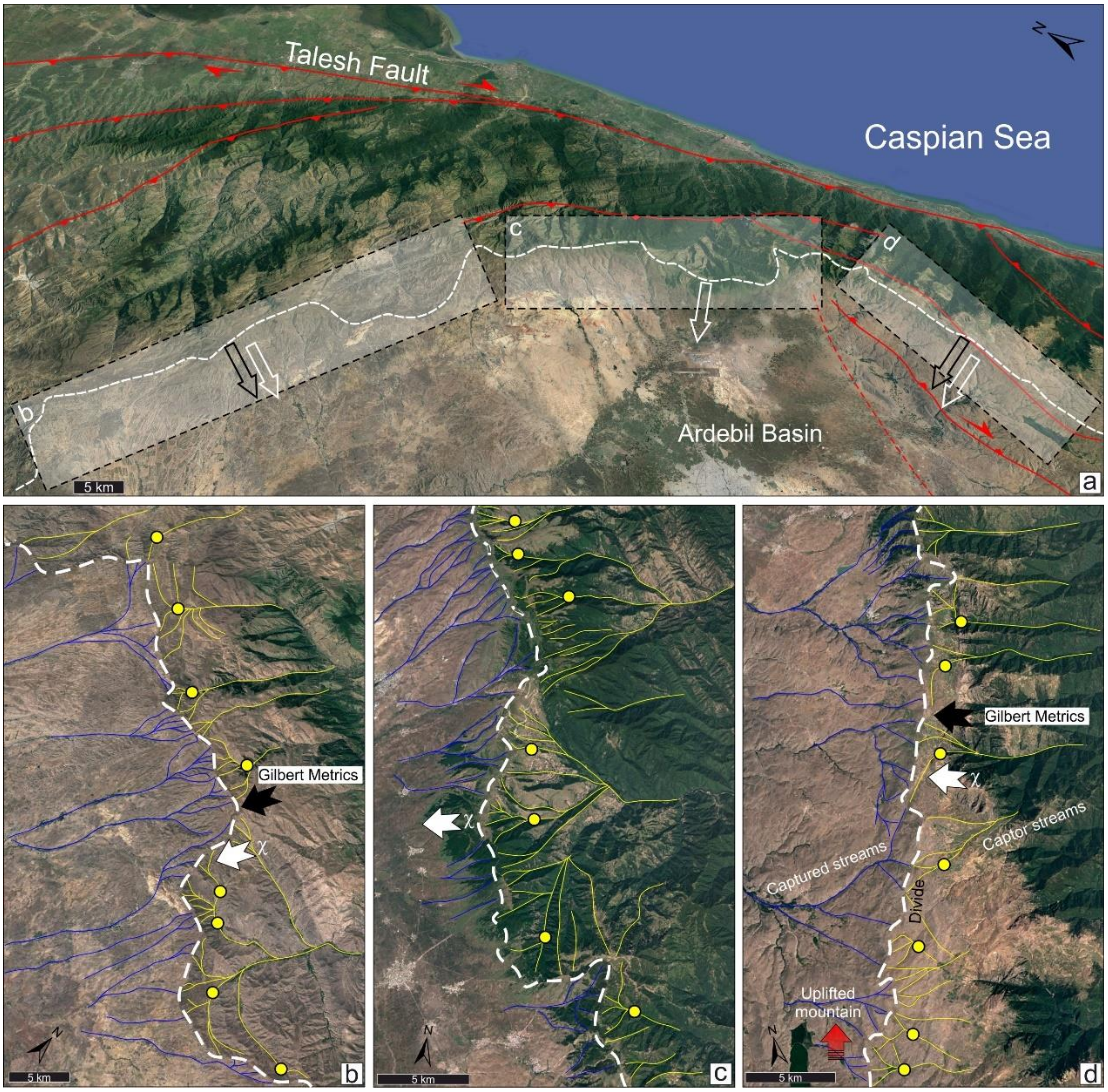

Figure 2.8. Drainage pattern evolution and channel configuration in the NW sector of the Iranian plateau. (a) Google earth image of the study area showing the position of the main divide with river networks. (b), (c), and (d) the evidence of river piracy and wind gaps in the northern, central, and southern sector, respectively. Note the strong topographic asymmetry across the divide and the orographic effect on precipitation as indicated by the vegetation pattern. White dashed line indicates the main drainage divide. Yellow circles show the locations of elbow of captures. White and black arrows illustrate the predicted divide mobility by χ and Gilbert metrics, respectively.

The comparison of χ_Q and χ maps (Fig. 2.5), shows a consistent pattern with χ_Q values that are two times higher than χ values. Furthermore, the difference between χ_Q-z and χ-z spaces in the three sectors of the mountain range shows the potential influence of spatially varying rainfall on the river profiles. Accordingly, contrasts in χ and χ_Q reflect differences in erosion rate across the divide induced by the rainfall pattern, that may potentially affect the divide motion.

2.5.2. Stream network analysis

2.5.2.1.Steepness index (k_{sn})

The steepness of channels is generally dependent on uplift rate, erodibility of the rocks, and climate (e.g., Kirby et al., 2003; Kirby and Whipple, 2001, 2012; Miller et al., 2013; Adams et al., 2020; Snyder et al., 2000; Duvall et al., 2004, Leonard et al., 2023). Therefore, assuming similar rock erodibility and climate, by using k_{sn} and other geomorphic indices, regional rock uplift rate patterns can be identified. The streams located in the eastern flank of the Talesh Mts. are dominantly in Eocene and Oligo-Miocene volcanic and volcaniclastic rocks, which are exposed to precipitation rates, ranging mostly from ~350 to 800 mm/yr (Fig. 2.2).

This part of the study area presents the highest k_{sn} and topographic slope values. Conversely, the lowest k_{sn} and slope values are observed in the Ardebil Basin in the interior of the plateau (Fig. 2.9a). The central and southern sectors of Talesh Mts. have higher HI (>0.5) and relief values (1200- 2100m) than the northern sector indicating a greater variation in elevation.

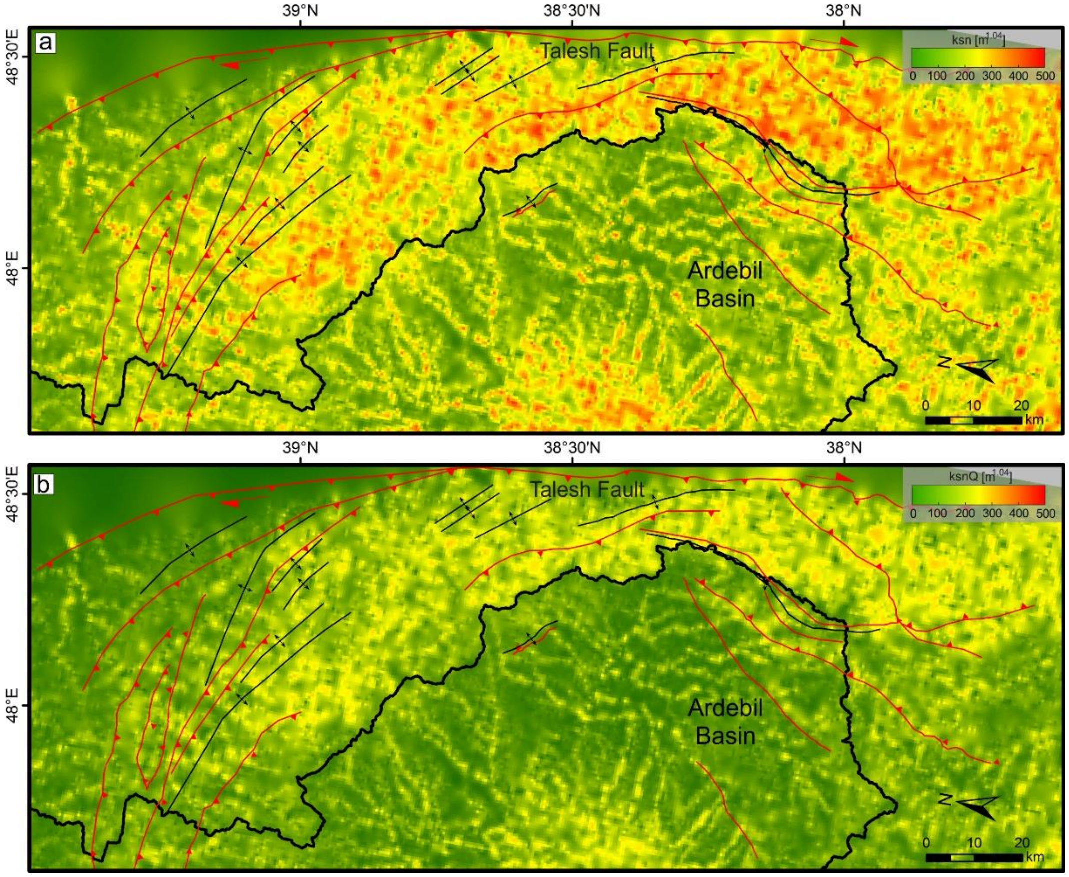

Figure 2.9. Interpolated maps of (a) normalized steepness index (k_{sn}), and (b) k_{snQ}. Note that values are systematically higher along the eastern slope of the Talesh Mts.

2.5.2.2.Modified steepness by spatial rainfall variability (k_{snQ})

The complexity of tectonically active regions such as Talesh Mts. provides an excellent opportunity to see the patterns of k_{sn} and k_{snQ} (Leonard et al., 2023; (Fig. 2.9) in understanding the fundamental mechanisms affecting landscape evolution. Accounting for variability in rainfall patterns amplifies the sensitivity of channel steepness to lithologic and tectonic controls on topography, thereby improving the accuracy of forecasts for erosion and rock uplift rates (Leonard et al., 2023). With similar uplift rate and rock type, catchments that experience greater amounts of precipitation are less steep than those with lower rainfall at steady state (Adams et al., 2020). In the study area, the pattern of k_{snQ} and χ_Q includes rainfall. Thus, k_{snQ} was used to isolate tectonic and lithologic elements and capture the impact of climate. The k_{snQ} values (Fig. 2.9b) are lower than the k_{sn} values by roughly two times. The same applies to the χ and χ_Q values (Fig. 2.5).

This pattern is typical of regions with low rainfall. In the χ_Q plots (χ_Q -elevation), k_{snQ} is the slope of the profiles, thus, a higher χ_Q means that there are lower k_{snQ} values on average throughout the catchment than k_{sn} values.

Additionally, by comparing the steepness index and k_{snQ} maps (Fig. 2.9) a possible interpretation could be that contrasts in k_{snQ} are smaller than k_{sn}. By correlating these two maps with the geological and precipitation maps, the high values of steepness index do not seem to be completely correlated to the lithologic domains nor to the distribution of precipitation rates, although precipitation may have a limited contribution to the landscape evolution of the region.

2.5.2.3.Knickpoints and incision analysis

The non-lithological knickpoints are located on the slope break changes in the χ-transformed profiles (Figs. 2.10, and 2.11), but lithological knickpoints may also record information on transience. In this study, the transient analysis focuses on non-lithological knickpoints. In terms of elevation, the major non-lithological knickpoints in different parts of the study area are located between 1000- 1500m, 600- 1200m, 2000- 2750m which reflect northern, central, and southern sectors, respectively (yellow stripes; (Fig. 2.11a,c,e, and g), and clustered roughly at values of χ of 2000- 4000. These knickpoints separate gentle upstream river segments from steep concave up downstream segments (different k_{sn} values; Fig. 2.11). The field photos of the knickpoints from the Google Maps Photos (source: http://earth.google.com) are provided in the Appendix chapter 2 (Figs. S2.7, S2.8, and S2.9).

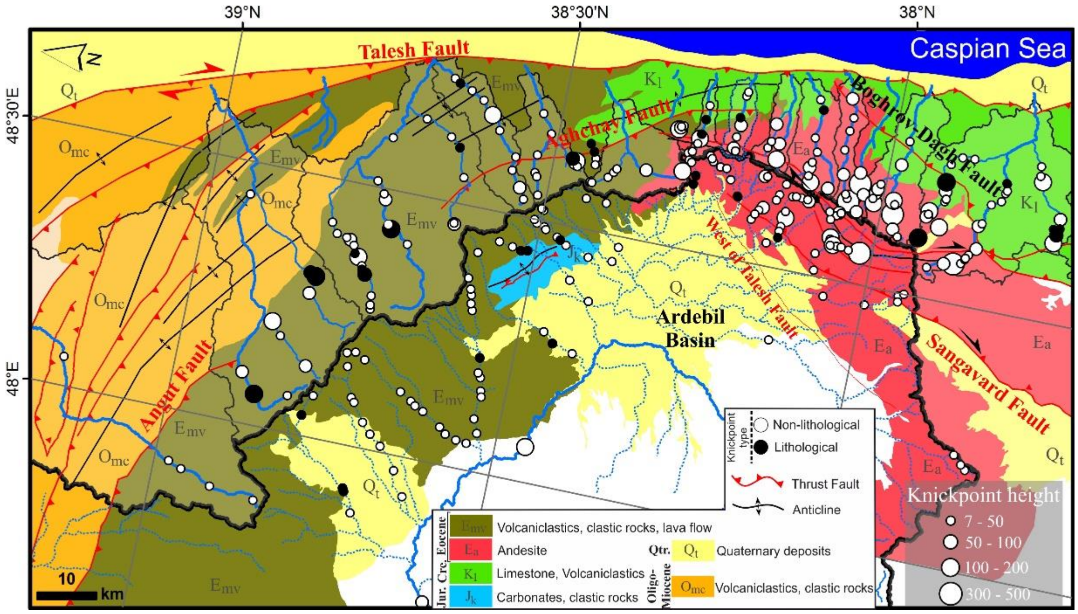

Figure 2.10. Spatial distribution of knickpoints in the three sectors of the Talesh Mts. Lithological and non-lithological knickpoints with their heights are represented on the geological map of the study area.

In the northern, central, and southern sectors of the range, the high-standing relict landscape has a mean k_{sn} of 130±4 m, 371±7 m, and 236±8 m respectively (Fig. 2.11). While, for the landscape downstream of the non-lithological knickpoints in these sectors, the mean k_{sn} values are 620±10 m, 414±12 m, and 1020±10 m (Fig. 2.11). The results of knickpoint analysis suggest the presence of a transient landscape with a long-term incision up to ~2500 m in the Talesh Mts (Fig. 2.12). This incision decreases considerably in the central sector down to ~700 m.

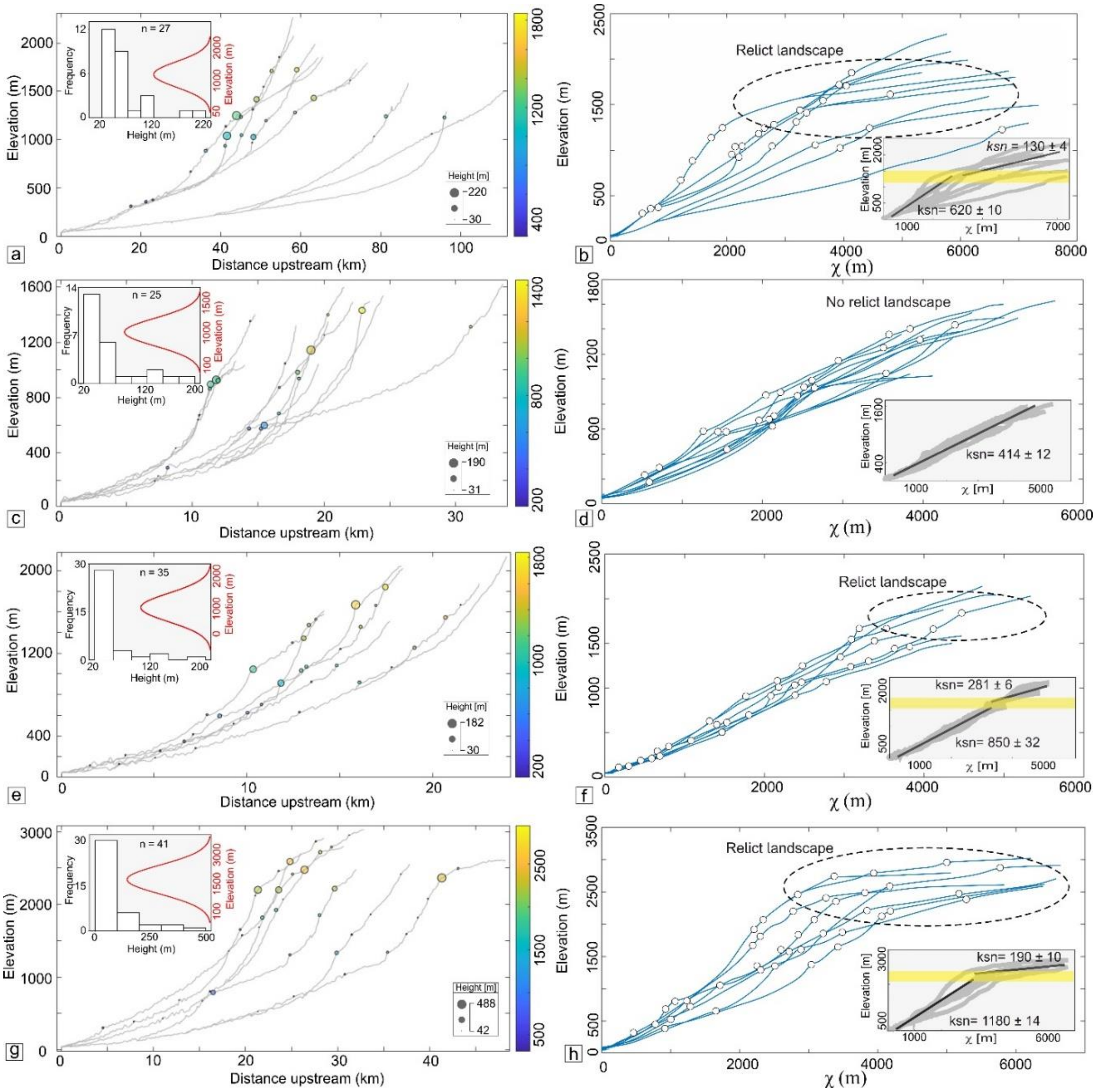

Figure 2.11. Longitudinal profiles and χ-transformed plots with major knickpoints. (a-b) northern sector, subbasins 1 to 3; (c-d) central sector, subbasins 4 to 7; (e-f) southern sector, subbasins 8 to 10; (g-h) southeastern sector, subbasins 11 to 13 of the Talesh Mts. The inset plots in the χ profiles indicate the mean regional k_{sn} values upstream and downstream of the highest knickpoints. The inset histogram in the longitudinal profiles represents the frequency distribution of the elevation and height of the knickpoints.

The main transient stream profiles in the northern sector, yielded a mean fluvial incision of ~ 800 m. In the central sector, where most of the rivers are in equilibrium, based on the main river profiles, the mean magnitude of fluvial incision is ~ 400 m, which is the lowest in the entire of the study area (Fig. 2.12b). In the southern sector, rivers are characterized by strong disequilibrium profiles with high-standing non-lithological knickpoints lying at the margin of a low-topographic relief and delimiting segments with high k_{sn} from those with low k_{sn} values, in the downstream and upstream portion of the fluvial channel, respectively. Estimates of fluvial incision for the southern sector of the mountains based on main river profiles of the catchments is ~1600 m which is the highest in all over of the mountain range (Fig. 2.12). The incision rates mentioned here may be influenced by the relative sea level drop which we will discuss later in the discussion.

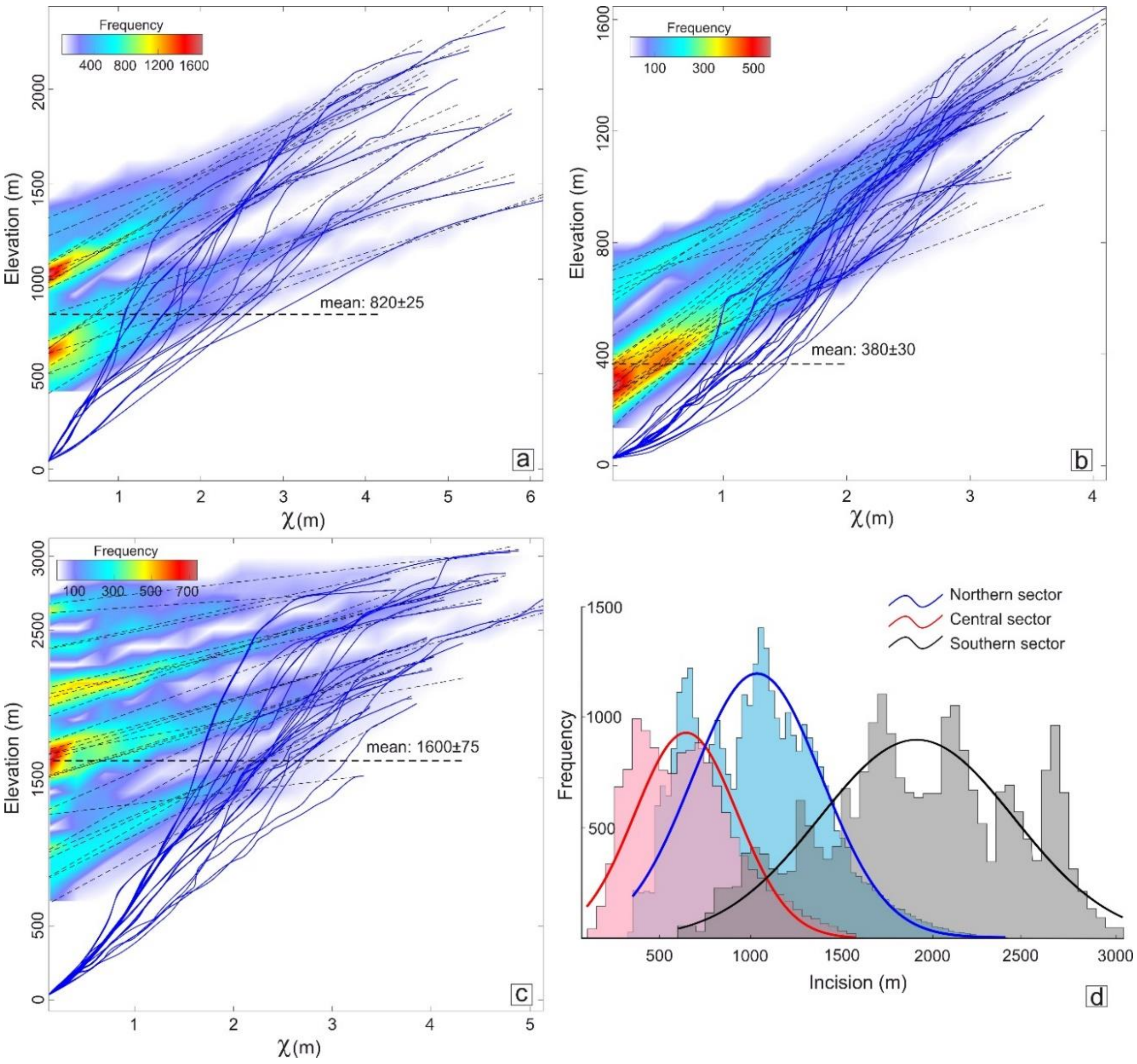

Figure 2.12. Modern longitudinal profiles and projections of the relict landscape in (a) north, (b) central, and (c) southern sectors of the range. The profile is constructed using the relict landscape, upstream of the major and highest knickpoints. (d) Histograms and frequency diagrams of magnitude of incision in the three sectors of the mountain range.

2.5.3. Rock strength investigation

In order to determine the rock strength in different parts of the study area and to isolate the effect of rock type on erodibility, the mechanical strength of rocks has been measured. Our research provides a multifaceted analysis of lithological characteristics (Fig. 2.1; Figs. 2.13, and 2.14), which impacts the erodibility of bedrock, divide stability and knickpoint migration in the study area. The outcomes of rock strength and range of uniaxial compressive strengths by using Schmidt hammer are documented and displayed on the standard Schmidt diagram.

Figure 2.1. Rock-type characteristics, and uniaxial compressive strength of rocks in the north, central, and south of the Talesh Mountains

Mountain sectors	Schmidt hammer value	Uniaxial compressive strength	Point load value (KN)	UCS (point-load)	Erodibility	Rock characteristics
Northern part	20- 60	63- 180	13- 42	66- 329	Very resistant	Very strong and competent igneous rocks. Andesite-basalt, breccia tuff, andesitic massive lithic tuff
Central part	5- 34	19- 33	2- 14	16- 97	Very erodible	Weak to very weak rock- crumbles with hammer blows. Igneous rocks; highly weathered and weakly compacted sedimentary rocks: Tuff, pyroclastics with volcanic clasts (andesite and basalt)
Southern part	20- 54	47- 135	7- 44	29- 169	Resistant	Very strong rock- hard to break with hammer. Moderately weathered and fractured. Competent igneous rocks: Porphyritic andesite, andesitic basalt

The Schmidt hammer results (Tables. S2.1-3) indicate that in the central Talesh Mts., the volcaniclastic units have the lowest UCS values (19- 33 MPa) amongst the three sectors (Fig. 2.14b). Competent andesite-basalt in the north, and strong andesite in the south have the highest uniaxial compressive strength ranging from 63 to180 and from 47 to 135 MPa, respectively. Although UCS results from point-load tests are compatible with Schmidt hammer results, the UCS range from point load tests is generally greater than that of ones obtained with the Schmidt hammer (Fig. 2.14c). This wide range of UCS values for the north, central, and southern sectors is 66- 329, 16- 97, and 29- 169 MPa, respectively. To a high extent, the rock-type characteristics, and UCS values in the north and southern sectors are similar. The results of point load tests are presented in Tables. S2.4-6 (see the Supplementary Materials).

Figure 2.13. Field photos showing the lithological units in the study area. (a) In the northern sector, resistant competent andesite, and andesite-basalt are exposed. (b), (c) close-up view of the rock units in the north of Talesh Mts. (d-f) In the central sector, pyroclastic, and week rock units are common, and variations in rock strength and weathering intensity exist. In this part due to higher precipitation, the vegetation cover is greater than in the north and southern sectors. (g-i) Eocene weathered andesite exposed in the southern sector with several joint systems and fractures. Roads and houses in all photos are for scale.

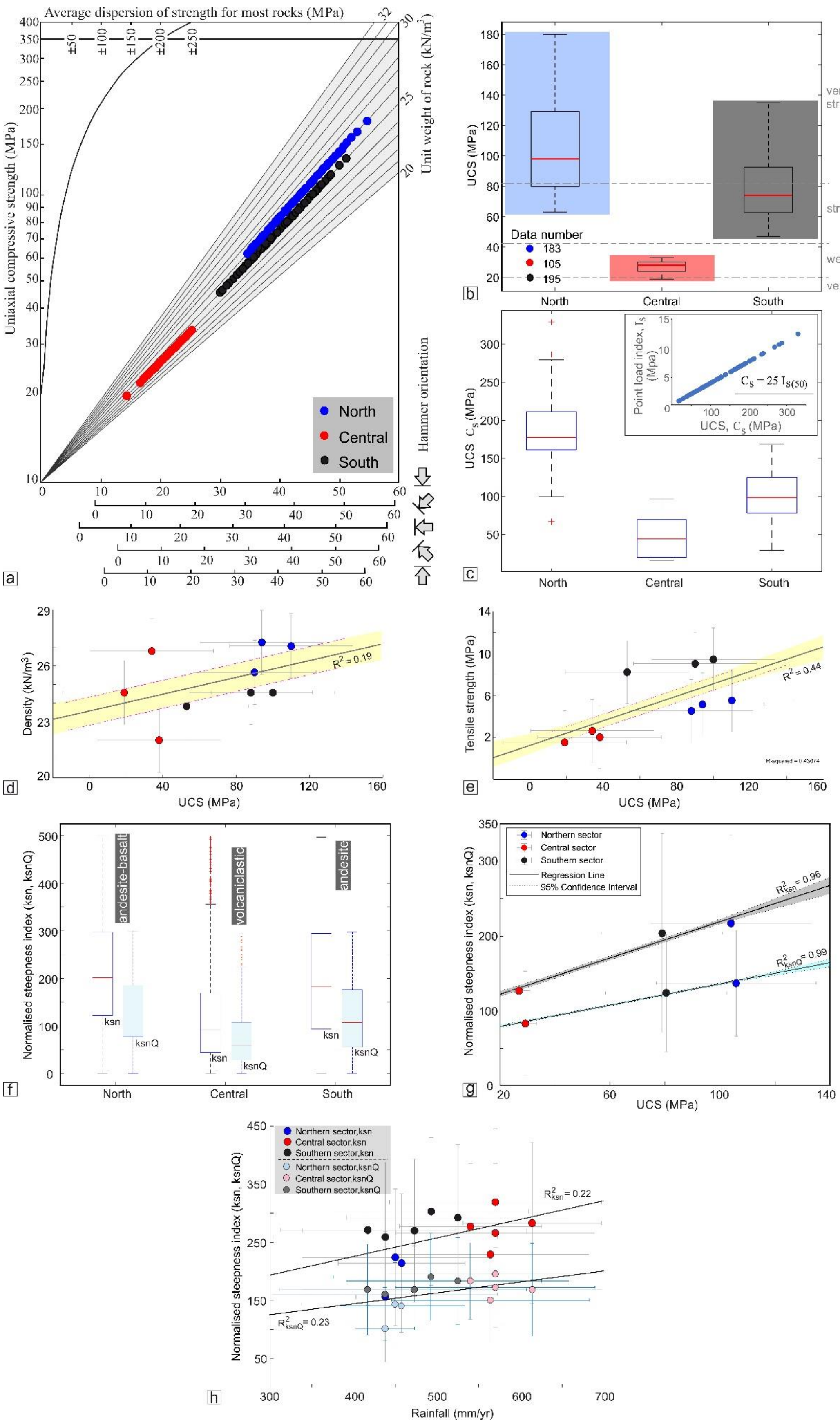
Average dispersion of strength for most rocks (MPa)
±50
±100
±150
±200
±250
Uniaxial compressive strength (MPa)
Unit weight of rock (kN/m³)
32
30
25
20
Hammer orientation
North
Central
South
a
UCS (MPa)
very strong
strong
weak
very weak
Data number
183
105
195
North
Central
South
b
UCS C_s (MPa)
Point load index, I_s (Mpa)
$C_s = 25\ I_{s(50)}$
UCS, C_s (MPa)
North
Central
South
c
Density (kN/m³)
$R^2 = 0.19$
UCS (MPa)
d
Tensile strength (MPa)
$R^2 = 0.44$
UCS (MPa)
e
Normalised steepness index (ksn, ksnQ)
andesite-basalt
volcaniclastic
andesite
ksn
ksnQ
North
Central
South
f
Normalised steepness index (ksn, ksnQ)
Northern sector
Central sector
Southern sector
Regression Line
95% Confidence Interval
$R^2_{ksn} = 0.96$
$R^2_{ksnQ} = 0.99$
UCS (MPa)
g
Northern sector,ksn
Central sector,ksn
Southern sector,ksn
Northern sector,ksnQ
Central sector,ksnQ
Southern sector,ksnQ
$R^2_{ksn} = 0.22$
$R^2_{ksnQ} = 0.23$
Normalised steepness index (ksn, ksnQ)
Rainfall (mm/yr)
h

Figure 2.14. Comparison between Schmidt hammer and point load test, and k_{sn}- k_{snQ} with mechanical rock strength and precipitation. See the main text and supplementary materials for details, and conversion of Schmidt hammer rebound values and Point Load Index values ($I_{s(50)}$) into uniaxial compressive strength (UCS). (a) Rebound data in each sector plotted on the Schmidt hammer chart. (b) and (c) Boxplots of rock strength and range of uniaxial compressive strengths in the north, central, and southern sectors by using Schmidt hammer and point load test, respectively. The inset in (c) upper right, reports the relationship between Point Load strength index and uniaxial compressive strength. The median is represented by a red line within each box. Box extent illustrates the interquartile range, and whiskers represent minimum and maximum values. (d) and (e) Relation between rock properties (mainly density) and tensile strength of the sampled rocks as a function of uniaxial compressive strength, respectively. (f) Average and standard deviation of k_{sn} and k_{snQ} in the three sectors of the mountain range for each lithological unit. (g) Linear regression values of k_{sn} and k_{snQ} versus UCS for each lithological unit. (h) Relationship and correlation between k_{sn}, k_{snQ} average values in the uplifted relict landscape and precipitation.

2.6. Discussion

2.6.1. Investigation of divide stability

Although the χ map suggests that all the divide segments are dynamic and migrate towards the interior of the plateau (Fig. 2.5a), the Gilbert metrics indicate that the drainage divide in the northern and southern parts of the Talesh Mts. is static (Figs. 2.6, and 2.7). Thus, both χ map and Gilbert metrics suggest that the central sector of the drainage divide is unstable and migrates to the southwest (i.e., to the plateau interior). Considering that instability of the divide segments denotes drainage area loss in the Ardebil Basin, these area changes should also result in stream power changes (e.g., Willett et al., 2014).

Therefore, since χ metric integrates the entire river catchment upstream from the base level and tells us about the erosion rate in the catchment scale, we can infer that erosion and uplift rate may be higher in the eastern side of the divide in its entire segments towards the wet flank of the mountain range. This inconsistency between χ and Gilbert metrics' results in the northern and southern sectors of the mountain range can be attributed to the spatial variability of rock uplift and/or erosional efficiency, which perturbs the χ over the longer timescales (e.g., Forte and Whipple 2018).

In the northern and southern sectors of the Talesh Mts, the divide segments are stable and virtually near the topographic crest of the range. Conversely, the segments in the central part are migrating southwest towards the low-relief side.

This may represent contrasting erosion rates across the divide which are reflected in the potential movement of these divide segments toward the interior of the plateau. The topography of the region, as indicated by agreement between all topographic metrics, suggests that divide instability in this part of the study area is due to piracy of the plateau rivers (Fig. 2.8). Due to piracy and headward erosion, the headwaters of the rivers got captured. The headwaters of the modern rivers (yellow color; Fig. 2.8b-d) who were flowing toward the interior of the plateau before the asymmetric uplift, are now flowing in the opposite direction to Caspian Sea due to divide mobility and capturing (Fig. 2.8).

Due to the middle Miocene and early Pliocene accelerated exhumation along the thrust and reverse faults in the northern and southern parts of the range (Madanipour et al., 2018), the divide migrated towards the high-uplift side and was positioned adjacent to the geometric center of the mountain. In these parts, the erosional wave related to the most recent uplift pulses has not reached the divide yet. Therefore, these sectors show symmetry and steady-state conditions according to the Gilbert metrics, since these metrics are measured locally at the divide and solely gives us information about the local erosion rates, and they may not detect far field influences that drive the long-term evolution. On the other hand, in the central part, the erosional wave reached the divide moving it toward southwest, as testified by Gilbert metrics which suggest asymmetry. In this sector, a limited contribution of the annual precipitation can be taken into consideration, since in the central sector it is more contrasting across the divide.

Generally, we can infer that the progressive motion of the divide in the central sector is due to the erosional wave reaching the divide. While at longer- wavelength and timescale, the main divide in all the three sectors is mobile (as suggested by χ) due to higher erosion/uplift rates in the wet flank of the Talesh Mts.

Thus, the erosional exhumation (Madanipour, 2023) due to higher precipitation (Figs. 2.3b, and 2.16c) and/or difference in the erodibility of rocks (Figs. 2.13, and 2.14) can be introduced as the main driver of transient landscape in the central sector. In the following paragraphs we discuss the role of each factor thoroughly.

2.6.2. Topographic and structural features of the study area

The Talesh Mts. which are bounded by the Talesh Fault to the east, represent a complex zone in terms of tectonic structures and surface processes. In order to decipher the signal of the inherited topography related to the uplift history and long-term fault activity, topographic analyses results are summarized in the swath profiles (Fig. 2.15). We constructed three across and one along-divide swath profiles (Figs. 2.3b, and 2.15) to document the distribution of minimum, mean, and maximum elevations as well as local relief, as a proxy of uplift-driven river incision. The along-strike swath profile (Fig. 2.15a) highlights the geometry and the extent of the elevated axial surface with local variations in topographic relief, mountain peaks and incised valleys. The high-standing landscape is mainly composed of Eocene andesite and volcaniclastic rocks.

Along the main drainage divide, in the northern Talesh Mts., the values of local relief are low, and swath profiles merge together, which is an indicator of stable areas with low incision. On the other hand, in central Talesh Mts. the high values of local relief document higher incision/uplift of the mountain range (Fig. 2.15a), and mean elevation approaches the maximum elevation in this section which could show a transient of adjustment to higher uplift rates (e.g., Pinter and Keller, 2002; Wobus et al., 2006b; Pérez-Peña et al., 2017).

In the central Talesh Mts, Hi values are between 0.5 and 0.75, which indicate mean elevations close to maximum elevations and, consequently suggesting the occurrence of a young transient landscape (Fig. 2.15a). Conversely, lower values of hypsometric integral in the northern and southern parts of the mountain indicate a mature landscape whose mean elevation is close to the minimum. This also shows that these parts of the divide have not yet experienced the erosional wave, or the erosional efficiency in these parts is considerably lower than the central part, which is in agreement with the position of the knickpoints.

In the along-strike P1 swath profile, the average variation between the maximum and minimum curves in the northern Talesh Mts. is very low (500- 1000m). In the central Talesh Mts. the variation is about 1400- 2000 meters, which is the highest value of the entire study area. Swath profiles indicate that the highest elevations and local relief (1200-2100 m) values are in the central and southern sectors of the range. These anomalies correlate with the highest values of DAI (Divide Asymmetry Index) (See the

Supplementary Materials) and the hypsometric integral in the study area (Fig. 2.15a). The analysis of the swath profiles suggests that uplift rates along the mountain range are not uniform which is consistent with other metrics/analysis (e.g., χ, k_{sn}, knickpoints, etc). Perpendicular to the general trend of the main divide (swath P1; Fig. 2.15a), topographic variations at the northern, central, and southern parts of the Talesh Mts. (swaths P2, P3, P4; Fig. 2.15b-d, respectively) have been evaluated. In swath P2, the values of local relief and hypsometric integral are low in the west side of the main divide (plateau interior) and increase toward the east in the middle of the profile (Fig. 2.15b), where the Ojagh-Gheshlagh anticline with a convex crest presents high local relief. In the central Talesh Mts., in swath P3 (Fig. 2.15c), adjacent to the divide point, there is an abrupt increase in hypsometric integral (THi*) from 0.25 to 0.6. Additionally, the local relief increases from 350 to 1000m. In the middle of the profile, in the anticline located in the footwall of the Aghchay Fault, local relief value increases. The southern sector of the Talesh Mts. reaches the highest elevation of the study area (maximum elevation of 3300 meters). In this sector, the range of local relief values are lower than those in the northern, and central parts, and most of the high values correlate with the location of the main faults (swath P4; Fig. 2.15d). In the eastern part of the main drainage divide the topography is dominated by several large anticlines and thrust faults (Fig. 2.3). This topographic contrast between the two sides of the divide is also reflected in the spatial variations of the topographic gradient, distribution of relief, elevation, and hypsometric integral (Fig. 2.15) which can be used to constrain the topographic evolution of the study area.

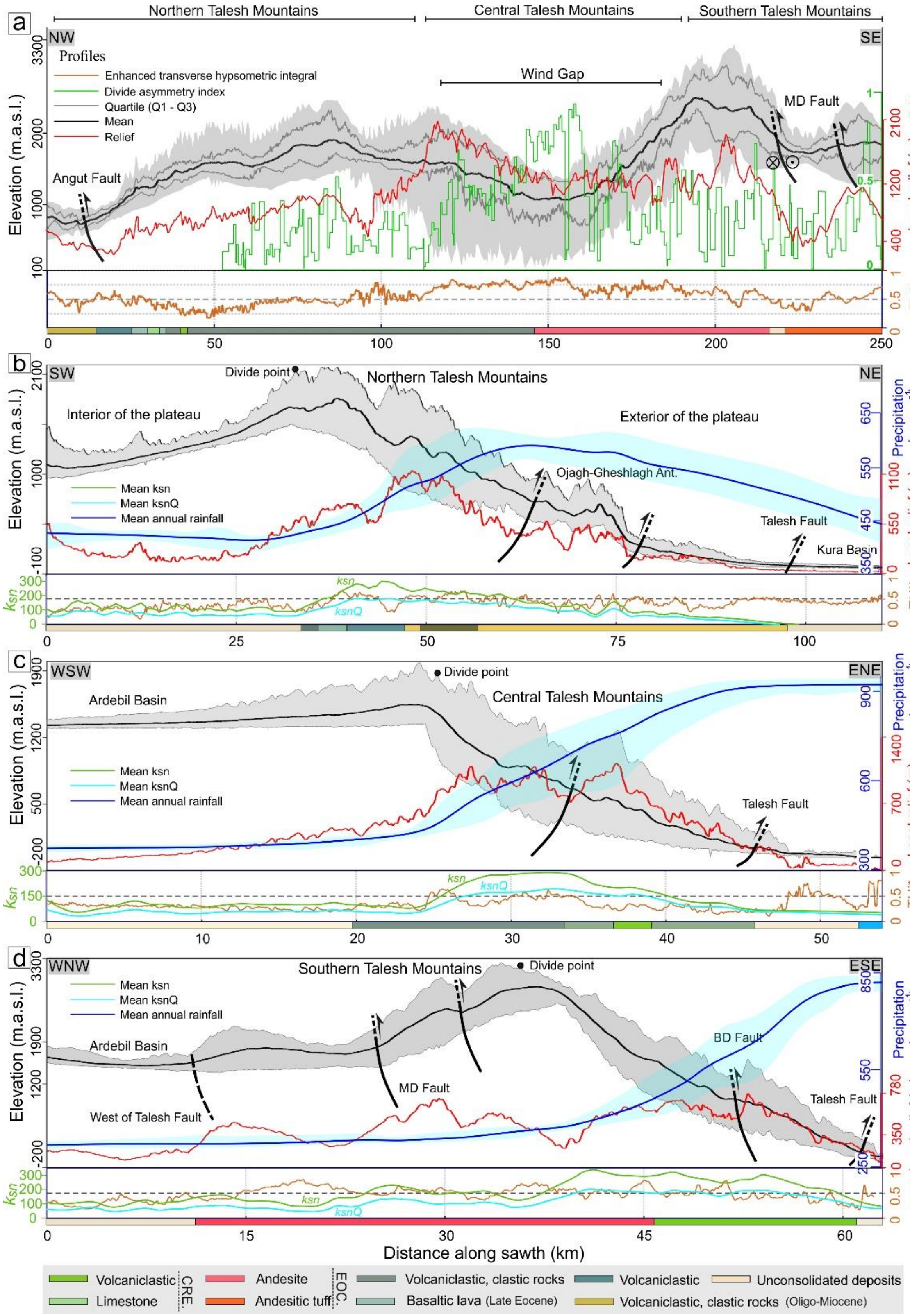

Figure 2.15. (a) Along (P1), and (b-d) across strike (P2 to P4) swath profiles of the Talesh Mountains. The swaths present a strong asymmetric topography and orographic precipitation across the main divide. In each

profile, local relief (red lines), enhanced transverse hypsometric integral (Thi*; orange lines), steepness index values (k_{sn} ;light green lines), k_{snQ} metric (light blue lines), and the precipitation rate (thick dark blue lines) are represented. In the swath P1 (a), divide asymmetry index (DAI) profile is illustrated with green color. Swath window is 20-km-wide. Location of the swaths are shown in Figure 3b, and S3b. In P2 to P4 swath profiles, the base level in the interior (left side of the swath) and exterior of the plateau (right side of the swath) is fixed at 40m. Note that in these profiles the base level in the interior of the plateau is not represented.

The distribution of k_{sn} and hillslope gradient of the study area are plotted in both east and west side of the main divide in order to reveal the asymmetric uplift (Fig. 2.16). Generally, the normalized channel steepness values decrease from east to west orthogonal to the main divide (Figs. 2.9 and 2.15), and they are markedly higher across the Talesh Mts. than that of the Ardebil Basin. Therefore, it can be concluded that the study area has likely experienced an asymmetric uplift pattern, with higher uplift rate on the eastern side of the divide and the mountain range (toward the Caspian Sea wet flank). Consequently, the topography in the eastern side of the main divide is steeper than that of in the western side. Thus, the higher k_{sn} testifies that topography in the exterior plateau has already adjusted to uplift rates with respect to the interior plateau (Figs. 2.16b and S2.3c).

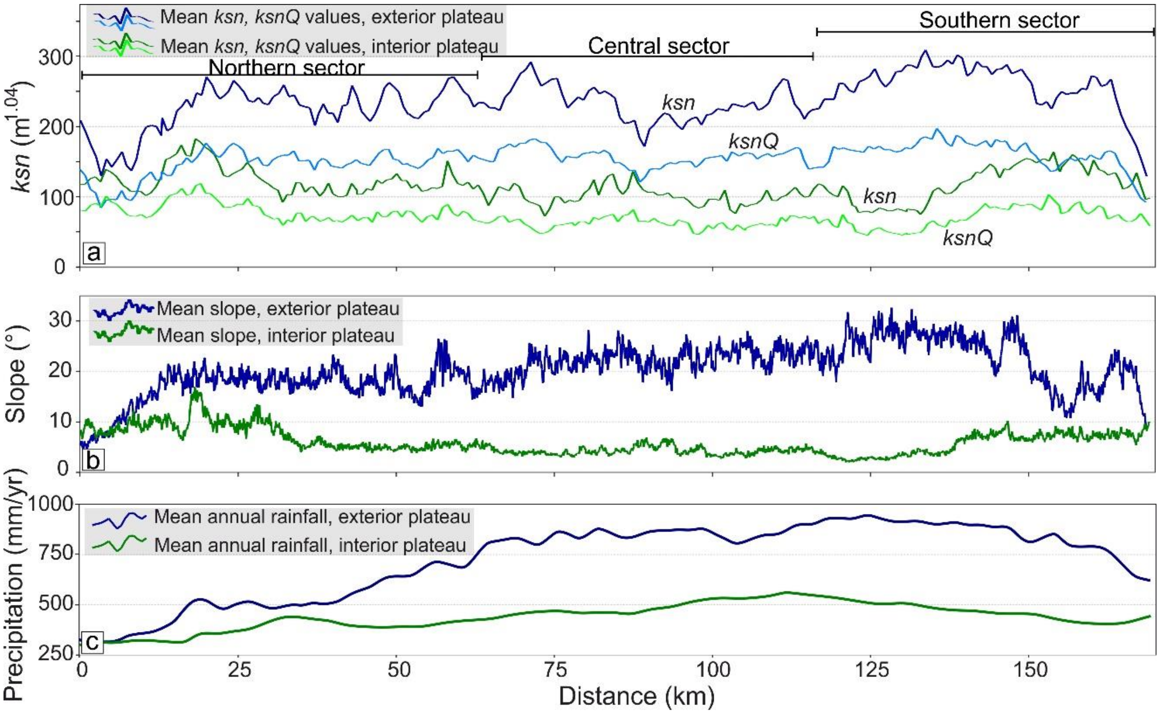

Figure 2.16. Profiles of the mean values of steepness index, gradient, and annual precipitation. (a), (b), and (c) Comparison of the k_{sn}- k_{snQ}, slope degree, and annual rainfall mean values between the two along the

main drainage divide of the Ardebil Basin, respectively in the interior and exterior (towards the wet flank of the range) of the plateau.

2.6.3. Transient topography and asymmetric uplift

The asymmetric uplift scenario agrees with accelerated middle Miocene exhumation at ~12 Ma as constrained by U-Th/He thermochronometric data along the thrust and reverse faults in the northern and southern Talesh Mts., and the limited exhumation in the central part (Madanipour et al., 2017). The thrust kinematics has been proposed for the faults in the Talesh Mts. during early Oligocene - middle Miocene when the regional convergence direction was toward northeast. In middle Miocene, due to a change in the regional convergence direction towards north, the strike-slip component became dominant in the central part of the Talesh Mts. (Madanipour et al., 2013; 2017 and 2018). Furthermore, GPS data suggest for the northern part of the range a minor component of NNE-SSW extension perpendicular to the mountains belt at a rate < 2 mm/yr. At the same time, for the southern and central parts of the Talesh Mts., 5- 6 mm/yr of horizontal shortening and 4-5 mm/yr of right-lateral strike-slip movements have been documented (e.g., Djamour et al., 2011; Madanipour et al., 2018). Hence, the Talesh Fault can be considered the main structure of the margin of the Iranian plateau, which controls rock uplift and caused asymmetric uplift of the Talesh Mts. Furthermore, the evidence of wind/water gaps and river piracy has been recognized by remote sensing analyses in the relict landscape (Fig. 2.8) suggesting a drainage reorganization following the asymmetric uplift, and/or erosion patterns.

The stability of the main drainage divides at the topographic crest of a mountain in the presence of homogeneous tectonic uplift, rock erodibility and precipitation rate, could be disturbed when the mountain experiences asymmetric uplift. Consequently, the main drainage divide will migrate towards the high-uplift side till it reaches a steady-state (e.g., Forte and Whipple, 2018; He et al., 2021a). Furthermore, in response to an asymmetric uplift, the divide movement direction could be from the high-uplift side towards the geometric center of the mountain to achieve a new steady-state (Ye et al., 2022). The strong variation in the normalized channel steepness index, topographic slope, elevation, and fluvial incision between the portions of the landscape downstream and upstream of the highest non-lithological knickpoints documents a transient condition of the Talesh Mts. topography. This transient state could be attributed to several processes, such as drainage reorganization, climate change, bedrock erodibility, eustatic sea level fall and tectonic uplift (e.g., Hancock and Kirwan, 2007; Kirby and Whipple, 2012; Miller et al., 2013, Ballato et al., 2015). In this study, drainage reorganization due to tectonic uplift and erosion appear to be the main cause of this transient state since there is evidence of knickpoints, and wind gaps related to river piracy processes (Figs. 2.8 and 2.10)

An increase in erosion rates due to climate variations (i.e., increase in precipitation rates) is also likely, and may have acted as an additional factor enhancing the divide mobility. The abrupt break in the river longitudinal profiles and $\chi - z$ plots at the highest non-lithological knickpoints and the position of the knickpoints in the χ space (Fig. 2.11b, d, f, and h) show that the two portions of the landscape upstream and downstream of these knickpoints erode at different rates (Schildgen et al., 2012; Miller et al., 2012; 2013; Olivetti et al., 2016; Clementucci et al., 2022). This is consistent with an increase in erosion and rock uplift rates propagating from the river outlet to the uppermost river segments (Miller et al., 2013; Gallen and Wegmann, 2017; Racano et al., 2021 and 2023). Consequently, the highest knickpoints represent a response of the fluvial system to an increase in rock uplift rates and hence mark a phase of topographic rejuvenation, while the uplifted relict landscape records the previous erosional conditions predating such an increase. Conversely, the minor and non-lithological knickpoints located in the lower segments of the fluvial network, at 200- 800 m and 400- 1500 m in the north, central, and southern sectors, respectively, can be attributed to a Quaternary climate forcing (e.g., Hancock and Kirwan, 2007; Clementucci et al., 2023). This pattern of knickpoints is spatially consistent and does not show any channel steepness variation across the knickpoints in the longitudinal profiles and the $\chi - z$ plot (Fig. 2.11b, d, f, and h).

The present geomorphic configuration and high elevation of the study area is caused by the interplay of internal and external forces in different temporal scales. In this matter, three phases of Cenozoic deformation were documented in the Talesh Mts. Based on thermochronometry data (zircon bedrock U-Th/He ages), exhumation started in the late Oligocene (~27–23 Ma) and then accelerated in the middle Miocene (~12 Ma) and the early Pliocene (5 Ma).

The last deformation phase resulted in exhumation along the thrust, reverse and strike-slip faults, which shaped the present-day architecture of the Talesh Mts. The late Oligocene phase (phase 1) which is recorded across the entire mountain range, caused shortening that was accommodated along reactivated and/or newly initiated thrust faults including the Sangavard, Boghrov-Dagh, and Angut faults. While the middle Miocene (phase 2) and early Pliocene (phase 3) phases are solely recorded in the northern and southern parts of the Talesh Mts. (Madanipour et al., 2017). Therefore, after phase 1, when the whole range uplifted, just the northern and southern parts of mountains were uplifted during phase 2 and 3, while, in the central part without any significant tectonic activity, the erosion was shaping the landscape, and decayed the topography. In the northern and southern parts, although the divide is suggested to be stable by the Gilbert metrics, divide mobility towards the interior of the plateau should occur once the erosional wave reaches the present divide position as also suggested by χ. The reason for such a stability is related to the erosional wave in the northern and southern parts of the Talesh Mts. that has not reached yet the divide after the latest uplift phases. Furthermore, in these parts, the erodibility of bedrock (Fig. 2.14) and the rate of precipitation (Figs. 2.3b, and 2.15) is lower which promote lower impact of surface processes and erosional dynamics than the central part of the range.

2.6.4. Climate variability and influence of orographic precipitation

Several studies have shown the mechanism and limitations of across-divide χ metric to assess the direction and rate of a migrating divide and interpret their spatial patterns in connection with tectonic forcing (e.g., Willett et al., 2014; Yang et al., 2015; Forte and Whipple, 2018; Winterberg and Willett, 2019; Su et al., 2020; Maneerat and Bürgmann, 2022). Across divide differences in χ may reflect differences in erosion rate and divide motion if rock uplift, rock erodibility, and climate is uniform. The divide migration can be produced by non-uniform climate condition or rock erodibility and hence χ map may suggest incorrect divide movement (e.g., Willett et al., 2014; Whipple et al., 2017; Forte and Whipple, 2018).

The impacts of weathering processes on erodibility and its variation in different parts of the mountain can be taken into consideration as an additional significant factor on the relative importance of rock strength (e.g., Chilton and Spotila, 2022; Shobe et al., 2017). Although the properties of rocks can considerably impact landscapes, this influence may not always be the most prominent factor. Therefore, the contrast in rock strength needs to be evaluated in relation to the magnitude of tectonic or climatic variation (Mitchell and Forte, 2023). Mountainous terrains commonly experience orographic precipitation patterns. Hence, if the erosion mechanisms in such landscapes are responsive to temporal or spatial fluctuations in rainfall, alterations in orographic precipitation patterns can significantly impact the mountain landscape evolution (Roe, 2005; Leonard and Whipple, 2021).

High elevations in the northern and southern sectors of the Talesh Mts. receive approximately 400- 500, and 500- 900 mm/year, respectively. Whereas the central sector experiences ~800- 1100 mm/year of rainfall (Figs. 2.3b, and 2.16c). The study area covers over 200 km along strike and includes variable lithologies that experienced several deformation episodes in the Cenozoic (Eocene, Miocene, Pliocene), alongside climatic fluctuations. The k_{sn} and k_{snQ} metrics reflect erosion rate patterns, and k_{snQ} gives the best remote estimate of spatial variations in erosion at the landscape scale (Leonard et al., 2023). Since k_{sn} fails to account for the distribution of precipitation, it forecasts higher erosion rates in the study area compared to k_{snQ}. The main divide effectively separates the zones where k_{sn} and k_{snQ} forecast higher erosion rates.

In the study area, basins with higher precipitation rate show higher values of steepness. These basins will reach equilibrium more rapidly and exhibit higher rates of erosion over time during the process of landscape adjustment, compared to basins that receive lower levels of precipitation (Ferrier et al., 2013). Furthermore, some catchments in the region with similar lithology, such as andesite and volcanoclastic rocks, that undergo contrasting rainfall, have identical k_{snQ} values, suggesting that rock uplift rates must be identical.

Therefore, the difference between k_{sn} and k_{snQ} suggests different spatial patterns of uplift/erosion rates. This difference between the two metrics highlights the erosion rate patterns in the study area. Across the main divide boundary in the southern and northern sectors, the precipitation rates are rather similar, while in the central parts, where the precipitation appears to be higher on the eastern flank, there is not that much difference in the k_{sn} values. Thus, precipitation is not a major factor affecting the geomorphic indices and does not dominate the topographic expression of the range, although it represents a potential factor controlling the topographic evolution of the study area. Hence, it seems that tectonic rock uplift/erosion rates govern the drainage evolution in the study area.

Additionally, in the central Talesh Mts., the rapid incision of the rivers may be caused by Caspian Sea base level fall which led to the onset of erosional exhumation in the eastern wet flank of the Talesh Mts. at ~ 5.6 Ma (e.g., Ballato et al., 2015; Madanipour, 2023), although we showed that also the erodibility of rocks plays a role in here.

2.6.5. Bedrock erodibility and landscape response time

In landscape evolution processes, in addition to climate and tectonics, bedrock erodibility and rock strength play an important role. In fact, heterogeneous exhumation of strong and weak bedrock units can repress and intensify erosion respectively (e.g., Allen et al., 2013; Giachetta et al., 2014; Forte et al., 2016; Gallen, 2018; Campforts et al., 2020; Zondervan et al., 2020a) and critically influence the development of localized topographic relief. Therefore, it is necessary to understand the effects of erodibility when interpreting landscape processes and patterns.

Difference in landscape response time to tectonic perturbations is a function of different factors including erodibility (Zondervan et al., 2020a), precipitation, drainage area, etc.
Our field observations and measurements have shown the influence of bedrock erodibility on the landscape of the region (Fig. 2.14). There may be substantial variations in the time it takes for fluvial and landscape systems to respond to tectonic disturbances. The northern and southern sectors are mostly characterized by transient river longitudinal profiles (Fig. 2.11b, and h). In general, 287 knickpoints have been recognized, which 34 of them are lithological knickpoints with a mean height of 50 m. The highest non-lithological knickpoints' heights in the north and southern sectors of the mountains are 120m and 498m respectively. In these areas the upstream show equilibrium profiles and are represented as straight segments in the χ space (Fig. 2.11). The southern sector has the highest non-

lithological knickpoints for the entire study area (six knickpoints with a height of 120- 200 m, and three knickpoints with a height of 300- 500m).

On the other hand, in the central sector, most of the river profiles are equilibrated, with a mean k_{sn} value of ~ 350. Altogether, the distribution of the highest knickpoints and the estimated values of fluvial incision (Fig. 2.12) indicate the concentration of high incision in the south and north of Talesh Mts. This is also correlated with a regional increase in k_{sn} values downstream of the major knickpoints. Furthermore, the concentration of high k_{sn} values specifically in the southern section, where also weaker rocks crop out with respect to the northern part, supports higher rates of uplift and/or erosion in these parts of the study area.

Based on Zondervan et al. (2020a), the erodibility of bedrock greatly influences the expression of knickpoints in the landscape. Consequently, when searching for tectonic signals in the landscape to investigate the histories of faulting, the effect of varying bedrock erodibility should be considered, and the strength of bedrock strongly controls the timescale over which such signals propagate upstream (e.g., Forte et al., 2016; DiBiase et al., 2018). In the central part of the study area, due to more erodible bedrock and maybe higher erosion, the propagation of knickpoints to the headwaters probably had been tens of kilometers within a relatively short time, and the lack of relict landscape in this sector does not allow us to constrain the magnitude of incision properly, that is why the estimated fluvial incision in this sector was the lowest all over the study area. Therefore, limited evidence in the river longitudinal profiles for tectonic perturbation is visible today. In contrast, in the north and southern sectors the presence of the resistant bedrock slows the migration of the wave of incision due to the initiation of the active reverse faults, and therefore, knickpoints are prominent in the river profiles. Furthermore, the effect of higher rainfall in the central part has increased the along-stream migration rate (celerity) of knickpoints, whereas the vertical rate and thus adjustment timescale is set by the uplift rate. Consequently, the lack of relict landscape in the central sector prevents us from estimating the minimum value of fluvial incision/rock uplift. The amount of fluvial incision should be greater than the southern and northern sectors because the relict landscape has been already eroded away by fluvial processes.

The rate of uplift/incision calculated here represents the minimum magnitude of rock uplift, since the Caspian Sea as the base level for all the rivers in the region has experienced several base level changes during the Late Cenozoic which was driven by the climate, tectonic processes, and the onset of subduction in the northern margin of the SCB (e.g., Axen et al., 2001; Allen et al., 2002; Forte and Cowgil, 2013; Ballato et al., 2015; Madanipour, 2023).

2.6.6. Erodibility-induced drainage divide mobility

In this study, it is anticipated that bedrock erodibility has a role in driving the mobility of drainage divide. Measuring and defining the erodibility of bedrock and the dynamics of drainage divide continue to be a significant issue. To tackle this problem, a comprehensive set of data on rock erodibility must be integrated with topographic measurements of the mobility of drainage divide in a mountain range (Bursztyn et al., 2015; Forte and Whipple, 2018; Zondervan et al., 2020b). In an active mountain belt like the Talesh Mts., the effect of lithologically-induced divide instability could be more complex. By combining assessments of variations in the erodibility of different rock types with geomorphic indicators of the movement of the drainage divide, we suggest a framework for the mobility of drainage divide caused by lithology, and higher erosional efficiency during the topographic growth of the Talesh Mts. range. The lithological units in the study area generally consist of Eocene andesite, andesitic basalt, volcaniclastics in the northern, volcanoclastic- clastic rocks in the central, and andesite in the southern of Talesh Mts. (Fig. 2.3a). The specific characteristics of the lithological units across various sectors of the range are represented in Tabe. 2.1. It seems that the higher density of rock joints and fractures in the south, with more precipitation and higher weathering rate is responsible for the lower rock strength in comparison to the northern sector.

In the context of rock strength, we also considered the horizontal movement of contact of hard and soft rock units which can enhance drainage divide mobility. Based on Mitchell and Forte (2023), topographic advection is defined as the horizontal component of changes in topography related to the horizontal component of rock uplift, which can have a profound impact on convergent orogens, such as Talesh Mts.

Therefore, pronounced transient responses within landscapes can be induced by the combination of horizontal tectonic displacements and variations in erodibility.

In the northern sector of the Talesh Mountains, the equilibrated landscape developed in a strong lithology that might be subjected to topographic advection. In the central sector, the dipping contact of pyroclastic units and andesite (Fig. 2.13d) has caused the faster migration of the divide through the landscape respect to the northern and southern parts. Thus, the central sector may have experienced horizontal rock motion, which would create topographic advection that has led to present landscape asymmetry (Figs. 2.15c, and 2.17).

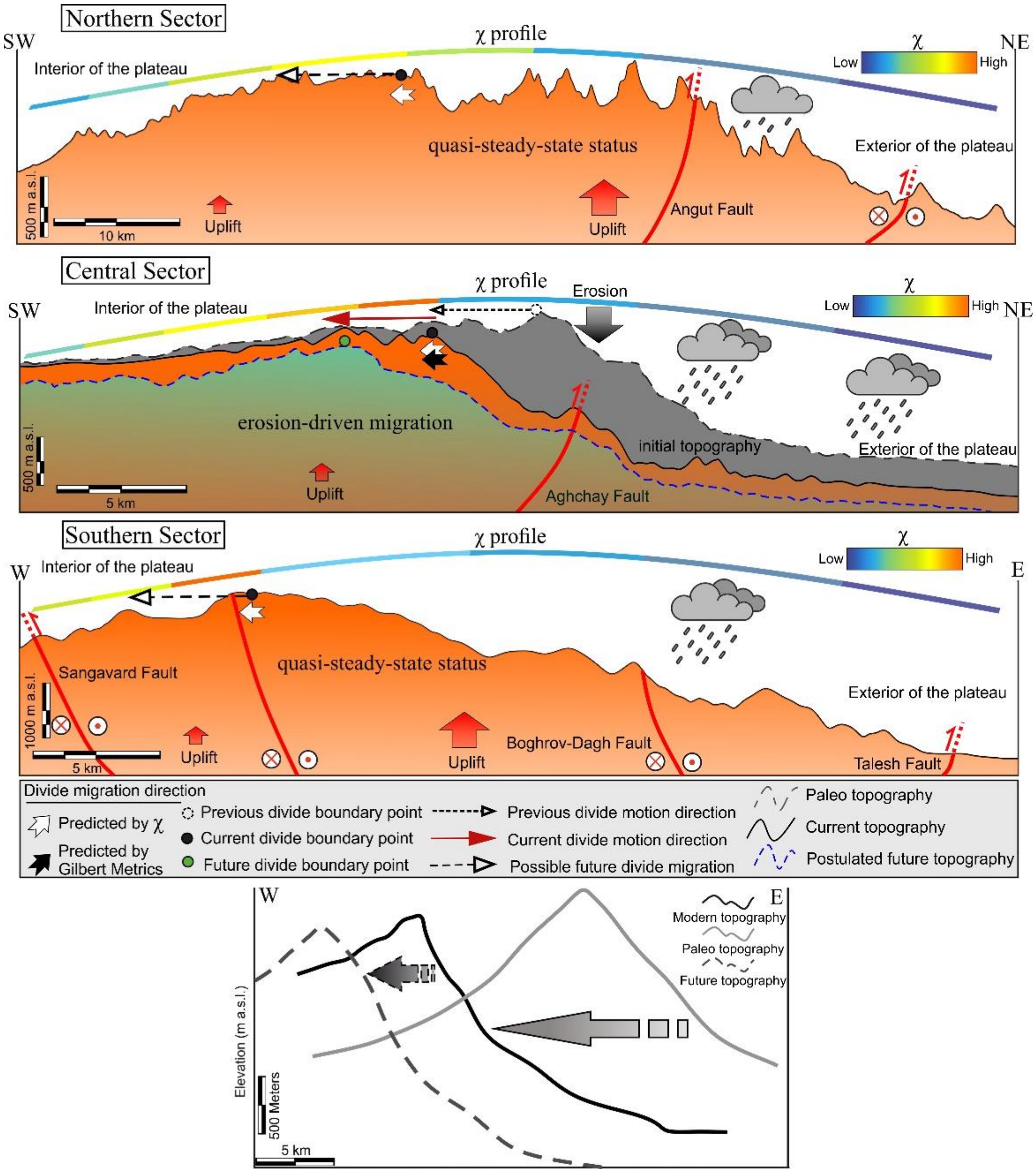

Figure 2.17. The general topographic architecture of the Talesh Mts. in its north, central, and southern sectors. Postulated topography of the range, and a simple landscape evolution model of the study area. Green and grey-shaded areas represent the postulated future and paleo topography, respectively. In the northern sector, the rate of precipitation is lower than the central and southern sectors. In this sector due to higher uplift rate in Miocene and Pliocene respect to the central part, divide moved towards the high-uplift side and reached a quasi-steady state. In the central sector, the exposure of soft rock units along the divide, consequently greater contrasts in erodibility have driven faster drainage divide mobility rates. In this sector, a SW-dipping contact of pyroclastic and volcanic hard rocks (raised by rock uplift and shifted horizontally by topographic advection; Figure. 2.13d), alongside higher precipitation rate (Figures. 2.3b, and 2.15c) caused intensified drainage divide migration towards the interior of the plateau. Furthermore, the drainage divide in this sector was offset from the center of the range in the direction of advection towards southwest. The landscape in the southern sector developed in strong lithology (andesite) and seems to be in equilibrium suggested by Gilbert metrics. Similar to the northern sector, the rate of uplift and exhumation was higher in the south due to thrust and reverse faults, respect to the central sector. While the rate of precipitation, and χ contrast values is higher in the southern sector.

Topographic advection leads to the displacement of the primary drainage in the direction of advection (He et al., 2021; Mitchell and Forte, 2023) towards the interior of the plateau. The weaker lithology in this sector accompanied with higher precipitation rate (relative to the other sectors) can cause the movement of the drainage divide (Fig. 2.17). Moreover, the contact of weak and strong rocks can be raised by rock uplift and shifted horizontally by topographic advection (e.g., Mitchell and Forte, 2023). The lithological condition of the southern sector of the range is roughly the same as the northern sector. The results show that the equilibrated landscape formed in a strong lithology.

As we mentioned earlier, apart from tectonic uplift, spatial variation in bedrock resistance affects the erodibility coefficient and k_{sn} (e.g., Mills, 2003; Whipple, 2004; Clementucci et al., 2022). In particular, topographic relief and bedrock erosion may potentially be influenced by spatial variation in precipitation. The lack of any strong relationship between k_{sn}, k_{snQ} and rainfall (Fig. 2.14h) is consistent with variable rock type and/or uplift since the study area is not at steady state. Although still a small positive correlation between k_{sn}, k_{snQ} and precipitation indicates that rainfall has a potential control on the contrasting erosion (Fig. 2.14h). We observed that resistant lithological units in the study area have higher k_{sn} average and UCS values on the relict landscape (Fig. 2.14f, and 2.14g).

Thus, we can conclude that various rock resistance and erodibility play a major role in the growth and decay of topographic relief when tectonic uplift is evenly distributed.

Conversely, we know that the topographic evolution in regions undergoing active deformation can be significantly influenced by the horizontal motion of rocks and the resulting advection of the topography, it is still important to consider the role of tectonic deformation since it can cause such regions to contain rocks with varying strengths (e.g., Willett et al., 2001; Sinclair et al., 2017; He et al., 2021; Mitchell and Forte, 2023). Thus, the presence of horizontal rock motion, a common characteristic of tectonically active regions, may contribute to landscape transience resulting from differences in rock strength. Although, distinguishing this effect from those resulting from tectonic or geodynamic processes would still pose a considerable challenge (Mitchell and Forte, 2023).

Thus, besides the role of topographic advection which can function as another factor of transmitting transient signals across landscapes (Mitchell and Forte, 2023), uplift and exhumation of the Talesh Mts. (Fig. 2.17) associated with the regional deformation due to the initial and final Arabia-Eurasia collision and subsequent structural reorganization in the early Oligocene, middle Miocene and early Pliocene (Madanipour et al., 2017), should be noted as the primary main cause predating such factors we mentioned in this paper.

2.7. Conclusion

The possible scenario for the whole divide’s behavior of the Talesh Mts. Range is associated with the contrasting erosion rates across the divide. The efficiency of erosion is primarily determined by the precipitation and the strength of exposed rocks. We can infer that divide is unstable in the study area in response to the asymmetric uplift and spatial variability of erodibility. Therefore, the divide instability in the NW of Iranian plateau is chiefly controlled by topography, especially slope and local topographic relief. While the precipitation rate has potentially been assisting, and magnifying divide mobility, reorganization of river networks and landscape transience. Our findings represent that climate does not exert a first order and strong control on topographic growth and erosional efficiency in the study area.

The Ardebil Basin main divide continues to migrate toward the interior of the plateau. This movement will continue until these segments reach a steady-state, or uplift/erosion rate becomes uniform again. Accordingly, the results show the presence of a localized uplift gradient along the divide that is holding the divide in place in the northern and southern parts. The χ metric is sensitive to this uplift rate gradient and represent the expected response of the divide when the uplift is evenly distributed. Furthermore, the Talesh Mts. which is undergoing active deformation indicates transient landscapes in the northern and southern sectors which present an uplifted relict landscape, that has also represented in swath profiles, knickpoints with high elevation, and slope map. The divide in these sectors appears to be stable because the landscape across the divide is similar and has low topographic relief. On the other hand, the topography can also be significantly influenced by advection, which has caused the asymmetric topography of the central sector due to erosion of weaker lithology. Thus, contrasting exhumation of strong bedrock units in the northern and southern sectors, and weak bedrock units in the central sector have suppressed and intensified erosion, respectively, and this heterogeneous exhumation of rocks initiated topographic reconfiguration mostly in the central Talesh Mts. In addition to the mechanisms of the horizontal motion of rocks, the role of uplift of the mountains in middle Miocene, and Pliocene cannot be ruled out of mechanisms responsible for divide mobility.

2.8. Acknowledgments

This research is part of the first author’s Ph.D. dissertation. The fieldwork has been founded by Sapienza University of Rome. Open Access Funding enabled and organized by Sapienza University of Rome within the CRUI-CARE Agreement.

2.9. References

Adams, B.A., Whipple, K.X., Forte, A.M., Heimsath, A.M., and Hodges, K.V., 2020, Climate controls on erosion in tectonically active landscapes: Science Advances, v. 6, p. eaaz3166, doi:10.1126/sciadv.aaz3166.

Agard, P., Omrani, J., Jolivet, L., Whitechurch, H., Vrielynck, B., Spakman, W., Wortel, R., 2011. Zagros orogeny: a subduction-dominated process. Geol. Mag. 148, 692–725.

Allen, M.B., Jones, S., Ismail-Zadeh, A., Simmons, M. and Anderson, L., 2002. Onset of subduction as the cause of rapid Pliocene-Quaternary subsidence in the South Caspian basin. Geology, 30(9), pp.775-778.

Allen, M. B., S. J. Vincent, G. I. Alsop, A. Ismail-Zadeh, and R. Flecker (2003), Late Cenozoic deformation in the South Caspian region: Effects of a rigid basement block within a collision zone, Tectonophysics, 366, 223–239.

Allen, M., J. Jackson, and R. Walker (2004), Late Cenozoic re-organization of the Arabia-Eurasia collision and the comparison of short-term and long-term deformation rates, Tectonics, 23, TC2008, doi:10.1029/2003TC001530.

Allen, G. H., Barnes, J. B., Pavelsky, T. M., & Kirby, E. (2013). Lithologic and tectonic controls on bedrock channel form at the northwest Himalayan front. Journal of Geophysical Research: Earth Surface, 118(3), 1806–1825. https://doi.org/10.1002/jgrf.20113

ASTM, 2008. Standard test method for determination of the point load strength index of rock and application to rock strength classifications. American Society for Testing and Materials Int West Cochohocken, PA, 22, pp.51-60.

Axen, G.J., Lam, P.S., Grove, M., Stockli, D.F. and Hassanzadeh, J., 2001. Exhumation of the west-central Alborz Mountains, Iran, Caspian subsidence, and collision-related tectonics. Geology, 29(6), pp.559-562.

Azad, S.S., Dominguez, S., Philip, H., Hessami, K., Forutan, M.R., Zadeh, M.S. and Ritz, J.F., 2011. The Zandjan fault system: Morphological and tectonic evidences of a new active fault network in the NW of Iran. Tectonophysics, 506(1-4), pp.73-85.

Ballato, P., N. R. Nowaczyk, A. Landgraf, M. R. Strecker, A. Friedrich, and S. H. Tabatabaei (2008), Tectonic control on sedimentary facies pattern and sediment accumulation rates in the Miocene foreland basin of the southern Alborz mountains, northern Iran, Tectonics, 27, TC6001, doi:10.1029/2008TC002278.

Ballato, P., 2009. Tectonic and climatic forcing in orogenic processes: the foreland basin point of view, Alborz mountains, N Iran (Doctoral dissertation, Universität Potsdam).

Ballato, P., Mulch, A., Landgraf, A., Strecker, M.R., Dalconi, M.C., Friedrich, A. and Tabatabaei, S.H., 2010. Middle to late Miocene Middle Eastern climate from stable oxygen and carbon isotope data, southern Alborz mountains, N Iran. *Earth and planetary science letters*, *300*(1-2), pp.125-138.

Ballato, P., C. E. Uba, A. Landgraf, M. R. Strecker, M. Sudo, D. F. Stockli, A. Friedrich, and S. H. Tabatabaei (2011), Arabia-Eurasia continental collision: Insights from late Tertiary foreland-basin evolution in the Alborz Mountains, northern Iran, Geol. Soc. Am. Bull., 123, 106–131.

Ballato, P., D. F. Stockli, M. R. Ghassemi, A. Landgraf, M. R. Strecker, J. Hassanzadeh, A. Friedrich, and S. H. Tabatabaei (2013), Accommodation of transpressional strain in the Arabia-Eurasia collision zone: New constraints from (U-Th)/He thermochronology in the Alborz mountains, N Iran, Tectonics, 32, 1–18, doi:10.1029/2012TC003159.

Ballato, P. and Strecker, M.R., 2014. Assessing tectonic and climatic causal mechanisms in foreland-basin stratal architecture: insights from the Alborz Mountains, northern Iran. Earth Surface Processes and Landforms, 39(1), pp.110-125.

Ballato, P., Landgraf, A., Schildgen, T. F., Stockli, D. F., Fox, M., Ghassemi, M. R., Kirby, E., & Strecker, M. R. (2015). The growth of a mountain belt forced by base-level fall: Tectonics and surface processes during the evolution of the Alborz Mountains, N Iran. *Earth and Planetary Science Letters*, *425*, 204-218. https://doi.org/10.1016/j.epsl.2015.05.051

Ballato, P., Cifelli, F., Heidarzadeh, G., Ghassemi, M.R., Wickert, A.D., Hassanzadeh, J., Dupont-Nivet, G., Balling, P., Sudo, M., Zeilinger, G. and Schmitt, A.K., 2017. Tectono-sedimentary evolution of the northern Iranian Plateau: insights from middle–late Miocene foreland-basin deposits. Basin Research, 29(4), pp.417-446.

Berberian, M., and G. C. P. King (1981), Towards a paleogeography and tectonic evolution of Iran, Can. J. Earth Sci., 5, 101–117.

Berberian, M. (1983), The southern Caspian: A compressional depression floored by a trapped, modified oceanic crust, Can. J. Earth Sci., 20,
163–183.

Berberian, M., 1997. Seismic sources of the Transcaucasian historical earthquakes. In: Giardini, D., Balassanian, S. (Eds.), Historical and Prehistorical Earthquakes in the Caucasus. Kluwer Academic Publishing, Dordrecht, Netherlands, pp. 233–311.

Broch, E. and Franklin, J.A., 1972, November. The point-load strength test. In International Journal of Rock Mechanics and Mining Sciences & Geomechanics Abstracts (Vol. 9, No. 6, pp. 669-676). Pergamon.

Burbank, D.W., Blythe, A.E., Putkonen, J., Pratt-Sitaula, B.G.A.B.E.T., Gabet, E., Oskin, M., Barros, A. and Ojha, T.P., 2003. Decoupling of erosion and precipitation in the Himalayas. *Nature*, *426*(6967), pp.652-655.

Bursztyn, N., Pederson, J.L., Tressler, C., Mackley, R.D., Mitchell, K.J., 2015. Rock strength along a fluvial transect of the Colorado Plateau – quantifying a fundamental control on geomorphology. Earth Planet. Sci. Lett. 429, 90–100. https://doi.org/10.1016/j.epsl.2015.07.042.

Buscher, J.T., Ascione, A. and Valente, E., 2017. Decoding the role of tectonics, incision and lithology on drainage divide migration in the Mt. Alpi region, southern Apennines, Italy. *Geomorphology*, *276*, pp.37-50.

Calvet, M., Gunnell, Y., & Farines, B. (2015). Flat-topped mountain ranges: Their global distribution and value for understanding the evolution of mountain topography. *Geomorphology*, *241*, 255-291. https://doi.org/10.1016/j.geomorph.2015.04.015

Campforts, B., Vanacker, V., Herman, F., Vanmaercke, M., Schwanghart, W., Tenorio, G. E., et al. (2020). Parameterization of river incision models requires accounting for environmental heterogeneity: insights from the tropical Andes. Earth Surface Dynamics, 8(2), 447–470. https://doi.org/10.5194/esurf-8-447-2020

Chilton, K.D. and Spotila, J.A., 2022. Uncovering the Controls on Fluvial Bedrock Erodibility and Knickpoint Expression: A High-Resolution Comparison of Bedrock Properties Between Knickpoints and Non-Knickpoint Reaches. *Journal of Geophysical Research: Earth Surface*, *127*(3), p.e2021JF006511.

Chilton, K. D. (2021). Point load testing to more effectively measure bedrock strength. Nature Reviews Earth & Environment, 0123456789(7), 43017. https://doi.org/10.1038/s43017-021-00180-w.

Clark, M. K., L. H. Royden, K. X. Whipple, B. C. Burchfiel, X. Zhang, and W. Tang (2006). Use of a regional, relict landscape to measure vertical deformation of the eastern Tibetan Plateau, J. Geophys. Res., 111, F03002, doi:10.1029/2005JF000294.

Clementucci, R., Ballato, P., Siame, L.L., Faccenna, C., Yaaqoub, A., Essaifi, A., Leanni, L. and Guillou, V., 2022. Lithological control on topographic relief evolution in a slow tectonic setting (Anti-Atlas, Morocco). *Earth and Planetary Science Letters*, *596*, p.117788.

Clementucci, R., Ballato, P., Siame, L.L., Faccenna, C., Racano, S., Torreti, G., Lanari, R., Leanni, L. and Guillou, V., 2023. Transient response to changes in uplift rates in the northern Atlas-Meseta system (Morocco). Geomorphology, p.108765.

Davoudzadeh, M., Lammerer, B. and Weber-Diefenbach, K., 1997. Paleogeography, stratigraphy, and tectonics of the tertiary of Iran. NEUES JAHRBUCH FUR GEOLOGIE UND PALAONTOLOGIE ABHANDLUNGEN, 205, pp.33-67.

Delchiaro, M., Della Seta, M., Martino, S., Nozaem, R. and Moumeni, M., 2023. Tectonic deformation and landscape evolution inducing mass rock creep driven landslides: the Loumar case-study (Zagros Fold and Thrust Belt, Iran). Tectonophysics, 846, p.229655.

DiBiase, R.A., Denn, A.R., Bierman, P.R., Kirby, E., West, N., Hidy, A.J., 2018. Stratigraphic control of landscape response to base-level fall, YoungWomans Creek, Pennsylvania, USA. Earth Planet. Sci. Lett. 504, 163–173. https://doi.org/10.1016/j.epsl.2018.10.005.

Djamour, Y., et al. (2010), GPS and gravity constraints on continental deformation in the Alborz mountain range, Iran, Geophys. J. Int., 183, 1287–1301.

Djamour, Y., P. Vernant, H. R. Nankali, and F. Tavakoli (2011), NW Iran-eastern Turkey present-day kinematics: Results from the Iranian permanent GPS network, earth and, Plant Sci. Lett., 307, 27–34.

Duvall, A., Kirby, E., & Burbank, D. (2004). Tectonic and lithologic controls on bedrock channel profiles and processes in coastal California. Journal of Geophysical Research: Earth Surface, 109(F3). https://doi.org/10.1029/2003JF000086

Expósito, I., Jiménez-Bonilla, A., Delchiaro, M., Yanes, J.L., Balanyá, J.C., Moral-Martos, F. and Della Seta, M., 2022. Geomorphic signature of segmented relief rejuvenation in the Sierra Morena, Betic forebulge, Spain. Earth Surface Dynamics, 10(5), pp.1017-1039.

Farr, T.G., Rosen, P.A., Caro, E., Crippen, R., Duren, R., Hensley, S., Kobrick, M., Paller, M., Rodriguez, E., Roth, L. and Seal, D., 2007. The shuttle radar topography mission. Reviews of geophysics, 45(2).

Ferrier, K.L., Huppert, K.L., and Perron, J.T., 2013, Climatic control of bedrock river incision: Nature, v. 496, p. 206–209, doi:10.1038/nature11982.

Fick, S.E. and Hijmans, R.J., 2017. WorldClim 2: new 1-km spatial resolution climate surfaces for global land areas. *International journal of climatology, 37*(12), pp.4302-4315.

Flint, J. J. (1974). Stream gradient as a function of order, magnitude, and discharge. *Water Resources Research,* 10, 969–973.

Forte, A.M. and Cowgill, E., 2013. Late Cenozoic base-level variations of the Caspian Sea: a review of its history and proposed driving mechanisms. Palaeogeography, Palaeoclimatology, Palaeoecology, 386, pp.392-407.

Forte, A.M., Whipple, K.X. and Cowgill, E., 2015. Drainage network reveals patterns and history of active deformation in the eastern Greater Caucasus. *Geosphere*, *11*(5), pp.1343-1364.

Forte, A. M., Yanites, B. J., & Whipple, K. X. (2016). Complexities of landscape evolution during incision through layered stratigraphy with contrasts in rock strength. Earth Surface Processes and Landforms, 41(12), 1736–1757. https://doi.org/10.1002/esp.3947

Forte, A.M., Whipple, K.X., 2018. Criteria and tools for determining drainage divide stability. Earth Planet. Sci. Lett. 493, 102–117. https://doi.org/10.1016/j.epsl.2018.04.026.

Forte, A.M. and Whipple, K.X., 2019. The topographic analysis kit (TAK) for TopoToolbox. Earth Surface Dynamics, 7(1), pp.87-95.

Fox, M. (2019). A linear inverse method to reconstruct paleo-topography. *Geomorphology*, *337*, 151-164. https://doi.org/10.1016/j.geomorph.2019.03.034

Franklin, J. A. (1985). Suggested method for determining point load strength. International Journal of Rock Mechanics and Mining Sciences, 22(2), 51–60. https://doi.org/10.1016/0148-9062(85)92327-7

Gallen, S. F. (2018). Lithologic controls on landscape dynamics and aquatic species evolution in post-orogenic mountains. Earth and Planetary Science Letters, 493, 150–160. https://doi.org/10.1016/j.epsl.2018.04.029

Gallen, S. F., & Wegmann, K. W. (2017). River profile response to normal fault growth and linkage: An example from the Hellenic forearc of south-central Crete, Greece. *Earth Surface Dynamics*, *5*(1), 161-186. https://doi.org/10.5194/esurf-5-161-2017

Geological Survey of Iran (1975), Geological Quadrangle Map of Iran, Masuleh Sheet, Scale 1:100,000, edited by R. G. Davis et al., Geological Survey of Iran, Tehran.

Geological Survey of Iran (1999), Geological Quadrangle Map of Iran, Kivi Sheet, Scale 1:100,000, edited by B. Hajialilo and H. Rezaei, Geological Survey of Iran, Tehran.

Ghorbani, M., 2013. A summary of geology of Iran. In The Economic Geology of Iran (pp. 45-64). Springer, Dordrecht

Giachetta, E., Refice, A., Capolongo, D., Gasparini, N.M., Pazzaglia, F.J., 2014. Orogen-scale drainage network evolution and response to erodibility changes: insights from numerical experiments. Earth Surf. Process. Landf.39, 1259–1268. https://doi .org /10 .1002 /esp .3579.

Gilbert, G.K., 1877. *Geology of the Henry mountains* (pp. i-160). Government Printing Office.

Goren, L., Fox, M., & Willett, S. D. (2014). Tectonics from fluvial topography using formal linear inversion: Theory and applications to the Inyo Mountains, California. *Journal of Geophysical Research: Earth Surface*, *119*(8), 1651-1681. https://doi.org/10.1002/2014JF003079

Goudie, A.S., 2006. The Schmidt Hammer in geomorphological research. *Progress in Physical Geography*, *30*(6), pp.703-718, doi: 10.1177/ 0309133306071954.

Guest, B., G. J. Axen, P. S. Lam, and J. Hassanzadeh (2006a), Late Cenozoic shortening in the west-central Alborz Mountains, northern Iran, by combined conjugate strike-slip and thin-skinned deformation, Geosphere, 2(1), 35–52.

Hack, J. T., 1957. Studies of longitudinal stream profiles in Virginia and Maryland (Vol. 294). US Government Printing Office.

Hancock, G., & Kirwan, M. (2007). Summit erosion rates deduced from 10Be: Implications for relief production in the central Appalachians. *Geology, 35*(1), 89-92. https://doi.org/10.1130/G23147A.1

He, C., Yang, C.-J., Turowski, J.M., Rao, G., Roda-Boluda, D.C. &Yuan, X.-P. (2021) Constraining tectonic uplift and advection fromthe main drainage divide of a mountain belt.Nature Communications,12(1), 544. Available from:https://doi.org/10.1038/s41467-020-20748-2

Hessami, K., Pantosi, D., Tabassi, H., Shabanian, E., Abbassi, M., Feghhi, K., Solaymani, S., 2003. Paleoearthquakes and slip rates of the North Tabriz Fault, NW Iran: preliminary results. Ann. Geophys. 46, 903–915.

Howard, A. D. (1994). A detachment-limited model of drainage basin evolution. *Water resources research*, *30*(7), 2261-2285. https://doi.org/10.1029/94WR00757

Jackson, M.P.A., Cornelius, R.R., Craig, C.H., Gansser, A., Stöcklin, J., and Talbot, C.J., 1990, Salt diapirs of the Great Kavir, central Iran: Boulder, Geological Society of America Memoir, v. 177, Geological Society of America, 139 p.

Jackson, J., K. Priestley, M. Allen, and M. Berberian (2002), Active tectonics of the South Caspian Basin, Geophys. J. Int., 148, 214–245.

Pinter, N. and Keller, E.A., 2002. Active tectonics: Earthquakes, uplift, and landscape.

Kirby, E., Whipple, K. X., Tang, W., & Chen, Z. (2003). Distribution of active rock uplift along the eastern margin of the Tibetan Plateau: Inferences from bedrock channel longitudinal profiles. *Journal of Geophysical Research: Solid Earth*, *108*(B4). https://doi.org/10.1029/2001JB000861

Kirby, E., & Whipple, K. (2001). Quantifying differential rock-uplift rates via stream profile analysis. *Geology*, *29*(5), 415-418. https://doi.org/10.1130/0091-7613(2001)029<0415:QDRURV>2.0.CO;2.

Kirby, E., & Whipple, K. X. (2012). Expression of active tectonics in erosional landscapes. *Journal of Structural Geology*, *44*, 54-75. https://doi.org/10.1016/j.jsg.2012.07.009.

Lague, D., 2014. The stream power river incision model: evidence, theory and beyond. *Earth Surface Processes and Landforms*, *39*(1), pp.38-61.

Leonard, J.S., Whipple, K.X. and Heimsath, A.M., 2023. Isolating climatic, tectonic, and lithologic controls on mountain landscape evolution. Science Advances, 9(3), p.eadd8915.

Leonard, J.S. and Whipple, K.X., 2021. Influence of spatial rainfall gradients on river longitudinal profiles and the topographic expression of spatially and temporally variable climates in mountain landscapes. Journal of Geophysical Research: Earth Surface, 126(12), p.e2021JF006183.

Madanipour, S., T. A. Ehlers, A. Yassaghi, M. Rezaeian, E. Enkelmann, and A. Bahroudi (2013), Synchronous deformation on the orogenic plateau margins, insights from the Arabia-Eurasia collision, Tectonophysics, 608, 440–451.

Madanipour, S., Ehlers, T.A., Yassaghi, A. and Enkelmann, E., 2017. Accelerated middle Miocene exhumation of the Talesh Mountains constrained by U-Th/He thermochronometry: Evidence for the Arabia-Eurasia collision in the NW Iranian Plateau. Tectonics, 36(8), pp.1538-1561.

Madanipour, S., Yassaghi, A., Ehlers, T.A. and Enkelmann, E., 2018. Tectonostratigraphy, structural geometry and kinematics of the NW Iranian Plateau margin: Insights from the Talesh Mountains, Iran. American Journal of Science, 318(2), pp.208-245.

Madanipour, 2023. Late Miocene-early Pliocene tectonic to erosional exhumation in the northwest of the Arabia-Eurasia collision zone. Earth Surface Processes and Landforms. https://doi.org/10.1002/esp.5583

Maneerat, P. and Bürgmann, R., 2022. Geomorphic expressions of active tectonics across the Indo-Burma Range. *Journal of Asian Earth Sciences*, *223*, p.105008.

McQuarrie, N., and D. J. J. van Hinsbergen (2013), Retrodeforming the Arabia-Eurasia collision zone: Age of collision versus magnitude of continental subduction, Geology, 41, 315–318, doi:10.1130/G33591.1.

Miller, S. R., Sak, P. B., Kirby, E., & Bierman, P. R. (2013). Neogene rejuvenation of central Appalachian topography: Evidence for differential rock uplift from stream profiles and erosion rates. *Earth and Planetary Science Letters*, *369*, 1-12.

Mills, H.H. (2003). Inferring erosional resistance of bedrock units in the east Tennessee mountains from digital elevation data. Geomorphology, v.55, pp.263–281.

Mitchell, N. and Forte, A.M., 2023. Tectonic advection of contacts enhances landscape transience. Earth Surface Processes and Landforms, doi:10.1002/esp.5559.

Montgomery, D.R., Balco, G. and Willett, S.D., 2001. Climate, tectonics, and the morphology of the Andes. *Geology*, *29*(7), pp.579-582.

Mouthereau, F., O. Lacombe, and J. Vergés (2012), Building the Zagros collisional orogen: Timing, strain distribution and the dynamics of Arabia/Eurasia plate convergence, Tectonophysics, 532–535, 27–60, doi:10.1016/j.tecto.2012.01.022.

Murphy, B. P., Johnson, J. P. L., Gasparini, N. M., Hancock, G. S., & Small, E. E. (2018). Weathering and abrasion of bedrock streambed topography. Geology, 46(5), 459–462. https://doi.org/10.1130/G40186.1

Olivetti, V., Godard, V., Bellier, O., & ASTER team. (2016). Cenozoic rejuvenation events of Massif Central topography (France): Insights from cosmogenic denudation rates and river profiles. *Earth and Planetary Science Letters*, *444*, 179-191. https://doi.org/10.1016/j.epsl.2016.03.049.

Pérez-Peña, J.V., Al-Awabdeh, M.O.H.A.M.M.A.D., Azañón, J.M., Galve, J.P., Booth-Rea, G. and Notti, D., 2017. SwathProfiler and NProfiler: Two new ArcGIS Add-ins for the automatic extraction of swath and normalized river profiles. *Computers & Geosciences*, *104*, pp.135-150.

Perron, J.T., Richardson, P.W., Ferrier, K.L. and Lapôtre, M., 2012. The root of branching river networks. *Nature*, *492*(7427), pp.100-103.

Perron, J. T., & Royden, L. (2013). An integral approach to bedrock river profile analysis. *Earth Surface Processes and Landforms*, *38*(6), 570-576. https://doi.org/10.1002/esp.3302.

Pike, R.J. and Wilson, S.E., 1971. Elevation-relief ratio, hypsometric integral, and geomorphic area-altitude analysis. *Geological Society of America Bulletin*, *82*(4), pp.1079-1084.

Racano, S., Schildgen, T. F., Cosentino, D., & Miller, S. R. (2021). Temporal and spatial variations in rock uplift from river-profile inversions at the Central Anatolian

Plateau southern margin. *Journal of Geophysical Research: Earth Surface*, *126*(8), e2020JF006027. https://doi.org/10.1029/2020JF006027

Racano, S., Schildgen, T., Ballato, P., Yıldırım, C. and Wittmann, H., 2023. Rock-uplift history of the Central Pontides from river-profile inversions and implications for development of the North Anatolian Fault. Earth and Planetary Science Letters, 616, p.118231.

Reilinger, R., McClusky, S., Vernant, P., et al., 2006. GPS constraints on continental deformation in the Africa-Arabia-Eurasia continental collision zone and implications for the dynamics of plate interactions. J. Geophys. Res. 111, B05411. doi:10.1029/2005JB004051.

Roe, G. H. (2005). Orographic precipitation. Annual Review of Earth and Planetary Sciences, 33(1), 645–671. https://doi.org/10.1146/annurev. earth.33.092203.122541

Scherler, D. and Schwanghart, W., 2020. Drainage divide networks–Part 1: Identification and ordering in digital elevation models. *Earth Surface Dynamics*, *8*(2), pp.245-259.

Schildgen, T. F., Cosentino, D., Bookhagen, B., Niedermann, S., Yıldırım, C., Echtler, H., ... & Strecker, M. R. (2012). Multi-phased uplift of the southern margin of the Central Anatolian plateau, Turkey: A record of tectonic and upper mantle processes. *Earth and Planetary Science Letters*, *317*, 85-95. https://doi.org/10.1016/j.epsl.2011.12.003

Schwanghart, W., & Scherler, D. (2014). TopoToolbox 2–MATLAB-based software for topographic analysis and modeling in Earth surface sciences. *Earth Surface Dynamics*, *2*(1), 1-7. https://doi.org/10.5194/esurf-2-1-2014.

Schwanghart, W., & Scherler, D. (2017). Bumps in river profiles: Uncertainty assessment and smoothing using quantile regression techniques. Earth Surface Dynamics, 5, 821–839. https:// doi.org/10.5194/esurf-5-821-2017

Sengör, A. M. C., and W. S. F. Kidd (1979), Post-collisional tectonics of the Turkish-Iranian plateau and a comparison with Tibet, Tectonophysics, 55, 361–376.

Shobe, C. M., Hancock, G. S., Eppes, M. C., & Small, E. E. (2017). Field evidence for the influence of weathering on rock erodibility and channel form in bedrock rivers. Earth Surface Processes and Landforms, 42(13), 1997–2012. https://doi.org/10.1002/esp.4163

Sinclair, H.D., Mudd, S.M., Dingle, E., Hobley, D.E.J., Robinson, R. &Walcott, R. (2017) Squeezing river catchments through tectonics:Shortening and erosion across the Indus Valley, NW Himalaya.Geo-logical Society of America Bulletin, 129(1–2), 203–217. Available from:https://doi.org/10.1130/B31435.1

Snyder, N. P., Whipple, K. X., Tucker, G. E., & Merritts, D. J. (2000). Landscape response to tectonic forcing: Digital elevation model analysis of stream profiles in the Mendocino triple junction region, northern California. *Geological Society of America Bulletin*, *112*(8), 1250-1263. https://doi.org/10.1130/0016-7606(2000)112<1250:LRTTFD>2.0.CO;2

Stampfli, G.M., Borel, G.D., Cavazza, W., Mosar, J. and Ziegler, P.A., 2001. Palaeotectonic and palaeogeographic evolution of the western Tethys and PeriTethyan domain (IGCP Project 369). *Episodes Journal of International Geoscience*, *24*(4), pp.222-228.

Stocklin, J., 1968. Structural history and tectonics of Iran: A review. American Association of Petroleum Geologists Bulletin, 52, 1229–1258

Su, Q., Wang, X., Lu, H. and Xie, H., 2020. Dynamic divide migration as a response to asymmetric uplift: an example from the Zhongtiao Shan, North China. *Remote Sensing*, *12*(24), p.4188.

Vernant, P., et al. (2004), Present-day crustal deformation and plate kinematics in the Middle East constrained by GPS measurements in Iran and northern Oman, Geophys. J. Int., 157, 381–398.

Vincent, S. J., M. B. Allen, A. D. Ismail-Zadeh, R. Flecker, K. A. Foland, and M. D. Simmons (2005), Insights from the Talysh of Azerbaijan into the Paleogene evolution of the South Caspian region, GSA Bull., 117(11/12), 1513–1533.

Walpersdorf, A., Manighetti, I., Mousavi, Z., Tavakoli, F., Vergnolle, M., Jadidi, A., Hatzfeld, D., Aghamohammadi, A., Bigot, A., Djamour, Y. and Nankali, H., 2014. Present-day kinematics and fault slip rates in eastern Iran, derived from 11 years of GPS data. *Journal of Geophysical Research: Solid Earth*, *119*(2), pp.1359-1383.

Whipple, K. X., & Tucker, G. E. (1999). Dynamics of the stream-power river incision model: Implications for height limits of mountain ranges, landscape response timescales, and research needs. *Journal of Geophysical Research: Solid Earth*, 104(B8), 17661-17674. https://doi.org/10.1029/1999JB900120.

Whipple, K. X. (2004). Bedrock rivers and the geomorphology of active orogens. *Annu. Rev. Earth Planet. Sci.*, *32*, 151-185. https://doi.org/10.1146/annurev.earth.32.101802.120356

Whipple, K.X., 2009. The influence of climate on the tectonic evolution of mountain belts, Nat.

Whipple, K.X., DiBiase, R.A. and Crosby, B.T., 2013. Bedrock rivers. Treatise on geomorphology (Vol. 9, pp. 550–573).

Whipple, K. X., DiBiase, R. A., Ouimet, W. B., & Forte, A. M. (2017). Preservation or piracy: Diagnosing low-relief, high-elevation surface formation mechanisms. *Geology*, *45*(1), 91-94. https://doi.org/10.1130/G38490.1

Willett, S.D., 1999. Orogeny and orography: The effects of erosion on the structure of mountain belts. *Journal of Geophysical Research: Solid Earth*, *104*(B12), pp.28957-28981.

Willett, S.D., Slingerland, R. & Hovius, N. (2001) Uplift, shortening, andsteady state topography in active mountain belts.American Journal ofScience, 301(4–5), 455–485. Available from:https://doi.org/10.2475/ajs.301.4-5.455

Willett, S. D., McCoy, S. W., Perron, J. T., Goren, L., & Chen, C. Y. (2014). Dynamic reorganization of river basins. *Science*, *343*(6175). https://doi.org/10.1126/science.1248765

Winterberg, S. and Willett, S.D., 2019. Greater Alpine river network evolution, interpretations based on novel drainage analysis. *Swiss Journal of Geosciences*, *112*, pp.3-22.

Wobus, C.W., Whipple, K.X. and Hodges, K.V., 2006b. Neotectonics of the central Nepalese Himalaya: Constraints from geomorphology, detrital 40Ar/39Ar thermochronology, and thermal modeling. Tectonics, 25(4).

Wobus, C., Whipple, K. X., Kirby, E., Snyder, N., Johnson, J., Spyropolou, K., Crosby, B., & Sheehan, D. (2006). Tectonics from topography: Procedures, promise, and pitfalls. *Special papers-Geological Society of America*, *398*, 55. https://doi.org/10.1130/2006.2398(04)

Yang, R., Willett, S.D. and Goren, L., 2015. In situ low-relief landscape formation as a result of river network disruption. *Nature*, *520*(7548), pp.526-529.

Yassaghi, A., and S. Madanipour (2008), Influence of a transverse basement fault on along strike variations in the geometry of an inverted normal fault: Case study of the Mosha Fault, Central Alborz Range, Iran, J. Struct. Geol., 30, 1507–1519.

Ye, Y., Tan, X. and Zhou, C., 2022. Initial topography matters in drainage divide migration analysis: Insights from numerical simulations and natural examples. *Geomorphology*, *409*, p.108266.

Zaitchik, B.F., Evans, J.P. and Smith, R.B., 2007. Regional impact of an elevated heat source: The Zagros Plateau of Iran. Journal of climate, 20(16), pp.4133-4146.

Zondervan, J. R., Whittaker, A. C., Bell, R. E., Watkins, S. E., Brooke, S. A. S., & Hann, M. G. (2020a). New constraints on bedrock erodibility and landscape response times upstream of an active fault. Geomorphology, 351, 106937. https://doi.org/10.1016/j.geomorph.2019.106937

Zondervan, J. R., Stokes, M., Boulton, S. J., Telfer, M. W., & Mather, A. E. (2020b). Rock strength and structural controls on fluvial erodibility: Implications for drainage divide mobility in a collisional mountain belt. Earth and Planetary Science Letters, 538, 116221. https://doi. org/10.1016/j.epsl.2020.116221

Chapter 3

Geochronology and Inverse modelling: Denudation rates, uplift history and landscape evolution

3. Cosmogenic ^{10}Be erosion rates and tectonic-climate interactions in NW margin of Iranian Plateau: Insights into coupling erosion and topographic development of collisional orogenic systems

Mohammad Moumeni[2,4*], Michele Delchiaro[1], Paolo Ballato[2], Marta Della Seta[1], Reza Nozaem[3], Dmitry Tikhomirov[4], Marcus Christl[5], Markus Egli[4]

[1] Department of Earth Sciences, Sapienza University of Rome, Rome, Italy
[2] Department of Sciences, Roma Tre University, Rome, Italy
[3] School of Geology, College of Science, University of Tehran, Tehran, Iran
[4] Geochronology Group, University of Zürich, Zürich, Switzerland
[5] Laboratory of Ion Beam Physics, ETH Zürich, Zürich, Switzerland

3.1. Abstract

The present-day landscape of the NW Iranian Plateau in the Arabia- Eurasia continental collision system resulted from the interplay between internal and external forces in different temporal scales. The Talesh Mountains along the NW margin of the plateau represent a complex zone in terms of tectonics and surface processes and show characteristics of a transient landscape resulting from a combination of spatially varying rainfall, bedrock erodibility contrasts, and active tectonics. Exploring the relationship between erosion patterns and topographic features enables us to investigate the contribution of these competing factors in the regional landscape evolution of active orogens. The erosion rates from cosmogenic meteoric ^{10}Be ranging from ~ 100 to 400 m/Myr, with lower values in the interior, and higher values in the plateau exterior correlate with topographic metrics. The spatial pattern of erosion rates shows that catchments in the eastern flank of the range along the plateau margin are eroding about twice as fast as basin in the plateau interior. These contrasting erosion rates caused the divide migration towards the plateau interior. Furthermore, our inverse modelling of the longitudinal profiles indicates a progressive rock-uplift rate from ~12 to 4 Ma up to ~0.5 mm/yr in the plateau exterior,

---

[*] Corresponding author: Mohammad Moumeni; Email: mohammad.moumeni@uniroma1.it
Address: Piazzale Aldo Moro, 5, 00185 Roma RM, Italy

which is attributed to the base-level fall of the Caspian Sea due to tectonic events. This event accelerated the bedrock river incision in the Talesh Mts. The differences in erosion rate are indicative of a long-wavelength morphological disequilibrium and landscape transience in response to asymmetric uplift due to tectonically induced base-level fall.

Keywords: Denudation rate; Topographic development; Bedrock erodibility; Cosmogenic meteoric ^{10}Be; Inverse modelling

3.2.Introduction

Investigating the interaction among tectonics, climate, lithology, and erosion, as well as, isolating their individual role implies an applied procedure to reveal the main governing factor/s controlling landscape characteristics of tectonically active regions (e.g., Beaumont et al., 1992; Kirby and Whipple, 2001 and 2012; Adams et al., 2020; Clementucci et al., 2022). In this context, establishing denudation patterns in mountain ranges provides important constraints on landscape evolution.

The Talesh Mountains. are a prominent tectonic range of the NW margin of the Iranian Plateau (Fig. 3.1), and represent a far-field effect of the Arabia- Eurasia collision. The eastern side of the range is bounded by the Talesh Fault, a major west-dipping thrust fault that juxtaposes Paleozoic to Cenozoic rock units over the supposed oceanic lithosphere and associated sediments of the South Caspian Basin (SCB) (e.g., Allen et al., 2003). The present geomorphic configuration and high elevation of the study area is caused by the interplay between internal and external forces across different temporal scales (Moumeni et al., 2023). This range represents a complex zone in terms of tectonic structures and surface processes and shows features of a transient landscape resulting from a combination of recent tectonic activity, spatial climate variation and rock strength contrasts (Fig. 3.1). Consequently, investigating the relationship between erosional patterns across and along strike, and topographic characteristics allows us to constrain the contribution of lithology, climate, and tectonics, as well as their contribution in controlling the landscape evolution.

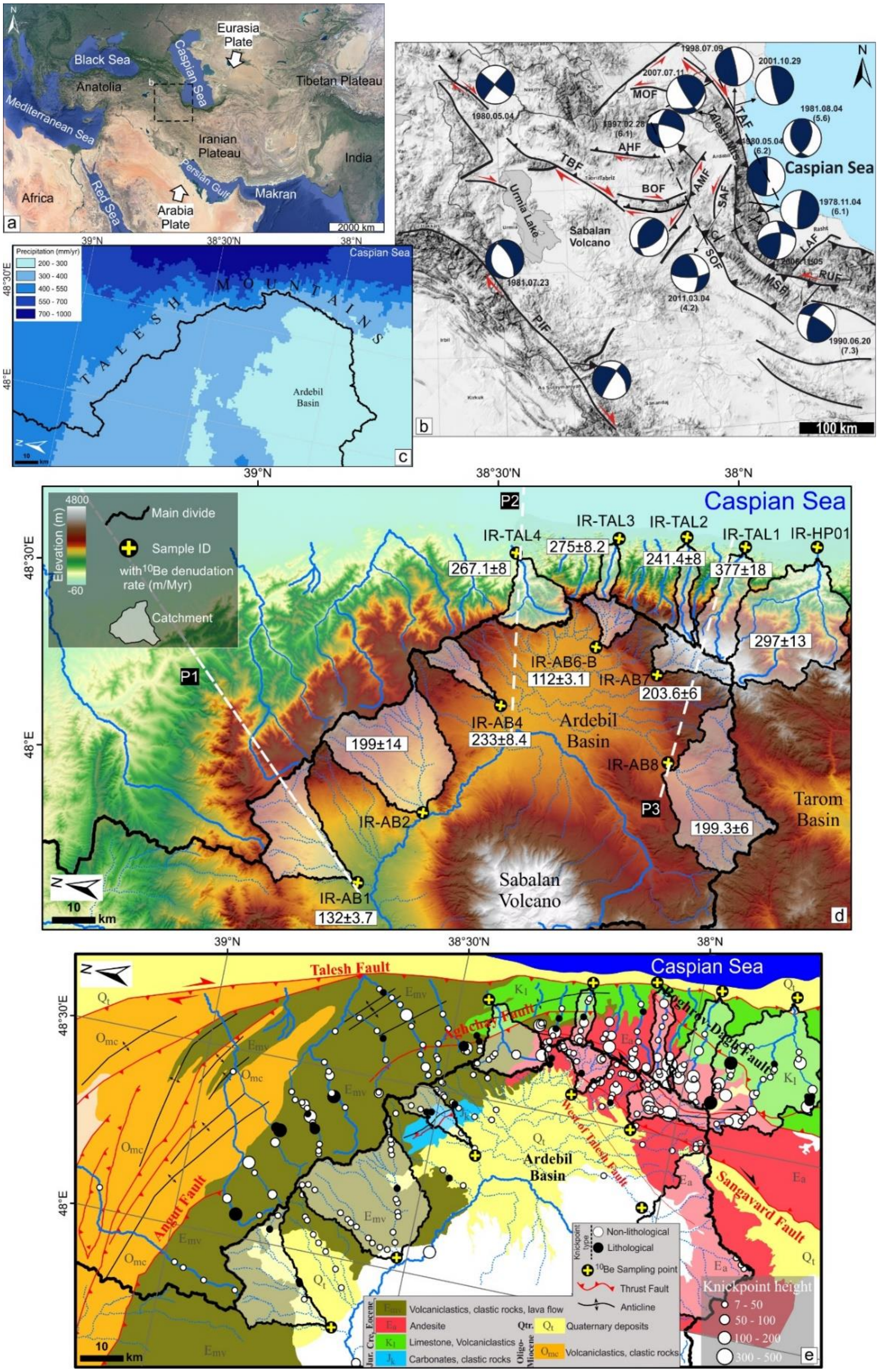

Figure 3.1. Location, geological structures, and map of the study area. (a) Arabia–Eurasia convergence zone. Location of the study area in NW Iranian Plateau is shown with black dashed rectangle. (b) Shaded-relief

Shuttle Radar Topography Mission (SRTM) image and simplified tectonic-seismotectonic map of NW Iran showing the major fault systems accommodating the Arabia-Eurasia plate convergence with earthquake focal mechanism solutions obtained from Hessami et al. (2003). The focal mechanisms are related to the main events in the northern and southern Talesh Mts. The density of earthquakes in the central sector is low with no major seismic events. Abbreviations: LAF: Lahijan Fault, TAF: Talesh Fault, MOF: Dasht-e-Moghan Fault, TBF: North Tabriz Fault, AHF: Ahar Fault, AMF: Ardebil-Mianeh Fault, SOF: Soltaniyeh Fault, MSF: Masuleh Fault, RUF: Rudbar Fault, SAF: Sangavar Fault, PIF: Piranshahr Fault, BOF: Bozqush Fault. (c) Average 30-years annual precipitation pattern from 1970-2000 (WorldClim climate database; Fick and Hijmans, 2017) of NW of Iran. (d) Topographic map of the Talesh Mts. with the ^{10}Be sampling locations, and their ID (Table. 3). White polygons indicate sampled-catchments boundaries. The thick black line indicates the main drainage divide. P1 to P3 (white dashed lines) show the locations of the 20-km-wide swath profiles shown in Figure 3.11. (e) Geological map of the Talesh Mts. (readapted after Madanipour et al. (2017) and references therein; Moumeni et al., 2023) showing the spatial distribution of lithological and non-lithological knickpoints. The sampling locations are shown with plus symbols within black circles.

Terrestrial Cosmogenic Nuclides (TCNs) can be used to derive ^{10}Be catchment-averaged denudation rate, a method that has been used in several studies to quantify short-term erosion rates in diverse geological, climatic, and morphological settings (e.g., Brown et al., 1992; von Blanckenburg, 2006; Portenga and Bierman, 2011; Granger and Schaller, 2014; Marshall et al., 2017; Forte et al., 2022; Clementucci et al., 2022; Leonard, et al., 2023; Kaveh-Firouz et al., 2023).

In the Talesh Mts. the role of erosional processes and/or uplift phases in the evolution of landscape has not been studied thoroughly. Thus, to explore the complete history of topography development of the region, we provided new insights by integrating millennial scale short-term denudation rates from detrital cosmogenic meteoric nuclide ^{10}Be concentrations and topographic analysis. Furthermore, we investigated the relationships of climate and lithology with catchment-averaged erosion rates and evaluate geomorphic evidence of the divide instability (Moumeni et al., 2023) with new dataset of erosion rates. We present 11 erosion rates derived from analysis of cosmogenic meteoric ^{10}Be of river-borne sediments on the eastern and western flanks of Talesh Mts. in the NW margin of the Iranian Plateau. The short-term denudation rates show a strong correlation with the topographic metrics. Additionally, for the first time we performed inverse modelling of the river longitudinal profiles to reconstruct the base level fall history of the region, which gives us insights into the timing and uplift rates of NW margin of the Iranian plateau in the context of topographic development and surface processes with the regional geodynamic of the region. Generally, the results represent spatially varying erosion rates on both sides of the mountain range (main drainage divide) which drives the divide mobility towards plateau interior in response to the uplift pattern due to tectonic-climate interactions.

3.3.Study area

3.3.1. Geodynamic and geological setting

The Arabia- Eurasia continental collision system is an active continental collision zones and is caused by the ongoing plate convergence between Arabia and Eurasia (Fig. 3.1a). Widespread collisional deformation began in the early-middle Miocene and involved a shortening and thickening processes across the Caucasus, Alborz, and Zagros Mts. (e.g., Allen et al., 2004; Ballato et al., 2011; Agard et al., 2011; Mouthereau et al., 2012; McQuarrie & van Hinsbergen, 2013; Allen, 2021; Lanari et al., 2023). During the late Cenozoic (possibly about 5 Ma ago) a plate tectonic reorganization of the entire Arabia-Eurasia convergence zone occurred (Allen et al., 2004) leading to the development of the present-day structural architecture of the Alborz and Talesh Mts. (Axen et al., 2001; Cifelli et al., 2015). The Talesh Mountains. are a prominent tectonic range of the NW margin of the Iranian Plateau and represent a far-field response to the Arabia- Eurasia collision (Ballato et al., 2017) (Fig. 3.1b-e). The eastern side of the range is bounded by the Talesh Fault, a major shallow, west-dipping thrust fault that juxtaposes the continental rocks of the Eurasia Plate over the supposed oceanic lithosphere and associated sediments of the South Caspian Basin (SCB) (e.g., Allen et al., 2003). The onset of mountain building processes and associated exhumation in the Talesh Mts. is thought to have occurred in Eocene to early Oligocene and is interpreted as the initial stage of the Arabia-Eurasia continental collision (Allen et al., 2004; Ballato et al., 2011, 2013; Madanipour et al., 2017, 2018). According to Madanipour et al. (2017), exhumation rates in the late Oligocene varied from the northern (~30 ± 10 m/Myr), to the central (~150 ± 30 m/Myr), and the southern (~70 ± 10 m/Myr) sectors of the Talesh Mts. During the middle Miocene, these rates accelerated to 270 ± 70 m/Myr, and 310 ± 80 m/Myr in the northern and southern sectors, respectively, while the central sector of the range experienced limited exhumation. Most of the shortening and exhumation in the Talesh Mts. started at ~12 Ma, most likely in response to the final phase of hard continental collision (Ballato et al., 2011; Madanipour et al., 2017; Chu et al., 2021).

In this context, it has been proposed that thrusting along the central Talesh Mts. prevailed in the earliest stages of mountain building processes during the early Oligocene - middle Miocene, while strike-slip faulting became dominant in the central part of the range in middle Miocene due to a change in the regional convergence direction from NNE to N (Madanipour et al., 2017 and 2018).

Paleozoic rock units in the Talesh Mts. include volcanic, clastic, and carbonate rocks, while the Mesozoic strata consist of Triassic- lower Jurassic carbonates and clastics (Fig. 3.1e). Intensive volcanism episodes along the southern margin of the Eurasian plate during the Paleocene–Eocene led to the deposition of a thick pile of volcaniclastic sediments in rapidly subsiding extensional sedimentary basins especially in the Talesh Mts. Early Cenozoic volcanic and volcaniclastic rock units are unconformably covered by late Cenozoic coarse to medium grained clastic rocks (e.g., Vincent et al., 2005; Madanipour, 2023 and references therein). In the northern and central sectors of the range, Cenozoic sedimentary, volcanic, and volcaniclastic sequences are widely exposed, while older lithological units are exposed only in the core of anticlines (Fig. 3.1e).

The early- middle Miocene topographic growth led to the establishment of an efficient orographic barrier, at least in the central Alborz, as suggested by paleoclimate data (Ballato et al., 2010). Today, approximately 1000 mm/yr of precipitation falls along the coast of the Caspian Sea on the eastern flank of the Talesh Mts., while the plateau interior receives less than 300 mm/yr (e.g., WorldClim database: Fick and Hijmans, 2017; Moumeni et al., 2023; Fig. 3.1c).

3.3.2. Regional seismicity

The oblique convergence between central Iran and the SCB is accommodated primarily by strain partitioning into range-parallel thrusts and strike-slip faulting (e.g., Allen et al., 2003; Jackson et al., 2002). The N-S striking Talesh thrust fault, which marks a prominent topographic boundary with the west SCB has been identified as a major active structure responsible for several destructive earthquakes in the past 1100 yr (e.g., Berberian 1983; Berberian & Yeats 1999). In this area, earthquake focal mechanisms show a N-trending and west-dipping shallow-angle thrust which accommodates the underthrusting of the SCB beneath the Talesh Mts. (Priestley et al., 1994; Berberian & Yeats 1999; Jackson et al., 2002). In the southern and central sector of Talesh Mts., the Masuleh and the Boghrov Dagh faults are the main active structures. There is no major seismic activity in the central sector of the Talesh Mts., while the seismicity concentrates in northern and southern structural bends of the range (e.g., Aziz Zanjani et al., 2013). In the Talesh Mts. the earthquake mechanisms are distinct from those of other parts of the Alborz range. Based on Jackson et al. (2002), they show thrusting on shallow-dipping faults with depths of 15-26 km. These active faults appear to be deeper than in the Alborz Mts. (Jackson et al., 2002). An earthquake of Ms 6.0 occurred in 1978, yielded a focal mechanism consistent with a low-angle thrust (Berberian, 1983). Two records of historical earthquakes (M ~6.1 in 1863; and M ~6.7 in 1896; Berberian and Yeats, 1999; Ambraseys & Melville 2005) occurred in pairs have been associated with the northern segment of the Masuleh Fault (Sangavar Fault). The concentration of the upper crustal seismicity around the Sangavar Fault suggests that this fault may have a role in the right-lateral northward motion of the Talesh relative to the SCB (Aziz Zanjani et al., 2013).

Across the Alborz Mountain, which accommodates ~5 ± 2 mm/yr of the overall present-day Arabian–Eurasian plates convergence (Vernant et al., 2004; Djamour et al., 2010), seismic activity primarily occurs in the upper crust with some infrequent events in the lower crust, especially in the western part of the range and in the Talesh Mts. (e.g., Engdahl et al., 2006).

3.3.3. Spatio- temporal patterns of collisional exhumation

The Pliocene rapid exhumation in the central Alborz, Greater Caucuses, and Talesh Mts., as well as the associated subsidence and the northward subduction of the South Caspian Block is reflected in widespread deformation along the northern margin of the NW sectors of the Iranian Plateau (e.g., Axen et al., 2001; Madanipour et al., 2013; and references therein). Generally, the landscape evolution of the western Alborz and Talesh Mts. is through tectonic processes since ~26 Ma (e.g., McQuarrie & van Hinsbergen, 2013). The results from Apatite Fission Track and apatite U-Th/He analyses (AFT/AHe) indicate that the exhumation rates were low and almost constant from ~50 to ~26 Ma across the northern and southern flanks of the western Alborz (Kaveh-Firouz et al., 2023 and references therein), which implies no significant tectonic or climatic event in the region. In the Talesh Mts. in the late Oligocene exhumation rates vary from ~150 ± 30 m/Myr in the central Talesh to ~30 ± 10 m/Myr and ~70 ± 10 m/Myr in the northern and southern sectors respectively (Madanipour et al., 2017).

Moreover, Madanipour et al. (2017) reconstructed the deformation history of the Talesh Mts. by using apatite and zircon bedrock U-Th/He cooling ages and detrital apatite fission track data. The bedrock and the detrital cooling ages suggest the initiation of deformation at ~27–23 Ma. An increase in exhumation due to hard collision of the Arabian and the Eurasian Plates (~26 Ma; e.g., Koshnaw et al., 2020) resulted in an increase in erosion rates until ~10 Ma, and a further acceleration in exhumation rates from ~10 to ~2.8 Ma (Kaveh-Firouz et al., 2023). Regarding this time interval for the acceleration of exhumation due to the isolation of the Caspian Sea and extreme base-level fall, we argue that the base level fall started at 5.5 and lasted until ~ca. 2.6 Ma. Thus, there is no base level fall from 10 to 5 Ma (e.g., Ballato et al., 2015; Lanari et al., 2023). This last phase considered to have caused the present-day high elevation and the curved geometry of the Talesh Mts. From late Oligocene to middle Miocene (~12 Ma), exhumation rates accelerated from 30 ± 10 m/Myr to 270 ± 70 m/Myr in the northern and from 70 ± 10 m/Myr to 310 ± 80 m/Myr in the southern parts of the Talesh Mts. (Madanipour 2023). In the central sector of the range, in the late Oligocene, exhumation rate was ~150 ± 30 m/Myr, and the accelerated middle Miocene phase is not recorded in the central sector, which during this period was experiencing dominant strike-slip deformation and limited rock exhumation (Madanipour et al., 2017, 2023). In the early Pliocene (~ 5.6 Ma) the steady-state exhumation rate of the central Talesh Mts. increased from 0.014 ± 0.003 to 0.11 mm/yr (Madanipour 2023). This rapid exhumation is related to the base-level fall of the Caspian Sea due to its isolation from the Paratethys and consequently the rapid incision of the rivers which drained the Talesh Mts. in the margin of the Iranian Plateau (Madanipour 2023).

By using the results of in situ ^{10}Be in NW Iran, Kaveh-Firouz et al. (2023) showed a decrease in erosion rates from early Pleistocene. This is consistent with the reactivation of strike-slip faults which has been induced by the Caspian block's clockwise rotation over the last 2 Ma (e.g., Mattei et al., 2017).

3.4.Materials and methods

To measure cosmogenic meteoric ^{10}Be catchment-averaged denudation rates, we collected 11 river-borne sediment samples from the plateau's interior and exterior on both sides of the main divide along the eastern wet flank of the Talesh Mts. and the western drier slopes of the Ardebil Basin. This method has been suggested as a geochronometer and tracer of Earth surface processes, a proxy for watershed erosion rate, and for studying landscape evolution (e.g., Jungers et al., 2009; Willenbring and von Blanckenburg, 2010; Graly et al., 2011). It can serve as a powerful tool, similar to the *in situ*-produced ^{10}Be cosmogenic nuclides, to derive erosion rates from detrital river sediments. Additionally, although in settings like coastal and islands ^{10}Be concentrations in rainfall are correlated with precipitation rate, the annual flux of meteoric ^{10}Be is independent of the precipitation rate (Willenbring and von Blanckenburg, 2010). Thus, the patterns of past precipitation rates do not affect ^{10}Be flux estimation over time. These characteristics make it a favorable option for applications of the ^{10}Be techniques in both modern and past sedimentary deposits, even in areas with variable rainfall patterns (Willenbring and Blanckenburg, 2010). Although in case where we have an orographic rainfall, the modern climate and rainfall patterns can be taken into account when estimating the erosion rates.

Furthermore, most of the sampled basins are in transient state with non-lithological knickpoints marking an upstream relict landscape (Moumeni et al., 2023). Thus, to investigate the erosional pattern within the river network, and their influence on shaping the landscape and controlling its evolution, we conducted an analysis of the stream network at the catchment scale and the drainage divide by using some MATLAB-based packages (TopoToolbox: Schwanghart and Scherler, 2014; DivideTools: Forte and Whipple, 2018; Topographic Analysis Kit: Forte and Whipple, 2019). Furthermore, we apply linear inversion to the catchments in order to reconstruct the landscape uplift history by inverting the river longitudinal profiles of the study area to acquire more information on the surface uplift rates.

3.4.1. ^{10}Be-derived denudation rates

In the method of deriving erosion rates using meteoric ^{10}Be, it is presumed that the ^{10}Be integrated delivery rate from the atmosphere equals the flux of ^{10}Be exiting the basin through sediment transport (Willenbring and von Blanckenburg, 2010). This allows calculation of basin-scale mass loss rates. We calculated the flux out of the basin by multiplying the sediment yield of the catchment with the concentration of meteoric ^{10}Be in these sediment samples (Equation. 1; Willenbring and von Blanckenburg, 2010; Padilla et al., 2018).

Meteoric ^{10}Be was extracted from river-borne sediments by applying a modified protocol (Horiuchi et al., 1999; Egli et al., 2010), which includes: (1) sieving and collecting a fraction of less than 2 mm; (2) milling about 5-10 g of sample into fine powder and igniting it at 550 °C for 3 hours to decompose organic matter; (3) adding ^{9}Be carrier in the form of $Be(NO_3)_2$ and leaching the sample in 16% HCl on the shaker overnight; (4) centrifuging the sample and collecting the leachates; (5) adjusting sample pH to 2 with NaOH solution and adding 1 ml of saturated EDTA solution to prevent formation of metal complexes (e.g., Mn, Fe); (6) increasing sample pH to 8, to separate the gel containing $Be(OH)_2$; (7) further increasing sample pH to 14 to separate $Be(OH)_2$ redissolved in the solution from $Fe(OH)_3$ gel; (8) decreasing sample pH to 2 with HCl solution and adding 1 ml of saturated EDTA again; (9) precipitating the gel containing $Be(OH)_2$ at pH 8 and redissolving the hydroxides in 20 ml of 0.4 M oxalic acid; (10) separating Be from the rest metals (e.g., Al, Ti) on the cation exchange resin-Bio-Rad AG50- X8; (11) precipitating $Be(OH)_2$ after sample volume reduction; (12) drying and calcinating $Be(OH)_2$ gel to obtain BeO; (13) mixing BeO with Nb powder and pressing it into a sample holder for AMS measurements.

The measurement of ^{10}Be/^{9}Be ratio took place at the ETH Zurich using MILEA AMS system (Maxeiner et al., 2019). The obtained ratios were normalized to in-house AMS standards (Christl et al., 2013) and corrected to a preparation blank. The range of ^{10}Be concentrations of the samples are presented in Table. 3.1.

Table 3.1. ^{10}Be content of the river-borne sediments. ^{a} Values corrected for preparation blank. Error includes AMS standard error. ^{b} Values without correction for preparation blank.

Sample name	^{10}Be/^{9}Be ^{a} (10^{-12})	SD ^{10}Be/^{9}Be ^{a} (10^{-12})	^{10}Be (at/g) ($\times 10^{6}$)	SD ^{10}Be (at/g) ($\times 10^{6}$)	SD ^{10}Be (%)
IR-TAL1	0.278	0.013	8.90	0.42	4.7
IR-TAL2	0.459	0.015	14.91	0.49	3.3

IR-TAL3	0.486	0.015	15.78	0.48	3.0
IR-TAL4	0.478	0.014	15.60	0.47	3.0
IR-HP01	0.332	0.015	10.73	0.48	4.5
IR-AB1	0.669	0.019	21.91	0.62	2.8
IR-AB2	0.411	0.029	13.16	0.94	7.2
IR-AB4	0.353	0.013	11.27	0.41	3.6
IR-AB6-B	0.358	0.011	11.55	0.36	3.1
IR-AB7	0.723	0.020	23.07	0.65	2.8
IR-AB8	0.330	0.010	10.61	0.33	3.1
BA28 (prep. blank)	0.006 [b]	0.001 [b]			

3.4.1.1.Determination of erosion rate using cosmogenic ^{10}Be

A uniform long-term meteoric ^{10}Be deposition rate is typically assumed when meteoric ^{10}Be is used to trace geomorphic processes. Uncertainties in calculated soil erosion rates are directly proportional to the uncertainty in local, long-term meteoric ^{10}Be deposition rates (e.g., Pavich et al., 1986; Graly et al., 2011), which should be resolved for different latitudes and precipitation regimes. Thus, we apply the calibration of long-term meteoric ^{10}Be delivery rates for improving the accuracy and precision of this isotope system. The application to meteoric ^{10}Be adsorbed within sediments follows the same approximation used for ^{10}Be produced "*in situ*", where the production of cosmogenic nuclides in a basin eventually equals the export of nuclides from the basin through erosion of sediment (Padilla et al., 2018). Thus, the following equation is used to estimate the denudation rate of the catchments:

$$D = {}^{Q}\!\big/_{\rho N_{surf}} \qquad (1)$$

where Q is the meteoric ^{10}Be flux into the surface (atom/m^{2}·year^{-1}), N_{surf} is the concentration of ^{10}Be into the surface in river-borne sediment (atom/kg) and ρ is the density of soil (kg/L). This equation indicates that the erosion rate is proportional to the local flux divided by the surface concentration. Thus, the role of bedrock erodibility in shaping the landscape can be explored in the region.

To estimate the local flux of meteoric ^{10}Be, we used three approaches (Table. 3.2), relying on model data (Field et al., 2006; Heikkilä 2007; Willenbring and von Blanckenburg, 2010), and based on an empirical method (Graly et al., 2011). The following equation estimates primary meteoric ^{10}Be fallout at any mid or low latitude (L), for modern precipitation rate (P) (Graly et al., 2011):

$$^{10}Be_{flux} = P\left(\frac{1.44}{1+e^{\left(\frac{(30.7-L)}{4.36}\right)}} + 0.63\right) \qquad (2)$$

However, interannual variation in site-specific meteoric ^{10}Be fluxes is low (Heikkilä et al., 2008), the empirical method suggested by Graly et al. (2011) takes the precipitation rate and latitude into consideration and predicts ^{10}Be fallout within 10–20% error. Therefore, we adjusted the meteoric ^{10}Be flux for these variables (Table. 3.2) and used the erosion rates derived with this procedure (Input Q3) for further analysis (Table. 3.2).

Table 3.2. The estimation of ^{10}Be depositional flux in the study area to compute the erosion rates. The meteoric ^{10}Be flux into the surface (Q) is calculated according to several models based on Field et al. (2006); Heikkilä (2007), for input Q1; Willenbring and von Blanckenburg (2010) for input Q2, and Graly et al. (2011) for input Q3.

Sample no. (catchments)	Latitude (N)	Longitude (E)	Precipitation (cm/yr)	Input Q1 $(atm\, m^{-2} yr^{-1})$	Input Q2 $(atm\, m^{-2} yr^{-1})$	Input Q3 $(atm\, m^{-2} yr^{-1})$
IR-TAL1	37°.57′	48°.53′	49.7	0.7×10^{10}	0.810×10^{10}	0.906×10^{10}
IR-TAL2	38°.05′	48°.53′	52.7	0.7×10^{10}	0.840×10^{10}	0.972×10^{10}
IR-TAL3	38°.13′	48°.50′	63.4	0.7×10^{10}	0.845×10^{10}	1.172×10^{10}
IR-TAL4	38°.26′	48°.47′	60.7	0.7×10^{10}	0.850×10^{10}	1.125×10^{10}
IR-HP01	37°.47′	48°.52′	47.3	0.7×10^{10}	0.807×10^{10}	0.860×10^{10}
IR-AB1	38°.39′	47°.49′	42.0	0.7×10^{10}	0.858×10^{10}	0.781×10^{10}
IR-AB2	38°.31′	48°.02′	38.1	0.7×10^{10}	0.853×10^{10}	0.707×10^{10}
IR-AB4	38°.26′	48°.22′	38.3	0.7×10^{10}	0.850×10^{10}	0.710×10^{10}
IR-AB6-B	38°.13′	48°.34′	37.8	0.7×10^{10}	0.845×10^{10}	0.699×10^{10}
IR-AB7	38°.05′	48°.31′	34.4	0.7×10^{10}	0.840×10^{10}	0.635×10^{10}
IR-AB8	38°.00′	48°.17′	31.0	0.7×10^{10}	0.835×10^{10}	0.571×10^{10}

3.4.2. Stream network and topographic analysis

The analysis of rivers longitudinal profiles provides useful information on landscape evolution of a region since they record information on climate changes, bedrock erodibility, and tectonics (e.g., Hack 1957; Kirby and Whipple, 2012; Whipple et al., 2013). There is a power-law relationship in river profiles which describes the variation of channel elevation in time (*dz/dt*) as a function of the channel slope (*S*) and upstream area (*A*) by assuming detachment-limited conditions (Flint, 1974; Kirby & Whipple, 2012):

$$dz/_{dt} = U - KA^{m}S^{n} \qquad (3)$$

where, *U* is the rock uplift rate, *K* is the erodibility coefficient controlled by lithology, climate and sediment load, *m* and *n* are empirical constants which depend on channel geometry, and erosion processes. Due to uplift in a steady-state *U=K*. Thus, we can rearrange Eq. (3) as:

$$k_{sn} = S\,A^{\theta_{ref}} \qquad (4)$$

where θ is the concavity index, which can be computed by means of a Bayesian Optimization ($\theta_{ref} = 0.52$) (Moumeni et al., 2023) and k_{sn} is the normalized river steepness index for such a θ_{ref}, which can be used as a proxy for the uplift rate when the lithological control, and magnitude of precipitation is constrained. The steepness index can be modified by replacing *A* with the product of the drainage area and average upstream rainfall (*P*) to account for the spatial rainfall gradient (Adams et al., 2020; Leonard and Whipple, 2021; Leonard et al., 2023):

$$k_{snQ} = SQ^{\theta_{ref}} \qquad (5)$$

where *Q* is the water discharge and k_{snQ} is an improved proxy for tectonics and climate. Furthermore, we applied an integral approach of the detachment-limited stream power model (e.g., Perron and Royden, 2013; Lague 2014) for the river profiles. By using χ we can determine how tectonic forcing generates variable topography throughout a river basin by assuming climate and rock strength are uniform (Willett et al., 2014). We used this approach to evaluate the divide stability (Moumeni et al., 2023) and to estimate the amount of incision in the interior and exterior of the plateau due to the uplift gradients by analyzing knickpoints and the projection of the relict river profiles. Knickpoints were extracted using *knickpointfinder* function in TopoToolbox (Schwanghart and Scherler, 2014) from the smoothed river profiles. The total magnitude of fluvial incision has been computed by using transient stream profiles upstream of the highest non-lithological knickpoints, by the difference between the reconstructed river profiles and modern base level in both sides of the range (drainage divide).

By assuming steady-state condition and spatially uniform uplift and erodibility, equation (4) can be rewritten into:

$$\chi = \int_{x_b}^{x} \left(\frac{A_0}{A(x)}\right)^{\theta_{ref}} dx. \qquad (6)$$

where x is the upstream distance, x_b is the distance at base level, and A_0 is a reference scaling area in this study (1 km^2). The χ-transform equation can be modified as χ_Q (e.g., Leonard and Whipple, 2021; Leonard et al., 2023):

$$\chi_Q = \int_{xb}^{x} \left(\frac{Q_0}{Q(x)}\right)^{\theta_{ref}} dx. \qquad (7)$$

where Q is the precipitation weighted *flowacc* grid, and Q_0 is a numerical value of the threshold in the same units as the *flowacc* grid (1 km^2). The χ_Q metric assumes that steepness scales with the product of drainage area and mean rainfall (k_{snQ}). Consequently, by using these metrics we analyzed the stream network in the plateau interior and exterior by extracting knickpoints, quantifying incision magnitude, and mapping the spatial distribution of k_{sn} , k_{snQ}, χ and χ_Q.

The river incision and hillslope erosion are important in this context since they are driven by rock uplift due to climate and topographic steepening which play a primary role in controlling the erosional dynamics of a landscape (Olivetti et al., 2016; Adams et al., 2020). Moreover, in addition to the χ metric, we used the Gilbert metrics (mean gradient, mean local relief, mean channel bed elevation; Whipple et al., 2017; Forte and Whipple, 2018) to analyze the stability of the drainage divide (Moumeni et al., 2023) and compare all the outcome with ^{10}Be derived erosion rates in the study area.

3.4.2.1.Linear inversion of river profiles

To infer the rock uplift history, we performed several linear inversions by inverting the longitudinal river profiles of the study area. Since, $n = 1$ does not affect the results of the inversion analysis (e.g., Roberts et al., 2012; Goren et al., 2014; Gallen, 2018; Pazzaglia & Fisher, 2022), we constrained the K value using the stream power incision model ($K = E/k_{sn}^{n}$) for the simplification of $n = 1$ since this approximation is valid for our setting. Thus, assuming no spatial uplift variations, the timescale (see Equation. 3) of a system to a perturbation (relative baselevel change) along a river profile (τ) is expressed by (Whipple & Tucker, 1999):

$$\tau = \int_{x_b}^{x} \frac{dx}{K(x')A(x')^{m}} \tag{8}$$

where τ is the response time of an uplift signal to propagate upstream from the baselevel x_b to a position x along the river (erosional wave), which depends on K, and the m-n exponents of the stream power equation.

We did the inverse modelling with both uniform and variable erodibility assumptions. The latter is dependent on the bedrock lithology (Gallen, 2018; Pazzaglia & Fisher, 2022). By the equation ($k_{sn} = E/K$), we calculated the spatial variability of the erodibility coefficient by using the geological map and from the best fit k_{sn} and the denudation rates. We defined 7 main domains of rock erodibility where the average value of the steepness index is also calculated. Thus, the erodibility values calculated here are not predetermined and show primary and secondary characteristics of the rocks which delineate the susceptibility to erosion (e.g., Molin et al., 2023). For the base level in the inversion analysis, we used the Caspian Sea base level in the plateau exterior, and a local base level in the Ardebil Basin for the interior plateau.

3.5.Results

3.5.1. ^{10}Be catchment-average denudation rate

Overall, the basin-wide denudation rates are consistent among the sampled catchments on both sides of the divide. The group of river samples collected from the eastern side of the divide in the exterior of the plateau are characterized by higher erosion rates (Fig. 3.2a).

These catchments drain the wet flank of the Talesh Mts. into the Caspian Sea directly. Conversely, catchments that drain the less steep surface of the plateau interior have lower erosion rates. ^{10}Be-derived basin-wide denudation rates in the interior of the plateau range from 112 to 233 m/Myr. On the plateau's exterior, erosion rates are two times higher ranging from 250 to 377 m/Myr (Fig. 3.2). The range of ^{10}Be catchment average denudation rates is reported in Table. 3.3. The river profiles of the sampled-catchments with the χ-elevation plots are presented in Figures. S3.1, and S3.2.

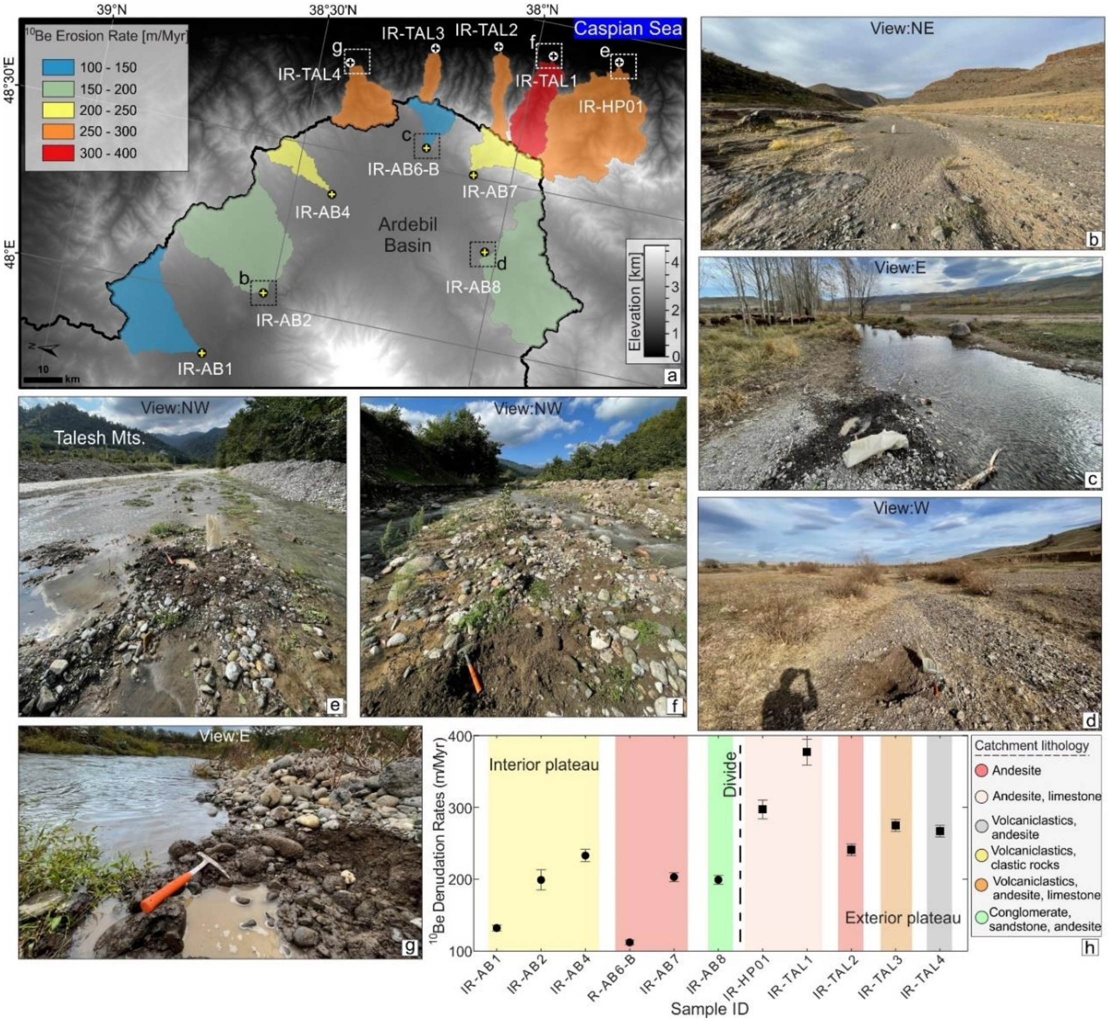

Figure 3.2. Overview of the erosion rates (input Q3; see Table. 3.3) and sampling locations in the study area. (a) ^{10}Be catchment-averaged erosion rates for all sampled basins (see rates in Table. 3.3). Sample location of the are shown by dots. (b-g) Field photos of representative sampled catchments at the mouths of rivers draining the plateau interior (b-d) and exterior (e-g). The location of the photos is indicated in panel (a). (h) Erosion rates for all catchments and associated major lithological units shown by different colors.

Table 3.3. ^{10}Be-drived erosion rates and topographic metrics with associated standard deviations for the eastern wet flank of the Talesh Mts (IR-TAL1-4 and IR-HP01), and the plateau interior in the Ardebil Basin (IR-AB1 to IR-AB8). The rates of denudation in Input Q1 to Q3 are m/Myr. The sediment yield is calculated by multiplying Input Q3 in density of quartz (2.7g/cm^3).

Sample ID	Catchment area (km^2)	Erosion rate (Q1)	Erosion rate (Q2)	Erosion rate (Q3)	STdev Q3	Average k_{sn}	STdev k_{sn}	Average k_{snQ}	STdev k_{snQ}	Average slope(°)	STdev slope	Average relief(m)	STdev relief	Sediment yield (t km^{-2} yr^{-1})
IR-TAL1	195	291.3	337.1	377.0	17.7	555.4	326.0	163.0	59.0	21.2	12.8	1099.1	276.3	1018
IR-TAL2	84	173.9	208.6	241.4	8.0	520.4	226.0	165.0	47.0	23.6	11.1	1036.6	141.9	652
IR-TAL3	51	164.3	198.3	275.0	8.3	403.2	206.0	179.0	60.0	23.3	11.3	1068.6	277.5	743
IR-TAL4	172	166.2	201.8	267.1	8.0	317.5	157.0	167.0	48.0	22.6	10.6	914.5	142.7	721
IR-HP01	591	241.6	278.6	296.8	13.4	478.7	266.0	171.0	55.0	21.6	12.0	1081.2	272.5	802
IR-AB1	349	118.3	145.0	132.0	3.7	92.5	60.0	65.0	37.0	6.1	4.9	242.5	83.0	356
IR-AB2	535	197.1	240.1	199.0	14.3	109.1	78.0	66.0	39.0	6.0	5.4	273.5	135.6	537
IR-AB4	88	230.1	279.4	233.4	8.4	138.0	60.0	87.0	37.0	9.9	7.1	408.0	163.5	630
IR-AB6-B	81	112.4	135.7	112.2	3.1	123.8	73.0	94.0	41.0	11.0	7.9	573.6	229.6	303
IR-AB7	126	224.4	269.3	203.6	6.3	306.0	250.0	103.0	52.0	13.0	8.4	662.8	100.7	550
IR-AB8	544	244.4	291.5	199.3	6.2	123.3	61.0	72.0	36.0	6.0	5.4	273.5	135.6	538

3.5.2. Topographic analysis and erosion rate

The steepness index (k_{sn}) is sensitive to variations in rock uplift rates and rock strength. The latter is commonly used to identify variations in the rates of tectonically driven channel incision (e.g., Snyder et al., 2000; Kirby and Whipple, 2001;Kirby et al., 2003; Wobus et al., 2003). To assess whether our TCNs-derived erosion rates scale to tectonically driven uplift, we plotted the basin-averaged k_{sn} (ranging from 100 to 300 m, and 400 to 555 in the internal and external margin of the plateau, respectively; Table 3.3) against the catchment erosion rates (Fig. 3.3a). We also conducted the same analysis for k_{snQ}, to compare the steepness indexes across regions spanning different climatic zones. There is a strong correlation between catchment-average erosion rate and the k_{sn} and k_{snQ} values for the entire data set (Fig. 3.3a; $R^2 = 0.88$ and 0.78, respectively). This suggests that k_{sn} is a reliable metric for predicting channel incision rates.

Furthermore, there is also a relationship between basin-wide denudation rates and mean basin slopes. Basin-averaged slopes range from 6 to 24° showing the highest values in the exterior of the plateau (Fig. 3.3b; Table 3.3). The basin-wide denudation rates are higher for watersheds having a steeper local relief (Fig. 3.3c). The basin-averaged local relief in the sampled basins range from 250 m to 1100 m reaching the maximum value in the southern sector of the Talesh Mts. in the eastern margin plateau (Table 3.3). The basin-wide denudation and mean annual precipitation rates exhibit a weak correlation across the catchments (Fig. 3.3d). When we compare the basin-averaged k_{sn}, and k_{snQ} with the precipitation rates, they give a stronger correlation (Fig. 3.4a, b).

Tensile and compressive strength of rocks have been suggested to control rock erodibility and hence to influence erosion (e.g., Turowski et al., 2023; and references therein). In the study area, however, there is no relationship between erosion rates and the uniaxial compressive strength (UCS) of rocks (Fig. 3.3e), although there is a strong correlation between the steepness values (k_{sn}, and k_{snQ}) of the relict landscape with the UCS (Fig. 3.3g, h; Fig. 3.4c, d).

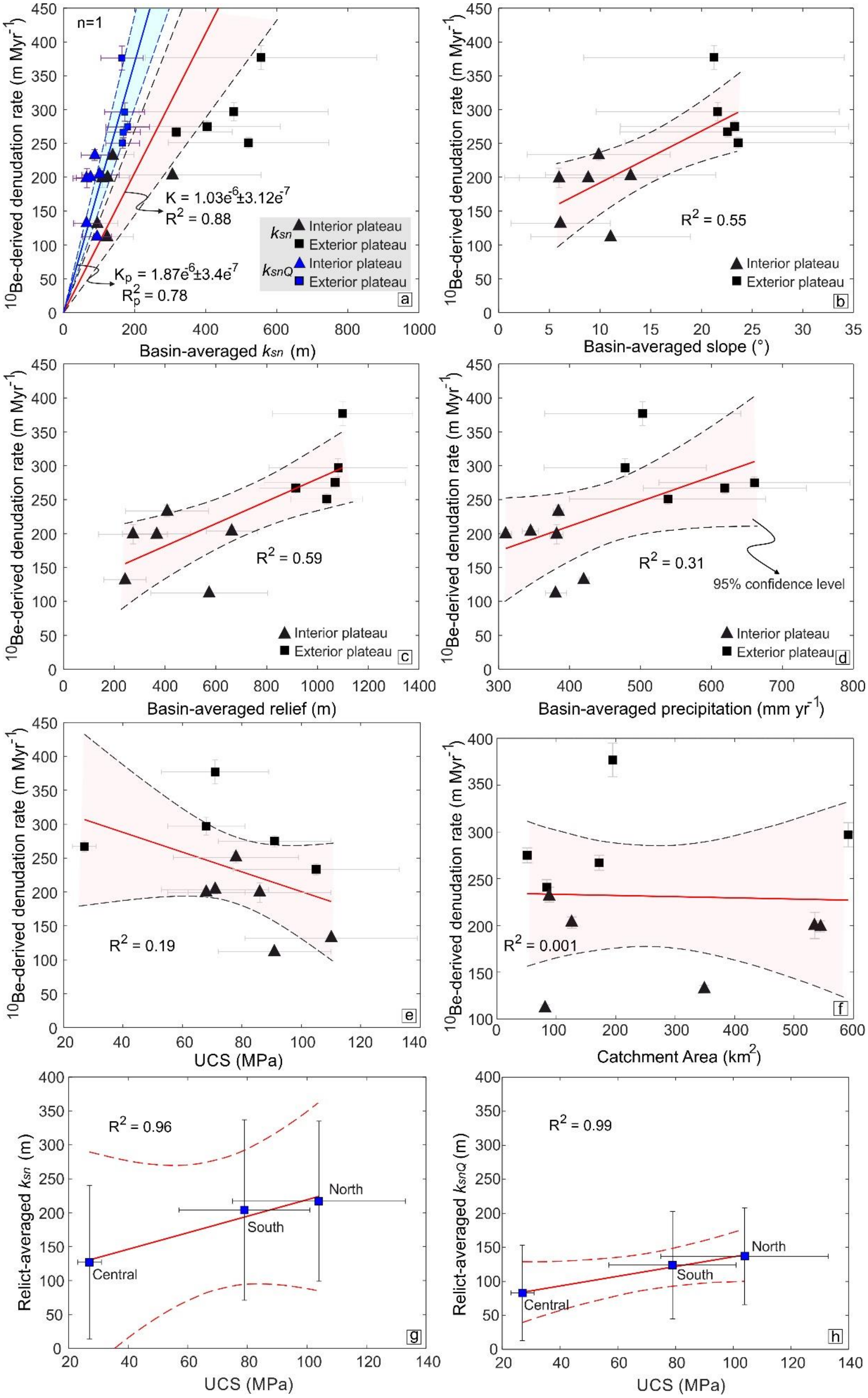
n=1
K = 1.03e-6±3.12e-7
R2 = 0.88
Kp = 1.87e-6±3.4e-7
Rp2 = 0.78
ksn
ksnQ
Interior plateau
Exterior plateau
a
10Be-derived denudation rate (m Myr-1)
Basin-averaged ksn (m)
0
200
400
600
800
1000
50
100
150
200
250
300
350
400
450
R2 = 0.55
b
Basin-averaged slope (°)
0
5
10
15
20
25
30
35
R2 = 0.59
c
Basin-averaged relief (m)
1200
1400
R2 = 0.31
95% confidence level
d
Basin-averaged precipitation (mm yr-1)
R2 = 0.19
e
UCS (MPa)
20
40
60
80
100
120
140
R2 = 0.001
f
Catchment Area (km2)
500
R2 = 0.96
Central
South
North
g
Relict-averaged ksn (m)
R2 = 0.99
h
Relict-averaged ksnQ (m)

Figure 3.3. ^{10}Be-derived catchment-averaged erosion rates versus basin-averaged (a) steepness index (k_{sn} and k_{snQ}), (b) slope, (c) local relief, (d) mean annual precipitation, and (e) uniaxial compressive strength. Note that the values of UCS represent the compressive strength of the rocks adjacent to the divide in the relict landscape and not for the entire catchment. (f) Relationship between erosion rate and catchment area. (g), (h) Linear regression values of ksn and ksnQ versus UCS for each lithological unit in the relict landscape adjacent to the main drainage divide. The solid line shows the forced linear best-fit, and the dashed line delimits the bootstrapped 95% confidence interval.

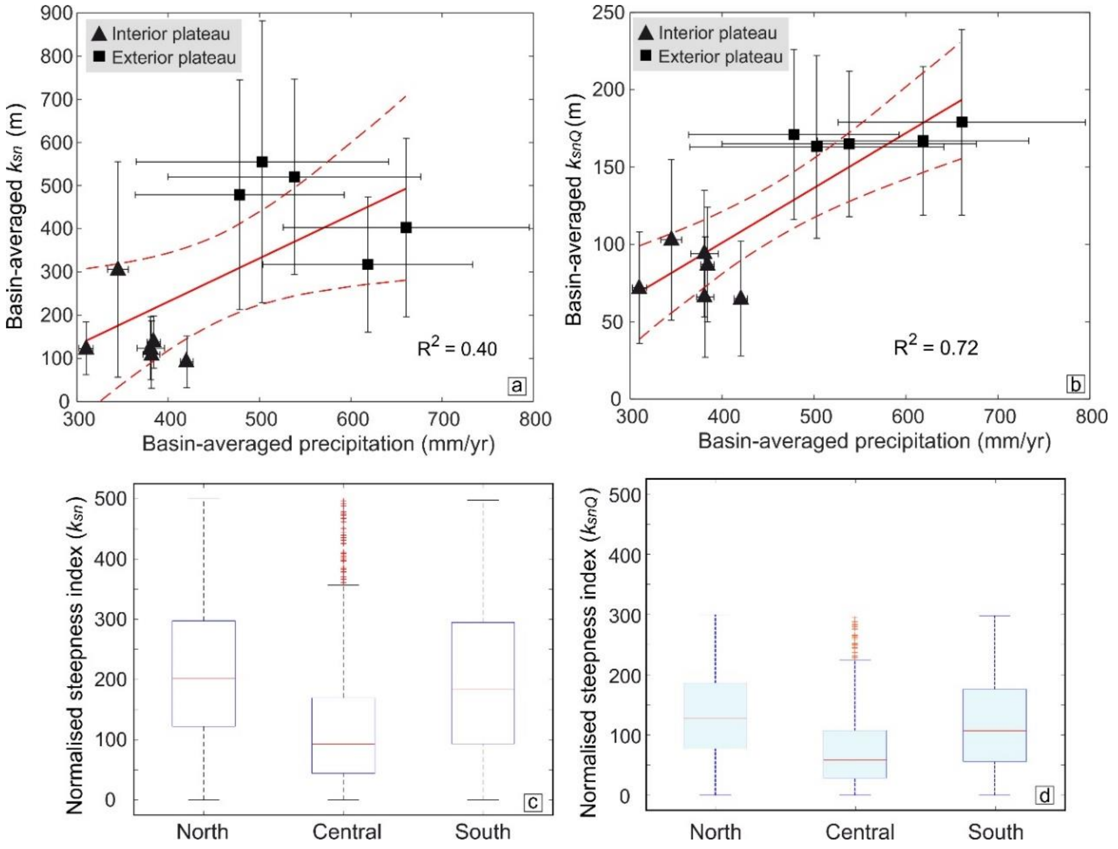

Figure 3.4. (a), (b) Correlation between precipitation and k_{sn}- k_{snQ} average values (c, (d) Average and standard deviation of k_{sn} and k_{snQ}, respectively, in the north (andesite-basalt), central (volcaniclastics), and southern (andesite) sectors of the Talesh Mts. relict landscape.

Additionally, the overall distribution of average erosion rates versus drainage area is quite scattered with no correlation (R^2=0.001; Fig. 3.3f), indicating that the erosion rates are independent of the drainage area. Overall, the basin-wide denudation rates are well correlated with the basin-averaged k_{sn}, hillslope gradient, and the local relief (R^2= 0.88, 0.55 and 0.59, respectively; Fig. 3.3), while they are moderately-well correlated with the basin-wide precipitation (R^2= 0.31; Fig. 3.3d). Finally, erosion rates scale with the inverse of the rock compressive strength (R^2= 0.19; Fig. 3.3e). In contrast, the steepness values in the relict landscape show a positive correlation with the UCS (Fig. 3.3g, h).

3.5.3. Quantifying fluvial incision

The magnitude of fluvial incision obtained from 31 river profiles range from ~200 to 1300 m in the plateau interior, whereas, in the exterior of the plateau the projection of 63 rivers profiles, gave a scattered pattern with values ranging from 300 to ~2800 m (Fig. 3.5). In general, from the interior towards the exterior of the plateau, the magnitude of fluvial incision and the knickpoints elevation increases.

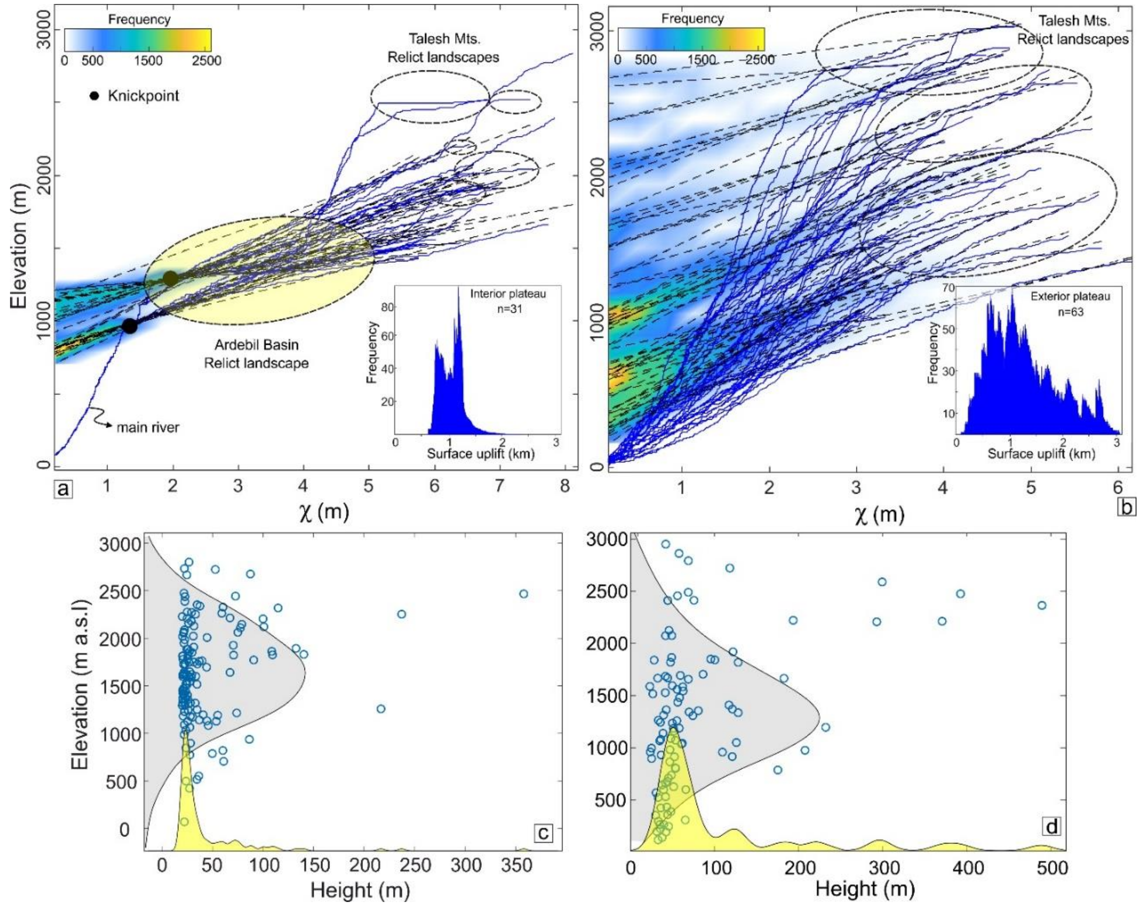

Figure 3.5. Modern longitudinal profiles (solid lines) and projections of the relict landscape (dashed black and grey lines) upstream of the highest knickpoints in χ plot in (a) plateau interior and (b) exterior. The insets show the fluvial incision which in the interior of the plateau is does not exceed ~1300 m. Whereas, in the plateau exterior it reaches almost twice as much ~2800 m. Dashed ellipses show the relict landscapes. (c), and (d) statistical analysis of knickpoints heights and elevations in the interior and exterior of the plateau, respectively.

In the plateau interior, 120 knickpoints have been extracted which are located at elevations between 70-2800 m (Fig. 3.1e). The majority of these knickpoints are small with an average height of ~30m (their height ranges from ~7 to 130m). Whereas, in the wet flank of the range in the exterior of the plateau, the height of knickpoints ranges from ~30 to 500m with an average value of 75m (more than 20 knickpoints with heights higher than 100m) (Fig. 3.1e).

3.5.4. Erodibility of the bedrock (erosion coefficient)

The bedrock erodibility parameter (*K* coefficient) can be quantified by the approximation of the stream power river incision model (Equation. 3) to a linear equation. Thus, the linear correlation between steepness values and our erosion rates dataset proposes that n parameter can be approximated to 1 (Fig. 3.3a). By plotting the normalized steepness index k_{sn} and k_{snQ} versus erosion rates, the erodibility values will be K=1.03 × 10^{-6} m/yr (R^2=0.88) and, K_P=1.87 × 10^{-6} m/yr (R^2=0.78), respectively (for $n=1$; Fig. 3.3a). In this case, K was estimated using the forced-origin linear regression. This result is consistent with estimates in tectonically active orogens where high density of rock fractures induced by tectonic deformation (e.g., Moumeni et al., 2023) leads to a general increase in bedrock erodibility with K values ranging between 10^{-6} and 10^{-3} $m^{0.1}$/yr (e.g., Stock and Montgomery, 1999; Kirby and Whipple, 2001; Molnar et al., 2007; Portenga and Bierman, 2011; Peifer et al., 2021). Furthermore, for this setting we calculated a power-law fit, using $n<1$, and $n>1$ which gives us the erodibility values of K=31.5±16.5 × 10^{-6} m/yr (R^2=0.69) and K=0.0013 × 10^{-6} m/yr (R^2=-0.89), respectively (Fig. S3.3). Additionally, if n was different from 1, the plot of denudation rate versus steepness would be non-linear. While the linear correlation in E versus k_{sn} supports the assumption that linear fit ($n = 1$) better explains the variability of erosion and channel steepness since it shows a higher R^2 (Fig. 3.3a). Consequently, the approximation of $n = 1$ could allow us to constrain bedrock erodibility for our study area effectively. We calculated k_{sn} and k_{snQ} for the seven main lithological units, and each sampled catchment (Fig. 3.6) to investigate if the steepness values are affected by the rock type and erodibility variations, which would affect the uplift rate. Furthermore, we present the K coefficient for each lithotype and catchment, and the contribution of each rock-type to the sampled catchments.

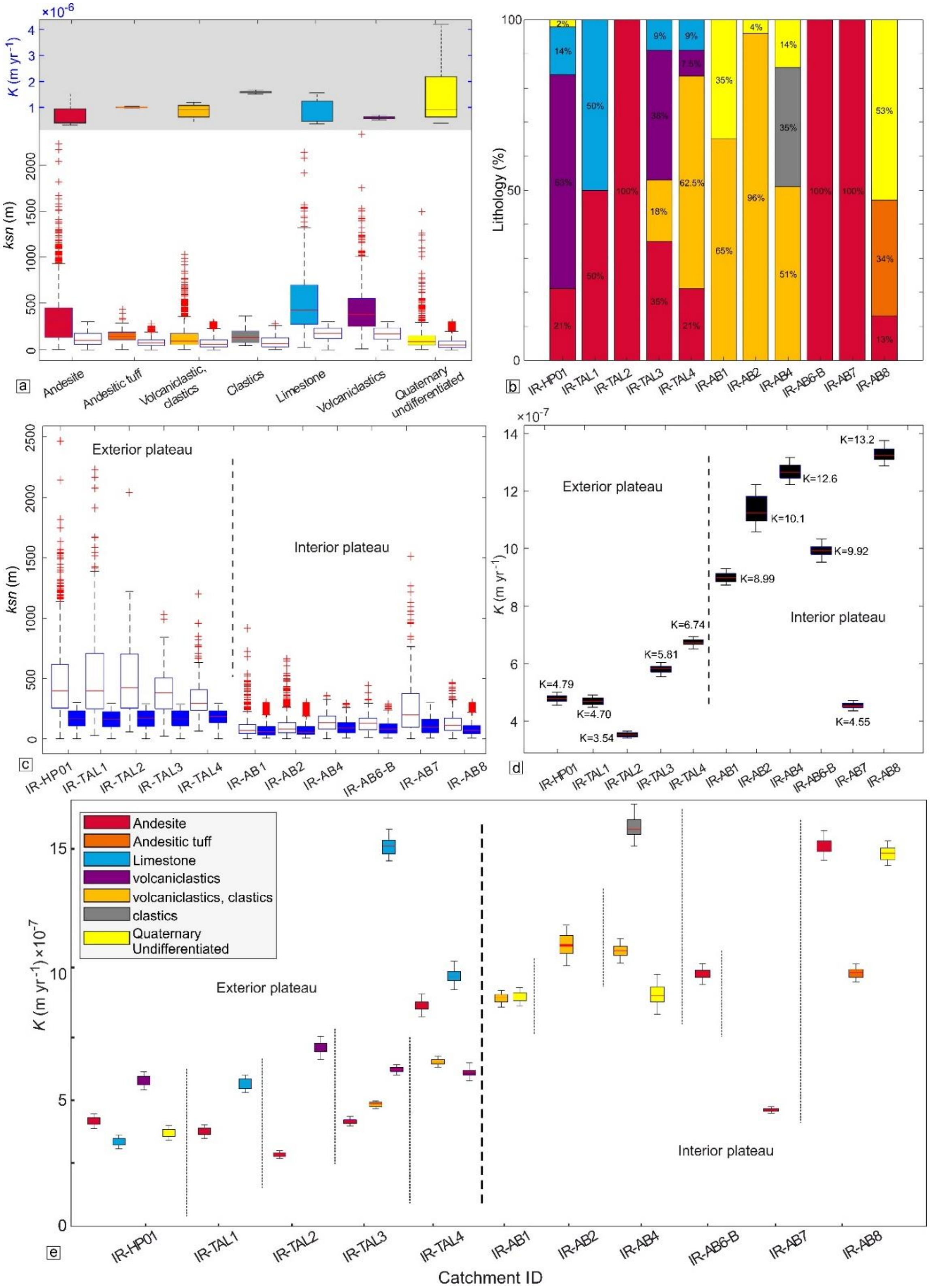

Figure 3.6. Comparison of rock types, erodibility and k_{sn}-k_{snQ} values. (a) k_{sn} (colored boxes) and k_{snQ} (white boxes) values for each outcropping lithological unit of the sampled catchments which inversion model of

river-profiles were performed. Inset (top) shows the calculated erodibility of each lithology. (b) Percentage of each lithology contribution to the catchments. (c) The variability of steepness values (k_{sn} and k_{snQ}; white and blue boxes, respectively) for the sampled catchments in the plateau interior and exterior. (d) Estimation of erodibility parameter (K) for each sampled catchment by dividing the denudation rate by the upstream average k_{sn}. The average K value for each catchment is shown. (e) K estimation for each rock type in the catchments. The thin dashed lines separate each catchment, and thick dashed line separates the catchments in the plateau interior and exterior.

The measurement of K coefficients for each lithotype (Table S3.1) and catchments from our ^{10}Be dataset yields a first-hand estimate of the erodibility and its relationship with the river steepness in the NW Iranian plateau. The catchments for which ^{10}Be analyses were done in the exterior plateau comprise andesite, volcaniclastics and limestone. In the plateau interior (Ardebil basin), most of the lithological units include volcaniclastics, clastic rocks, andesite, and Quaternary undifferentiated units.

The mean and range of the k_{sn} values for each lithology (Fig. 3.6a) does not show strong variations, except for the limestone, andesite and volcaniclastic rocks exhibiting the widest range of erodibility values. The values of k_{snQ} are more homogenous for all the rock types. On the catchment scale, the basins of the plateau exterior present higher values of k_{sn} and k_{snQ} by a factor of two compared to the catchments of the plateau interior. Moreover, the bedrock erodibility of the catchments in the plateau exterior (ranging from ~3.5 to 7×10^{-7} m/yr) is almost 2 times lower than the ones of the interior of the plateau (~9 to 13×10^{-7} m/yr).

3.5.5. Uplift rates and timing

To reconstruct the base level fall history of the region, we performed the linear inversion by inverting 11 longitudinal river profiles in the interior (six catchments; Fig. 3.7) and exterior (five catchments; Fig. 3.8) plateau by using $n = 1$, $\theta_{ref} = 0.5$, and $K=1.03 \times 10^{-6} \pm 3.12 \times 10^{-7}$ m/yr. Besides the non-uniform rock type inversion models, we also used the uniform erodibility inversion to reduce the variability in the rock-uplift rate. The inverted river profiles indicate minor differences (±75 m) between real and modeled river elevations (Fig. S3.4). Thus, the average modeled χ plots of the catchments show a good fit with the average trend of the real χ plots.

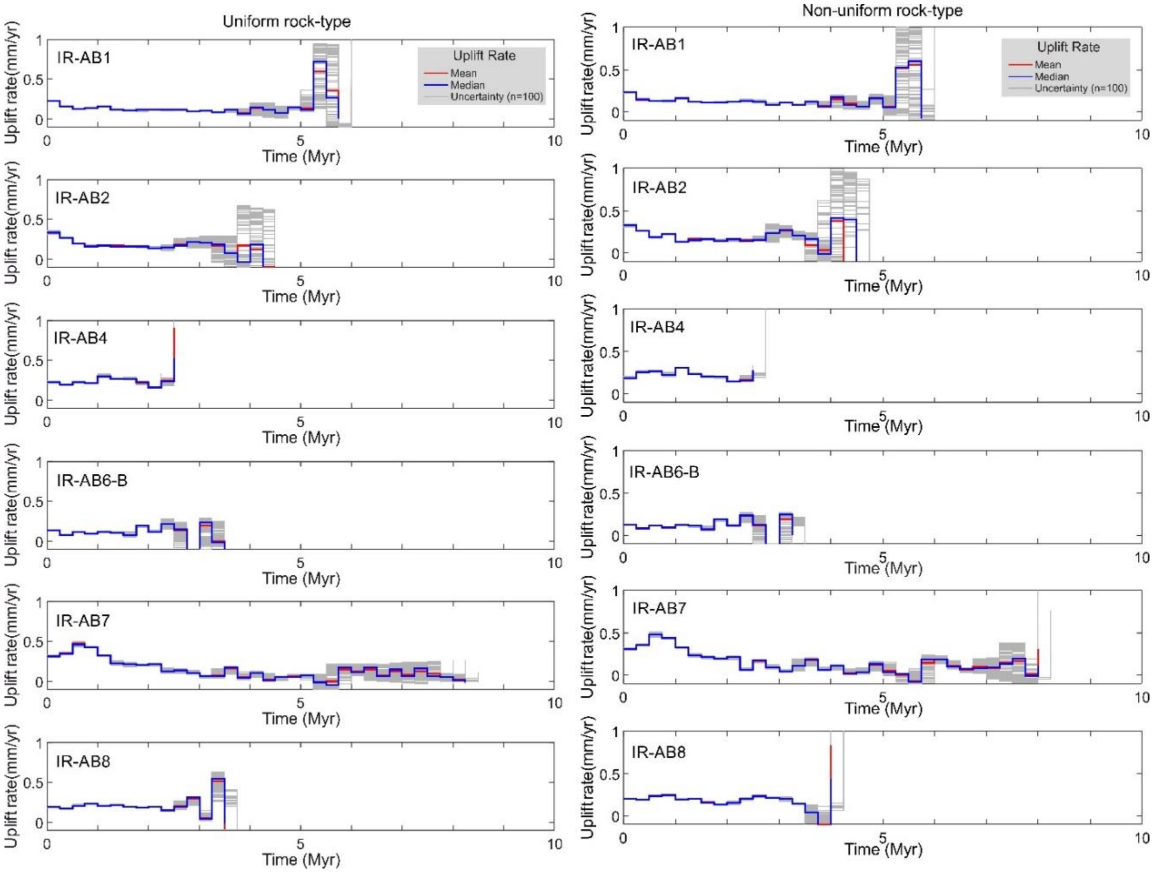

Figure 3.7. Inversion models of the river longitudinal profiles in the plateau interior. τ-U plots of the modeled base-level fall rates with uniform rock type (left), and non-uniform rock types (right)

The inversion results and the relative uplift rates inferred from Monte Carlo simulations for each catchment of the plateau interior (Fig. 3.7) indicate that the uplift rate variability is <0.1 mm/yr for both uniform and non-uniform rock-type (Fig. 3.7), except for two catchments (IR-AB1, IR-AB2) that have a variability of ~±0.1 mm/yr between 6 and 4 Ma.

On the plateau exterior, the relative uplift rate variability increases to >±0.2 mm/yr for each time step for ages older than 10 Ma (Fig. 3.8). The rivers in the plateau interior and exterior have different shapes as documented by the χ plots (Figs. S3.1, and S3.2), and consequently are recording a different uplift and evolution. Thus, by using mean, standard deviation and error of all inversions, we made two integrated plots for the plateau interior and exterior separately. The results indicate consistent relative rock uplift histories. For the plateau interior, the inversion models showed consistent results for both scenarios of uniform and non-uniform rock-type erodibility. In the northern sector (IR-AB1, IR-AB2 catchments) the relative uplift rate slightly increased up to 0.13 mm/yr from 5 to 4 Ma, and then remained constant until 1

Ma. During the last 1 Ma, the relative uplift rate increased to ~0.25- 0.35 mm/yr (Fig. 3.7). Towards the central sector (IR-AB4, IR-AB6-B catchments) the relative uplift rate is almost constant for the last 2 Ma. In the Ardebil basin, the inversion of catchment IR-AB7 (southern sector) resolve longer time scale (up to ~ 8 Ma). From 8 to 6 Ma, the inversion shows constant relative rock uplift rates of 0.13 mm/yr. Then the rates decrease abruptly to ~ 0. From 3 Ma, they start to increase gradually until they reach a maximum value of 0.45 mm/yr at about 0.5 Ma. Thereafter, they decrease again until present to ~0.35 mm/yr.

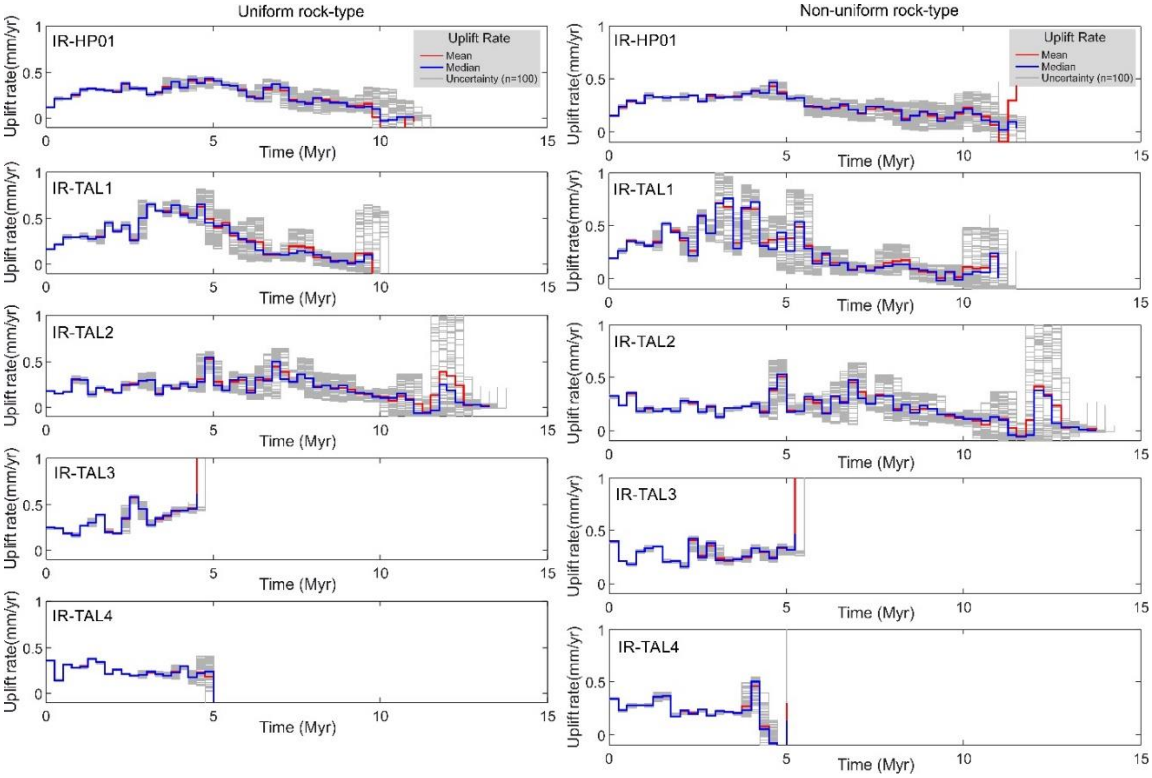

Figure 3.8. Inversion models of the river longitudinal profiles in the plateau exterior. τ-U plots of the modeled base-level fall rates with uniform rock type (left), and non-uniform rock types (right)

On the plateau exterior, in the southern Talesh Mts. (IR-HP01, IR-TAL1, IR-TAL2 catchments; Fig. 3.8) at ~11 to 10 Ma, we observe a gradual increase in the relative rock uplift rate up to 0.6 mm/yr, at ~ 4 Ma. This long-term increasing trend was followed by a decrease to ~ 0.2 mm/yr from 2.5 Ma to present. In the central Talesh Mts. (IR-TAL3, IR-TAL4 catchments; Fig. 3.8) the relative uplift rate increased to ~ 0.3- 0.35 mm/yr at 2.5 Ma, followed by a decrease to 0.2 mm/yr at 2 to 1.5 Ma.

In a nutshell, we can recognize one main time span of relative rock uplift rate in the plateau interior during the last 5 Ma, and two major time spans on the plateau exterior from ~ 10 to 4 Ma, and from 4 Ma to the present. The inversion results for the plateau interior suggest constant relative rock uplift rates of ~ 0.2 to 0.3 mm/yr. In this general constant trend, some minor changes occurred with a tolerance value of ~ 0.2 mm/yr (e.g., IR-AB7 catchment). In the plateau exterior, we have one significant general increasing trend followed by a gradual decrease in the rock uplift rate from ~ 3 Ma to < 0.2 mm/yr. On the exterior of the plateau, the uplift pattern was characterized by a gradual increase in uplift rates from ~ 12 to 10 Ma, and a final decrease in the last 2 Ma.

3.6. Discussion

3.6.1. Worldwide denudation rates comparison with the study area

Our results indicate that the millennial-scale basin-averaged denudation rates on the plateau interior are lower (< 250 m/Myr), than those on the plateau exterior (~250- 400 m/Myr) (Fig. 3.2a; Table. 3.3). The highest erosion rates are recorded in the southern sector of the range (> 300 m/Myr; IR-HP01, IR-TAL1) on the plateau exterior. In the central sector the erosion rates are mostly homogenous (~ 270- 275 m/Myr; IR-TAL3, 4) in the plateau exterior. The lowest erosion rates are documented in the central sector of the range within the plateau interior (~112 m/Myr; IR-AB6-B). The basins are in an equilibrium in the plateau interior, except IR-AB6-B, and IR-AB7 in the southern sector (see Appendix Chapter 3). Thus, most of our data represent erosion rates of channels adjusted to rock uplift rates. In the plateau exterior, all catchments have transient profiles. Hence, they exhibit erosion rates of both an upstream relict landscape and a downstream steep segment. In this case the ^{10}Be concentration contains a mixed signal and presents a denudation rate that averages the rates from both landscape in a basin.

The determined erosion rates in this study are comparable to rates observed in different geodynamic settings within tectonically active mountain ranges (Fig. 3.9), such as the Bolivian Andes (Safran et al., 2005), Tibet (Harkins et al., 2007; Ouimet et al., 2009), San Gabriel Mountains (DiBiase et al., 2010), Greater Caucasus (Forte et al., 2022), Western Alborz Mts. (Kaveh-Firouz et al., 2023), and Central Pontides (Racano et al., 2023). In the

Bolivian Andes, the short-term erosion rates range from 200- 1400 m/Myr. In this setting climate and lithology do not appear to exert first-order controls on catchment-averaged denudation rates (Safran et al., 2005).

In the northeastern sectors of the Tibetan plateau, the erosion rates range from 56 to 107 m/Myr (Fig. 3.9). These values are comparable to our ^{10}Be erosion rates in the plateau interior (Figs. 3.2a and 3.9). In this region, the covariance between denudation rates and k_{sn} indicates that channels are adjusted to long-wavelength differential rock uplift across the range (Harkins et al., 2007). The erosion rates at the eastern margin of the Tibetan Plateau ranges from 40 to 580 m/Myr. These values are also comparable to the exterior of the plateau of our study area. In this context, Ouimet et al. (2009) suggested that channels ultimately drive landscape adjustment to increasing rates of relative base-level fall in tectonically active settings. In another tectonic setting, millennial erosion rates across the San Gabriel Mountains in southern California range from 35 to 1100 m/Ma, which is consistent with both decadal sediment fluxes and long-term exhumation rates inferred from low temperature thermochronometry (DiBiase et al., 2010). Towards the northwest of the Talesh Mts., in the Greater Caucasus, basin-averaged ^{10}Be erosion rates range from 25-5600 m/Myr. These rates match long-term exhumation and short-term decadal scale rates (Forte et al., 2022).

Adjacent to our study area, the basin-averaged erosion rates range from 15 to 300 m/Myr in the northwest of Iranian plateau and western Alborz Mts. Kaveh-Firouz et al. (2023) proposed that the landscape of the western Alborz was controlled by the late Oligocene-Miocene tectonic activity, while in the Plio-Quaternary a coupling between tectonics and climate became dominant. Conversely, in the plateau interior the landscape was chiefly controlled by tectonic processes rather than climate. Given that topography is the result of tectonics and that tectonics, (together with lithology and climate) controls erosion rates, we must assume that the processes of landscape evolution for the Alborz-Talesh Mts. and the Plateau are the same. A comparison of our results with a global compilation of average catchment slope and denudation rates (Portenga and Bierman, 2011), reveals that our data falls into two distinct groups (Fig. 3.9). The extracted k_{sn} values from all catchments are plotted versus the catchment-average erosion rates (Fig. 3.3a). The results showed that the catchment-averaged k_{sn} and k_{snQ} were good proxies for predicting the erosion rates because higher erosion rates correspond to higher steepness values and vice versa (correlation coefficient of 0.88 and 0.78, for k_{sn} and k_{snQ} respectively). Generally, the erosion rates and k_{sn} values in the study area are comparable to those from the Greater Caucasus (Forte et al., 2022) in the northwest of the Talesh Mts, and the western Alborz (Kaveh-Firouz et al., 2023) (Fig. 3.9a). The plateau exterior has a higher incision (Fig. 3.5) and many major knickpoints (Fig. 3.1e), whereas the low-relief plateau interior has a lower erosion with equilibrated river profiles and fewer major knickpoints. Variations in the steepness index reflect the non-uniform rock uplift in the study area and difference in erodibility of the bedrock. The catchments of the plateau exterior showed similar erosion rates when comparing the denudation rates with k_{sn}/k_{snQ} (Fig. 3.3a). This can be attributed to lithological control or variability in precipitation. Since lithology is homogenous across the plateau exterior, we can rule out this factor. When plotting the denudation rates versus k_{snQ} it can be seen that they follow a line, which shows the effect of precipitation on erosion rates on the plateau exterior (Fig. 3.3a).

The measured denudation rates present a strong sensitivity and correlation to the basin-averaged slope gradient, k_{sn}, and topographic relief (Fig. 3.3). These observations suggest that the denudation processes in the Talesh Mts. are not only controlled by lithological characteristics (i.e., rock strength), but can also be attributed to the presence of a transient topography. This implies that there is a coupling among hillslope processes, river incision, denudation, and topography.

3.6.2. Incision variability in plateau interior and exterior

The ^{10}Be-derived erosion rates exhibit a correlation with the k_{sn} index (Fig. 3.3a), which is generally correlated with tectonic activity (Kirby and Whipple, 2001; Lague and Davy, 2003; Safran et al., 2005). This highlights the control of channel incision processes on the patterns of catchment-averaged erosion rates. On the exterior of the plateau, rivers that exhibit a transient state (Fig. 3.5b) in response to increased uplift and denudation rates correlate well with k_{sn} and the basin-mean gradient (Figs. 3.3 and 3.9). In such conditions, from the last rock uplift change, enough time has passed, or the denudation was fast enough to allow the hillslope to adjust to the local base level in the rejuvenated part of the catchment. Thus, this is the case for relict landscapes in the downstream portion of a catchment. While the upstream segment has not adjusted to the new base level fall and hence is still eroding at lower, older rates (e.g., Kirby and Whipple, 2011; Olivetti et al., 2016). On the plateau interior, there are two generations of relict landscapes (Fig. 3.5a). The highest one is located at elevations greater than 1500 m a.s.l. This generation of landscapes (Fig. 3.5b) is related to the short-wavelength uplift in the Talesh Mts. caused by the thrust faulting and changes in rock uplift rate. The relict landscape in the plateau interior located at elevations lower than ~1500 m a.s.l. This relict landscape that can be discerned by a major knickpoint in the Ardebil Basin, indicates the long-wave erosion in the plateau interior due to the reginal uplift (Fig. 3.5a).

The highest k_{sn}, slope, and local relief values are measured for the catchments of the wet flank of Talesh Mts. (plateau exterior). In contrast, the lowest k_{sn}, slope, and local relief values were found in the drier basins of the plateau interior (Fig. 3.3). This is consistent with the highest millennial-scale erosion rates in the plateau exterior and indicates that the region is experiencing an asymmetric uplift (Figs. 3.2a and 3.5), because the plateau interior adjusts to an elevated local base level (Ardebil basin), while the plateau exterior has always adjusted to the Caspian Sea (global sea level or slightly lower elevation).

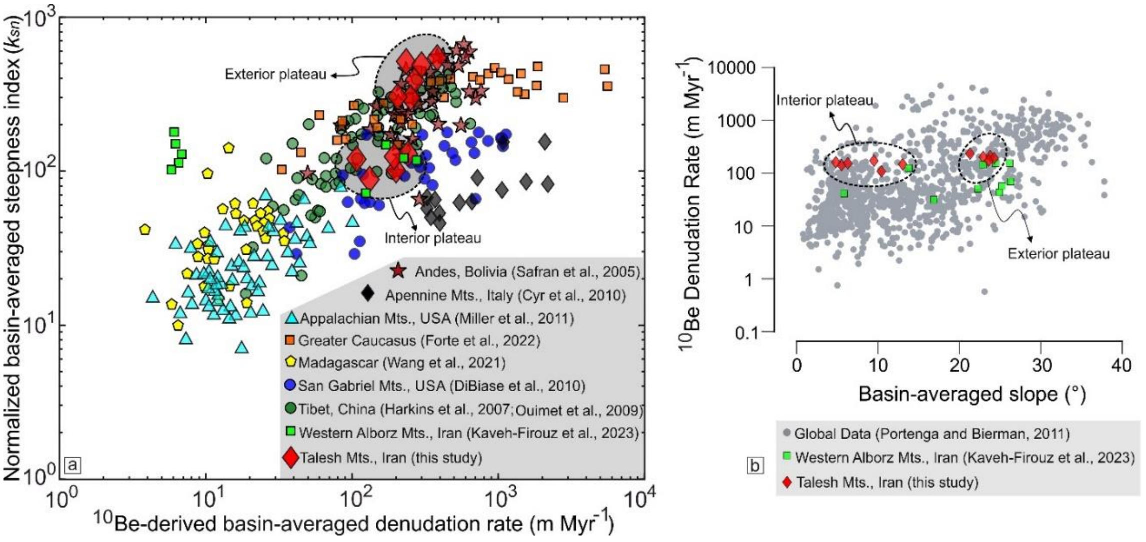

Figure 3.9. Cosmogenic-derived denudation rates of the study area and different tectonic settings plotted against (a) normalized channel steepness index (re-adapted after Kirby and Whipple, 2012, and Olivetti et al., 2016), and (b) basin-averaged slopes (data from Portenga and Bierman, 2011).

The basins in the study area, especially the ones on the wet flank of the Talesh Mts., have some of the highest k_{sn} values measured worldwide (Fig. 3.9a). These high values support the concentration of erosion on the eastern flank. In contrast, towards the plateau interior, the lower erosion rates, gentler slopes (Fig. 3.9b), lower river steepness (Fig. 3.9a), and lower values of incision (Fig. 3.5) indicate a lower tectonic activity by a factor of ~ 2.

3.6.3. Topographic features and erosion rate

To unravel the impact of factors controlling the landscape evolution of the plateau margin, we explored the correlation among the topographic metrics with ^{10}Be-derived denudation rates measured on both sides of the Talesh Mts. There is a strong correlation between erosion rates and topographic metrics. Precipitation, however, shows a moderate correlation with erosion rates, which may be due to the interactions of several factors controlling the landscape.

3.6.3.1. Catchment gradient and erosion

The Miocene- Pliocene increase in exhumation rates (Madanipour et al., 2017) associated with the base-level fall and faulting along the Talesh Fault, has produced steeper slopes along the external margin of the plateau (Fig. 3.3b). The high erosion rates along the eastern slopes of the Talesh Mts. can be explained by the presence of channels that are steeper than those in the interior of the plateau (Fig. 3.2b-g; Table. 3.3). Additionally, the divide mobility towards the plateau interior gave rise to an increase in the sediment budget along the wet flank of the Talesh Mts. (Table. 3.3). This highlights the role of active tectonics along the Talesh Fault (thrust kinematics in its northern and southern segments) in dictating the patterns of erosion and the evolution of landscape along the plateau margin since the early Miocene (e.g., McQuarrie & van Hinsbergen, 2013; Koshnaw et al., 2019; Paknia et al., 2021).

3.6.3.2. Local relief and erosion

The basin-averaged relief shows a positive correlation with the catchment-averaged denudation rates (R^2=0.59; Fig. 3.3c). The interior of the plateau is characterized by a relatively low relief and low slope values (Table. 3.3). The high relief and steep slopes are mostly found along the divide line. The low denudation domain of plateau interior corresponds to a low-relief landscape with limited river incision (Fig. 3.5), that gently dips westward from the drainage divide from ~2000 to 1300 m a.s.l. (northern sector), ~1900 to 1400 m a.s.l. (central sector), and ~3000 to 1500 m a.s.l. (southern sector). These catchments show equilibrated river profiles without large knickpoints (except for the southern sector) (Fig. 3.5).

3.6.3.3. Climate impact on erosion

Changes in orographic precipitation patterns can have an impact on the evolution of mountain landscapes (e.g., Roe, 2005; Leonard and Whipple, 2021). High elevations in the north and southern sectors of the range receive 400-500 mm/year and 500-900 mm/year of rainfall, respectively. The central sector receives 800- 1100 mm/year of rainfall (Figs. 3.3b, and 3.1c). However, this spatially varying rainfall does not seem to have a distinct effect on the erosion rates, since the basin-averaged precipitation rates show only a weak to moderate correlation with basin-averaged denudation rates (R^2=0.31; Fig. 3.3d). Such conditions are typical of convergence zones like the Greater Caucasus (Forte et al., 2022) because spatial patterns in erosion rates mostly indicate regional tectonics with little sensitivity to precipitation.

3.6.3.4. Rock strength impact on erosion

The rates of erosion can be affected by different mechanical properties of rock types (Whipple, 2004). When the landscape is in equilibrium (uplift=erosion), rock types do not influence the erosion rates, but they affect steepness and topographic relief (e.g., Whittaker 2012). At the regional (basin) scale, lithological variations in different parts of the range do not have any significant effects on k_{sn} and catchment-average denudation rate, as there is no notable correlation between erosion rates and the UCS values (R^2=0.19; Fig. 3.3e). This poor correlation suggests that erosion rates are not mostly controlled by rock strength (Fig. 3.3e). However, at the scale of the drainage divide (in the immediate vicinity of the divide), the UCS of rock units adjacent to the divide present a strong positive correlation with the k_{sn} and k_{snQ} values in the relict portion of the landscape (R^2>0.95; Fig. 3.3g-h). Although the lithological characteristics of a region can have local effects on landscape transience (Moumeni et al., 2023), they are unlikely to be a first-order governing factor in catchment-wide denudation rates (e.g., Clementucci et al., 2022). Additionally, it is noteworthy that passive exhumation of rock units having variable strength plays an important role in generating the topographic relief (e.g., Piefer et al., 2020; Clementucci et al., 2022; and reference therein). Thus, the lack of correlation between erosion rates and UCS in the study area does not fully exclude the role of lithology on shaping the landscape.

The lack of correlation between basin-averaged erosion rate and UCS may have multiple underlying causes. The geotechnical parameters of rocks such as compressive and tensile strength often exhibit co-variation, preventing the evaluation of erodibility in fluvial impact erosion. In addition, the compressive strength, tensile strength, and density of rocks in the study area are correlated with each other (Moumeni et al., 2023) but not with erosion rate (Fig. 3.3e).

3.6.4. Evolution of the drainage divide

In the northern and southern sectors of the divide, the Gilbert metrics suggest that the divide is stable, while χ indicates that the divide is mobile in all its segments (Fig. 3.10). The strength of the rocks adjacent to the divide on the relict landscape is not homogenous. In the northern and southern sectors, the UCS of the rock units are high, while in the central sector they are the lowest (Fig. 3.4c, d). These features show that the divide escarpment in the north and south has not yet reached an advanced stage of erosion and has not extended towards the headwaters. In the central sector, almost the entire relict landscape has been eroded away and the headward erosion is incising the plateau interior where a big scarp has formed.

The difference in erodibility of the rocks can be considered as a potential factor inducing the instability of the divide solely in the central sector of the Talesh Mts. Therefore, spatial zones of localized divide instability are associated with differences in rock strength and fluvial piracy events. Consequently, χ metric which is consistent with our erosion rates dataset (Fig. 3.10) indicates potential future divide movement on a regional scale.

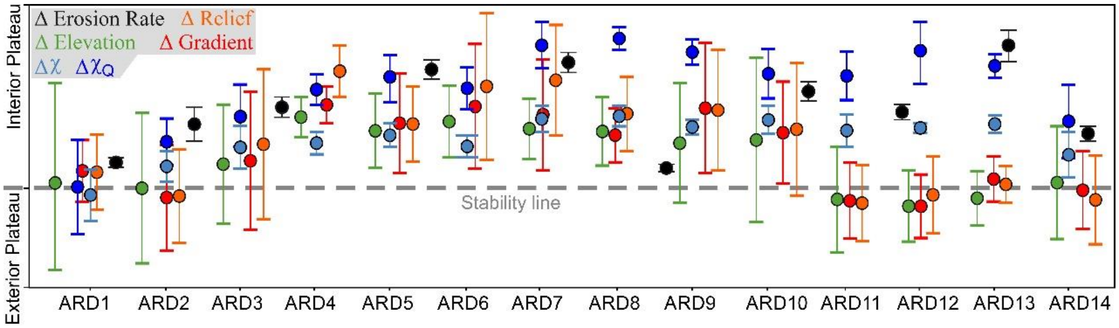

Figure 3.10. Standardized delta plots for the main drainage divide segments based on the results of Gilbert metrics, χ, χ_Q (Moumeni et al., 2023) and erosion rates in the region. Regarding Gilbert metrics results, Δ relief, Δ elevation, Δ gradient, Δχ, and $\Delta\chi_Q$ indicate the instability and the potential divide mobility direction. The grey dashed line shows the divide stability line, which if a single divide segment touches the line, that segment is stable in that metric. The values above and below the divide stability lines suggest divide instability and movement toward the interior and the exterior of the plateau, respectively.

We projected the denudation rates along swath profiles orthogonal to the mountain range (Fig. 3.11).

3.6.4.1. Erosion and χ metric

The contrasting erosion rates across the range caused the migration of the drainage divide towards the interior of the plateau (i.e., towards lower erosion rate), as illustrated by the χ values (Fig. 3.10). The pattern of divide migration and the associated differences in erosion rate are indicative of a long wavelength morphological disequilibrium and landscape transience, with the stream network in the process of reorganization in response to the asymmetric uplift (e.g., Olivetti et al., 2016). The timing of rock uplift is associated with the early Oligocene to early Pliocene regional deformation induced by the Arabia-Eurasia continental collision (Madanipour et al., 2017).

In the interior of the plateau, Apatite U-Th/He single grain cooling ages range from nearly 30 to 50 Ma (see profiles BB' and CC'; Madanipour et al., 2017). If we assume that the youngest (ca. 30 Ma) ages are fully reset and to a first approximation recorded monotonic and steady cooling, the mean exhumation rates averaged over the last 30 Ma would be 60-70 m/Myr (considering a mean surface T of 10°C and a constant geothermal gradient of 25°C/km). Conversely, in the plateau exterior, Apatite U-Th/He single grain cooling ages range from 5 to 13 and 4 to 20 Ma (profile BB' and CC', respectively, of Madanipour et al., 2017). This gives exhumation rates of 100 to 500 m/My, averaging over the last 20 and 5 Ma, respectively. The difference in long-term exhumation rates between the interior and the exterior of the plateau is consistent with the ^{10}Be cosmogenic millennial-scale denudation rates (average value of ~ 300 m/Myr for plateau exterior, and ~180 m/Myr for plateau interior), although the ^{10}Be results in the plateau interior suggest that an increase in erosion rates must have occurred in recent times. Furthermore, in terms of river incision, the wet flank of Talesh Mts. on the eastern side of the divide is characterized by major knickpoints with high elevation (elevated relict landscape) and high incision rate downstream of the knickpoints (Figs. 3.1e and 3.5). Thus, a recent rejuvenation event is needed to make such a landscape transient. Rock uplift rates from the Oligocene to Pliocene can be considered the main factor that incising the bedrocks in the mountain range which generated the knickpoints. Therefore, the difference in the rock uplift rate in the plateau exterior in response to the changes of the Caspian Sea base-level fall is the main reason for the divide migration.

Therefore, for the catchments that have a relict landscape (IR-HP01, IR-TAL1, IR-TAL2; Fig. S3.2) in the plateau exterior, the incision wave associated with the base level fall has not reached yet the drainage divide which is also suggested by Gilbert metrics (Moumeni et al., 2023). Consequently, it cannot have triggered divide migration. Evidence for this observation is the time scale of our river inversion analyses for these catchments that is > 10 Ma (Figs. 3.8 and 3.12). Based on our inverse models of the river profiles for the central sector which are in equilibrium (IR-TAL3, IR-TAL4; Fig. S3.2), the divide migration may have started ~ 5 Ma. This change in the uplift rate and base level fall generated an erosional wave propagating upstream along the river from the Caspian Sea base-level, which followed by an abrupt increase in incision rate, and made the main divide unstable in this sector (Figs. 3.10 and 3.11).

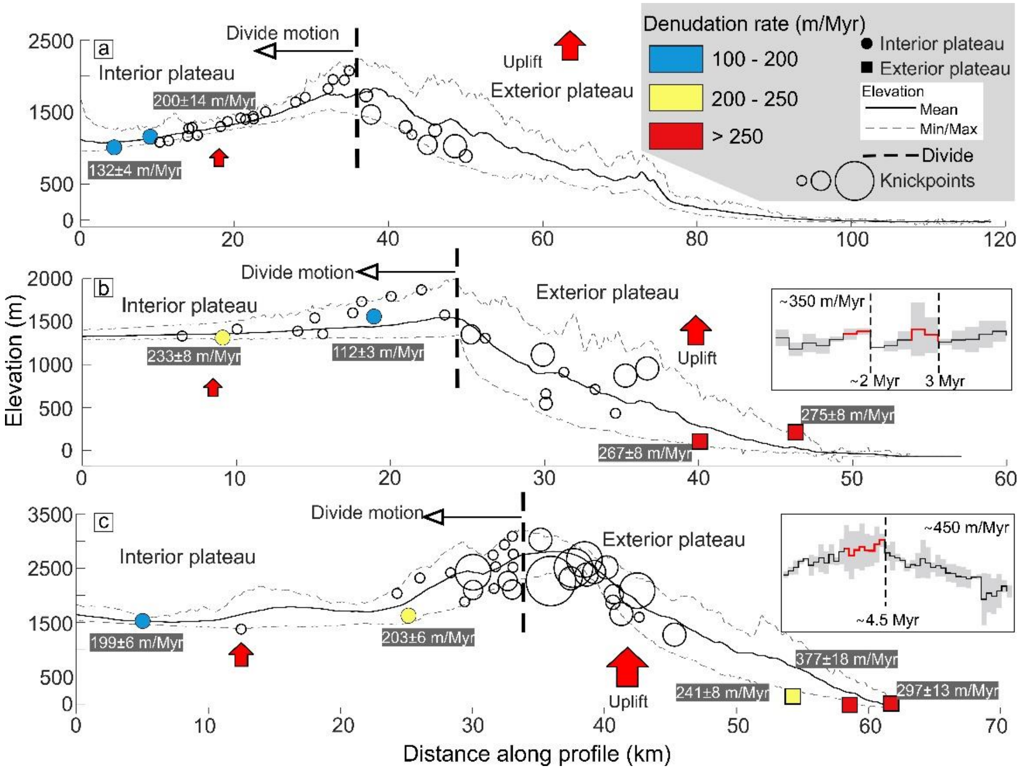

Figure 3.11. Schematic evolution of the Talesh Mts. and divide reorganization in response to the increased uplift rates. ^{10}Be-derived denudation rates projected along the swath profile orthogonal to the main divide in the (a) P1: northern sector, (b) P2: central sector, and (c) P3: southern sector of Talesh Mts. The locations of the swath profiles are indicated in Figure 1d. The size of the knickpoints corresponds to their heights.

3.6.5. Uplift history of the region

The longitudinal river profiles and fluvial inversion analysis enabled us to infer two main time steps of the uplift history of the plateau exterior. Rock uplift rates in the plateau exterior were higher than those in the interior. This difference may be the result of two different mechanisms acting at different wavelengths. Generally, the uplift on the wet flank of the Talesh Mts. in the plateau exterior can be attributed to tectonics. The combination of structural and low-temperature thermochronological data suggests an acceleration in exhumation rates at ~ 12 Ma (Madanipour et al., 2017). This is consistent with our river inversion analysis which indicates a progressive increase in rock-uplift rates from ~12 to 4 Ma, when peak values of ~0.5 mm/yr were reached (Fig. 3.12). Following this peak, the inverted rock uplift rates decreased up to values in the same order of magnitude of our

^{10}Be-derived erosion rates. This rock uplift pattern agrees with that one obtained from the fluvial longitudinal profiles in the adjacent Eastern Anatolia Plateau (Molin et al., 2023).

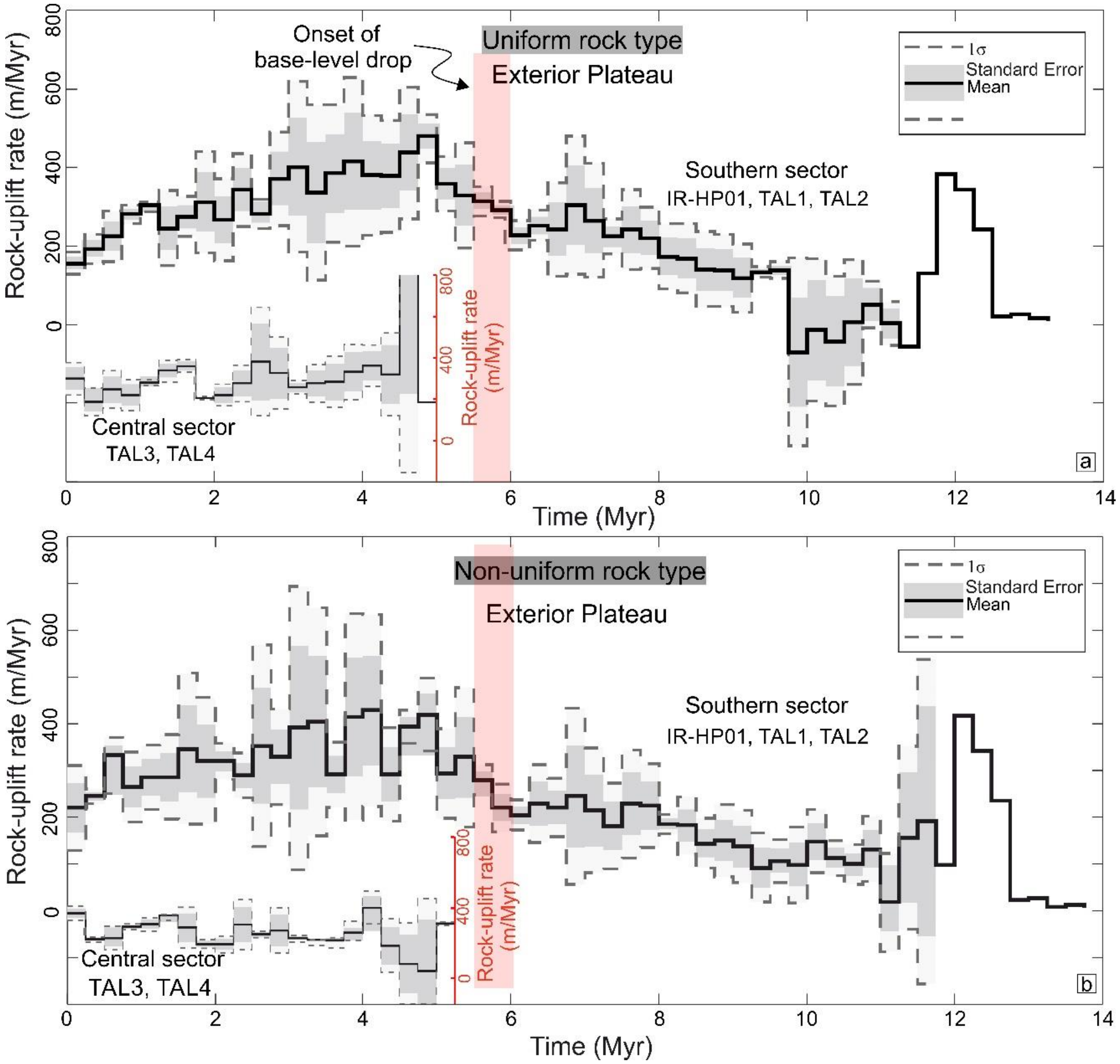

Figure 3.12. Relative rock-uplift history obtained from the river-profile inversion for the plateau exterior. Mean, standard deviation, and standard error from the inversion analysis of 5 river profiles (IR-HP01, IR-TAL1, IR-TAL2; Southern sector, and IR-TAL3, IR-TAL4; Central sector- in the inset lower left) for (a) uniform rock-type, and (b) non-uniform rock-type scenario. The projection of each river profile is provided in detail in the Figs. 3.7 and 3.8). The highlighted red colors show the main base-level changes in the region.

The 4 Ma peak values in uplift rates include the effect of the 0.6 to 1.5 km lowering of the Caspian Sea base-level triggered by the isolation from the Paratethys from ~6 to 3.2 Ma (e.g., Forte and Cowgill, 2013; Van Baak, et al., 2013). Moreover, it may also incorporate the inferred Pliocene regional tectonic reorganization associated with crustal shortening and thickening processes in the Iranian Plateau and more in general across the northern sectors of the Arabia–Eurasia collision zone (Allen et al., 2004; Ballato et al., 2015; Madanipour 2023). The surface effect to the increased uplift rates induced by both enhanced tectonic activity and base level lowering, was an acceleration of bedrock river incision in the plateau exterior. This led to the development of a steeper landscape and to an increase in sediment influx into the southern Caspian Basin (Ballato et al., 2015 and references therein). In the northern and southern Talesh Mountains, the wave of incision recording such a Pliocene acceleration has not reached yet the upstream reaches of the Talesh Mts catchments as also observed in the Alborz Mts. (Ballato et al., 2015).

Our inversion shows that major changes in the gradient of the longitudinal/ χ profiles, correspond to major changes in relative rock uplift rates. Therefore, the youngest/oldest uplift rates reflect changes in the downstream/upstream portions of the river channel. In the southern sector, since all the river profiles show a common shape in χ-space (Fig. S3.2) and belong to neighboring catchments, are expected to have a similar uplift history, which is also the case for the rivers in the central sector. In the southern and northern Talesh Mts. we have a relict landscape that records changes in relative uplift rate occurred around 10 Ma. This landscape cannot record the acceleration at 5 to 3 Ma because such an incision wave is at lower elevation. The 2000 m fluvial incision does not record a 5 My old history but a10 My old history.

In the central sector of the Talesh Mts., the time scale of the relative rock uplift rates goes back to ~ 5 Ma and show a rather uniform pattern with minor changes at ~2.5 and 1.5 Ma (Fig. 3.12) which corresponds to the base level drop of the Caspian Sea. This means that the wave of incision went through the entire catchments in this sector and a new equilibrium has been reached. Furthermore, in the central Talesh Mts. detrital AFT data testify a lower magnitude of Miocene exhumation, which has been attributed to a dominant strike-slip tectonic regime (Madanipour et al., 2018).

From ~3 Ma, the uplift rates in the southern sector decreased gradually to ~0.2 mm/yr. Generally, the lower relative uplift rates in the central sector compared to the southern sector (Fig. 3.12) may be due to a combination of higher rainfall in the central sector or weaker substrate (volcaniclastics and clastics; Fig. 3.6) since the erodibility of the catchments in this sector (IR-TAL3, IR-TAL4) is greater compared to the other catchments in the southern sector (Fig. 3.6). Based on these observations we suggest that the central and southern sectors of the range did not share the same uplift history at least during the last ~3 Ma. Except for 5 to 3 Ma time interval, the uplift rates in our inversion analysis are linked to tectonic activity (faulting). Nevertheless, our inversion models support the idea that relative base-level fall as the main factor for the uplift rate predating the other agents such as climate and bedrock erodibility which may just act locally. For the plateau interior we considered a local base level (~ 1300 m a.s.l.) upstream of the main knickpoint (above the capture point) in the Ardebil basin. In the last 2 Ma (Pleistocene) the inversion models for the rivers in the northern part show a slight increase in the uplift rate (Fig. 3.7). This is also the case for a river in the southern part of the Ardebil basin (IR-AB7; Fig. 3.7) which shows the longest time scale in the plateau interior and indicates a gradually increasing uplift rate from 3 Ma which reaches its peak value (0.5 mm/yr) at ~ 0.7 Ma. For the plateau interior these minor differences in the uplift rate may be attributed to localized fault uplift due to reverse fault systems in the north and southern parts of the basin.

3.6.6. Tectonics implication and feedback with climate

The Talesh Mts. act as an orographic barrier intercepting moisture originating from the Caspian Sea and triggering more arid conditions in the interior of the plateau (Moumeni et al., 2023). Additionally, towards the exterior of the plateau steeper slopes, a rugged relief and higher denudation rates are encountered. The base level drop of the Caspian Sea during the Pliocene affected the erosion rates in the study area (e.g., Popov et al., 2010; Yanina, 2012; Ballato et al., 2015; Madanipour, 2023), which is also well documented in the inversion model of the river profiles. The fluctuations of the Caspian Sea base-level due to tectonic-climate variations influenced the pattern of exhumation and erosion across the western Alborz and Talesh Mts. (e.g., Nadirov et al., 1997; Ballato et al., 2015) during the late Miocene-early Pliocene. The base-level fall in the Caspian Sea (from ~6 to 3 Ma) correlates with increased/decreased exhumation rates along the northern/southern flank of the central Alborz Mts. (Ballato et al., 2015). Enhanced river incision caused by this base-level drop (Fig. 3.5), led to asymmetric exhumation and a significant increase in sediment flux (Table. 3.3) into the Caspian Basin as also documented by the deposition of the

Productive Series (more than 6 km of sediments in ~3 Myr; e.g., Allen et al., 2002). These sediments were sourced from all the orogens surrounding the South Caspian Basin and may have led to rapid sediment loading, with underthrusting and subduction of the Caspian Basin beneath the central Alborz Mts. (Ballato et al., 2015) and the central Caspian Basin (e.g., Allen et al., 2002), respectively. Although, such an underthrusting focused tectonic deformation along the wetter northern flank of the central Alborz Mts. The pattern of rock uplift is decoupled exhumation rates averaged over the last 3 Ma and decadal erosion rates (Ballato et al., 2015 and references therein) suggesting that the orogen is not affected by a climatically controlled tectonic regime. Consequently, tectonics appears to be as the main driver of erosional patterns along the margins of the Iranian Plateau (e.g., Ballato et al., 2015; Madanipour, 2023; Kaveh-Firouz et al., 2023). Our findings agree with previously published data in the western Alborz Mts. (Kaveh-Firouz et al., 2023), and Greater Caucasus (Forte et al., 2022). Climate has had an effect on the denudation rates. However, it did not exert a first-order control (Fig. 3.3d). Available data suggest a sort of equilibrium between uplift and erosion (steady-state topography) which possibly goes back to the late Miocene as suggested by the river profiles downstream of the knickpoints in the northern and southern sectors of Talesh Mts. It should be noted that the relict landscape in these sectors cannot be linked to the base level drop at 6 to 3 Ma. Our inversion results in the southern sector goes back to 12 to 10 Ma, which means the landscape must have formed before the increase in the uplift rate at 10 Ma. These observations have major two implications. First, despite the Talesh thrust which is highly oblique with respect to the regional plate convergence direction, strain partitioning processes dominate, and strike slip faulting occurs in the plateau interior. This is quite different from the conclusions of previous studies. As suggested by the thermochronometry data and the river inversion analysis, such strain partitioning may have been active since ~10 Ma. The obtained uplift rates are comparable with those in the eastern Anatolia Plateau (Molin et al., 2023). Thus, it can be assumed that there might be regional processes connected to the uplift history in this study. They propose that the uplift history of the Eastern Anatolian Plateau (EAP) is chiefly described by a slow emergence with low uplift rate that granted the development of low relief landscapes at elevation higher than ~1500 m. From the inversion analysis they found that first increase in uplift rate occurred ~10 Ma and accelerated since 5 Ma which possibly made most of the modern topography (Molin et al., 2023 and references therein). They suggest that the progressive increase in uplift rate (~11-10 Ma) is associated with the slab break-off (Molin et al., 2023 and references therein). This acceleration in surface uplift rate triggered the headward erosion wave and the development of a landscape with steeper channels downstream compared to the ones in the upstream segments. Second, the eastern wet flank of the Talesh Mts. has higher values of k_{sn}, higher erosion rates (cosmogenic meteoric^{10}Be) and exhumation rates (thermochronology data; Madanipour et al., 2017) and higher precipitation rates. The higher precipitation rates assist in removing the sediments efficiently. This may have probably hampered the progradation of the deformation front towards the foreland (Caspian Basin) because the Talesh thrust is a 10 My-old-structure. Although the precipitation in the study area weak to moderately correlates with our erosion dataset, it does not mean that there is not feedback of rainfall on the landscape and erosion patterns. It has been shown that runoff variability plays a major role in controlling erosion (e.g., DiBiase and Whipple, 2011; Forte et al., 2022). Moreover, in the eastern flank of the Talesh Mts. there is a strong vegetation cover compared to the western drier flank. This pronounced vegetation protects soil and reduces the erosional efficiency (e.g., Torres Acosta et al., 2015). In general, we suggest that in the Talesh Mts. there are indications of feedback among several mechanisms. The erosion rates are set by tectonics and the efficiency of surface processes/runoff variability, which is driven by climate, control the orogenic architecture (i.e., orogen expansion vs fixed deformation front). This together with lithology regulate the shape of topography in the region.

3.7.Conclusion

A new dataset of 11 catchment-averaged denudation rates is presented for the northwestern sectors of the Iranian Plateau using cosmogenic meteoric ^{10}Be contents measured in river-borne sediments. The erosion rates on the plateau exterior are approximately two times higher than in the interior of the plateau. Catchment-averaged erosion rates ranged from ~ 100 to 400 m/Myr and strongly correlate with topographic metrics (k_{sn} , slope, relief) and moderately with the precipitation rate. Thus, climate does not seem to exert a dominant role on controlling the erosion rates. These rates are comparable to long-term exhumation rates (averaged over 30 Ma and 4 to 20 Ma for the plateau interior and exterior, respectively) derived from apatite U-Th/He cooling ages, although on the plateau interior, our ^{10}Be rates indicated that a recent acceleration in erosion must have occurred. Thus, for the last several million years, the difference in erosion rates across the plateau and consequently the divide has persisted. The difference in erosion rates across the drainage divide has generated a southwest-west migration of the divide towards the plateau interior as also confirmed by contrasting values of the χ metric. Furthermore, our analysis shows that the landscape has experienced a late Cenozoic topographic rejuvenation as documented by the transient stream networks. The spatial distribution of the gradient and k_{sn} index marks a low-relief, high-standing landscape upstream of the major non-lithological knickpoints and a steep portion in the downstream area. This highly dissected topography represents the eastern wet flank of the Talesh Mts. and presents higher erosion rates than the lower-relief landscape of the plateau interior (i.e., the Ardebil Basin). The reconstructed uplift history using inverse modelling of fluvial profiles indicate a progressive increase in the rock-uplift rate at ~12-10 Ma with peak values up to ~0.5 mm/yr at ~ 4 Ma. We propose that the preservation of the relict landscapes in the southern and northern sectors of the Talesh Mts. document a former uplift regime that changed around ~10 Ma when an increase in uplift rate occurred. Consequently, the steep landscape downstream of the relict landscape adjusted to the new uplift rate that increase around 6 Ma and decreased progressively from 2 Ma. In contrast, in the central sector of the range, the catchments present equilibrated river profiles with relative uplift rates obtained from the fluvial inversion covering a maximum time scale of ~5 Ma. Collectively, these observations suggest that the km-scale base-level drop of the Caspian Sea that occurred between ~ 6 and 3 Ma played a major role in reshaping the landscape and possibly triggered enhanced tectonic activity due to sedimentary unloading. Finally, the occurrence of an orographic barrier and the match between uplift (inferred from GPS and fluvial inversion) and ^{10}Be erosion rates together with the occurrence of a mountain front that has remained fixed over the last 10 Ma, suggest the occurrence of a possible feedback among topography, tectonics and surface processes/climate that was probably established sometime during the last 10 Ma. Thus, we propose feedback of several mechanisms including tectonics, surface processes driven by climate which control the orogenic architecture, together with lithological characteristics modulate the topographic evolution in the Talesh Mts.

3.8.References

Acosta, V.T., Schildgen, T.F., Clarke, B.A., Scherler, D., Bookhagen, B., Wittmann, H., von Blanckenburg, F. and Strecker, M.R., 2015. Effect of vegetation cover on millennial-scale landscape denudation rates in East Africa. Lithosphere, 7(4), pp.408-420.

Adams, B.A., Whipple, K.X., Forte, A.M., Heimsath, A.M. and Hodges, K.V., 2020. Climate controls on erosion in tectonically active landscapes. Science Advances, 6(42), p.eaaz3166.

Agard, P., Omrani, J., Jolivet, L., Whitechurch, H., Vrielynck, B., Spakman, W., Wortel, R., 2011. Zagros orogeny: a subduction-dominated process. Geol. Mag. 148, 692–725.

Allen, M.B., Vincent, S.J., Alsop, G.I., Ismail-zadeh, A. and Flecker, R., 2003. Late Cenozoic deformation in the South Caspian region: effects of a rigid basement block within a collision zone. Tectonophysics, 366(3-4), pp.223-239.

Allen, M., J. Jackson, and R. Walker (2004), Late Cenozoic re-organization of the Arabia-Eurasia collision and the comparison of short-term and long-term deformation rates, Tectonics, 23, TC2008, doi:10.1029/2003TC001530.

Allen, M. B. (2021). Arabia-Eurasia collision. Encyclopedia of Geology, 436–450. https://doi.org/10.1016/b978-0-12-409548-9.12522-9.

Ambraseys, N.N. and Melville, C.P., 2005. A history of Persian earthquakes. Cambridge university press.

Axen, G.J., Lam, P.S., Grove, M., Stockli, D.F. & Hassanzadeh, J. (2001) Exhumation of the west-central Alborz Mountains, Iran, Caspian subsidence, and collision-related tectonics. Geology, 29(559), 562. Available from: https://doi.org/10.1130/0091-7613(2001)029<0559: EOTWCA>2.0.CO;2.

Aziz Zanjani, A., Ghods, A., Sobouti, F., Bergman, E., Mortezanejad, G., Priestley, K., Madanipour, S. and Rezaeian, M., 2013. Seismicity in the western coast of the South Caspian Basin and the Talesh Mountains. Geophysical Journal International, 195(2), pp.799-814.

Ballato, P., Mulch, A., Landgraf, A., Strecker, M.R., Dalconi, M.C., Friedrich, A. and Tabatabaei, S.H., 2010. Middle to late Miocene Middle Eastern climate from stable oxygen and carbon isotope data, southern Alborz mountains, N Iran. Earth and planetary science letters, 300(1-2), pp.125-138.

Ballato, P., C. E. Uba, A. Landgraf, M. R. Strecker, M. Sudo, D. F. Stockli, A. Friedrich, and S. H. Tabatabaei (2011), Arabia-Eurasia continental collision: Insights from late Tertiary foreland-basin evolution in the Alborz Mountains, northern Iran, Geol. Soc. Am. Bull., 123, 106–131.

Ballato, P., D. F. Stockli, M. R. Ghassemi, A. Landgraf, M. R. Strecker, J. Hassanzadeh, A. Friedrich, and S. H. Tabatabaei (2013), Accommodation of transpressional strain in the Arabia-Eurasia collision zone: New constraints from (U-Th)/He thermochronology in the Alborz mountains, N Iran, Tectonics, 32, 1–18, doi:10.1029/2012TC003159.

Ballato, P., Landgraf, A., Schildgen, T. F., Stockli, D. F., Fox, M., Ghassemi, M. R., Kirby, E., & Strecker, M. R. (2015). The growth of a mountain belt forced by base-level fall: Tectonics and surface processes during the evolution of the Alborz Mountains, N Iran. Earth and Planetary Science Letters, 425, 204-218. https://doi.org/10.1016/j.epsl.2015.05.051

Ballato, P., Cifelli, F., Heidarzadeh, G., Ghassemi, M.R., Wickert, A.D., Hassanzadeh, J., Dupont-Nivet, G., Balling, P., Sudo, M., Zeilinger, G. and Schmitt, A.K., 2017. Tectono-sedimentary evolution of the northern Iranian Plateau: insights from middle–late Miocene foreland-basin deposits. Basin Research, 29(4), pp.417-446.

Beaumont, C., Fullsack, P. and Hamilton, J., 1992. Erosional control of active compressional orogens. Thrust tectonics, pp.1-18.

Berberian, M., 1983. The southern Caspian: a compressional depression floored by a trapped, modified oceanic crust. Canadian Journal of Earth Sciences, 20(2), pp.163-183.

Berberian, M. and Yeats, R.S., 1999. Patterns of historical earthquake rupture in the Iranian Plateau. Bulletin of the Seismological society of America, 89(1), pp.120-139.

Brown, E.T., Edmond, J.M., Raisbeck, G.M., Bourlès, D.L., Yiou, F. and Measures, C.I., 1992. Beryllium isotope geochemistry in tropical river basins. Geochimica et Cosmochimica Acta, 56(4), pp.1607-1624.

Christl, M., Vockenhuber, C., Kubik, P.W., Wacker, L., Lachner, J., Alfimov, V., Synal, H.A., 2013. The ETH Zurich AMS facilities: Performance parameters and reference materials. Nucl. Instrum. Methods Phys. Res. Sect. B, 294, 29–38. doi.org/10.1016/j.nimb.2012.03.004

Chu, Y., Allen, M.B., Wan, B., Chen, L., Lin, W., Talebian, M., Wu, L., Xin, G. and Feng, Z., 2021. Tectonic exhumation across the Talesh-Alborz Belt, Iran, and its implication to the Arabia-Eurasia convergence. Earth-Science Reviews, 221, p.103776.

Cifelli, F., Ballato, P., Alimohammadian, H., Sabouri, J. and Mattei, M., 2015. Tectonic magnetic lineation and oroclinal bending of the Alborz range: Implications on the Iran-Southern Caspian geodynamics. Tectonics, 34(1), pp.116-132.

Clementucci, R., Ballato, P., Siame, L.L., Faccenna, C., Yaaqoub, A., Essaifi, A., Leanni, L. and Guillou, V., 2022. Lithological control on topographic relief evolution in a slow tectonic setting (Anti-Atlas, Morocco). Earth and Planetary Science Letters, 596, p.117788.

Cyr, A.J., Granger, D.E., Olivetti, V. and Molin, P., 2010. Quantifying rock uplift rates using channel steepness and cosmogenic nuclide–determined erosion rates: Examples from northern and southern Italy. Lithosphere, 2(3), pp.188-198.

DiBiase, R.A. and Whipple, K.X., 2011. The influence of erosion thresholds and runoff variability on the relationships among topography, climate, and erosion rate. Journal of Geophysical Research: Earth Surface, 116(F4).

DiBiase, R.A., Whipple, K.X., Heimsath, A.M. and Ouimet, W.B., 2010. Landscape form and millennial erosion rates in the San Gabriel Mountains, CA. Earth and Planetary Science Letters, 289(1-2), pp.134-144.

Djamour, Y., Vernant, P., Bayer, R., Nankali, H.R., Ritz, J.F., Hinderer, J., Hatam, Y., Luck, B., Le Moigne, N., Sedighi, M. and Khorrami, F., 2010. GPS and gravity constraints on continental deformation in the Alborz mountain range, Iran. Geophysical Journal International, 183(3), pp.1287-1301.

Engdahl, E.R., Jackson, J.A., Myers, S.C., Bergman, E.A. and Priestley, K., 2006. Relocation and assessment of seismicity in the Iran region. Geophysical Journal International, 167(2), pp.761-778.

Egli, M., Brandová, D., Böhlert, R., Favilli, F. and Kubik, P.W., 2010. 10Be inventories in Alpine soils and their potential for dating land surfaces. Geomorphology, 119(1-2), pp.62-73.

Fick, S.E. and Hijmans, R.J., 2017. WorldClim 2: new 1-km spatial resolution climate surfaces for global land areas. International journal of climatology, 37(12), pp.4302-4315.

Field, C.V., Schmidt, G.A., Koch, D. and Salyk, C., 2006. Modeling production and climate-related impacts on 10Be concentration in ice cores. Journal of Geophysical Research: Atmospheres, 111(D15).

Flint, J.J., 1974. Stream gradient as a function of order, magnitude, and discharge. Water Resources Research, 10(5), pp.969-973.

Forte, A.M. and Cowgill, E., 2013. Late Cenozoic base-level variations of the Caspian Sea: a review of its history and proposed driving mechanisms. Palaeogeography, Palaeoclimatology, Palaeoecology, 386, pp.392-407.

Forte, A.M., Whipple, K.X., 2018. Criteria and tools for determining drainage divide stability. Earth Planet. Sci. Lett. 493, 102–117. https://doi.org/10.1016/j.epsl.2018.04.026.

Forte, A.M. and Whipple, K.X., 2019. The topographic analysis kit (TAK) for TopoToolbox. Earth Surface Dynamics, 7(1), pp.87-95.

Forte, A.M., Leonard, J.S., Rossi, M.W., Whipple, K.X., Heimsath, A.M., Sukhishvili, L., Godoladze, T. and Kadirov, F., 2022. Low variability runoff inhibits coupling of climate, tectonics, and topography in the Greater Caucasus. Earth and Planetary Science Letters, 584, p.117525.

Gallen, S.F., 2018. Lithologic controls on landscape dynamics and aquatic species evolution in post-orogenic mountains. Earth and Planetary Science Letters, 493, pp.150-160.

Goren, L., Fox, M. and Willett, S.D., 2014. Tectonics from fluvial topography using formal linear inversion: Theory and applications to the Inyo Mountains, California. Journal of Geophysical Research: Earth Surface, 119(8), pp.1651-1681.

Graly, J.A., Reusser, L.J. and Bierman, P.R., 2011. Short and long-term delivery rates of meteoric 10Be to terrestrial soils. Earth and Planetary Science Letters, 302(3-4), pp.329-336.

Granger, D.E. and Schaller, M., 2014. Cosmogenic nuclides and erosion at the watershed scale. Elements, 10(5), pp.369-373.

Hack, J. T., 1957. Studies of longitudinal stream profiles in Virginia and Maryland (Vol. 294). US Government Printing Office.

Harkins, N., Kirby, E., Heimsath, A., Robinson, R. and Reiser, U., 2007. Transient fluvial incision in the headwaters of the Yellow River, northeastern Tibet, China. Journal of Geophysical Research: Earth Surface, 112(F3).

Heikkilä, U., Beer, J. and Alfimov, V., 2008. Beryllium-10 and beryllium-7 in precipitation in Dübendorf (440 m) and at Jungfraujoch (3580 m), Switzerland (1998–2005). Journal of Geophysical Research: Atmospheres, 113(D11).

Heikkilä, U., 2007. Modeling of the atmospheric transport of the cosmogenic radionuclides 10Be and 7Be using the ECHAM5-HAM General Circulation Model.

Hessami, K., Jamali, F. and Tabassi, H., 2003. Map of major active faults of Iran. Ministry of Science, Research and Tecnology, International Institute of Earthquake Engineering and Seismology (IIEES), Tehran, Iran.

Horiuchi, K., Minoura, K., Kobayashi, K., Nakamura, T., Hatori, S., Matsuzaki, H. and Kawai, T., 1999. Last-Glacial to Post-Glacial 10Be fluctuations in a sediment core from the Academician Ridge, Lake Baikal. Geophysical research letters, 26(8), pp.1047-1050.

Jackson, J., Priestley, K., Allen, M. and Berberian, M., 2002. Active tectonics of the south Caspian basin. Geophysical Journal International, 148(2), pp.214-245.

Jungers, M.C., Bierman, P.R., Matmon, A., Nichols, K., Larsen, J. and Finkel, R., 2009. Tracing hillslope sediment production and transport with in situ and meteoric 10Be. Journal of Geophysical Research: Earth Surface, 114(F4).

Kaveh-Firouz, A., Burg, J.P., Haghipour, N., Mandal, S.K., Christl, M. and Mohammadi, A., 2023. Tectonics, base-level fluctuations, and climate impact on the Eocene to Present-day erosional pattern of the Arabia-Eurasia collision zone (NNW Iranian Plateau and west Alborz Mountains). Tectonics, p.e2022TC007684.

Kirby, E. and Whipple, K., 2001. Quantifying differential rock-uplift rates via stream profile analysis. Geology, 29(5), pp.415-418.

Kirby, E., Whipple, K.X., Tang, W. and Chen, Z., 2003. Distribution of active rock uplift along the eastern margin of the Tibetan Plateau: Inferences from bedrock channel longitudinal profiles. Journal of Geophysical Research: Solid Earth, 108(B4).

Kirby, E., & Whipple, K. X. (2012). Expression of active tectonics in erosional landscapes. Journal of Structural Geology, 44, 54-75. https://doi.org/10.1016/j.jsg.2012.07.009.

Koshnaw, R.I., Stockli, D.F. and Schlunegger, F., 2019. Timing of the Arabia-Eurasia continental collision—Evidence from detrital zircon U-Pb geochronology of the Red Bed Series strata of the northwest Zagros hinterland, Kurdistan region of Iraq. Geology, 47(1), pp.47-50.

Koshnaw, R.I., Stockli, D.F., Horton, B.K., Teixell, A., Barber, D.E. and Kendall, J.J., 2020. Late Miocene deformation kinematics along the NW Zagros fold-thrust belt, Kurdistan region of Iraq: Constraints from apatite (U-Th)/He thermochronometry and balanced cross sections. Tectonics, 39(12), p.e2019TC005865.

Lague, D. and Davy, P., 2003. Constraints on the long-term colluvial erosion law by analyzing slope-area relationships at various tectonic uplift rates in the Siwaliks Hills (Nepal). Journal of Geophysical Research: Solid Earth, 108(B2).

Lague, D., 2014. The stream power river incision model: evidence, theory and beyond. Earth Surface Processes and Landforms, 39(1), pp.38-61.

Lanari, R., Boutoux, A., Faccenna, C., Herman, F., Willett, S.D. and Ballato, P., 2023. Cenozoic exhumation in the Mediterranean and the Middle East. Earth-Science Reviews, p.104328.

Leonard, J.S. and Whipple, K.X., 2021. Influence of spatial rainfall gradients on river longitudinal profiles and the topographic expression of spatially and temporally variable climates in mountain landscapes. Journal of Geophysical Research: Earth Surface, 126(12), p.e2021JF006183.

Leonard, J.S., Whipple, K.X. and Heimsath, A.M., 2023. Isolating climatic, tectonic, and lithologic controls on mountain landscape evolution. Science Advances, 9(3), p.eadd8915.

Madanipour, S., Ehlers, T.A., Yassaghi, A., Rezaeian, M., Enkelmann, E. and Bahroudi, A., 2013. Synchronous deformation on orogenic plateau margins: Insights from the Arabia–Eurasia collision. Tectonophysics, 608, pp.440-451.

Madanipour, S., Ehlers, T.A., Yassaghi, A. and Enkelmann, E., 2017. Accelerated middle Miocene exhumation of the Talesh Mountains constrained by U-Th/He thermochronometry: Evidence for the Arabia-Eurasia collision in the NW Iranian Plateau. Tectonics, 36(8), pp.1538-1561.

Madanipour, S., Yassaghi, A., Ehlers, T.A. and Enkelmann, E., 2018. Tectonostratigraphy, structural geometry and kinematics of the NW Iranian Plateau margin: Insights from the Talesh Mountains, Iran. American Journal of Science, 318(2), pp.208-245.

Madanipour, 2023. Late Miocene-early Pliocene tectonic to erosional exhumation in the northwest of the Arabia-Eurasia collision zone. Earth Surface Processes and Landforms. https://doi.org/10.1002/esp.5583.

Marshall, J.A., Roering, J.J., Gavin, D.G. and Granger, D.E., 2017. Late Quaternary climatic controls on erosion rates and geomorphic processes in western Oregon, USA. GSA Bulletin, 129(5-6), pp.715-731.

Mattei, M., Cifelli, F., Alimohammadian, H., Rashid, H., Winkler, A. and Sagnotti, L., 2017. Oroclinal bending in the Alborz Mountains (Northern Iran): New constraints on the age of South Caspian subduction and extrusion tectonics. Gondwana Research, 42, pp.13-28.

Maxeiner, S., Synal, H.A., Christl, M., Suter, M., Müller, A., Vockenhuber, C., 2019. Proof-of-principle of a compact 300 kV multi-isotope AMS facility. Nucl. Instrum. Methods Phys. Res. Sect. B, 439, 84-89. doi.org/10.1016/j.nimb.2018.11.028

McQuarrie, N., and D. J. J. van Hinsbergen (2013), Retrodeforming the Arabia-Eurasia collision zone: Age of collision versus magnitude of continental subduction, Geology, 41, 315–318, doi:10.1130/G33591.1.

Miller, S.R., Sak, P.B., Kirby, E. and Bierman, P.R., 2011, December. Bumps in the long road to flat. In AGU Fall Meeting Abstracts (Vol. 2011, pp. EP41D-0653).

Molnar, P., Anderson, R.S. and Anderson, S.P., 2007. Tectonics, fracturing of rock, and erosion. Journal of Geophysical Research: Earth Surface, 112(F3).

Molin, P., Sembroni, A., Ballato, P. and Faccenna, C., 2023. The uplift of an early stage collisional plateau unraveled by fluvial network analysis and river longitudinal profile inversion: The case of the Eastern Anatolian Plateau. Tectonics, 42(8), p.e2022TC007737.

Moumeni, M., Delchiaro, M., Della Seta, M., Nozaem, R., Ballato, P., Leonard, J.S., Clementucci, R. and Rouhi, J., 2023. Interplay between tectonics and surface processes in the evolution of mountain ranges: Insights from landscape dynamics, uplift, and active deformation of Talesh Mountains (NW Iranian Plateau margin). Geomorphology, p.109029.

Mouthereau, F., O. Lacombe, and J. Vergés (2012), Building the Zagros collisional orogen: Timing, strain distribution and the dynamics of Arabia/Eurasia plate convergence, Tectonophysics, 532–535, 27–60, doi:10.1016/j.tecto.2012.01.022.

Nadirov, R.S., Bagirov, E., Tagiyev, M. and Lerche, I., 1997. Flexural plate subsidence, sedimentation rates, and structural development of the super-deep South Caspian Basin. Marine and Petroleum Geology, 14(4), pp.383-400.

Olivetti, V., Godard, V., Bellier, O. and Aster Team, 2016. Cenozoic rejuvenation events of Massif Central topography (France): Insights from cosmogenic denudation rates and river profiles. Earth and Planetary Science Letters, 444, pp.179-191.

Ouimet, W.B., Whipple, K.X. and Granger, D.E., 2009. Beyond threshold hillslopes: Channel adjustment to base-level fall in tectonically active mountain ranges. Geology, 37(7), pp.579-582.

Padilla, S., López-Gutiérrez, J.M., Sampath, D.M.R., Boski, T., Nieto, J.M. and García-León, M., 2018. Determination of denudation rates by the measurement of meteoric 10Be in Guadiana river sediment samples (Spain) by low-energy AMS. Journal of Environmental Radioactivity, 189, pp.227-235.

Paknia, M., Ballato, P., Heidarzadeh, G., Cifelli, F., Hassanzadeh, J., Vezzoli, G., Mirzaie Ataabadi, M., Ghassemi, M.R. and Mattei, M., 2021. Neogene tectono-stratigraphic evolution of the intermontane Tarom basin: Insights into basin filling and plateau building processes along the northern margin of the Iranian Plateau (Arabia-Eurasia collision zone). Tectonics, 40(3), p.e2020TC006254.

Pavich, M.J., Brown, L., Harden, J., Klein, J. and Middleton, R., 1986. 10Be distribution in soils from Merced River terraces, California. Geochimica et Cosmochimica Acta, 50(8), pp.1727-1735.

Pazzaglia, F.J. and Fisher, J.A., 2022. A reconstruction of Apennine uplift history and the development of transverse drainages from longitudinal profile inversion.

Peifer, D., Persano, C., Hurst, M.D., Bishop, P. and Fabel, D., 2021. Growing topography due to contrasting rock types in a tectonically dead landscape. Earth Surface Dynamics, 9(2), pp.167-181.

Perron, J. T., & Royden, L. (2013). An integral approach to bedrock river profile analysis. Earth Surface Processes and Landforms, 38(6), 570-576. https://doi.org/10.1002/esp.3302.

Popov, S.V., Antipov, M.P., Zastrozhnov, A.S., Kurina, E.E. and Pinchuk, T.N., 2010. Sea-level fluctuations on the northern shelf of the Eastern Paratethys in the Oligocene-Neogene. Stratigraphy and Geological Correlation, 18, pp.200-224.

Portenga, E.W., Bierman, P.R., 2011. Understanding Earth's eroding surface with 10Be. GSA Today 21 (8), 4–10. http://dx.doi.org/10.1130/G111A.1.

Priestley, K., Baker, C. and Jackson, J., 1994. Implications of earthquake focal mechanism data for the active tectonics of the South Caspian Basin and surrounding regions. Geophysical Journal International, 118(1), pp.111-141.

Racano, S., Schildgen, T., Ballato, P., Yıldırım, C. and Wittmann, H., 2023. Rock-uplift history of the Central Pontides from river-profile inversions and implications for development of the North Anatolian Fault. Earth and Planetary Science Letters, 616, p.118231.

Roberts, G.G., Paul, J.D., White, N. and Winterbourne, J., 2012. Temporal and spatial evolution of dynamic support from river profiles: A framework for Madagascar. Geochemistry, Geophysics, Geosystems, 13(4).

Roe, G. H. (2005). Orographic precipitation. Annual Review of Earth and Planetary Sciences, 33(1), 645–671. https://doi.org/10.1146/annurev. earth.33.092203.122541.

Safran, E.B., Bierman, P.R., Aalto, R., Dunne, T., Whipple, K.X. and Caffee, M., 2005. Erosion rates driven by channel network incision in the Bolivian Andes. Earth Surface Processes and Landforms: The Journal of the British Geomorphological Research Group, 30(8), pp.1007-1024.

Schwanghart, W., & Scherler, D. (2014). TopoToolbox 2–MATLAB-based software for topographic analysis and modeling in Earth surface sciences. Earth Surface Dynamics, 2(1), 1-7. https://doi.org/10.5194/esurf-2-1-2014.

Snyder, N.P., Whipple, K.X., Tucker, G.E. and Merritts, D.J., 2000. Landscape response to tectonic forcing: Digital elevation model analysis of stream profiles in the Mendocino triple junction region, northern California. Geological Society of America Bulletin, 112(8), pp.1250-1263.

Stock, J.D. and Montgomery, D.R., 1999. Geologic constraints on bedrock river incision using the stream power law. Journal of Geophysical Research: Solid Earth, 104(B3), pp.4983-4993.

Turowski, J.M., Pruß, G., Voigtländer, A., Ludwig, A., Landgraf, A., Kober, F. and Bonnelye, A., 2023. Geotechnical controls on erodibility in fluvial impact erosion. EGUsphere, 2023, pp.1-31.

Van Baak, C.G., Vasiliev, I., Stoica, M., Kuiper, K.F., Forte, A.M., Aliyeva, E. and Krijgsman, W., 2013. A magnetostratigraphic time frame for Plio-Pleistocene transgressions in the South Caspian Basin, Azerbaijan. Global and planetary change, 103, pp.119-134.

Vernant, P., Nilforoushan, F., Chery, J., Bayer, R., Djamour, Y., Masson, F., Nankali, H., Ritz, J.F., Sedighi, M. and Tavakoli, F., 2004. Deciphering oblique shortening of central Alborz in Iran using geodetic data. Earth and planetary science letters, 223(1-2), pp.177-185.

Vincent, S. J., M. B. Allen, A. D. Ismail-Zadeh, R. Flecker, K. A. Foland, and M. D. Simmons (2005), Insights from the Talysh of Azerbaijan into the Paleogene evolution of the South Caspian region, GSA Bull., 117(11/12), 1513–1533.

Von Blanckenburg, F., 2006. The control mechanisms of erosion and weathering at basin scale from cosmogenic nuclides in river sediment. Earth and Planetary Science Letters, 242(3-4), pp.224-239.

Wang, Y., Willett, S.D., Wu, D., Haghipour, N. and Christl, M., 2021. Retreat of the great escarpment of Madagascar from geomorphic analysis and cosmogenic 10Be concentrations. Geochemistry, Geophysics, Geosystems, 22(12), p.e2021GC009979.

Whipple, K.X. and Tucker, G.E., 1999. Dynamics of the stream-power river incision model: Implications for height limits of mountain ranges, landscape response timescales, and research needs. Journal of Geophysical Research: Solid Earth, 104(B8), pp.17661-17674.

Whipple, K.X., 2004. Bedrock rivers and the geomorphology of active orogens. Annu. Rev. Earth Planet. Sci., 32, pp.151-185.

Whipple, K.X., DiBiase, R.A. and Crosby, B.T., 2013. Bedrock rivers. Treatise on geomorphology (Vol. 9, pp. 550–573).

Whipple, K. X., DiBiase, R. A., Ouimet, W. B., & Forte, A. M. (2017). Preservation or piracy: Diagnosing low-relief, high-elevation surface formation mechanisms. Geology, 45(1), 91-94. https://doi.org/10.1130/G38490.1

Whittaker, A.C., 2012. How do landscapes record tectonics and climate?. Lithosphere, 4(2), pp.160-164.

Willenbring, J.K. and von Blanckenburg, F., 2010. Meteoric cosmogenic Beryllium-10 adsorbed to river sediment and soil: Applications for Earth-surface dynamics. Earth-Science Reviews, 98(1-2), pp.105-122.

Wobus, C.W., Hodges, K.V. and Whipple, K.X., 2003. Has focused denudation sustained active thrusting at the Himalayan topographic front?. Geology, 31(10), pp.861-864.

Yanina, T.A., 2012. Correlation of the Late Pleistocene paleogeographical events of the Caspian Sea and Russian Plain. Quaternary International, 271, pp.120-129.

Chapter 4

General conclusion

In this PhD research, I provide first-order constrains to understand the topographic evolution of the Talesh Mts. in the NW margin of Iranian Plateau which are a prominent tectonic range and show characteristics of a transient landscape resulting from a combination of several factors. For this, I analyzed the river network in the scale of drainage divide and catchments, which translate tectonics, lithology, climate, and base level fall signals throughout the landscape. For this purpose, I devised a workflow (Fig. 4.1) which enables us to analyze and interpret the potential impact of the combined effects of variable erodibility, rock strength, orographic rainfall and recent tectonic events and phases of uplift rates in the landscape evolution of mountain ranges.

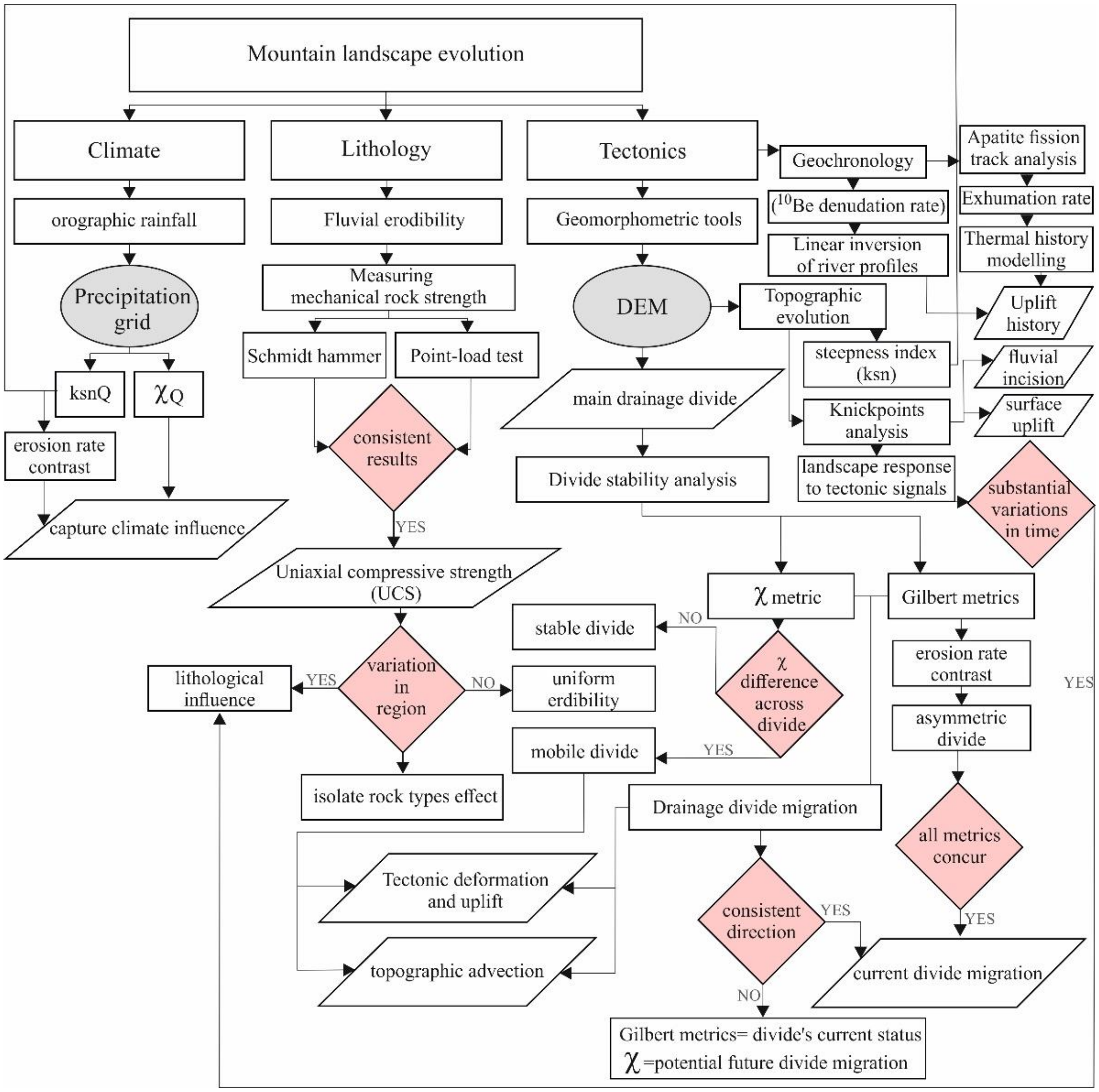

Figure 4.1. Workflow for studying the topographic evolution of an orogenic system by isolating the contributions of tectonics, climate and lithology on present day topography of a landscape

Consequently, I integrated a quantitative analysis of geomorphic data and 10Be cosmogenic meteoric denudation rates to unravel the surface deformation, uplift mechanisms and river network evolution. In the scale of drainage divide, the main divide of the Talesh Mts. range in its whole segment is responding to a contrasting erosion rate across orogen. The efficiency of erosion is primarily determined by the precipitation and the strength of exposed rocks. We can infer that divide is unstable in the study area in response to the asymmetric uplift and spatial variability of erodibility. Therefore, the divide instability in the NW of Iranian plateau is chiefly controlled by topography, especially slope and local topographic relief. While the precipitation rate has potentially been assisting, and magnifying the divide mobility, reorganization of river networks and landscape transience. Our findings represent that climate does not exert a first order and strong control on topographic growth and erosional efficiency in the study area.

The main divide continues to migrate toward the interior of the plateau. This movement will continue until these segments reach a steady-state, or uplift/erosion rate becomes uniform again. Accordingly, the results show the presence of a localized uplift gradient along the divide that is holding the divide in place in the northern and southern parts. The χ metric is sensitive to this uplift rate gradient and representing the expected response of the divide when the uplift is evenly distributed. Furthermore, the Talesh Mts. which is undergoing active deformation indicates transient landscapes in the north and southern sectors which present an uplifted relict landscape. The divide in these sectors appears to be stable because the landscape across the divide is similar and has low topographic relief. On the other hand, the topography can also be significantly influenced by advection, which has caused the asymmetric topography of the central sector due to erosion of weaker lithology. Thus, contrasting exhumation of strong bedrock units in the northern and southern sectors, and weak bedrock units in the central sector have suppressed and intensified erosion, respectively, and this heterogeneous exhumation of rocks initiated topographic reconfiguration mostly in the central Talesh Mts. In addition to the mechanisms of the horizontal motion of rocks, the role of uplift of the mountains in middle Miocene, and Pliocene cannot be ruled out of mechanisms responsible for divide mobility. In the scale of catchments, this study presents a new dataset of 11 catchment-averaged denudation rates derived from cosmogenic meteoric ^{10}Be concentrations measured in river-borne sediments along two sides of the main drainage divide (plateau interior and exterior). The erosion rates in the plateau exterior are approximately two times higher than in the interior of the plateau. Catchment-averaged erosion rates ranging from ~ 100 to 400 m/Myr correlate strongly with topographic metrics (k_{sn} , slope, relief) and moderately with precipitation rate. These rates are relatively comparable to long-term exhumation rates (averaged over 30 Ma and 4 to 20 Ma for the plateau interior and exterior, respectively) derived from apatite U-Th/He cooling ages, although in the plateau interior, ^{10}Be rates indicates that an acceleration in erosion must have occurred.

Thus, for the last several million years, the difference in erosion rates across the plateau and consequently the divide has persisted. The difference in erosion rates across the drainage divide generate southwest-west migration of the divide towards the plateau interior which is confirmed by contrasting values of the χ metric. Additionally, the inverse correlation of denudation rates with compressive strength of rocks indicates that lithology does not play a significant and regional role in divide mobility. Nevertheless, our results suggest that the difference in the erodibility of rocks can produce a transient landscape on a local scale.

Furthermore, our analysis shows that the landscape in the region has experienced late-Cenozoic rejuvenation which is documented by the transient stream networks. The spatial distribution of gradient and steepness index marks a low-relief, high-standing landscape upstream of the major knickpoints from the incised steep parts in the downstream, which shows the occurrence of phase/s of topographic rejuvenation in the study area. Furthermore, the highest sediment yields, and erosion observed in the eastern wet flank of the Talesh Mts. where channel network is steep and highly incised. The reconstructed uplift history with inverse modelling indicates a progressive increase in the rock-uplift rate at ~12 Ma which reached its peak at ~ 4 Ma up to ~0.5 mm/yr. We propose that the relict landscapes in southern and northern sectors document the uplift rate changes ~10 Ma. Since such an incision wave is at lower elevation this landscape cannot record the acceleration at 5 to 3 Ma. In contrast, in the central sector with a ~ 5 Ma time scale of uplift rates, the incision wave went through the catchments and a new state of equilibrium has been reached. This corresponds well to the Caspian Sea base level drop. Considering that the base level oscillates through time the inverted uplift rates mostly reflect tectonic uplift. Only the acceleration in uplift rates at 6 to 5 Ma should be caused by the base level drop. This process affected the landscape surface by accelerating the bedrock river incision. Consequently, we propose feedback of several mechanisms including tectonics, surface processes driven by climate which control the orogenic architecture, together with lithological characteristics modulate the topographic evolution in the Talesh Mts.

Generally, in this study, I explored the relationship between erosion patterns and topographic features on landscape evolution by analyzing river network and quantifying the timing and magnitudes of rock uplift rates with geochronology methods. The approach proposed in this study provides an innovative workflow to study mountainous landscapes and investigate their evolution patterns by considering all the effects of potential factors which can be diverse from one landscape to another.

Supplementary Chapter 5

5.1. Introduction

One of the fundamental objectives of tectonic geomorphology is to comprehend the mechanisms that regulate the topographic expression of dynamic mountain belts. Fluvial terrace deposits and landforms can reveal crucial details about river incision and vertical tectonic deformation in this setting. They can also be used to analyze how tectonic, climatic, and sea-level changes interact (e.g., Wegmann and Pazzaglia, 2002, 2009; Gallen et al., 2015; Ramírez-Herrera et al., 2021). In mountainous regions, strath terraces which form due to river incision and record rivers downcutting to their modern position, can be used to derive histories of landscapes evolution and to quantify river incision and rock uplift rates (e.g., Burbank and Anderson, 2011; Pazzaglia, 2013; Zondervan et al., 2020a, 2022). For determining spatiotemporal differences in long-term uplift rates and resolving crustal fault activity, strath terrace incision rates are frequently used.

Thus, fluvial strath terraces in the NW of Iranian Plateau were used as markers for rock uplift and deformation by using stimulated luminescence (OSL) dating techniques (e.g., Aitken, 1998; Rhodes, 2011; Rittenour, 2018) which has made it possible to establish the chronology of terraces by dating fluvial sediments atop terrace straths (Fuller et al., 2009; Fu et al., 2019). Consequently, the fluvial bedrock incision rates can be calculated by using depositional ages of aggraded sediments along the main river of the Ardebil Basin (Fig. S5.1). Thus, to understand the 10^3–10^4-year timescale of tectonic evolution, we combined geological field evidence, chronologically constrained geomorphic markers, and morphometric analysis of the study area.

This study's main goal is to evaluate the Ardebil Basin's Holocene vertical deformation rates. In addition, we will measure long-term tectonic uplift rates in this area to constrain the uplift history. In addition to morphometric analysis of a river basin, we mapped and dated river terraces along the main river (Fig. S5.2). Incision rates are calculated using strath heights and related OSL ages as a proxy for uplift rates.

5.2. Geology and geomorphological setting

The Ardebil Basin in the northwest of Iranian Plateau is considered a sedimentary basin which is bounded by some of the most important tectonic features of NW of Iran such as Talesh Mountains to the northeast and east, Masuleh-Dagh Fault (MD) to the east, and Sabalan volcano to the west (Fig. S5.1). The basement of the basin is composed of Eocene andesite and Miocene marl and sandstone which are also exposed in the southeast and center of the basin (Fig. S5.1). In the most parts of the basin, these units are overlain by Pliocene tuff, marl, conglomerate, sandstone freshwater limestone, and Quaternary tuff, volcanic ashes, and plain deposits. Most of the area of the basin is covered by silt and clay. The Qarasu River (ESE- WNW) in the Ardebil Basin which is the largest in the region originates in Talesh Mountains, flows along the NW of Iranian Plateau and cut through the Ardebil Basin at an average about 1400 m above sea level and finally overflows into the Caspian Sea (Fig. S5.1).

The Balikhalichay and Bosjin Rivers in the central and eastern margin of the Ardebil Basin with a NE-SW strike flow towards northeast and joint the Qarasu River. Along the banks of the Balikhalichay river, there were no evidence of alluvial terraces. The river cuts deep into the Neogene bedrocks, and it seems that due to the high velocity of incision there was no time for the alluvial terraces to be deposited.

On the other hand, in the eastern margin of the basin, a series of strath terraces have been developed along the banks of the Bosjin river (Fig. S5.2). Identifying fluvial terraces in the study area is challenging on google earth images, topographic maps and even in the fieldwork. Therefore, the only way to identify terrace remnants was to look for fluvial sediments exposed in natural outcrops or road-cuttings in the field.

Based on the elevation of the strath surface of bedrock, in total three generations of terraces, T1- T3 with their respective height above the active river channel have been identified (T1: the lowest and youngest terrace; and T3 the subsequent higher strath) (Fig. S5.2). These terraces are located over the lacustrine deposits and have a bedrock strath surface in clay, and siltstones.

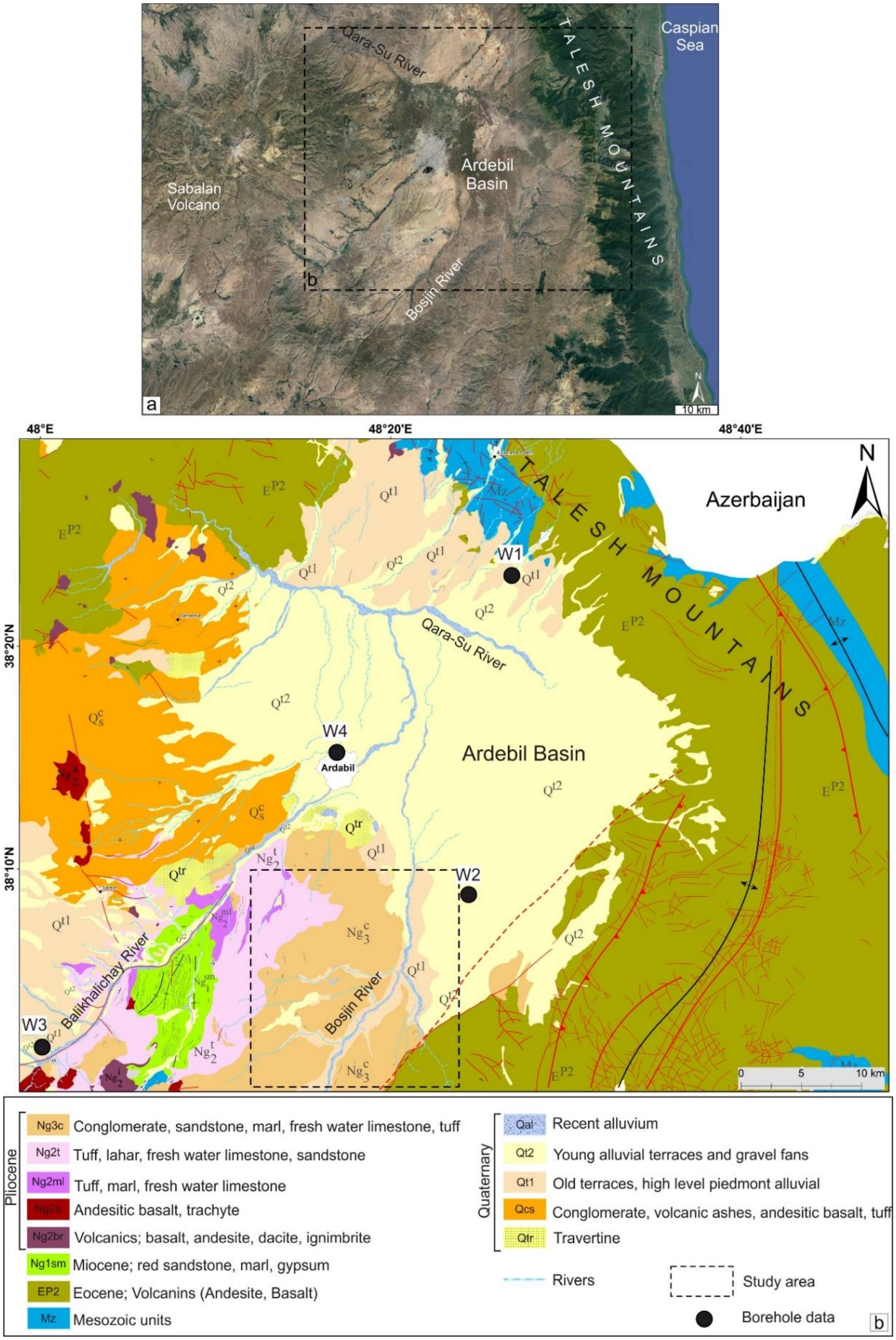

Figure S5.1. Location of the study area. (a) Ardebil Basin in NW of Iranian Plateau. (b) Geological map of the Ardebil Basin and surrounding areas. The study area is shown with black dashed rectangle.

The OSL ages of the samples from sand lenses within the gravel layers are considered to be very close to the formation ages of the terraces (e.g., Yan et al., 2021).

The sedimentary characteristics of strath deposits were mapped and recorded. Generally, the fluvial sediments included alternate layers of cross-bedded fine to medium sized sand and silt and with pebble conglomerate (gravel to cobble size clasts). The pebbles are moderately rounded which may show significant fluvial transport. The lacustrine deposits comprised of clay, silt and fine sand.

5.3. Methods

5.3.1. Terrace mapping and fieldwork

To avoid the complications of terraces with the same elevations but different formation ages, the river profile analyzed to check if their formations are controlled by knickpoint migration (e.g., Yan et al., 2021; Guo et al., 2012). The fieldwork has been conducted along the banks of the Bosjin river. Remote mapping of the terraces was done first using DEM and Google Earth images. The flat surfaces with their relative elevation from the river course have been extracted (Fig. S5.2; Fig. S5.3). We chose 3 sites (S1-S3) to study the lacustrine and alluvial deposits (Fig. S5.2).

In general, after cleaning the section face, four samples were collected systematically by horizontally hammering 3.5-cm diameter and 30-cm long stainless-steel tubes. We named the terraces using increasing numbers for increasing age (and height above the active channel), such that T1 is our youngest and lowest strath terrace. The details of the samples are presented in Fig. S5.2. To prevent further exposure to light and moisture loss, the tubes are wrapped with aluminum foils and adhesive tape.

The OSL ages of these samples will be utilized to construct an age-depth model for the terrace deposits.

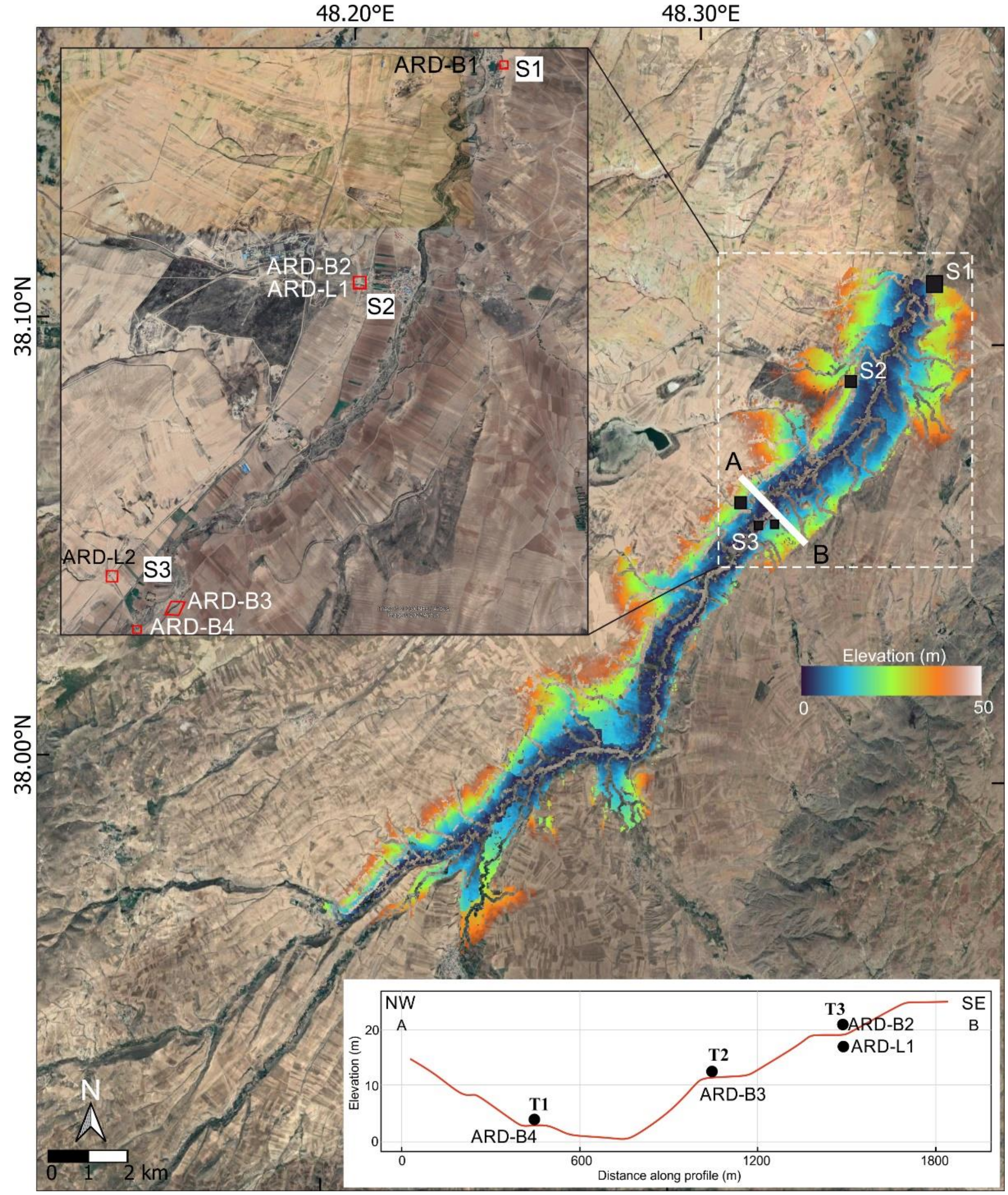

Figure S5.2. Google map of the study area with projection of flat surfaces. The studied stations in the Ardebil Basin along the Bosjin river are presented. The inset (lower right) show the profile view of the different levels of flat surfaces and the sampled points.

5.3.2. Topographic Position Index

Topographic position index (TPI) is a scale-dependent phenomenon. It can extract different types of features and delineate landforms more accurately. This index compares the elevation of each cell in a DEM to the mean elevation of a specified neighborhood around that cell (Weiss, 2001). Positive values of TPI show locations that are higher than the average of their surroundings, as determined by the neighborhood (ridges). On the other hand, negative values of this index indicate locations that are lower than their surroundings (valleys) (Weiss, 2001). Values which are near zero, are either flat areas (slope~0) or areas of constant slope where the slope of the point is significantly greater than zero. Based on Weiss (2001), this index can be defined as following:

$$tpi < scalefactor \geq int\Big(\big(dem - focalmean(dem, annulus, irad, orad)\big) + 0.5\Big) \quad (1)$$

where, *scalefactor* is the outer radius in map units, *irad* and *orad* is inner and outer radius of annulus in cells respectively.

Since the identified geomorphic markers are flat surfaces associated with fluvial terraces, these surfaces can be extracted (Fig. S5.3) by the above equation. We performed the *TPI* calculations using the '*roughness'* function in *TopoToolBox* (Schwanghart and Scherler, 2014).

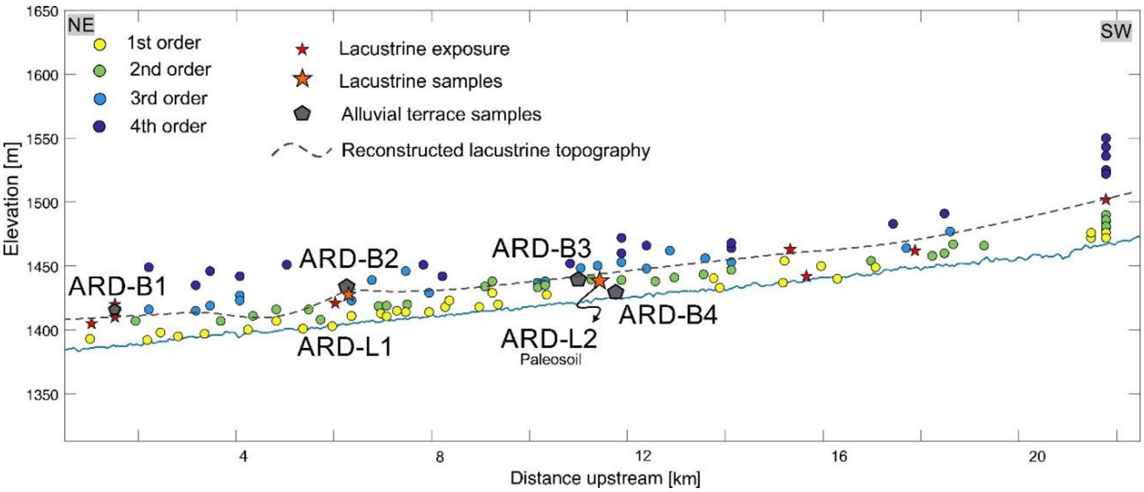

Figure S5.3. Projection of the flat surfaces (4 orders) along the Bosjin river longitudinal profile with the location of the sampling points

5.4. Results

5.4.1. Field evidence of geomorphic markers

In site S1, we observed a generation of alluvial terrace juxtaposed to the lacustrine deposit. In this boundary a vertical fault with a dip of 83° towards southeast and a NW-SE strike detected (Fig. S5.4). Furthermore, lacustrine deposits show a slight tilting about 12° toward ESE.

Figure S5.4. Field evidence from Site S1 along the Bosjin river. A near vertical fault has been documented that cuts the lacustrine and alluvial deposit.

Moving toward upstream the Bosjin river in site S2, a generation of alluvial terrace overlays the lacustrine deposit (red clay and silt with fine sand). The boundary between these deposits is an erosional surface (Fig. S5.5), so the lacustrine sample was taken about 1m below this surface. Additionally, also in this site the lacustrine deposit shows about 14° of tilting toward SE.

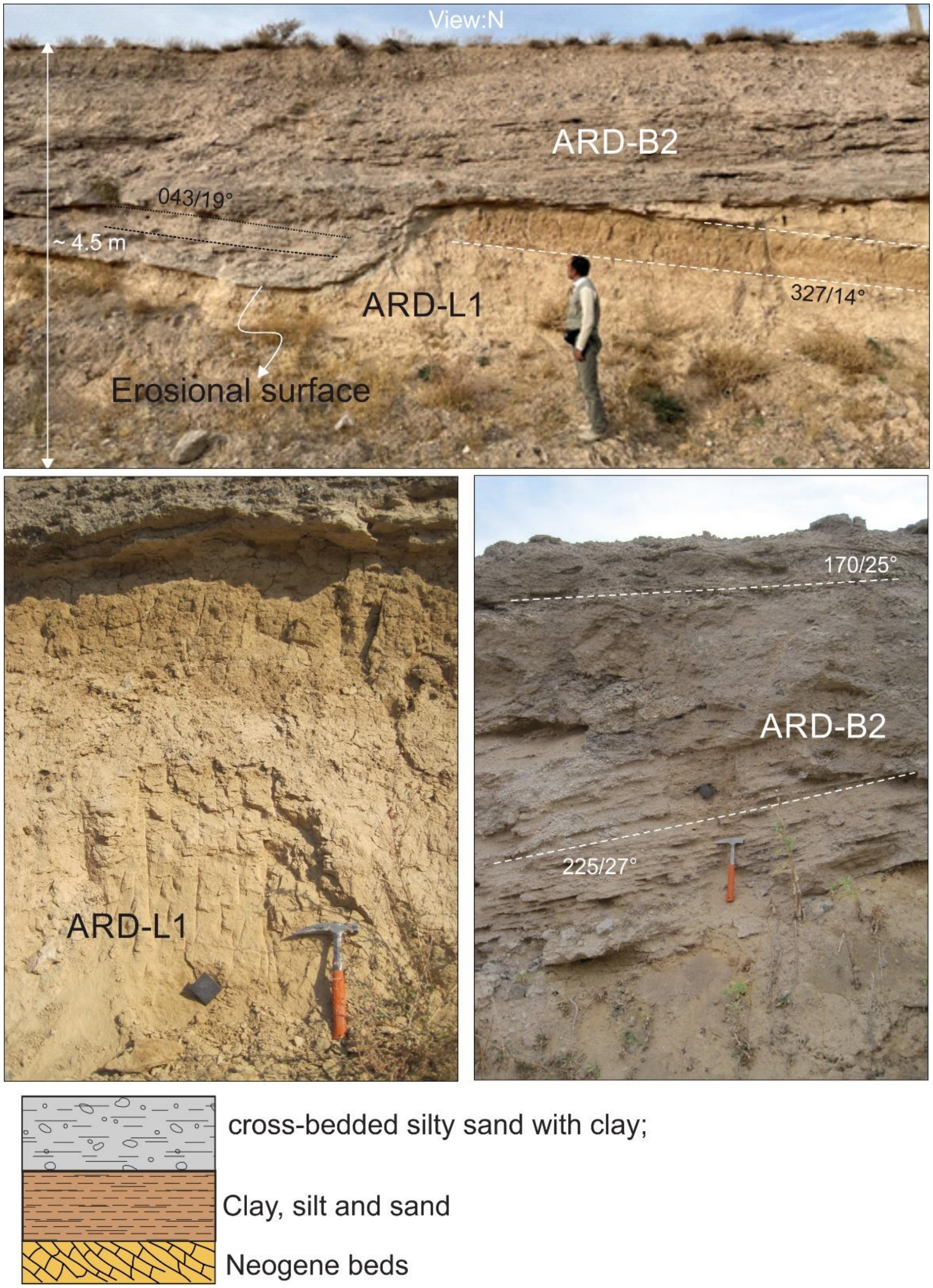

Figure S5.5. Geomorphic markers dated with OSL method in Site S2. The sedimentological structure, stratigraphy column of the outcrop with the sampling point presented.

In this section, in addition to the lacustrine, we also took a sample from alluvial terrace in this site (Fig. S5.5). In site S3, we did the field survey in three stations (Fig. S5.6; Fig. S5.7). In one of the stations, the alluvial terrace has been observed which overlies the lacustrine deposit. In terms of sedimentology, this terrace comprises fine-grain sand with poorly sorted gravel and cobble clasts (Fig. S5.6). Moreover, we detected a fracture with ESE-WNW strike with a dip of 53° toward south (Fig. S5.6).

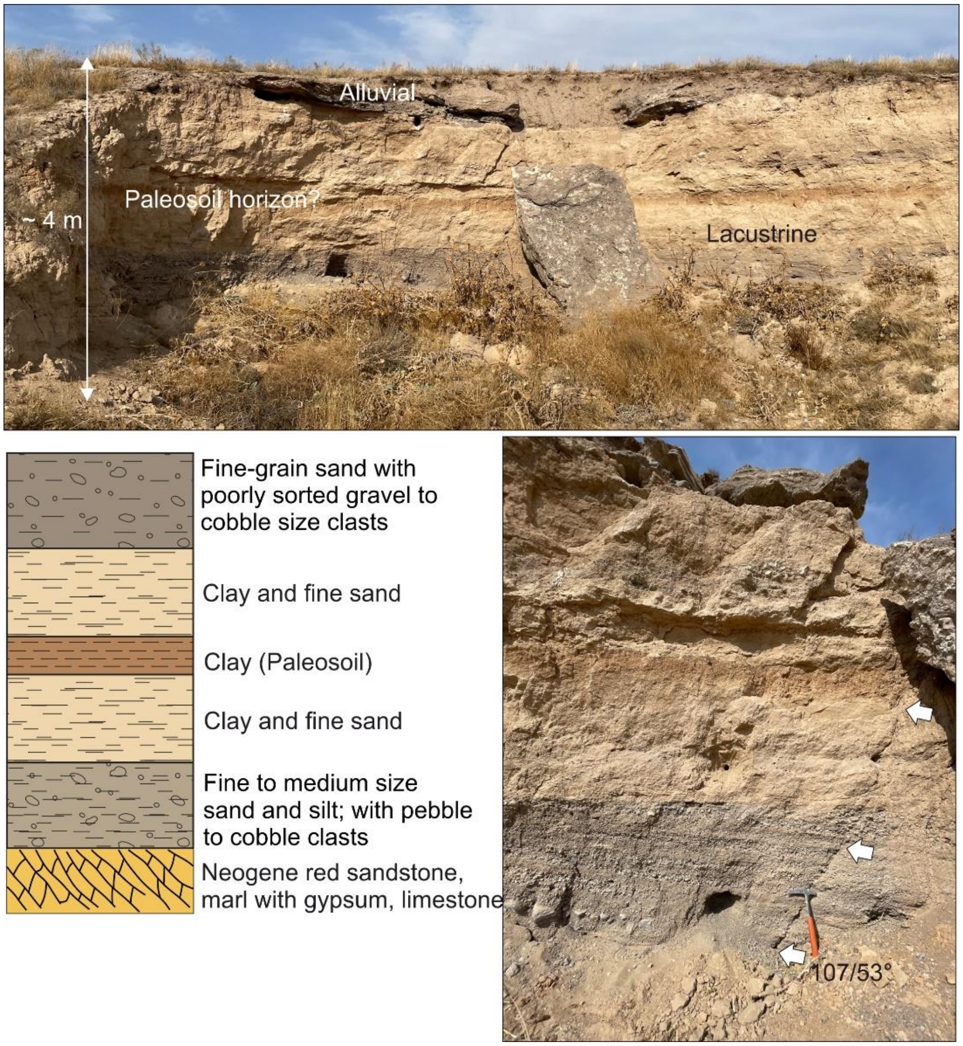

Figure S5.6. Field evidence of Site S3 (lacustrine, alluvial deposit) with stratigraphy column.

In the middle of section, a brown layer (clay) which can be a paleosoil horizon exposed. In the other two stations, adjacent to the previous one, two other generations of alluvial terraces have been detected (Fig. S5.7).

Two samples were taken from these terraces (ARD-B3, ARD-B4). These terraces are composed of fine to medium size cross-bedded sand and silt with clay with gravel to cobble sized clasts (Fig. S5.7).

Figure S5.7. Field photo of the geomorphic markers in Site 3 dated with OSL method.

Moreover, based on all these observations, and since we do not have the absolute OSL ages of the lacustrine and strath terraces deposits yet, we present the hypothesized profile of the lacustrine and alluvial terrace of the Bosjin river (Fig. S5.8).

Finally, we used four boreholes data in different parts of the Ardebil Basin, we devised a stratigraphic column of the near-surface deposits of the Ardebil Basin with a maximum depth of 50 m. The data show that almost below the 30 m from the surface, there is clay deposit which likely is part of the lacustrine deposit which we documented its surface exposure in the filed survey (well no.2; Fig. S5.9)

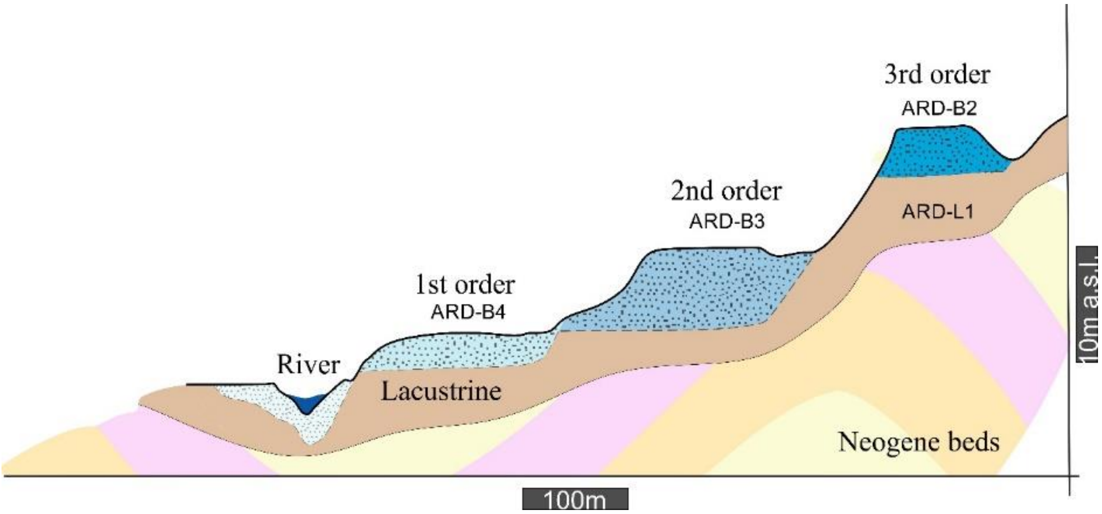

Figure S5.8. Profile sketch of the lacustrine and alluvial terrace of the Bosjin river in the Ardebil Basin.

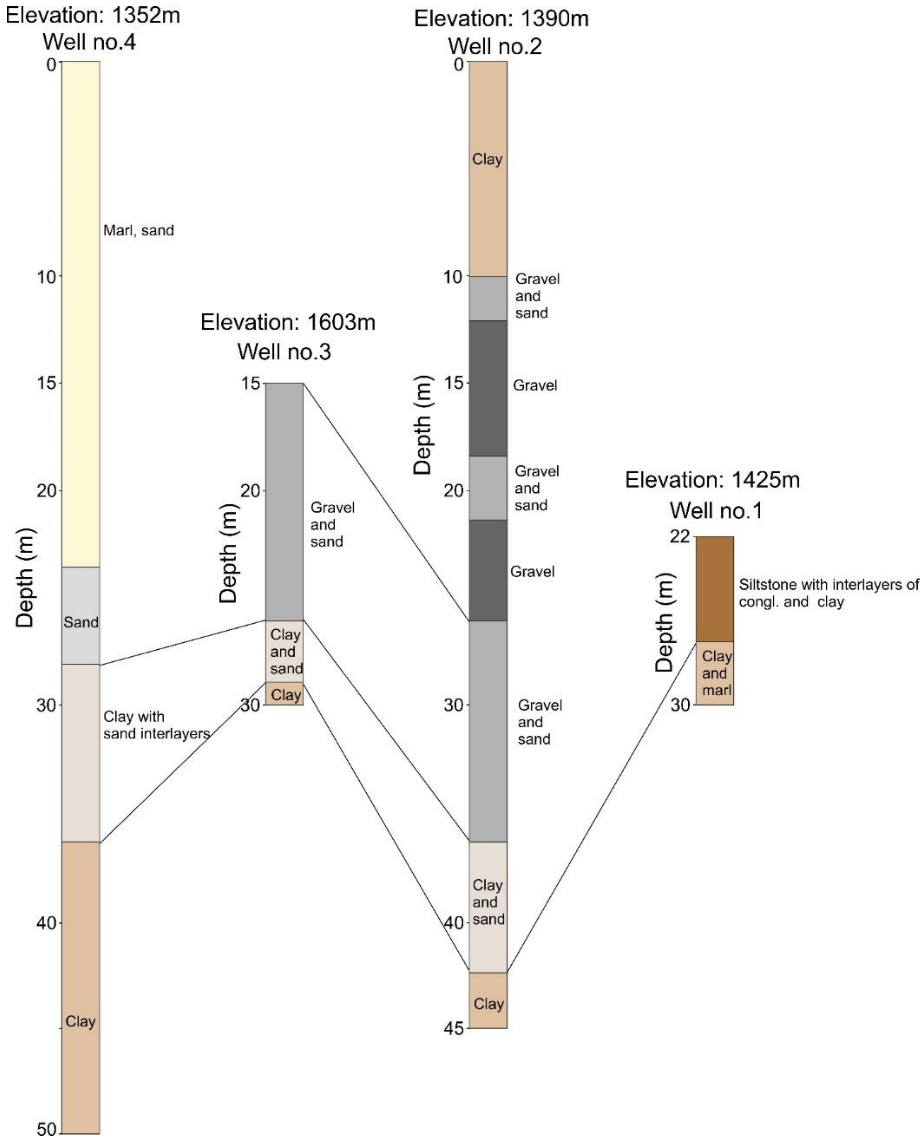

Figure S5.9. Stratigraphic column from four borehole data in the northeast (well no.1), southwest (well no.3), southeast (well no.2) and central (well no.4) of the Ardebil Basin.

5.5. References Supplementary Chapter 5.

Aitken, M.J., 1998. Introduction to optical dating: the dating of Quaternary sediments by the use of photon-stimulated luminescence. Clarendon Press.

Burbank, D.W. and Anderson, R.S., 2011. Rates of erosion and uplift. Tectonic Geomorphology. John Wiley & Sons, Ltd, pp.195-242.

Fu, X., Cohen, T.J. and Fryirs, K., 2019. Single-grain OSL dating of fluvial terraces in the upper Hunter catchment, southeastern Australia. Quaternary Geochronology, 49, pp.115-122.

Fuller, T.K., Perg, L.A., Willenbring, J.K. and Lepper, K., 2009. Field evidence for climate-driven changes in sediment supply leading to strath terrace formation. Geology, 37(5), pp.467-470.

Gallen, S.F., Pazzaglia, F.J., Wegmann, K.W., Pederson, J.L. and Gardner, T.W., 2015. The dynamic reference frame of rivers and apparent transience in incision rates. Geology, 43(7), pp.623-626.

Guo YJ, Zhang JF, Qiu WL, Hu G, Zhuang MG and Zhou LP, 2012. Luminescence dating of the Yellow River terraces in the Hukou area, China. Quaternary Geochronology 10: 129–135, DOI 10.1016/j.quageo.2012.03.002.

Pazzaglia, F.J., 2013. Fluvial terraces. In: Shroder, J.F. (Ed.), Treatise on Geomorphology. Academic Press, pp. 379–412.

Ramírez-Herrera, M.T., Gaidzik, K. and Forman, S.L., 2021. Spatial Variations of Tectonic Uplift-Subducting Plate Effects on the Guerrero Forearc, Mexico. Frontiers in Earth Science, 8, p.573081.

Rhodes, E.J., 2011. Optically stimulated luminescence dating of sediments over the past 200,000 years. Annual Review of Earth and Planetary Sciences, 39, pp.461-488.

Rittenour, T.M., 2018. Dates and rates of earth-surface processes revealed using luminescence dating. Elements: An International Magazine of Mineralogy, Geochemistry, and Petrology, 14(1), pp.21-26.

Schwanghart, W., & Scherler, D. (2014). TopoToolbox 2–MATLAB-based software for topographic analysis and modeling in Earth surface sciences. Earth Surface Dynamics, 2(1), 1-7. https://doi.org/10.5194/esurf-2-1-2014.

Wegmann, K.W. and Pazzaglia, F.J., 2002. Holocene strath terraces, climate change, and active tectonics: The Clearwater River basin, Olympic Peninsula, Washington State. Geological Society of America Bulletin, 114(6), pp.731-744.

Wegmann, K.W. and Pazzaglia, F.J., 2009. Late Quaternary fluvial terraces of the Romagna and Marche Apennines, Italy: Climatic, lithologic, and tectonic controls on terrace genesis in an active orogen. Quaternary Science Reviews, 28(1-2), pp.137-165.

Weiss A.D. (2001). Topographic position and landforms analysis. In: ESRI User Conference, San Diego, CA

Yan, Y.Y., Zhang, J.F., Hu, G. and Zhou, L.P., 2021. Luminescence chronology of the Yellow River terraces in the Heiyukou area, China, and its implication for the uplift rate of the Ordos Plateau. Geochronometria, 48(1), pp.325-338.

Zondervan, J.R., Whittaker, A.C., Bell, R.E., Watkins, S.E., Brooke, S.A. and Hann, M.G., 2020a. New constraints on bedrock erodibility and landscape response times upstream of an active fault. Geomorphology, 351, p.106937.

Zondervan, J.R., Stokes, M., Telfer, M.W., Boulton, S.J., Mather, A.E., Buylaert, J.P., Jain, M., Murray, A.S. and Belfoul, M.A., 2022. Constraining a model of punctuated river incision for Quaternary strath terrace formation. Geomorphology, 414, p.108396.

Appendix Chapter 2.

Concavity index

Finding the precise *mn*-ratio which is also termed as θ or concavity index is required for analysing of river profiles based on the stream-power model (SPL). Concavity index is correlated with the uplift rate, and shows concavity degree of the channel, that is defined by *m* (area index) and *n* (gradient index):

$$\theta = {}^{m}/_{n} \tag{1}$$

In active orogens, rivers represent higher values of θ (varies between 0.35 and 0.60), while the lower values of this index are related to the river profiles which is in equilibrium or steady state (e.g. Kirby & Whipple, 2001; Snyder et al., 2000). River profiles which are in a dynamic equilibrium between uplift and incision are concave upward. The concavity derives from the SPL which states that along-river gradients S are proportional to upslope area A exponentiated by the negative *mn*-ratio:

$$S \sim A^{-{}^{m}/_{n}} \tag{2}$$

Although in many studies this is considered as a standard value of 0.45, for different study areas this value may differ. Furthermore, some indices such as steepness (k_{sn}), chi (χ) and extraction of knickpoints are extremely prone to the *mn*-ratio changes (Gailleton et al., 2021), therefore, concavity index should be calculated accurately. In order to find an acceptable value of the *mn*-ratio, *mnoptim* function of *TopoToolbox* which uses Bayesian Optimization with cross-validation was used. Bayesian Optimization finds a minimum of a scalar-valued function in a bounded domain (Schwanghart and Scherler, 2014). The *mnoptim* function uses χ analysis to linearize long-river profiles (Perron and Royden, 2013). With several drainage networks or river catchments, it picks a random subset of these networks to fit a *mn*-ratio and after that tests it with another set of drainage basins (Schwanghart and Scherler, 2014). In that case, it can be assessed that how well a *mn*-ratio derived in one catchment can be applied to another. Because the study area consists of several small and large drainage basins, it is more precise to use *mnoptim* function which finds an optimal value in a subset of the basins and tests it with the remaining catchments by using cross-validation. The result of applying Bayesian Optimization in the study area is shown in Fig. S2.2

Divide asymmetry index (DAI)

In order to quantify the morphologic asymmetry of a divide, the across-divide difference in hillslope relief which normalized by the across-divide sum in hillslope relief is applied, which its absolute value is called divide asymmetry index (Scherler and Schwanghart, 2020). This index is expressed as:

$$DAI = \left|\frac{\Delta HR}{\sum HR}\right| \tag{3}$$

Where, ΔHR is the across-divide difference in hillslope relief, and $\sum HR$ is the across-divide sum in hillslope relief. Therefore, this index is solely based on hillslope relief (*HR*) values, and ranges between 0 and 1 for highly symmetric and asymmetric divides, respectively.

The predicted migration direction of the Ardebil Basin main divide is derived from the orientation of the divide segments and their mean *DAI* magnitude (Fig. S2.5). In addition, we distinguished drainage divide segments in the study area are asymmetric by using across-divide difference in hillslope relief (Fig. S2.5). Some segments of the divide which are very close to the rivers in elevation are quite asymmetric (Fig. S2.5). Divides with anomalously low hillslope relief are close to rivers, and asymmetric in shape, which can be interpreted to be mobile and depicting beheaded valleys or future capture events (Scherler and Schwanghart, 2020).

In Fig. S2.5, the profile view of the divide network shows the minimum height of the drainage divide edges above the adjacent rivers by divide distance which is colored by the *DAI*. In the profile, deviations occur at ~ 40–45, ~ 60, ~ 70-75, and ~ 110-120 km divide distance and are typically associated with asymmetric divides. Highly asymmetric divides are furthermore found at low divide distances (< 20 km). Therefore, it can be concluded that most of the anomalous divides determined based on hillslope relief, flow distance, and divide asymmetry (Scherler and Schwanghart, 2020) are unstable and migrating with time. Based on the obtained results, the divide migration in the central part, from higher to lower relief, would result in area loss for the Ardebil Basin.

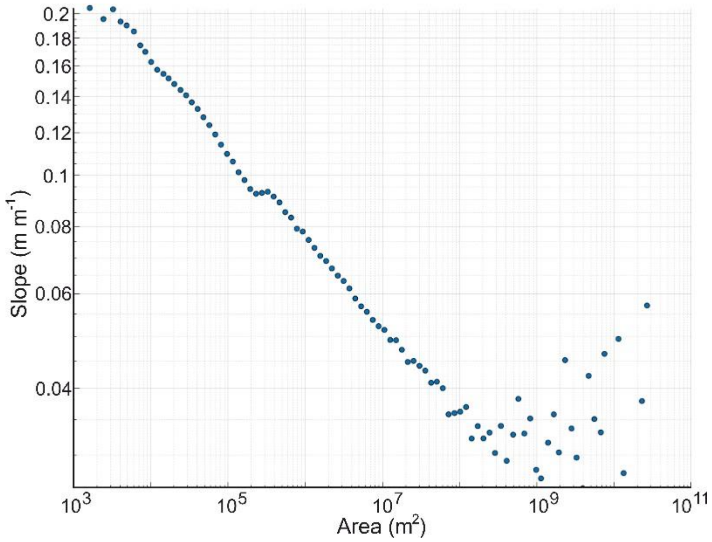

Figure S2.1. Slope-area plot of the study area for threshold determination of rivers. By using Vergari et al. (2019) procedure, the flow accumulation threshold for the fluvial domain was calculated in the study area. Thus, the drainage network with a threshold of 1 km^2 has been defined.

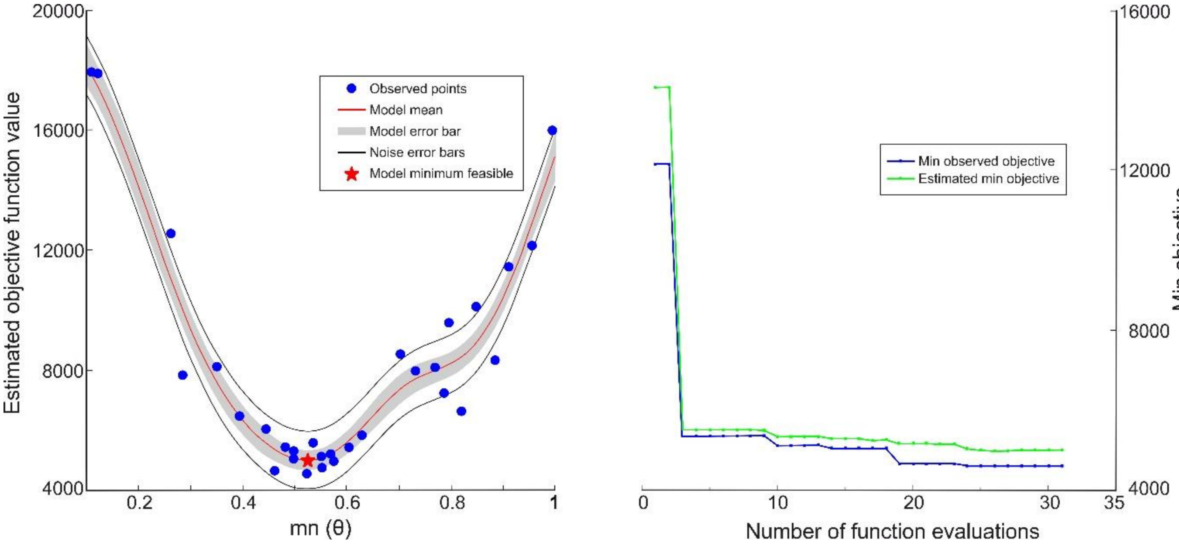

Figure S2.2. Objective function model, and the results of Bayesian optimization of *mn*-ratio for the study area

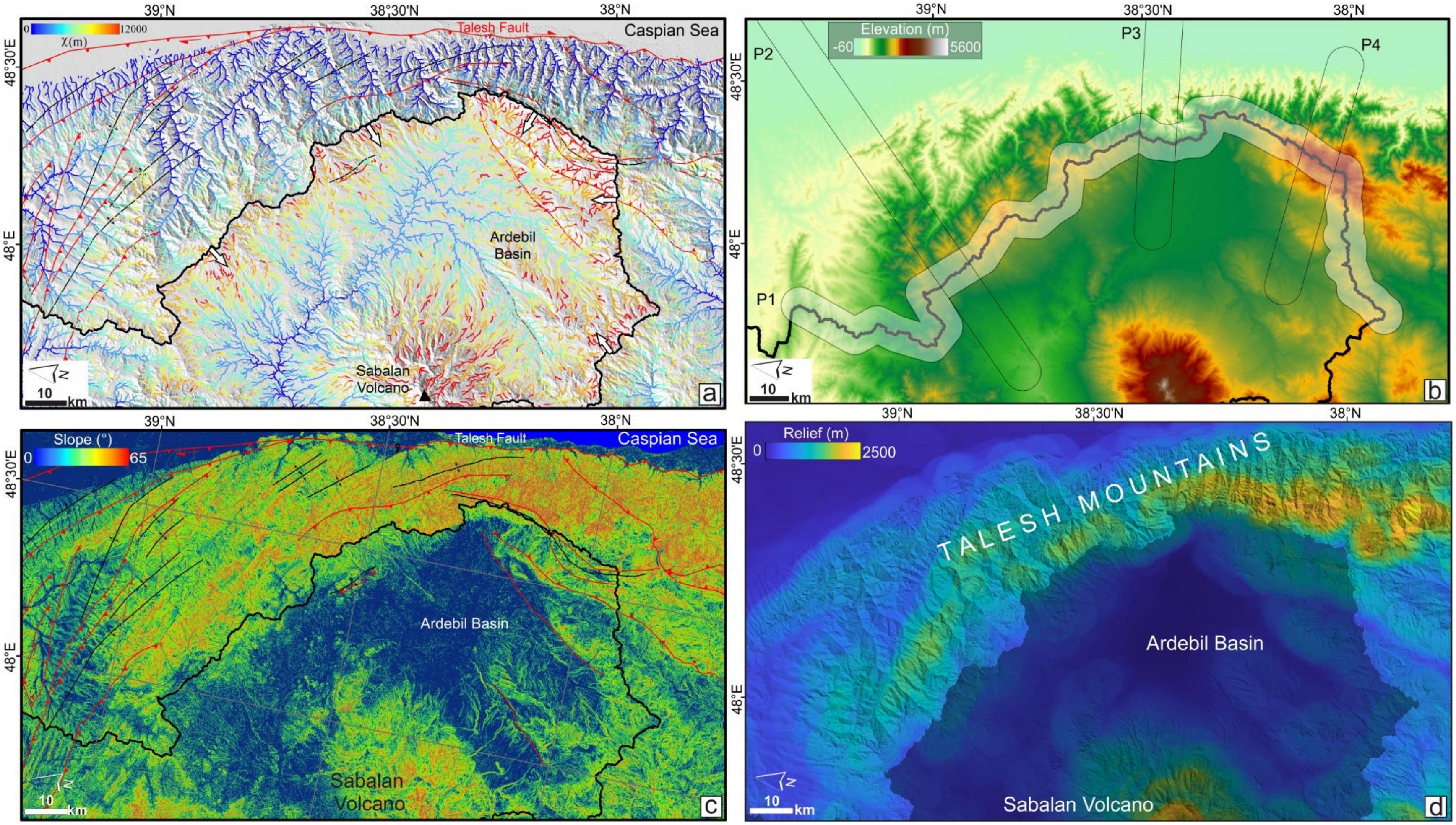

Figure S2.3. Result maps of the divide stability analysis. The thick black line represents the main drainage divide position. (a) The χ map across the Ardebil Basin's main divide with the main faults and folds. Divide migration direction is shown by white arrows. The map illustrates strong contrasts between the χ values of the channel heads on the two sides of the divide (high χ on the interior of the plateau, towards Ardebil Basin and low χ on the eastern side of the Talesh Mountains, towards Caspian Sea. (b – d) Gilbert metric maps (elevation, mean gradient, and local relief with 5*5km window, respectively). P1 to P4 illustrate the locations of 20-km-wide swath profiles of topography in the study area.

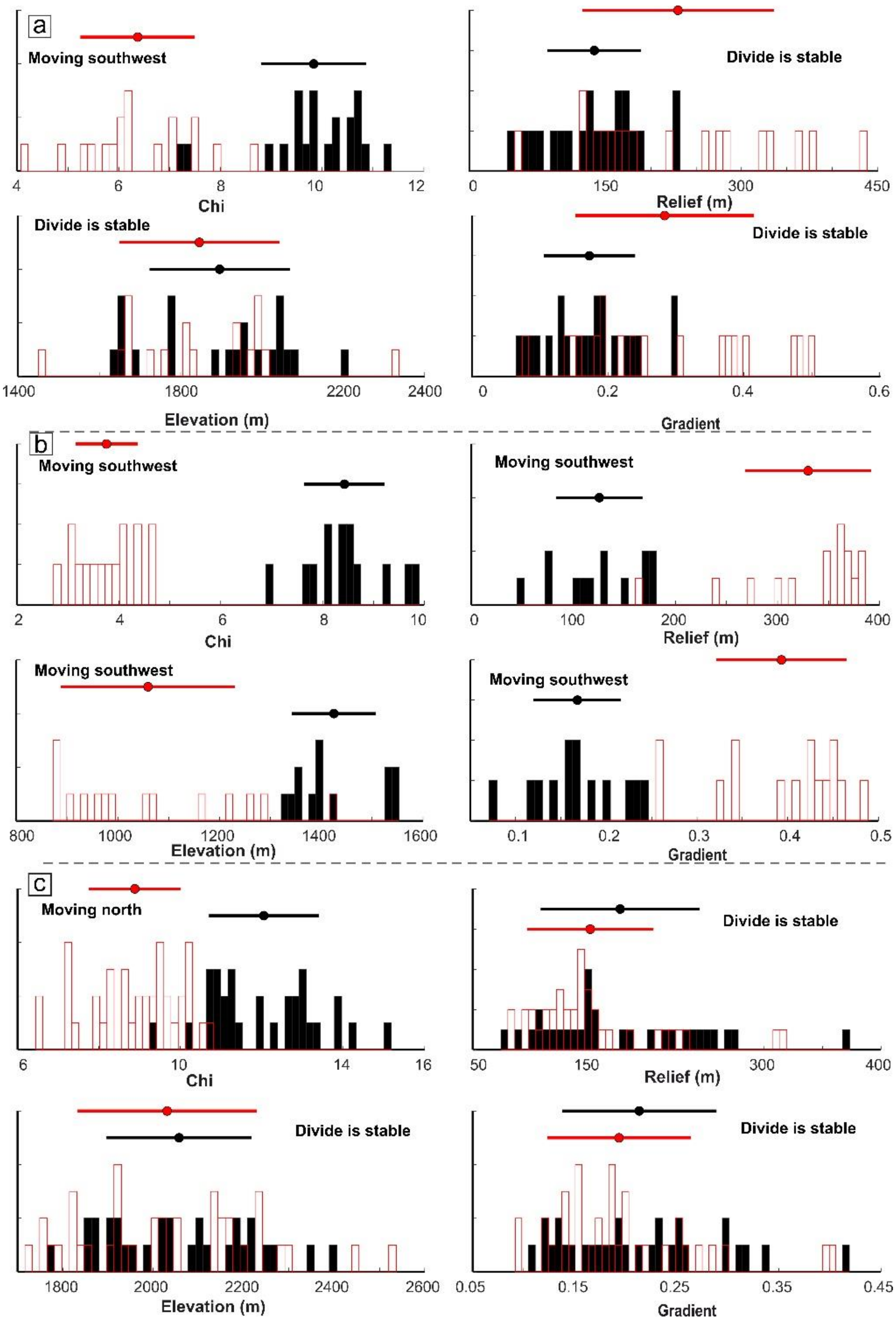

Figure S2.4. Divide stability histograms by applying the precipitation grid as a weight to the flow accumulation. (a), (b), (c) Three samples histograms of divide metric for the ARD3, ARD6, and ARD14 segments, which are representative histograms of the north, central, and southern sectors of the Ardebil Basin main drainage divide. Histograms with black rectangles exhibit watersheds in the interior of the plateau, and histograms with red fillings show watersheds on the exterior of the plateau (wet flank of the Talesh Mountains towards Caspian Sea).

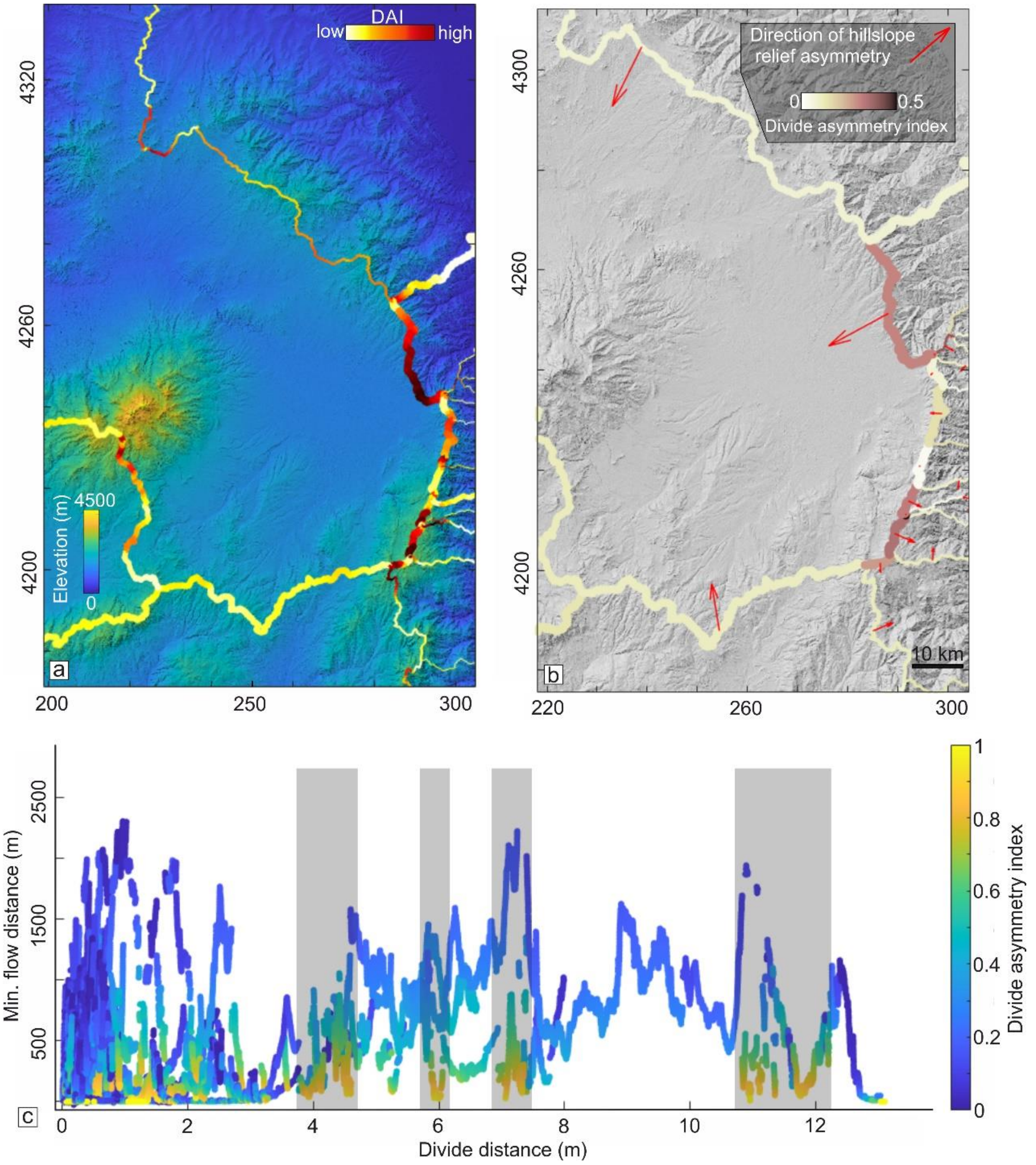

Figure S2.5. The results of the drainage divide asymmetry analysis. (a) Color-coded divide of the Ardebil Basin with magnitude of the asymmetry. (b) Drainage divide asymmetry and direction of lower hillslope relief. Divide network overlaid on the hillshade image. Divides are colored by the divide asymmetry index (*DAI*). Arrows on the divide segments show the direction of the asymmetry. The length of the arrows corresponds to the average *DAI*. (c) Profile view along the divide network of the Ardebil Basin. Colors represent *DAI*, and gray-shaded areas are indicative of regions with low hillslope relief and flow distance.

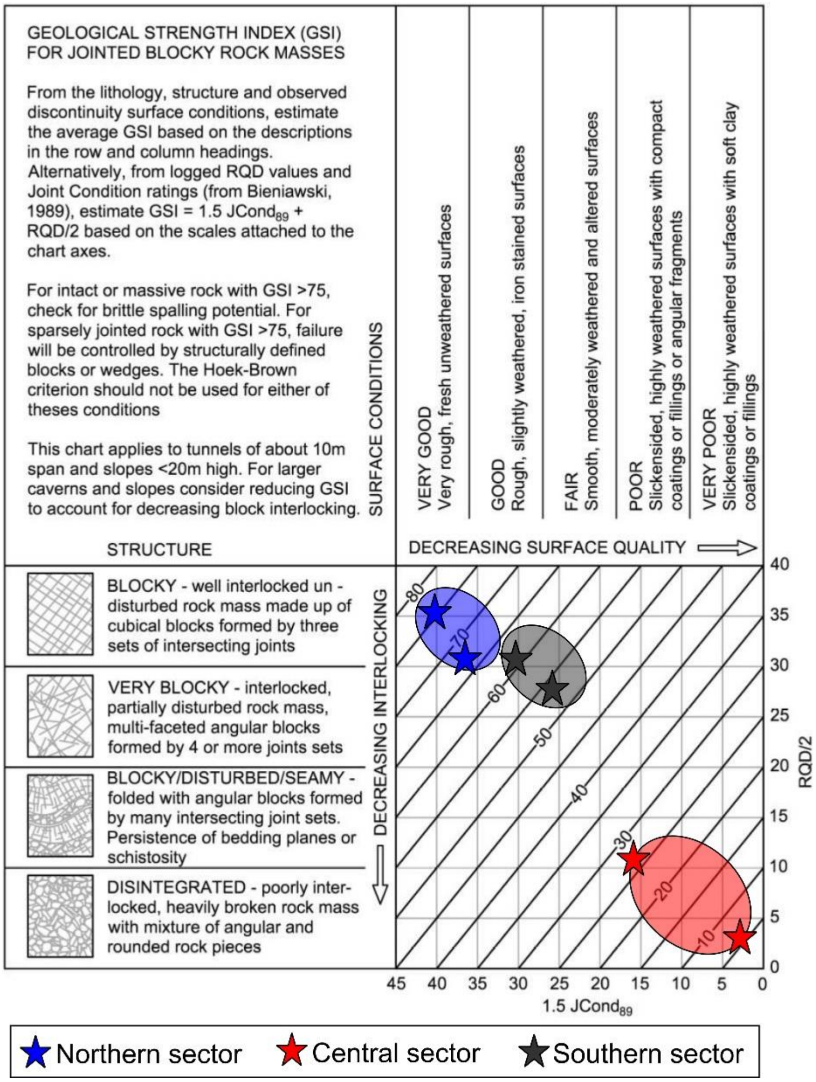

Figure S2.6. Chart for determining the geological strength index (GSI) of jointed rock mass by Hoek et al. (2013) in the Talesh Mts. Blue, red, and black star represent the UCS site measurements and point-load test sample locations in the northern, central, and southern sector, respectively. The GSI index range for the northern, and southern sectors are 65- 70 and 55- 65 respectively, while for the central sector is between 5-30.

Figure S2.7. Field photos of the major knickpoints in the northern sector of the Talesh Mountains taken from Google Maps Photos (source: http://earth.google.com).

Figure S2.8. Field photos of the major knickpoints in the central sector of the Talesh Mountains taken from Google Maps Photos (source: http://earth.google.com).

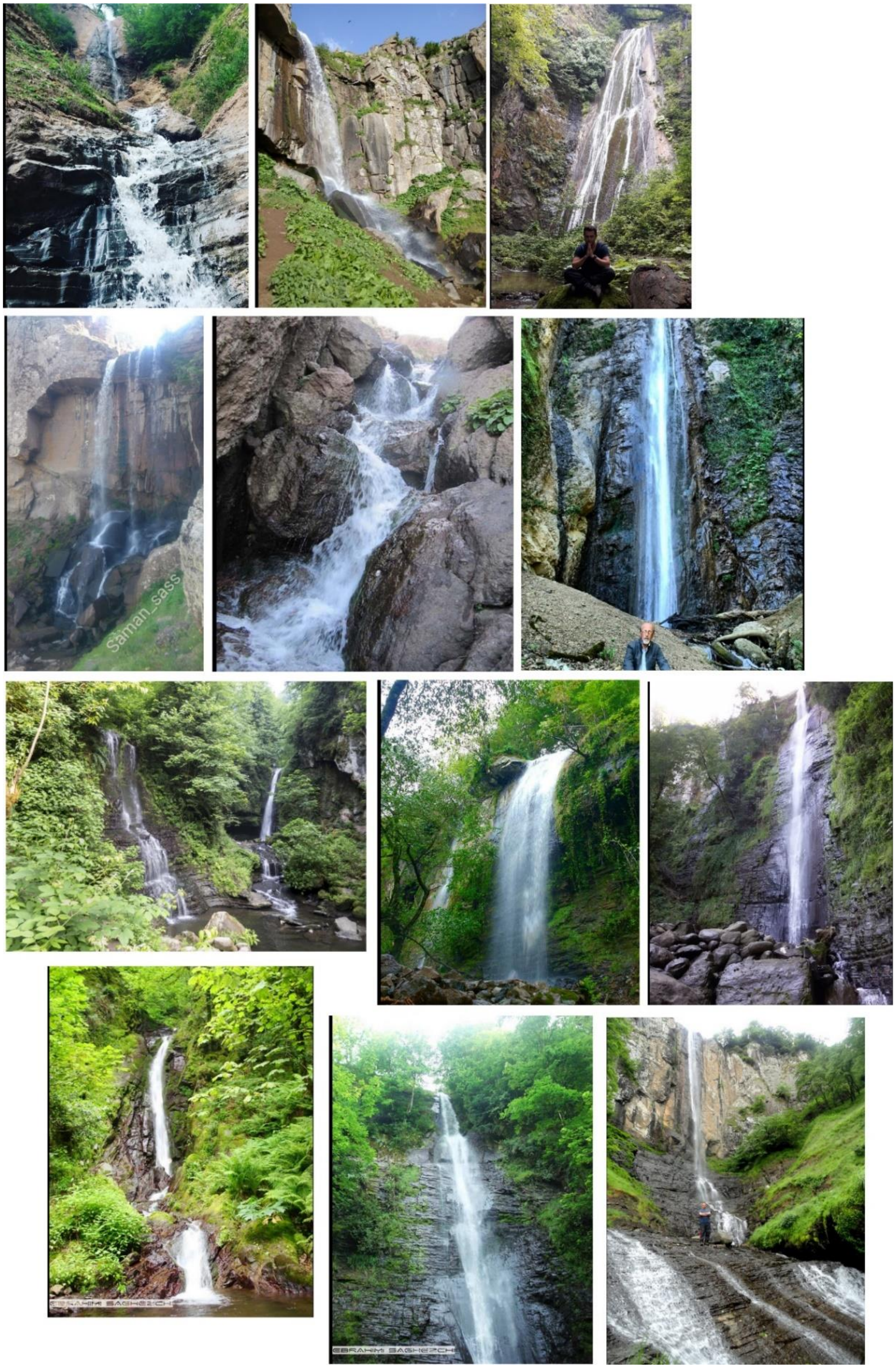

Figure S2.9. Field photos of the major knickpoints in the southern sector of the Talesh Mountains taken from Google Maps Photos (source: http://earth.google.com).

Table S2.1. Specific gravity determination for the rock samples in the north Talesh Mountains.

Sample no.	SCH7	SCH7b	SCH8
In-air weight of sample (g)	1414.1	1564.8	1877.1
In-air weight of sample + stearin (g)	1450.4	1598.1	1904.7
Immersed weight of sample + stearin (g)	846.0	998.0	1194.2
Stearin weight (g)	36.3	33.3	27.6
Stearin density (g/cm³)	0.903	0.903	0.903
Stearin volume (cm³)	40.20	36.88	30.56
Water volume (cm³)	604.40	600.10	710.50
Adjusted volume (cm³)	564.20	563.22	679.94
Specific gravity (g/cm³)	2.506	2.778	2.761
Weight for unit volume (kN/m³)	24.58	27.25	27.07

Average weight per unit volume	2.682 g/cm³	26.30 kN/m³
Standard deviation	0.152	1.49

Table S2.2. Specific gravity determination for the rock samples in the central Talesh Mountains.

Sample no.	SCH5	SCH6
In-air weight of sample (g)	1701.2	1708.3
In-air weight of sample + stearin (g)	1751.0	1761.3
Immersed weight of sample + stearin (g)	938.0	1077.3
Stearin weight (g)	49.8	53.0
Stearin density (g/cm³)	0.903	0.903
Stearin volume (cm³)	55.15	58.69
Water volume (cm³)	813.0	684.0
Adjusted volume (cm³)	757.85	625.31
Specific gravity (g/cm³)	2.245	2.732
Weight for unit volume (kN/m³)	22.01	26.79

Average weight per unit volume	2.488 g/cm³	24.40 kN/m³
Standard deviation	0.244	2.39

Table S2.3. Specific gravity determination for the rock samples in the south Talesh Mountains.

Sample no.	SCH1	SCH2	SCH4
In-air weight of sample (g)	1492.2	2175.5	2178.0
In-air weight of sample + stearin (g)	1449.0	2192.8	2214.0
Immersed weight of sample + stearin (g)	839.0	1342.0	1304.6
Stearin weight (g)	19.8	17.3	36.0

Stearin density (g/cm^3)	0.903	0.903	0.903
Stearin volume (cm^3)	21.93	19.16	39.87
Water volume (cm^3)	610.0	850.80	909.40
Adjusted volume (cm^3)	588.07	831.64	869.53
Specific gravity (g/cm^3)	2.430	2.616	2.505
Weight for unit volume (kN/m^3)	23.83	25.65	24.56

Average weight per unit volume	2.517 g/cm^3	24.68 kN/m^3
Standard deviation	0.093	0.92

Table S2.4. Results of point-load test for the rock samples in the north Talesh Mountains.

Test no.	W (mm)	D (mm)	D/W	P (KN)	D^2_e (mm^2)	D_e (mm)	I_s (MPa)	F	$I_{s(50)}$ (MPa)
1	121	41	0.34	33	6316.54	79.48	5.22	1.23	6.44
2	83	35	0.42	23	3698.76	60.82	6.22	1.09	6.79
3	107	42	0.39	29	5721.94	75.64	5.07	1.20	6.11
4	54	48	0.89	22	3300.24	57.45	6.67	1.06	7.10
5	61	40	0.66	25	3106.70	55.74	8.05	1.05	8.45
6	40	25	0.63	17	1273.24	35.68	13.35	0.86	11.47
7	44	25	0.57	21	1400.56	37.42	14.99	0.88	13.16
8	71	25	0.35	17	2260.00	47.54	7.52	0.98	7.35
9	69	20	0.29	13	1757.07	41.92	7.40	0.92	6.83
10	104	60	0.58	42	7945.01	89.13	5.29	1.30	6.86
11	96	49	0.51	25	5989.32	77.39	4.17	1.22	5.08
12	104	35	0.34	26	4634.59	68.08	5.61	1.15	6.45
13	92	28	0.30	25	3279.87	57.27	7.62	1.06	8.10
14	63	30	0.48	26	2406.42	49.06	10.80	0.99	10.71
15	62	27	0.44	17	2131.40	46.17	7.98	0.96	7.69
16	45	29	0.64	17	1661.58	40.76	10.23	0.91	9.33
17	94	29	0.31	22	3470.85	58.91	6.34	1.08	6.82
18	77	34	0.44	22	3333.34	57.74	6.60	1.07	7.04
19	73	20	0.27	17	1858.93	43.12	9.15	0.94	8.56
20	118	82	0.69	23	12319.9	111.0	1.87	1.43	2.67
21	100	64	0.64	25	8148.73	90.27	3.07	1.30	4.00
22	72	76	1.06	22	6967.17	83.47	3.16	1.26	3.98
23	72	45	0.63	31	4125.30	64.23	7.51	1.12	8.41
24	81	30	0.37	21	3093.97	55.62	6.79	1.05	7.12

25	81	51	0.63	31	5259.75	72.52	5.89	1.18	6.97
26	64	48	0.75	22	3911.39	62.54	5.62	1.11	6.22
27	59	30	0.51	22	2253.63	47.47	9.76	0.98	9.54
28	58	29	0.50	16	2141.59	46.28	7.47	0.97	7.22
29	67	40	0.60	24	3412.28	58.41	7.03	1.07	7.54
30	45	32	0.71	22	1833.46	42.82	12	0.93	11.19

Estimate of simple compressive strength (MPa) 20-25 $I_{s(50)}$	150.14 - 187.67
Estimation of indirect tensile strength (MPa) 0.8 $I_{s(50)}$	9.38

Mean $I_{s(50)}$	7.51 MPa
Standard deviation	2.23

Table S2.5. Results of point-load test for the rock samples in the central Talesh Mountains.

Test no.	W (mm)	D (mm)	D/W	P (KN)	D^2_e (mm^2)	D_e (mm)	I_s (MPa)	F	$I_{s(50)}$ (MPa)
1	92	65	0.71	9	7613.97	87.26	1.18	1.28	1.52
2	81	52	0.64	8	5362.88	73.23	1.49	1.19	1.77
3	57	28	0.49	5.50	2032.09	45.08	2.71	0.95	2.58
4	96	50	0.52	9	6111.55	78.18	1.47	1.22	1.80
5	86	40	0.47	6	4379.94	66.18	1.37	1.13	1.55
6	83	45	0.54	10	4755.55	68.96	2.0	1.16	2.43
7	76	45	0.59	14	4354.48	65.99	3.22	1.13	3.64
8	70	75	1.07	10	6684.51	81.76	1.50	1.25	1.87
9	70	75	1.07	6	6684.51	81.76	0.90	1.25	1.12
10	61	25	0.41	8	1941.69	44.06	4.12	0.94	3.89
11	57	35	0.61	12	2540.11	50.40	4.72	1.00	4.74
12	66.5	37	0.56	10	3132.81	55.97	3.19	1.05	3.36
13	53	45	0.85	10	3036.68	55.11	3.29	1.04	3.44
14	100	65	0.65	4.20	8276.06	90.97	0.51	1.31	0.66
15	115	85	0.74	6	12445.9	111.6	0.48	1.43	0.69
16	92	47	0.51	3.50	5505.49	74.20	0.64	1.19	0.76
17	65	42	0.65	2.50	3475.94	58.96	0.72	1.08	0.77
18	111	85	0.77	7	12013.0	119.60	0.58	1.42	0.83

Estimate of simple compressive strength (MPa)	41.60 - 52.00

20-25 $I_{s(50)}$	
Estimation of indirect tensile strength (MPa) 0.8 $I_{s(50)}$	2.60

Mean $I_{s(50)}$	2.08 MPa
Standard deviation	1.27

Table S2.6. Results of point-load test for the rock samples in the south Talesh Mountains.

Test no.	W (mm)	D (mm)	D/W	P (KN)	D^2_e (mm^2)	D_e (mm)	I_s (MPa)	F	$I_{s(50)}$ (MPa)
1	117	65	0.56	27	9862.99	98.40	2.79	1.36	3.78
2	117	50	0.43	17	7448.45	86.30	2.28	1.28	2.92
3	98	65	0.66	21.50	8110.54	90.06	2.65	1.30	3.45
4	83	45	0.54	20	4755.55	68.96	4.21	1.16	4.86
5	59	45	0.76	21	3380.45	58.14	6.21	1.07	6.65
6	86.5	30	0.35	7	3304.06	57.48	2.12	1.06	2.26
7	74	45	0.61	9	4239.89	65.11	2.12	1.13	2.39
8	56	25	0.45	9	1782.54	42.22	5.05	0.93	4.68
9	62	32	0.52	14	2526.11	50.26	5.54	1	5.56
10	60	30	0.5	11	2291.83	47.87	4.80	0.98	4.71
11	57.5	35	0.61	10	2562.39	50.62	3.90	1.01	3.92
12	60.7	22	0.36	8	1700.28	41.23	4.71	0.92	4.31
13	111	90	0.81	22.50	12720.1	112.78	1.77	1.44	2.55
14	61	85	1.39	19	6601.75	81.25	2.88	1.24	3.58
15	77	35	0.45	13	3431.38	58.58	3.79	1.07	4.07
16	99	50	0.51	6	6302.54	79.39	0.95	1.23	1.17
17	79	50	0.63	24	5029.30	70.92	4.77	1.17	5.58
18	77	50	0.65	14	4901.97	70.01	2.86	1.16	3.32
19	67	30	0.45	8	2559.21	50.59	3.13	1.01	3.14
20	69	42	0.61	7	3689.85	60.74	1.90	1.09	2.07
21	87	25	0.29	9	2769.30	52.62	3.25	1.02	3.33
22	61	40	0.66	9	3106.70	55.74	2.90	1.05	3.04
23	65	33	0.51	9	2731.10	52.26	3.30	1.02	3.36
24	133	75	0.56	44	12700.56	112.70	3.46	1.44	4.99
25	97	75	0.77	32	9262.82	96.24	3.45	1.34	4.64
26	97	50	0.52	21	6175.21	78.58	3.40	1.23	4.17
27	87	65	0.75	13	7200.17	84.85	1.81	1.27	2.29

28	84	45	0.54	12	4812.85	69.37	2.49	1.16	2.89
29	75	42	0.56	18	4010.70	63.33	4.49	1.11	4.99
30	85	35	0.41	12	3787.89	61.55	3.17	1.10	3.48
31	65	42	0.65	20	3475.94	58.96	5.75	1.08	6.20
32	62	45	0.73	13	3552.34	59.60	3.66	1.08	3.96
33	57	35	0.61	13	2540.11	50.40	5.12	1.00	5.14
34	73	20	0.27	11	1858.93	43.12	5.92	0.94	5.54
35	52	40	0.77	17	2648.34	51.46	6.42	1.01	6.50
36	75	30	0.40	10	2864.79	53.52	3.49	1.03	3.60
37	50	38	0.76	16.50	2419.16	49.18	6.82	0.99	6.77
38	50	45	0.90	12	2864.79	53.52	4.19	1.03	4.32

Estimate of simple compressive strength (MPa) 20-25 $I_{s(50)}$	81.15 - 101.44
Estimation of indirect tensile strength (MPa) 0.8 $I_{s(50)}$	5.07

Mean $I_{s(50)}$	4.06 MPa
Standard deviation	1.35

References appendix Chapter 2.

Gailleton, B., Mudd, S.M., Clubb, F.J., Grieve, S.W.D. and Hurst, M.D., 2021. Impact of changing concavity indices on channel steepness and divide migration metrics. *Earth and Space Science Open Archive ESSOAr*.

Hoek, E., Carter, T.G. and Diederichs, M.S., 2013, June. Quantification of the geological strength index chart. In ARMA US Rock Mechanics/Geomechanics Symposium (pp. ARMA-2013). ARMA.

Kirby, E. and Whipple, K., 2001. Quantifying differential rock-uplift rates via stream profile analysis. Geology, 29(5), pp.415-418.

Perron, J.T. and Royden, L., 2013. An integral approach to bedrock river profile analysis. Earth Surface Processes and Landforms, 38(6), pp.570-576.

Scherler, D. and Schwanghart, W., 2020. Drainage divide networks–Part 1: Identification and ordering in digital elevation models. Earth Surface Dynamics, 8(2), pp.245-259.

Schwanghart, W. and Scherler, D., 2014. TopoToolbox2-MATLAB-based software for topographic analysis and modeling in Earth surface sciences. Earth Surface Dynamics, 2(1), pp. 1-7.

Snyder, N.P., Whipple, K.X., Tucker, G.E. and Merritts, D.J., 2000. Landscape response to tectonic forcing: Digital elevation model analysis of stream profiles in the Mendocino triple junction region, northern California. Geological Society of America Bulletin, 112(8), pp.1250-1263.

Vergari, F., Troiani, F., Faulkner, H., Del Monte, M., Della Seta, M., Ciccacci, S., and Fredi, P. (2019). The use of the slope–area function to analyse process domains in complex badland landscapes. Earth Surface Processes and Landforms, 44(1), 273- 286. https://doi.org/10.1002/esp.4496

Appendix Chapter 3.

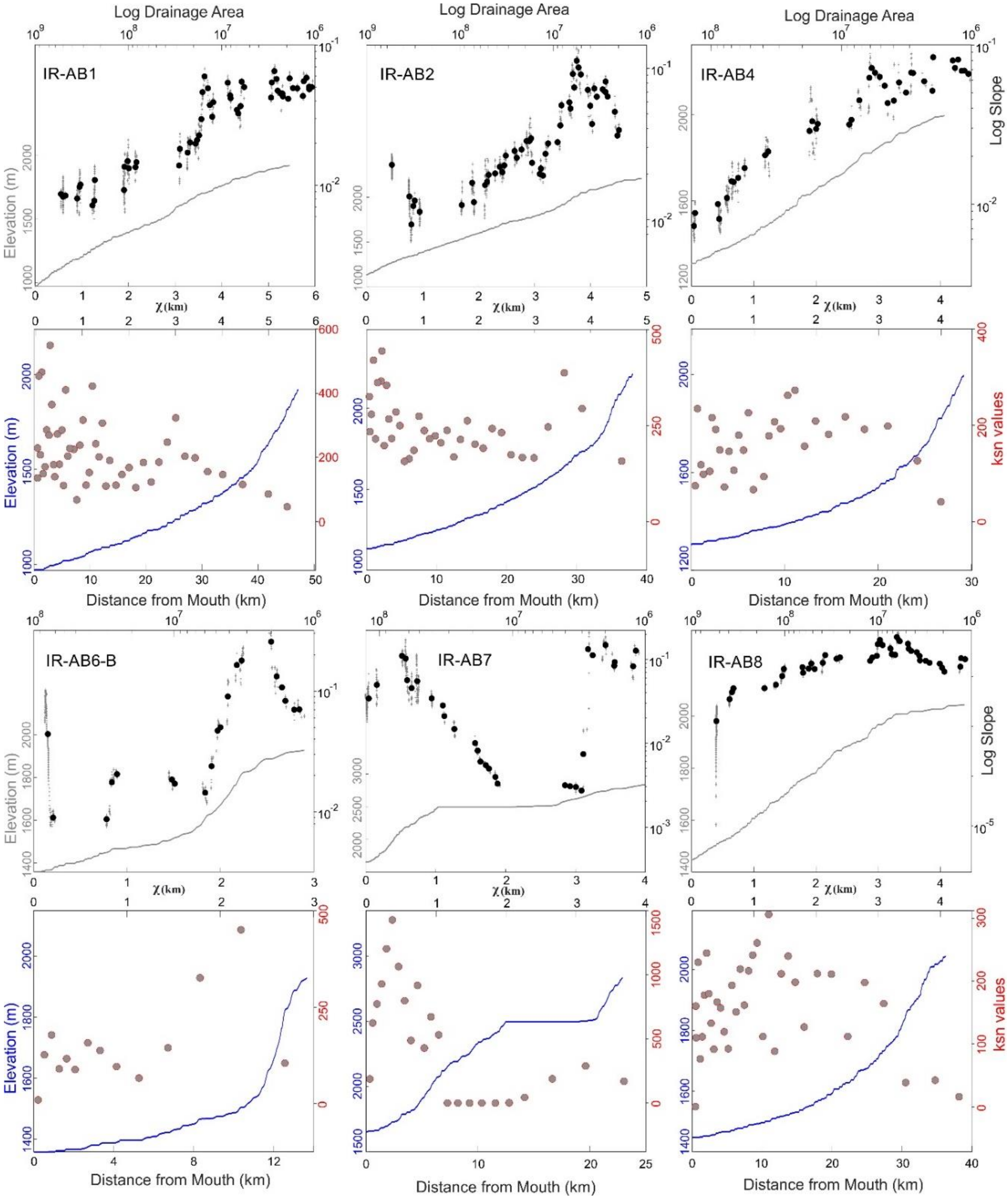

Figure S3.1. Sampled-catchment river profiles in the plateau interior. Profiles at the top show log-log slope-area (black dots) and χ-elevation plots (black solid lines). Profiles at the bottom represent longitudinal river profiles (solid blue lines) and χ versus k_{sn} values (gray dots).

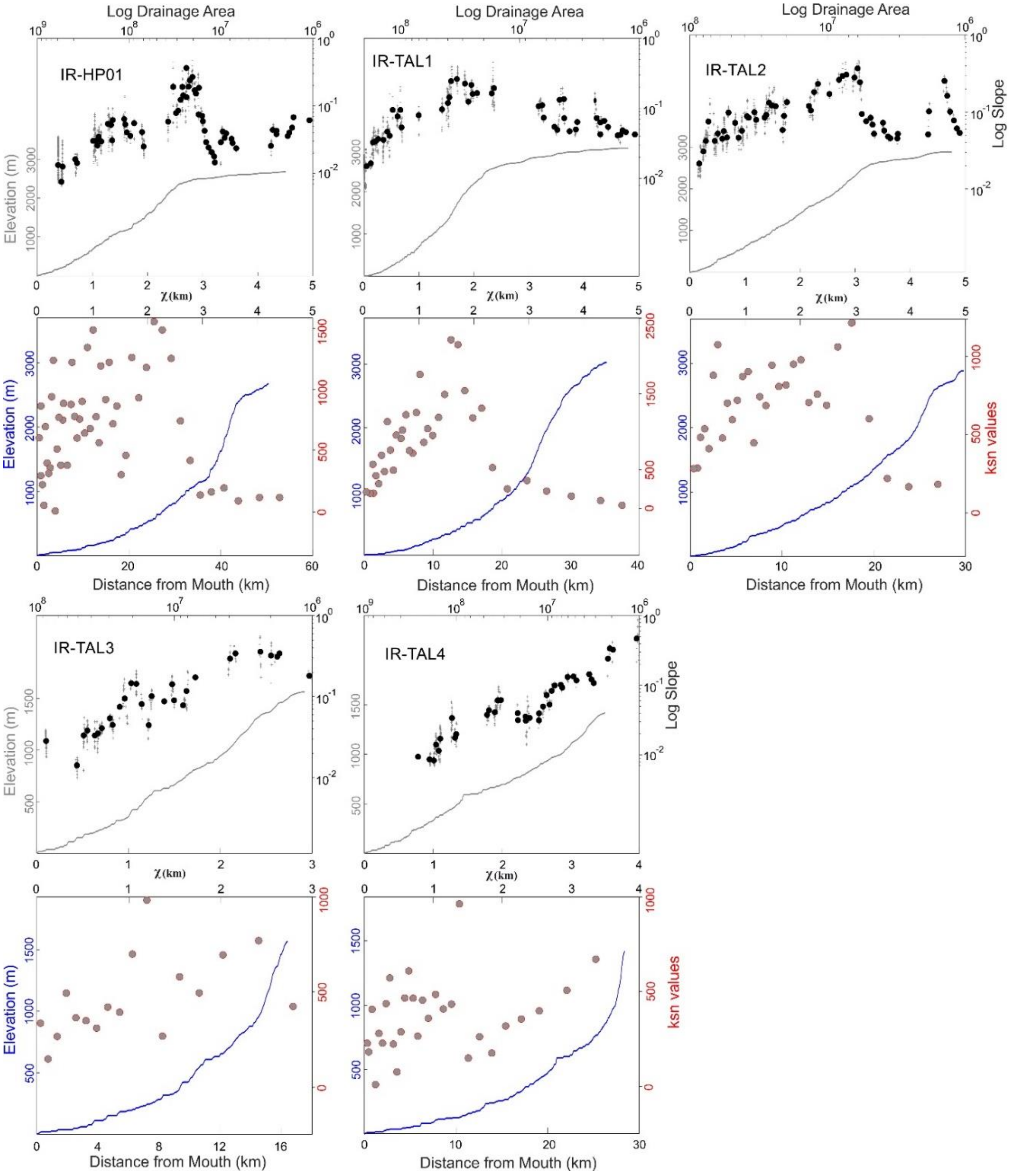

Figure S3.2. Sampled-catchment river profiles in the plateau exterior. Profiles at the top show log-log slope-area (black dots) and χ-elevation plots (black solid lines). Profiles at the bottom represent longitudinal river profiles (solid blue lines) and χ versus k_{sn} values (gray dots).

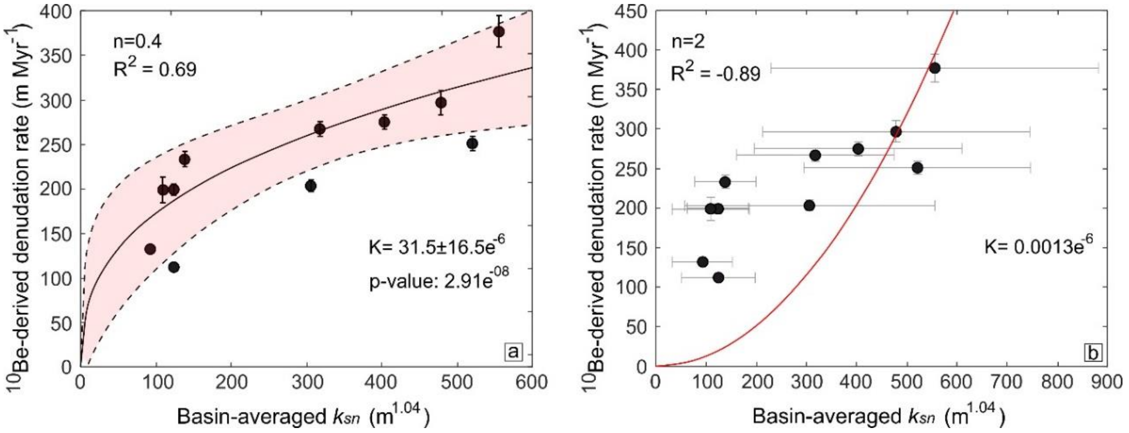

Figure S3.3. ^{10}Be-derived catchment-averaged erosion rates versus basin-averaged (a) steepness index

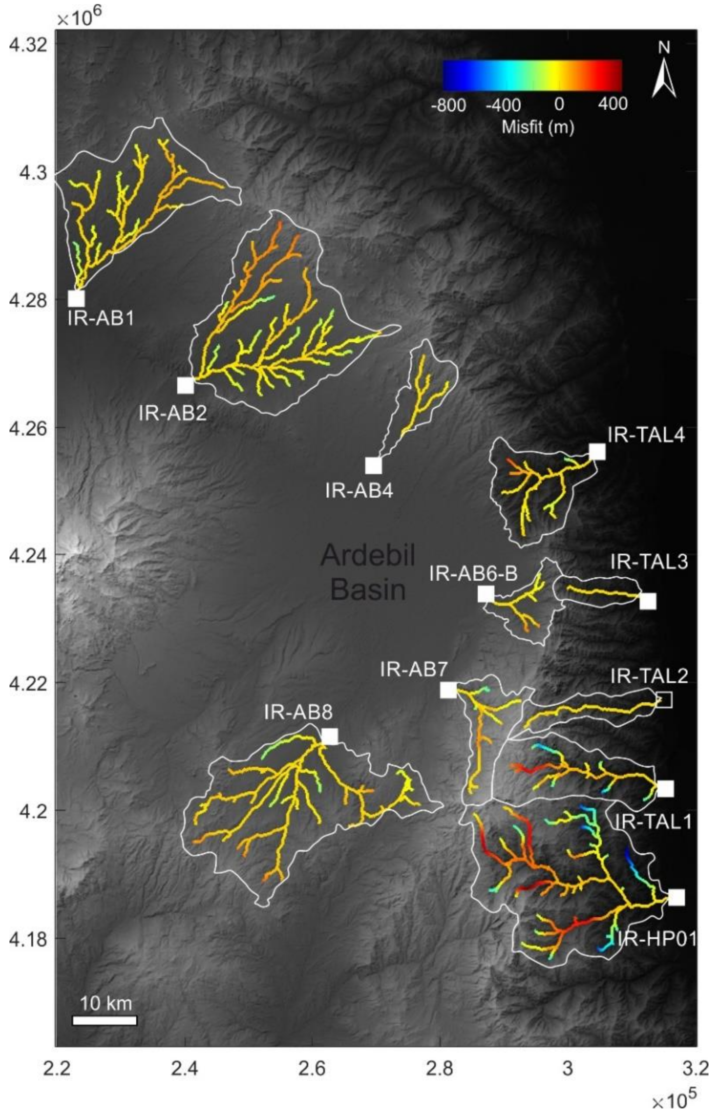

Figure S3.4. Difference map between real and modeled elevations of the sampled catchments in the study area for the river inversion analysis

Table S3.1. Rock erodibility domains in the study area

Domain	Lithology	Mean erodibility ($K \times 10^{-6}$ m yr^{-1})	Area (km^2)	Percentage (%)
1	Andesite	0.68±0.38	656	23.2
2	Andesitic tuff	1.01±0.018	179	6.33
3	Volcaniclastics, clastics	0.85±0.25	900	31.84
4	Clastics units	1.58±0.04	32	1.13
5	Limestone	0.86±0.43	219	7.74
6	Volcaniclastics rocks	0.69±0.044	378	13.4
7	Quaternary	1.51±1.33	463	16.36